Utilising inkjet printing for tissue engineering

Thesis submitted to the University of Sheffield for the degree of Doctor of Philosophy

Christopher Tse

Department of Mechanical Engineering

October 2015

ACKNOWLEDGEMENTS

I would like to thank my supervisor Dr. Patrick Smith for welcoming me into the Smith group, for his continuous guidance, encouragement, support and friendship. It has been an absolute pleasure to work under Patrick, and there are few academics who showed so much compassion with their students.

I would like to thank my co-supervisor Prof. Sheila MacNeil who gave me the opportunity to work and study within Sheffield, and gave guidance to my PhD. Without her actions and welcoming me into her group, the opportunities presented to me throughout my time in Sheffield would not have happened, and therefore I am eternally grateful for her confidence in my abilities.

I would like to thank my co-supervisor Prof. John Haycock who provided great insight and guidance with work relating to nerves. John allowed me to take part in many events showcasing the capabilities of 3D printing and bioprinting, and I built a strong relationship within his group.

I would like to thank the support and guidance from individuals who have contributed to enabling me to complete my research; Nii Armah, James Clarke, Ahssad Fiaz, Piotr Geca, Nicola Green, Joe Lemmens, Shweta Mittar, Tom Paterson, Colin Sherborne, Dharaminder Singh, Jonathan Stringer for his bright ideas together with Patrick Smith, Vicky Yeung, Yi Zhang.

I would like to thank friends who have made my time in Sheffield an absolute pleasure, who I will miss very much as they all progress with their own careers and dreams; Daniel Backhouse, Elliot Carrington, Ali Chan, Wayne Chiu, Candi Chu, Anna van Doorn, Vian Fu, Zijing Huo, Amie Kim, Anna Lai, Andrew Newton, Lena Nixon, Katerina Iotova, Ariadna Ribés, Matilda Rimbaud, Aman Singh, Josh Stroud, Alex Stross, Gadam Sung, Kassandra Talbot, Ian Tsang, Tereza Vaňková, Vishanth Vijayakumar, Siu Wong, Vinnie Yip, Norihiro Yoshitome, Tracy Tong Yu, Felicia Zhou.

I would like to thank my family; Cheung Hing Tse, Yin Foon An, Boris Patta, Valérie Tse Bresler, Vernon Li, Raymond Li.

ACRONYMS

%	percentage
°C	degrees Celsius
ρ	liquid density
γ	surface tension
μ	liquid viscosity
μg	microgram
μl	microliter
μm	micrometer
μm^2	square micrometre
2D	two dimensional
3D	three dimensional
FCS	foetal calf serum
cm	centimetre
cm^2	square centimetre
cm^3	cubed centimetre
DAPI	4‟,6 diamidino-2-phenylindole
DMEM	Dulbecco's Modified Eagle's Medium
ECM	extracellular matrix
FITC	Fluorescein isothiocyanate
g	gram
h	height
l	length
mg	milligram
min	minute
ml	millilitre
mm	millimetre

MTT	(3-(4,5-Dimethylthiazol-2-yl)-2,5-diphenyltetrazolium bromide)
n	technical repeat
nm	nanometre
Oh	Ohnesorge number
Pa	Pascal
Psi	pounds per square inch
PBS	phosphate-buffer saline
pH	potential of hydrogen
r	radius
Re	Reynolds number
SD	standard deviation
TCP	tissue culture plastic
TRITC	tetramethyl rhodamine isothiocyanate
V	Volume
v/v%	percentage by volume
We	Webers number
wt%	percentage by weight
z	Z number

SUMMARY

The field of tissue engineering has the potential to improve the quality of life of individuals through combining the knowledge of engineering and life sciences in creating engineered biological substitutes that repair, support and enhance tissue function.

Inkjet printing is a versatile tool that can be used for a broad range of applications. Ubiquitous in households, offices and industry, there has been growing interest in the use of inkjet printing for biological applications. Inkjet printing allows the user to deposit nano-picolitre volume of inks of low viscosity with high precision and high repeatability. Within this thesis, inkjet printing was used to explore its applications in the life sciences, with jetting behaviour and scaffold design optimised.

The creation of cell-friendly scaffolds was investigated. Gelatin scaffolds, crosslinked with inkjet printed glutaraldehyde were fabricated. Fibroblasts were seeded onto these fabricated scaffolds and shown to proliferate without hindrance, allowing a method to create sub-millimetre cell-friendly fibres for tissue engineering applications.

The ability for inkjet printing to create scaffolds to control cell alignment was investigated. Cell orientation can be controlled through inkjet printing paraffin wax to restrict cell proliferation on a substrate. Paraffin wax is not harmful or toxic to cells, and cells were able to grow within the negative spaces between the wax patterns, to create aligned cell culture as cells proliferated. An advantage with the wax scaffolds was that the wax scaffold was readily removable with a scalpel that allowed further analysis of cell behaviour when proliferating into an unrestricted space. A proportion of cells was also detached upon wax removal, proportional to cell density within the wax scaffold and wax channel width. After wax removal, cell cultures quickly lost their ordered appearance within 3 days as they proliferated randomly across the substrate.

The creation of *in vitro* vasculature models through the use of a combination of inkjet-printed wax, PDMS moulding and wax-loss method to create medical phantoms for the study of rheological behaviour was studied. The scalloping behaviour of the printed wax vessel was reduced in the final

phantom created, as there would be a thin lining of wax that covers the interior of the PDMS mould after wax removal, making the vessel smoother.

Cell printing of neuronally relevant cells were investigated. NG108-15 and porcine Schwann cells (along with fibroblasts to act as a control experiment) were inkjet printed, studying cell viability during and after inkjet printing. It was concluded that cells were not significantly damaged during inkjet printing over a wide range of voltages (50 V-230 V), and no correlation was seen to show an increase in cell death with increasing voltages. Inkjet printed NG108-15 cells showed they produced longer neurites compared to control samples after 7 days. Further to results, it was confirmed that cell printing is limited to a duration of less than 40 minutes due to cell aggregation within the reservoir of the printing system, causing a steady significant decrease in cell numbers during printing.

List of Figures

Figure 1.1.1 Overview of critical issues in tissue engineering 25

Figure 1.1.2 Diagram depicting a tissue engineering concept that involves seeding cells within a tissue engineered scaffold 27

Figure 1.1.3 Schematic diagram of the electrospinning process, and an image of fibres created through electrospinning 28

Figure 1.1.4 Schematic diagram of an example of photolithography used to fabricate a PDMS stamp from a master having relief structures in photoresist on its surface. 29

Figure 1.1.5 Illustration of the procedure used to pattern proteins and cells using microfluidic channels 29

Figure 1.2.1 micrograph of typical top surface morphology of alginate scaffold made with 3% alginate and 0.03 m calcium chloride 31

Figure 1.2.2 Effect of substrate mechanical properties on fibroblast actin cytoskeleton on fibroblasts grown polyacrylamide gels with varying stiffness. Fibroblasts on soft materials had no stress fibres compared with fibro-blasts on stiffer materials that do have articulated stress fibres with defined orientations 32

Figure 1.2.3 [Left] Schematic depictions (a) and SEM images (b) of representative nanotopography geometries. Three basic nanotopography geo-metries include nanograting (458 tilt, scale bar 5 mm), nanopost array(158 tilt, scale bar 5 mm), and nanopit arrays (08 tilt, scale bar 1 mm). [Right] Epithelial cells growing in the direction of the orientation of a nanograted surface, compared to a smooth surface for control, as shown with light and confocal microscopy 33

Figure 1.2.4 Histomorphometric analysis of nerves (or graft) that were cultured on different substrate surfaces 35

Figure 1.3.1 Inkjet printed PLGA on polystyrene substrates, with stem cells preferentially growing on PLGA. Images taken 5 days after cell seeding. Scale bar = 500 mm. 37

Figure 1.3.2 Laser-guided direct writing of living cells. This example shows embryonic chick spinal cord cells moving on a glass cover slip. Arrow heads mark the position of cells 38

Figure 1.4.1 Example of a commercial product that mimics arterial bifurcation vasculature, with features to mimic different stenosed vessel geometries. Such tools can help medical professionals to better understand the rheological conditions in their patients 40

Figure 1.5.1 4 types of additive manufacturing systems 41

Figure 1.5.2 Examples of structures created with extrusion technology. a) extrusion printing system, b) biologically relevant structures created with extrusion printing, c) scanning electron microscopy of cross-section of scaffold d) shows proliferation of cells in biocompatible porous scaffold created with extrusion technology 43

Figure 1.5.3 Schematic elucidating the tissue printing process using an additive manufacturing technique 44

Figure 1.6.1 Schematic diagram showing the principles of operation of a) continuous inkjet (CIJ) printer b) thermal drop on demand (DOD) c) piezoelectric DOD 47

Figure 1.7.1 X-ray image of the printhead used within this document. The image illustrates a glass nozzle tube with 50μm inner diameter which is sleeved with a tube-type piezoelectric element 48

Figure 1.7.2 Diagrams depicting each stage of droplet formation caused by the actuation of the piezoelectric crystal in the printhead. A) showing the identification of each section of the diagram. B) upon the application of voltage into the piezoelectric actuator, the piezo actuators move radially outward, creating a negative pressure within the chamber. C) this negative pressure moves to both ends of the chamber, with half the amplitude. D) The negative pressure reaches the nozzle tip (closed end) and returns with the same phase, whilst the negative pressure returning from the open end has its phase reversed. In live experiments, steps (B-D) can be seen clearly as the liquid within the nozzle can be seen to be sucked into the nozzle; caused by the build-up of negative pressure within the chamber. E) all this occurs and the piezoelectric actuator returns back to position and causes a positive pressure to be produced. F) the acoustic waves formed by the piezoelectric actuator moving radially outward and inward combine together. G) the two waves moving towards the open end cancel each other out (positive+negative wave), and the waves traveling to the nozzle stack together (positive+positive wave). The overall product is a large positive acoustic wave being produced that moves to the nozzle 49

Figure 1.7.3 Examples of principle printed-line behaviours: a) individual drops; b) scalloped; c) uniform; d) bulging; e) stacked coins. Morphology is dependent on droplet spacing and inter-droplet drying, Drop spacing decreases from left to right 52

Figure 1.7.4 Graphical representation of the formation of different line behaviours proportional to inter-droplet spacing and inter-droplet drying 53

Figure 1.7.5 Generation of coffee staining. With a volatile liquid with nanoparticles, the rate of evaporation is larger at the edges compared to the centre, leading to the nanoparticles being transported to the pinned contact angle 54

Figure 1.7.6 Through the use of difference solvents, the deposition of nanoparticles can be controlled to create varying steepness of valleys within coffee stained structures 55

Figure 1.8.1 Images depicting different principles of extrusion bioprinting technology: e) extrusion in air; f) extrusion dispensing in fluid; g) dispensing spheroids of cells in air; h) dispensing spheroids of cells in fluid; i) a step-by-step process of a self-assembled tubular structure through bioprinting of spheroids 56

Figure 1.8.2 Theoretical eveolution of bioprinting 57

Figure 1.8.3 Inkjet printing was used to print collagen onto agarose coated glass slides that allowed directed cell positioning 59

Figure 1.8.4 Neurons growing on inkjet patterned collagen substrates 59

Figure 1.8.5 Hydrophobic inks were printed to create the desired channels in between the spacing of two hydrophobic coated glass slides. a) Y-shaped figure printed on the slide. Photographs of the Y-shaped channel, b) near the inlets, c) near the outlet when the injection rate was 5 ml/min, and d) near the outlet when the rate was 0.5 ml/min 60

Figure 1.8.6 Viability of HT1080 cells as determined by a live–dead assay after inkjet printing different printing parameters 61

Figure 1.8.7. Quantitative cell printing showed percentage of drops containing cells varied linearly except for the highest concentration 63

Figure 1.9.1 Gelatin scaffolds used for tissue engineering cultured in well plates 67

Figure 1.9.2 Printing setup during the printing paraffin wax scaffolds 67

Figure 1.9.3 Patterning hydrophobic barriers in paper by wax printing 68

Figure 2.1.1 Photograph showing the Microfab piezoelectric printer used for this study, with magnified images of the CCD camera, printhead holding platform, and printhead during jetting 70

Figure 2.2.1 Light microscopy images of NG108s cultured with foetal calf serum on day 1 (A) and day 3 (B), and an overlay of highlighting the spindle-like dendritic protrusions in white (C). NG108s cultured without foetal calf serum on day 1 (D) and day 3 (E) and an overlay of highlighting the spindle-like dendritic protrusions in white (F). Scale bar = 200 µm. 73

Figure 2.4.1 A typical script that is used for Bitmap applications 76

Figure 2.4.2 Key to understanding the Bitmap script 77

Figure 2.5.1Schematic diagram of how the phantoms were made; A) Molten paraffin wax, heated to 75°C in the inkjet printer, is printed onto a glass slide to create a channel. B) A pipette is used to pipette out a droplet of paraffin wax on top of the printed wax, which will later become the aneurism. C) Sample is placed in a petri dish, PDMS is poured into the petri dish, placed under vacuum to remove bubbles and left overnight. D) Once the PDMS has fully cured, a scalpel knife is used to cut out the sample. E) Blunt ended needles were used to pierce through the PDMS and make contact with the wax and air at both ends of the phantom. F) The sample is heated to 80°C and a syringe pump is used to remove the wax from inside the phantom, creating a hollow cavity within the PDMS scaffold 79

Figure 2.5.2 Images of fabricated negative phantoms using paraffin wax. A) Wax samples ready for PDMS moulding. B) After the PDMS has set, a scalpel was used to cut the sample out of the petri dish. C) Piercing the ends of the channel, the sample was placed in an oven at 80°C and the wax was sucked out. D) Microscope image of printed line (channel) and pipetted aneurism that combine together to form the phantom. Scale bar = 2 mm 80

Figure 2.5.3 Identifying each section of the phantom Left) raw image captured of microbeads flowing through a phantom Right) the same image edited to show contract between fluid cavity (white) and surrounding PDMS (black). The dimensions of the phantom is more clearly seen when fluorescent beads are passing through. Scale bar = 1000 µm 81

Figure 3.1.1 Gelatin is denatured collagen, and the various reactions pathways shown here can be related to the crosslinking of gelatin (i.e. Coll-NH_2 = Collagen-amine group) 83

Figure 3.2.1 Photograph showing gelatin scaffolds that were soaked in 8% glutaraldehyde in 5 hours. This concentration and amount of time for crosslinking was too much, and when cells and cell media was added, the media and the scaffold turned brown, indicating that the crosslinked gelatin was toxic and was not a viable scaffold 86

Figure 3.2.2 Visual analysis of fibroblasts. (Left) fibroblasts grown on 2% gelatin, 30 minutes of 0.125% glutaraldehyde, day 1. (Right) fibroblasts grown on 2% gelatin, 30 minutes of 0.50% glutaraldehyde, day 1. Scale bar = 200 µm 86

Figure 3.2.3 A set of three graphs showing the optical density reading of fibroblasts on gelatin hydrogels crosslinked with glutaraldehyde, 1 day after seeding 40,000 cells. Key indicates the experimental parameters i.e. "4% gel 1 hour" = on 4% gelatin and crosslinked for 1 hour. Optical density readings are MTT assays that give an indication of metabolic activity of cells in culture. Concentrations of 0% glutaraldehyde are controls. n = 1 89

Figure 3.2.4 Optical density reading of fibroblasts on gelatin hydrogels crosslinked with glutaraldehyde, after 3 days after seeding 40,000 cells. Only reading above 0.1 were plotted, as any value below 0.1 were considered not sufficiently viable. Key indicates the experimental parameters i.e. "4% gel 1 hour" = on 4% gelatin and crosslinked for 1 hour. Optical density readings are MTT assays that give an indication of metabolic activity of cells in culture. Concentrations of 0% glutaraldehyde are controls. n=1 89

Figure 3.3.1 Screen-capture of a successful jetting of a droplet of 1% glutaraldehyde (w/w in water), scale bar = 100 µm 92

Figure 3.4.1 Image showing the hatch pattern designed for printing onto gelatin. A droplet spacing of 100 µm was used, and the distance between each connection within the pattern would be 2.5 mm across 93

Figure 3.4.2 Photographs of inkjet printed glutaraldehyde onto a bed of 4% gelatin on a glass slide. The samples were cut out into segments that would fit into a well in a 6-well plate, using a scalpel 94

Figure 3.4.3 Image showing an experimental procedure where the crosslinked samples were put into labelled 6 well plates prior to washing away the uncrosslinked gelatin 94

Figure 3.4.4 A collection of images showing crosslinked gelatin scaffolds being washed with hot water in well plates. The samples shown here are samples that were crosslinked with 25% glutaraldehyde and left overnight for 24 hours. Only samples that were crosslinked with 10-25% glutaraldehyde and allowed to crosslink for 24 hours created sufficiently mechanically strong scaffolds. All other samples that were created were too flimsy and collapsed on their own structure during the washing and cell seeding stages 95

Figure 3.4.5 Washed samples of 25% glutaraldehyde-crosslinked gelatin on (Left) a petri dish and (Right) when reacted in a tub of gelatin. Because of the restrictions of not being able to diffuse further in the z-axis when pipetted onto a bed of gelatin on a petri dish, the residual glutaraldehyde in the crosslinked gelatin is highly concentration in the centre, and is highly toxic to cells. When there is no restriction to glutaraldehyde diffusion, there is no concentric accumulated of residual glutaraldehyde, and would not pose the same toxicity 97

Figure 3.5.1 Crosslinked gelatin pattern created with an inkjet printer. 25% glutaraldehyde was printed onto a bed of 4% gelatin with a droplet spacing of 100 µL, left for 24 hours for crosslinking to take place, and then compartmentalised in well plates prior to washing with 50°C distilled water 5 times to remove uncrosslinked gelatin and residual glutaraldehyde 98

Figure 3.5.2 Microscopy images of fibroblasts seeded onto crosslinked gelatin through inkjet printing glutaraldehyde onto a bed of gelatin. Images taken 1, 2 and 3 days after cell seeding respectively. Enlarged images can be found in Figure 3.5.4. Scale bar = 300 µm 99

Figure 3.5.3 Microscopy images of fibroblasts seeded onto crosslinked gelatin created with inkjet printing. Images taken 1, 2 and 3 days after cell seeding respectively. Scale bar = 300 µm 100

Figure 3.5.4 Enlarged microscopy images of fibroblasts seeded onto crosslinked gelatin through inkjet printing. Images taken 1, 2 and 3 days after cell seeding respectively. Scale bar = 150 µm 101

Figure 3.5.5 Confocal image of a cross-section of the middle of a gelatin scaffold beam stained for actin (red; phalloidin-TRITC) and nuclei (blue; DAPI) 102

Figure 3.5.6 A sequence of 2D images of a 3D projected crosslinked gelatin scaffold with seeded fibroblasts after 1 day, stained for actin (red; phalloidin-TRITC) and nuclei (blue; DAPI). Scale bar = 250 µm 103

Figure 3.5.7 A sequence of 2D images of a 3D scaffold that shows fibroblasts grown on glutaraldehyde-crosslinked gelatin. A 3D image was generated through the stacking of multiple confocal images to create a z-

stack. Stained for actin (red; phalloidin-TRITC) and nuclei (blue; DAPI), day 3 after cell seeding. Cells proliferated significantly more on the surface side where cell seeding took place. Cells can be seen to infiltrate within the gelatin and grow within the scaffold. Scale bar = 250 µm *104*

Figure 4.2.1 Viscosity values of paraffin wax over a range of temperatures, which was Newtonian when molten. Printing parameters below 20 mPa.s was optimal for printing *109*

Figure 4.2.2 A collection of images showing the jetting molten wax with carrying jetting parameters, noting the variance in droplet size, from 45-17 µm. Note that conventional research had pointed out that, as a rule of thumb, the droplet size deposited onto the substrate would be roughly twice the diameter of the nozzle used. Droplets of 35 µm were easily created with a 50um diameter nozzle, through optimising the jetting parameters and the ease of forming single droplets with paraffin wax. Scale bar = 200 µm *110*

Figure 4.2.3 Inkjet printing an array of paraffin wax at 70°C, with droplet spacing of 140um between each droplet. Left; showing an example of successful droplet jetting with parameters outlined in Table 1. Right; using ImageJ and setting the appropriate scale bar, the diameter of the droplets could be measured. Wax diameter = 32.5 µm, SD+ 1.53 µm. Sample size= 10. Scale bar = 500 µm *110*

Figure 4.2.4 Decreasing the droplet spacing allows individual droplets to merge together to form a solid single line. Left to right; droplet spacing starts at 120 µm, and decreasing 10 µm per image, until a final droplet spacing of 20 µm can be seen in the last image. Bulging can be seen with a droplet spacing of 30 µm, and with 20 µm, the droplets begin staking on top of one another, creating a sloped wall with height. Scale bar = 1 mm *112*

Figure 4.3.1 More organic printed scaffolds could be created that were just as easy to print, as shown here with a wax patterned tree on a glass slide. *113*

Figure 4.3.2 Scaled-up versions of the original printed circuitry pattern, to show scaling is not an issue with the inkjet printing technique. The wax was submerged in blue ink to show contrast between the glass and wax. The thickest channels measured to be 80 µm, and decreased to 50, 34, 37, 20 and 11.5 µm to the smallest channel respectively. Scale bar of unexpanded image = 20 mm, scale bar of expanded images = 200 µm *114*

Figure 4.3.3 Glass slide with a variety of inkjet printed patterns *115*

Figure 4.3.4 Scaled-up versions of the original printed circuitry pattern, to show scaling is not an issue with the inkjet printing technique. The smallest resolution channels that were produced were 3.5 µm, as shown in the top right enlarged image, with 10 µm inlets. Scaled-up versions had 14 µm, 31 µm and 31 µm and 71 µm for channel widths and inlets respectively. The wax was submerged in blue ink to show contrast between the glass and wax. Scale bar of unexpanded image = 10 mm, scale bar of expanded images = 200 µm *116*

Figure 4.3.5 Enlarged image of microprocessor pattern to show 3.5 µm width channels. Scale bar = 200 µm *117*

Figure 4.3.6 Inkjet printed microdevices using wax. Left: showing samples created with the inkjet printer with the circuitry pattern on cover slips placed inside a petri dish. Middle: Enlarged image of the inkjet printed wax circuitry pattern on a glass cover slip. Several imaged were merged with Photoshop CS3 to create a large enough image of the whole pattern. Scale bar = 1 mm Right: Black and white bitmap image used to create the circuitry pattern *118*

Figure 4.4.1 A cross section of a design of a microdevice. Wax (grey) is sandwiched between two pieces of glass. The need for multiple layers of wax to create appropriate dimensions for fluid flow needs to be balanced by the number of layers. (Left) if one layer was printed, the width would be large, and the height too low. (middle) has similar unsuitable width/height ratio. (Right) this design would be best, whereby the width and height are similar *119*

Figure 4.4.2 Examples of Bitmaps used for printing 2.5D structures. These patterns were printed successively on top of each other to create height within the structures that created separate channels for cell isolates 120

Figure 4.4.3 Images showing the creation of 2.5D structures for the creation of microdevices. Several hundred layers was printed on a glass substrate. The sample has a height of 4 mm 120

Figure 4.4.4 The resultant 2.5D print on glass substrate. A regular pattern was printed four separate times, and from top to bottom, was printed with 10, 30, 60 and 100 repeats respectively 121

Figure 4.4.5 Microscopic images of the honeycomb structured paraffin wax. A-C were repeated 30 times, D-F were repeated 60 times. D and F were imaged captured at an angle to show the dimensions of the structures 122

Figure 4.4.6 With respect to Cyfuse's proprietary bioprinting; Regenova, spheroids are acquired through an automated process of detecting the suitable size of the cell aggregate and then being manipulated by a robotic syringe. Images compiled from acquired from Regenova's promotional video; https://www.youtube.com/watch?v=6SMiCgli8TQ 122

Figure 4.5.1 A 20x20 array of wax droplets on glass, with a droplet spacing of 40 µm between the centre of each droplet. Droplet diameter averages 17 µm. Scale bar = 400 µm 124

Figure 4.5.2 Microscopy images of fibroblasts seeded onto wax arrays after 3 days in culture. (100 um and 60 um droplet spacings) 125

Figure 4.5.3 Microscopy image of RN22s after 1 day of culture on wax arrays with 50um droplet spacing. There is a minimum of 16um channel between each leading edge of a droplet to the adjacent droplet. This channel length was too large, and cells were not organised within the arrays as ordered as 40 µm array scaffolds. Scale bar= 200 µm 126

Figure 4.5.4 Enlarged image of the array in Figure 4.5.1. Wax droplets with droplet spacing of 40um, and each dot being separated by 16 µm at their leading edge to adjacent dots. Average diameter = 34.08 µm, with SD= 0.729, x=10. Scale bar = 160 µm 127

Figure 4.5.5 Cell alignment caused by wax guidance. Top) showing wax arrays 40 µm apart, with RN22s seeded onto the glass substrate after 1 day of culture. Bottom) showing a control sample with RN22s growing on a plain glass slide to show disorder of orientation with respect to the neuritic protrusions. Scale bar = 160 µm and 200 µm 128

Figure 4.5.6 Inkjet printed wax patterns. Top) showing an example of possible microfluidic patterns that can be created, which can allow nerve cells to be seeded and different topological features to be tested under the same environment i.e. straight lines, no features (control) and dot arrays features. Bottom left) an example of a different version of a custom axon isolation device, Bottom right) enlarged image. Neuronal cells would be seeded in areas with the yellow circles, and their neurites could traverse through the channels to join with neighbouring cell bodies 130

Figure 4.6.1 Micrographs of simple patterns that were created using the inkjet printer 132

Figure 4.6.2 Analysis of printed wax patterns. Left) Micrographs of printed wax on glass. Right) same image with additional measurements. Magnified light microscopy images are shown in the small frame. Bar = 200 µm 133

Figure 4.6.3 Micrographs of (a) fibroblasts after 24 hours, (b) Schwann cells after 24 hours. Bars = 50µm and 40µm respectively 135

Figure 4.6.4 Microscopy images of cells proliferating in wax patterned environments. Left) a wax pattern where fibroblasts are proliferating and orientating along the channel after 2 days in culture. Right) the same picture after processing with OrientationJ to highlight the alignment of cells within the channel. Channel widths are 40 µm and 60 µm and bar = 100 µm 136

Figure 4.6.5 Microscopy images of cells proliferating in wax patterned environments. Left) fibroblasts grown between wax patterns after 3 days of culture. Right) The orientation of fibroblasts cells are better visualised using OrientationJ Direction. Top) The widths of the channels were 60um and 36um, Bottom) 145um and 135um, respectively. Scale bar = 200um 137

Figure 4.6.6 Cells confined in a cross-shaped pattern. The width of the horizontal arm is kept constant at 200 mm while the width of the vertical arm varies from 100 mm to 600 mm. (Colour codes show the cellular orientation). r is the ratio of the width of the vertical arm to that of the horizontal one. The central part of the pattern is perfectly oriented in the first three situations. Depending on r, it is either the vertical or the horizontal arm that imposes its orientation. In situation B, the orientation is dominated by the horizontal or vertical (as illustrated here) arm with equal probabilities 137

Figure 4.6.7 Light microscopy and confocal micrograph images that showed Schwann cells differentiated and aligned between two compartments through an open channel (bar a-b = 100 µm, c-d = 200 µm); (a) printed paraffin wax on glass; (b) confocal image after 2 days of Schwann cells cultured on wax structures, stained for actin (green; phalloidin-FITC) and nuclei (blue; DAPI) and with the wax removed; (c) Schwann cells differentiated and remained within the confines of the wax structures, with the channel width that spanned several cell widths; (d) confocal image of Schwann cells after 7 days of culture, cells were seen firmly adhered and aligned with the orientation of the channel. Stained for actin (green; phalloidin-FITC) and nuclei (blue; DAPI). Channel widths averaged 30 µm (i.e. the confines of the wax) 138

Figure 4.7.1 Cells proliferating within the confines made with patterned wax. Area = 0.1 mm^2, width 115 µm, total cells remaining after wax removal = 85%. Showing example of when wax removal displaces very little cells (fibroblasts), due to the cell concentration on the surface being around 200 cells/mm^2, and having a channel width of 115 µm. Scale bar = 100 µm 140

Figure 4.7.2 Light microscopy image showing a 55 µm wax channel with fibroblasts seeded into the substrate. The majority of cells detached when the wax was lifted off. Around 441 cells/mm^2. Scale bar = 100 µm 141

Figure 4.7.3 Confocal micrograph image that shows fibroblasts cultured on a glass substrate. Stained for actin (green; phalloidin-FITC) and nuclei (blue; DAPI). Channel widths averaged 30 µm (i.e. the confines of the wax), with cell density of around 850 cells/mm^2. Scale bar = 100 µm 142

Figure 4.7.4 Cells (fibroblasts) growing on a glass substrate being restricted by a wax structure. Upon removal of the wax, the layer of visible cells within the 175 µm channel are also lifted off, but what remains are cells that have differentiated between the glass and wax. Scale bar 100 µm 143

Figure 4.7.5 Images of remaining cells after removal of wax on samples that had overconfluent cells on the surface. The outline of the wax can be clearly seen. Left: curved wax structure from top left leading to bottom right. Right: three channels joined at the centre, with channels coming from top right, left and bottom right. Scale bar=100 µm 143

Figure 4.8.1 Wax scaffolds that were made for experiments regarding how cells behaved after wax removal. Scale bar = 100 µm 147

Figure 4.8.2 Three sets of microscopy images of fibroblast cell patterns after wax removal. First image shows cell patterns immediately after wax removal, and each subsequent image were taken 24hrs after the preceding image. Scale bar = 100 µm 148

Figure 4.8.3 Micrographs having being processed with OrientationJ to highlight the alignment of cells. (a) fibroblasts aligning within wax structures, (b) immediately after wax removal, (c) 24 hours and (d) 48 hrs after wax removal taken in the same sample regiona of interest. Bar = 50 µm 149

Figure 5.2.1 A 3D representation of how the shapes shown in Figure 5.2.2 were created. A) The molten wax droplet was pipetted on top of the wax line, and depending on how fast the molten wax solidified determined the final shape investigated. B) Flow of fluorescent micro beads through the phantoms created in part by inkjet printing. Flow is faster in the inner curve of the phantom compared to the outer curve, as shown by the speed distortion from the fluorescent microbeads travelling at the inner curve of the phantom. Scale bar = 3 mm and 1 mm respectively 155

Figure 5.2.2 Phantoms created with inkjet printing and wax-loss method in PDMS. (A-C) showing epifluorescent images of phantoms created using inkjet printed wax and pipetted wax. (D-F) Showing the depiction of different channel shapes that were tested fabricated with inkjet printed wax-loss with PDMS. The original image was edited with Paint to make the contrast between the open area and PDMS clearer. Scale bar = 1000 µm 156

Figure 5.2.3 A set of consecutive images of microbeads flowing through a phantom, created with wax-loss PDMS fabrication. Due to the 3D nature of the phantom, many of the fluorescent beads move out of focus and back into focus over time. Each image was taken 50 ms apart. Scale bar = 1000 µm 157

Figure 5.2.4 shows the images shown in Figure 5.2.3, with an overlay of a set of fluorescent beads that were tracked through each frame by using the Manual Tracker plugin in ImageJ. Scale bar = 1000 µm 158

Figure 5.2.5 Fluid flow within different flow phantoms created with wax-loss PDMS fabrication. Analysing the flow of fluorescent microbeads through the phantom at a steady flow rate, a general consensus of fluid flow rate can be created; red lines indicate flows which were fastest, with yellow lines showing the slowest flows with the phantom. Scale bar = 1000 µm 159

Figure 5.2.6 Representative images of how the phantoms looked like if the analysed area was zoomed out slightly; showing more of the narrow channel created through wax-loss of inkjet printed wax and their angles of entry. Note that the fluid flow direction travelled from top to bottom. Also note the angle at which the fluid enters the aneurism is steepest with C), which is explained later why vortex behaviours can be seen with this phantom and not seen in the other phantoms created. The angles of entry and exit can be compared as around 165°, 150° and 100° respectively to each image. Scale bar = 1000 µm 160

Figure 5.2.7 Approximation of turbulent flow within the respected phantoms, simulated by examining consecutive images of fluorescent micro bead movement in the fluid. Scale bar = 1000 µm 161

Figure 5.2.8 Magnified image of inkjet printed negative mould of a channel. Note the roughness and how curved areas are digitised, leaving indentations within the structure to mimic curvature. Scale bar = 500 µm 162

Figure 5.2.9 Diagrams of understanding fluid flow. Top) Topology of inkjet printed wax, and the ideal finish which would be smooth. Arrows represent the flow of fluid. Top right) Coloured dots are representations of the turbulence (vorticity distribution) of a non-smooth channel, compared to a smooth channel. Bottom) With wider channels, the turbulent effects of the surface topography of the wax used would be reduced when fluid flows through the vessel 163

Figure 5.2.10 Representation of printed wax in PDMS mould (left). When the sample is heated up to 80°C and the wax flushed out of the PDMS mould, it was expected that not all the wax would be extracted out (right). A thin layer of wax would line the interior of the vessel, smoothening the perceived roughness that was originally caused by the scalloping effect of printed lines 163

Figure 6.2.1 Analysis of mean viability of cells assessed using trypan blue staining immediately after inkjet printing, with standard deviation error bars at different voltages with each cell type. The blue bars represent 40 V and 80 V respectively, derived from Saunder's work with printing HT1080 cells. N=30 169

Figure 6.2.2 Velocity of inkjet printed droplets landed on the substrate. An increase in voltage equated to an increase in velocity, and therefore energy. This factor was not considered significant to the viability of the printed cells, as they were jetted into wells containing cell media, dampening the impact of the cells into the well plate 170

Figure 6.3.1 MTT assay results of printed and non-printed Schwann cells after 1, 3 and 7 days on different substrate surfaces, printed at 80 V, with standard deviation. N=3 172

Figure 6.3.2 Light microscopy images of Schwann cells grown on fibronectin surface coatings (A-C) Inkjet printed at 80 V, Schwann cells on day 1 (A), day 3 (B), day 7 (C). (D-F) Control Schwann cells seeded with a pipette onto fibronectin coatings on day 1 (D), day 3 (E), day 7 (F). Scale bar = 200 µm 173

Figure 6.3.3 Light microscopy images of Schwann cells grown on poly-L-lysine surface coatings (A-C) Inkjet printed at 80 V, Schwann cells on day 1 (A), day 3 (B), day 7 (C). (D-F) Control Schwann cells seeded with a pipette onto poly-L-lysine coatings on day 1 (D), day 3 (E), day 7 (F). Scale bar = 200 µm 173

Figure 6.3.4 Light microscopy images of Schwann cells grown on TCP surface coatings (A-C) Inkjet printed Schwann cells on day 1 (A), day 3 (B), day 7 (C). (D-F) Control Schwann cells seeded with a pipette onto TCP coatings on day 1 (D), day 3 (E), day 7 (F). Scale bar = 200 µm 174

Figure 6.3.5 MTT assay results of NG108-15 neuronal cells when grown with serum in media after inkjet printing (80 V), with standard deviation. N=3 174

Figure 6.4.1 Confocal micrograph images showing Schwann cells stained for actin (green; S100β) and nuclei (blue; DAPI). Top micrographs show inkjet printed Schwann cells at 80 V after 1, 3 and 7 days respectively. Bottom micrographs show control samples without inkjet printing after 1, 3 and 7 days respectively. Bar = 200 µm 176

Figure 6.5.1 Example of greyscale micrographs of NG108-15 cells after inkjet printing at 80 V and cultured without serum, after 1, 3 and 7 days respectively. Bar = 100 µm 177

Figure 6.5.2 Quantitative measurements of NG108-15 cells that include standard deviation of average longest neurite length (A), percentage of cells bearing neurites (B) and number of neurites (C). Cells were cultured in serum-free cell medium to induce differentiation and the generation of neurites. (n = 50) 178

Figure 6.6.1 Number of cells deposited through inkjet printing over time 40,000 cells/mL 181

Figure 6.6.2 A) Schematic of printer design. Over time, cells within the bioink aggregate to the bottom of the reservoir and are unable to travel through the inlet and reach the printhead. B) Close-up of reservoir to highlight the occurrence of cell aggregation at the bottom of the reservoir over time 182

Figure 6.6.3 Microscopy images in sets of two of cell solution contained in; (A) holder, (B) printhead, (C) reservoir, (D) PTFE tubing. Adjacent images of each labelled image highlights cells using white. Cell solutions were extracted through using flushing with trypsin to detach cells. Cell can be seen in the reservoir and PTFE tubing. Scale bar = 200 µm 183

Figure 6.7.1 Cell printing over time. A) Initial condition for the cell suspension in the printer. The suspension has a uniform cell concentration. B) Over a few minutes, gravitational and inertial forces pulls cells downwards, causing a slight build-up of cells at the bottom of the vial. C) At longer periods of time, cells

aggregate more, decreasing the total cells being jetted out of the printer, until a clump of cells form and is sucked into the printer tubing, which will eventually cause a clog at the printhead. D) To remove this problem, the cell media can be aspirated with a negative purge, causing a disruption in the vial containing the cells. If this is done at too short of a duration, the concentration of cells in the cell media would not be uniform, and when the setup is re-optimised, a higher concentration of cells may be deposited due to taking up a pool of higher concentration cell solution that hasn't been mixed uniformly. E) If the cell solution is mixed thoroughly, the cell solution would have a uniform cell concentration again, and this can be re-introduced to the printing setup *185*

Figure 6.7.2 Cell count over time. The system was aspirated at 30 minutes and 55 minutes (vertical lines) *186*

Figure 6.8.1 Through the manipulation of droplet spacing, non-interconnected spaces suitable for deposition of individual cells can be created, whereby the spaces are suitable for single cells to occupy. The grid structure was created through using the same droplet spacing of 40 µm, but the inkjet printing parameters were altered to create smaller droplets. Scale bar = 100 µm *190*

Figure 6.8.2 Step-by-step depiction of creating spatially patterned co-culture. (A) Plain substrate, (B) inkjet print a relevant wax mold, (C) seed cell type A onto the substrate, whereby the cells will adhere to the substrate where there is no wax present, (D) physically remove wax to only leave the adhered cells on the substrate, (E) Seed cell type B onto the substrate to create a bespoke co-culture with selectively arranged cells *191*

Figure 6.81 graph showing viscosity values of varying gelatin concentrations at different temperatures through the use of a rheometer. Line drawn at 10 m.Pas to indicate maximum printability level of inkjet printing *192*

Figure 6.8.2 (Above) and (Bottom) show inkjet printed gelatin on a glass cover slip. 4% gelatin was put inside the inkjet printing system, and the temperature increased to 30°C. Each time a successful droplet formation could be produced, printing became clogged and failed within 5 minutes of cleaning the apparatus. This made optimising the droplet spacing and printing parameters difficult. Therefore printing gelatin was not considered in future experiments, but instead, glutaraldehyde was printed onto a bed of gelatin *192*

Figure 16.8.1 Images taken at 50 µs apart, showing the movement of fluorescent micro beads traveling through the phantom. Using Manual Tracker (a plugin in ImageJ), individual beads could be tracked through each consecutive image. This allowed the tracking of beads travelling through the phantom. Scale bar = 1000 µm *204*

Figure 16.8.2 another method of analysing the data set captured with epifluorescent microscopy with the phantoms created; knowing the exposure time and the size of the micro beads, the motion blur can be used to extrapolate the speed of the beads in the phantom *205*

List of Tables

Table 1 viscosity behaviour of 25% glutaraldehyde (w/w in water) at different temperatures. Data taken from manufacturer's website; http://www4.mpbio.com/ecom/docs/proddata.nsf/(webtds2)/198595 91

Table 2 detailing printing parameters of printing 1% glutaraldehyde. When printing other concentrations of glutaraldehyde, the printing parameters were tweaked to compensate for the difference in rheology 92

Table 3 main printing parameters used when printing paraffin wax, at 70-80°C 109

Table 4 shows how the percentage of cells remaining after wax removal is different depending on the width of the channel and concentration of cells. Note: Negative = all cells in the open space created between the wax pattern were removed, and what was left were cells that differentiated underneath the patterned environment (i.e. Figure 4.7.4 and Figure 4.7.5) 145

Table 5 showing data gathered through adding different concentrations of glutaraldehyde onto different concentrations of gelatin, at 5 µL and left overnight. The samples were then washed in warm water to remove uncrosslinked gelatin, and the diameter of crosslinked gelatin was measured. Using this value, and knowing the height of the gelatin, the amount of crosslinking could be calculated, with a dimensionless number can be created to give a value to the amount of gelatin was crosslinked with glutaraldehyde (n=3). No data shown for 0.50% glutaraldehyde with 2% gelatin as the construct was too fragile and washed off during the removal of uncrosslinked gelatin 193

CONTENTS

ACKNOWLEDGEMENTS 2

ACRONYMS 3

SUMMARY 5

1 LITERATURE REVIEW 23

1.1 Introduction to Tissue Engineering Strategies 23

1.2 Factors that affect viability of Tissue Engineered scaffolds 30
1.2.1 Porosity in Tissue Engineering 30
1.2.2 Substrate stiffness in Tissue Engineering 32
1.2.3 Substrate surface topography 33
1.2.4 Physiochemical characteristics in Tissue Engineering 33
1.2.5 Biological characteristics in Tissue Engineering 34

1.3 Cell interactions with tissue engineered scaffolds 35
1.3.1 Cell seeding in Tissue Engineering 35
1.3.2 Tailored Cell Patterning 36
1.3.3 Creation of extracellular matrix by deposited cells 38

1.4 Phantoms for medical applications 39

1.5 Additive Manufacturing 40

1.6 Inkjet printing 45
1.6.1 Continuous Inkjet Printing 46
1.6.2 Drop-on-Demand Inkjet Printing 46
1.6.2.1 Thermal DOD 47

1.7 Understanding factors involved in Inkjet Printing 48
1.7.1 Generation and jetting of the droplet 48
1.7.2 Drop/substrate interaction 51
1.7.3 Controlling the final shape 52
1.7.4 Coffee Staining 53

1.8 Current state of the art of Inkjet Printing 55
1.8.1 Printing non-cellular materials 57
1.8.2 Printing of cells 60
1.8.3 Three dimensional structures 63
1.8.4 Reactive printing 64
1.8.5 Limitations of inkjet printing 64

1.9 Materials used in thesis 65
1.9.1 Gelatin 65
1.9.2 Paraffin wax 67

1.10 Objective of thesis 68

2 MATERIALS AND METHODOLOGY 69

2.1 Inkjet Printing System 69

2.2 Cell types, culture methods and handling 70
2.2.1 Cell types 70
2.2.1.1 Dermal fibroblasts 70
2.2.1.2 RN22 Schwann cells 70
2.2.1.3 NG108-15 neuronal cells 70
2.2.2 Porcine Schwann Cells 71
2.2.3 Cell culture 71
2.2.3.1 Induce differentiation to NG108-15 neuronal cells 71
2.2.3.2 Well plate modification for Schwann cell culture after Inkjet Printing 71
2.2.4 Cell seeding 71
2.2.5 Cell analysis 72
2.2.5.1 Trypan blue staining for cell viability immediately after inkjet printing 72
2.2.5.2 MTT metabolic activity for assessing cell viability 1, 3 and 7 days post printing 72
2.2.5.3 Neurite analysis of NG108-15 neuronal cells 1, 3 and 7 days after inkjet printing 73
2.2.5.4 S-100β, immunolabelling for identification of Schwann cells 74
2.2.5.5 FITC-Phalloidin and DAPI Immunolabelling for F-actin and nucleus of cells 74
2.2.6 Confocal microscopy 74
2.2.7 Aggregation of cells during inkjet printing 75

2.3 Creating crosslinked gelatin scaffolds 75
2.3.1 Gelatin hydrogels 75
2.3.2 Glutaraldehyde 75
2.3.3 Crosslinked gelatin washing 76

2.4 Printing patterned wax environments 76
2.4.1 Wax removal 78

2.5 Creating phantoms 78
2.5.1 Paraffin wax 78
2.5.2 PDMS 78
2.5.3 Making the phantom samples 78
2.5.4 Analysis of phantoms 80

3 CREATING CROSSLINKED GELATIN SCAFFOLDS FOR CELL SEEDING 82

3.1 Overview 82
3.1.1 Brief of work carried out for Chapter three 83

3.2 Seeding fibroblasts onto glutaraldehyde-crosslinked-gelatin. 84
3.2.1 Introduction 84
3.2.2 Results 85

3.3 Optimal printing conditions of glutaraldehyde printing 91

3.4 Inkjet printing glutaraldehyde to crosslink gelatin 93
3.4.1 Introduction 93
3.4.2 Results 95

3.5 Cell seeding onto inkjet-printed-glutaraldehyde-crosslinked-gelatin 98
3.5.1 Introduction 98
3.5.2 Results 99

3.6 Conclusion 104

4 CELL GUIDANCE STRUCTURES FABRICATED WITH INKJET PRINTED WAX .. 106

4.1 Overview 106

4.2 Printing paraffin wax 108
4.2.1 Introduction 108
4.2.2 Results 109

4.3 Creation of microfluidic devices 113
4.3.1 Introduction 113
4.3.2 Results 113

4.4 Creating 2.5D structures 119
4.4.1 Introduction 119
4.4.2 Results 120

4.5 Wax patterning for neurite analysis 123
4.5.1 Introduction 123
4.5.2 Results 123

4.6 Inkjet printing of wax guides/ orientation/ cell study experiments 132
4.6.1 Introduction 132
4.6.2 Results: Formation of wax guides 132
4.6.3 Results: Cell orientation studies 134

4.7 Removal of Wax Structures 139
4.7.1 Introduction 139
4.7.2 Results: Varying channel widths 140
4.7.3 Results: Varying cell concentration prior to wax removal 141

4.8 Cell migration after removal of wax 147
4.8.1 Introduction 147
4.8.2 Results 147

4.9 Conclusion 150

5 CREATION OF PHANTOMS 152

5.1 Overview 152

5.2 Results 154

5.3 Conclusion 164

6 CELL PRINTING 165

6.1 Overview 165

6.2 Viability of inkjet printed cells immediately after printing 168
6.2.1 Introduction 168
6.2.2 Results 169

6.3 Schwann and NG108 neuronal cell proliferation 1, 3 and 7 days after inkjet printing 171
6.3.1 Introduction 171
6.3.2 Results 172

6.4 Schwann cell purity after inkjet printing 175
6.4.1 Introduction 175
6.4.2 Results 176

6.5 NG108-15 neuronal cell phenotype after inkjet printing on days 1, 3 and 7 176
6.5.1 Introduction 176
6.5.2 Results 177

6.6 Cell printing behaviour 180
6.6.1 Introduction 180
6.6.2 Results 180

6.7 Aspirating the printer to reset bioprinting printing behaviour 184
6.7.1 Introduction 184
6.7.2 Results 185

6.8 Conclusions 188

7 FUTURE DIRECTIONS 189

8 APPENDIX ONE 192

9 APPENDIX TWO 201

10 APPENDIX THREE 206

10.1 Oral Presentations 206

10.2 Poster Presentations 206

10.3 Awards 206

10.4 Publications 206

11 REFERENCES..... 208

1 Literature Review

1.1 Introduction to Tissue Engineering Strategies

Tissue engineering is defined as the delivery of living elements into the patient to restore, maintain and improve tissue function lost due to injury and disease.[1] Simply put, tissue engineering is the fabrication, or transplantation, of biological tissue that can be placed into a living organism (predominantly human beings) with minimal harmful side effects. An individual could have a decreased level of quality of life, through disease and injury that limits their movement and interaction with others, or even have a life-threatening condition. Such examples include the debilitating effects of burn injuries, nerve damage and genetic diseases. It is possible to utilise the technology and knowledge gained from different industries (such as microelectronics fabrication) now more than ever to advance the field of tissue engineering. With the miniaturisation of computer chips and easier fabrication of materials that are more cost effective, the field of biomedicine is ripe to employ the tools of today (e.g. inkjet printing) to maintain the health of the population tomorrow. Tissue engineering aims to alleviate such ailments and restore an individual's quality of life, which may have been permanently reduced without intervention.

Small injuries can be healed effectively by the body without interference; a minor cut that breaks the skin quickly scabs over. However some injuries are more serious and require intervention to prevent permanent loss of function, scarring or mobility. In these situations, tissue engineering can be employed. The earliest example of tissue engineering was the use of skin grafts, whereby healthy tissue was taken from another location and transplanted (i.e. grafted) onto the target area. There are three forms of grafts, defined by their source, these are:

- Autografts – where the tissue is taken from a different area of the patient e.g. skin from the buttocks being used to heal a facial burn. The drawback of this method is that a healthy area of the patient has to be damaged to heal the wound in question. In essence, the patient now has two wounds.

- Allografts – where tissue is taken from a different member of the same species, e.g. human to human skin grafts. Although cadavers were a popular source of allografts, a patient needed to take regular medication to inhibit their immune system from rejecting the foreign tissue.
- Xenografts – where the tissue is taken from a different species, e.g. pigs and monkeys used as a source of skin for humans. Along with the disadvantages associated with allografts, xenografts also have an ethical dilemma since animals are exploited. Some religions, e.g. Judaism and Islam, have prohibitions regarding swine, which result in adherents of these faiths refusing xenografts. Additionally, there can be discussions to what makes an individual a human being, and the societal responses of a procedure.

Grafting is an imperfect solution to a serious chronic problem within society, as donor shortages are frequent and worsen every year, culminating in the deaths of patients on the waiting list for organ transplants. There is no "holy grail" tissue engineering solution that is all-encompassing for disease and injury. There can be a variety of approaches to heal an individual, and a balance of advantages and limitations must be considered to determine the best route of treatment. There are significant challenges within tissue engineering, with 4 main branches that researchers have investigated; biomaterial creation and implementation, cell source and their refinement, angiogenesis of engineered tissues and drug delivery systems. Figure 1.1.1 shows an overview of these challenges and the choices available to create them: 1) Biomaterials are required to repair damaged tissue, which can originate from different sources, can be injectable or implanted and all need to be safe upon introduction into the patient. 2) Cell sources are a significant issue as they need to be cultured from the patient. Due to immunohistochemical markers that are unique to each individual, only cells derived from the patient will be compatible with themselves (unless other measures are introduced such as chemotherapy). The acquirement of the cells can be problematic, as it would require them to be extracted from the patient, thereby injuring them in the process. After which, sorting the cells and selecting the right ones can be very difficult and require excessive use of time and resources. 3) Angiogenesis is essential if the implanted tissue is going to be viable in the long term of the life of the patient. Without a steady blood supply to the new organ/tissue, the cells will die due to insufficient nutrient uptake and accumulation of waste in the local area, causing

necrosis of the tissue. 4) Drug delivery systems may not be directly implantable into the patient, but they serve to facilitate tissue engineering applications. Notes: ESC, embryonic stem cell; MSC, mesenchymal stem cell; EPC, endothelial progenitor cell; HSC, hematopoietic stem cell; VEGF, vascular endothelial growth factor; bFGF, basic fibroblast growth factor; PDGF, platelet-derived growth factor; and TGF-b, transforming growth factor-b.

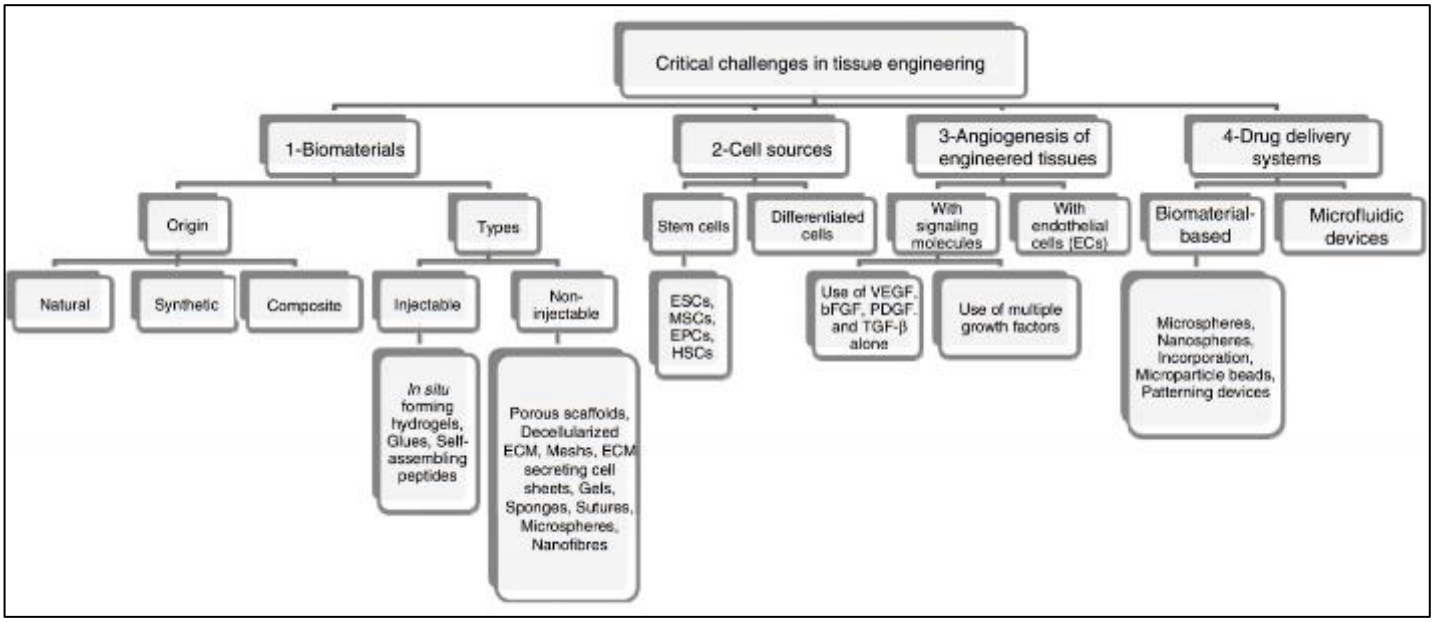

Figure 1.1.1 Overview of critical issues in tissue engineering. Taken from Naderi et al. 2011.[2]

Although a focus is placed on using tissue engineered scaffolds for the wellbeing of patients, another demand for tissue engineered constructs comes from the pharmaceutical and cosmetic industry. Prior to releasing new products for consumers to purchase, all drugs/lotions/cosmetics need to be approved by governments in their respective countries to guarantee that these substances do not damage public health. The US has the Food and Drug Administration (FDA), whilst the UK has Medicines & Healthcare products Regulatory Agency (MHRA). Many of these approval procedures require animal testing, to allow researchers to understand the effects of such drugs on living organisms, and also to investigate disease states, that are considered unethical to inflict on a human. A reduction in animal testing is steadily increasing within the scientific community, with the Three Rs tenet as a foundation for more use of tissue engineered substitutes to animal testing. The tenet refers to the Replacement, Reduction, and Refinement (Fleckneall 2002) of the use of animals in scientific research. Since March

2009, European Council Directive 76/768/EEC has been enforced, which prohibits the use of animals for irritation, corrosive and phototoxicity tests when alternative means are available, which increased interest in creating *in vitro* models for testing purposes.

A biological scaffold is a broad term used to describe materials, typically derived from the extra cellular matrix that is biocompatible and can be used to seed cells and be used in a clinical and pharmacological applications. A viable biological scaffold needs to have an architecture that is compatible and comparable with the relevant native tissue and cells. Different tissues (e.g. skin, cartilage, bone, blood vessels, skeletal muscle, bladder, liver and kidney) contain different mechanical, chemical and physical properties, which define the tissue and direct cell behaviour. These properties can be found in the extracellular matrix of tissue, and artificial scaffolds are created that mimic these key chemical and physical factors that also provide mechanical strength while the extracellular matrix is being generated. The wealth of knowledge generated through understanding and creating tissue engineered constructs has been steadily accumulated from scientific research. Yet for commercial and real-life impact, the products of such research need to be easy to fabricate, cost-effective, reliable and survive the research and development process.

The exemplar model for an ideal tissue replacement for injury or disease requires a combination of relevant seeded cells (to repopulate the tissue), biomaterial scaffold (for the cells to grow on and proliferate) and extra-cellular matrix components (ECM) (to direct cell growth into the right lineage) for tissue formation (Figure 1.1.2). Figure 1.1.2 outlines the expected approach (Dvir et al, 2011) in delivering a tissue engineered construct into a patient. Initially, cells (Fig. 1.1.2a) are isolated from the patient and cultivated. Cells from another species and from another person are likely to cause immunological rejection of the fabricated tissue. The cell population is (Fig. 1.1.2b) expanded, before the cells (Fig. 1.1.2c) are seeded in to porous scaffolds together with growth factors, small molecules, and micro- and/or nanoparticles. The cell constructs are further cultivated in bioreactors (Fig. 1.1.2d) to provide an environment similar to the native conditions of the host. Finally, implantation of the tissue engineered, cell seeded construct (Fig. 1.1.2e) on the defect is carried out to restore function.

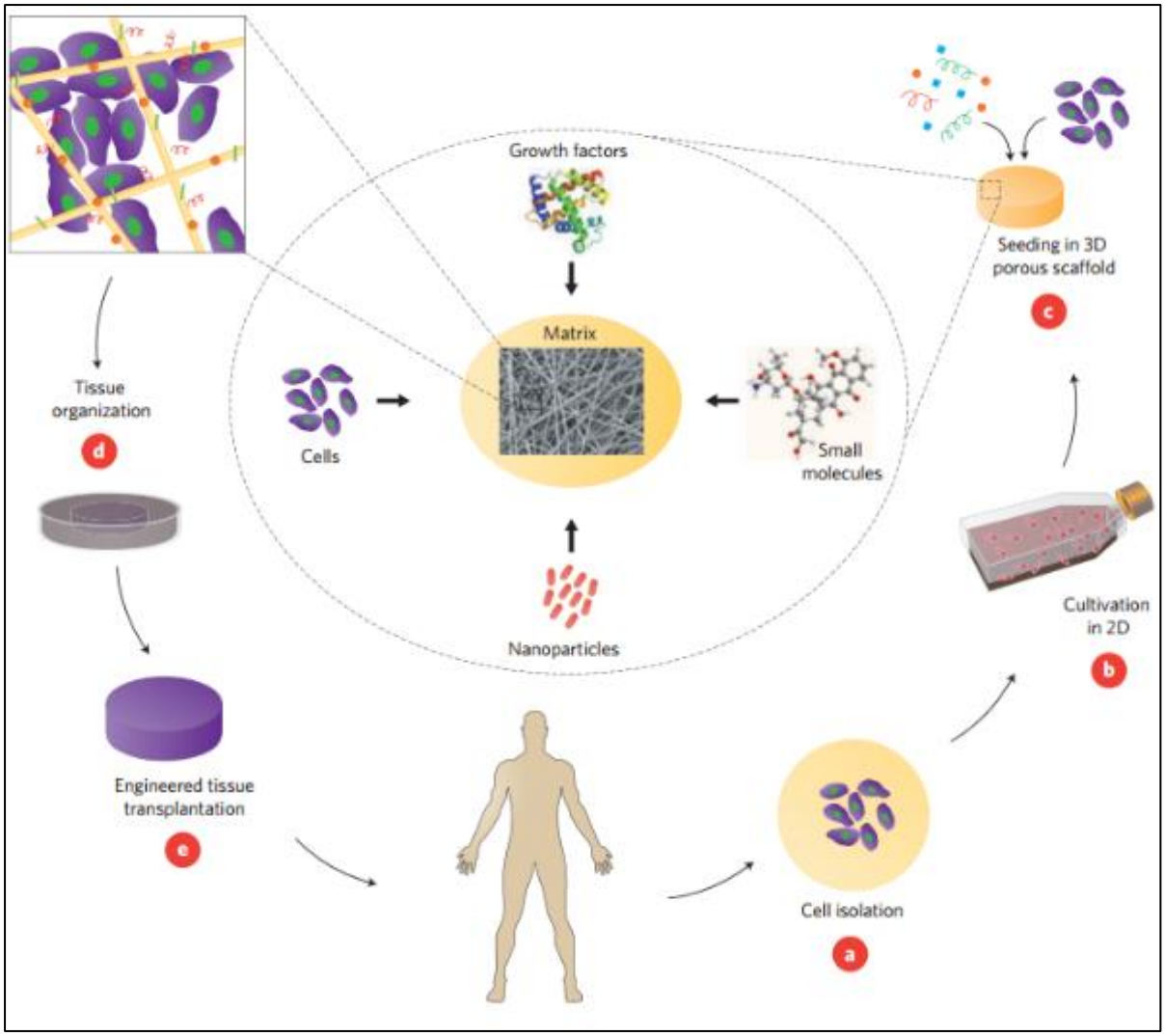

Figure 1.1.2 Diagram depicting a tissue engineering concept that involves seeding cells within a tissue engineered scaffold. Taken from Dvir et al. 2011.[4]

The example shown in Figure 1.1.2 shows an ideal methodology. But realistically when the patient has been admitted to medical care, there are too many complications, limited by our knowledge of engineering tissue, to adopt this method as standard practice; a) isolating cells would cause further injury to the patient b) expanding the extracted cells into a sufficient population may require many weeks of culturing, costing too much time, labour and resources c) there is not a solid methodology to seed cells into a 3D scaffold to have a homogenous deposition of cells (more about cell deposition will be discussed in later chapters) d) more research is required to optimise bioreactor conditions to mimic native biological environment e) more research is required to understand the interactions between the patient and transplanted engineered tissue.

There are many types of biomaterials, all of which can be created through different techniques to generate physiologically different traits. Outlined below are examples of techniques such as electrospinning, photolithography, soft lithography and inkjet printing, that are used to fabricate scaffolds;

There are many types of biomaterials, all of which can be created through different techniques;

Electrospinning - With electrospinning, an electrical charge directs very fine fibres (typically several micrometres down to tens of nanometres) from a liquid reservoir to a charged collector.[5] Fibres can be made to be aligned, or random (Figure 1.1.3), and can be made from a variety of polymers such as polyethylene oxide, polystyrene, polyether urethane, poly-lactic acid, polycaprolactone.[5–9] Electrospinning can be combined with other methods to create a multicomponent scaffold with different cell types sandwiched between each layer,[10] or have cells electrospun within the fibres.[11]

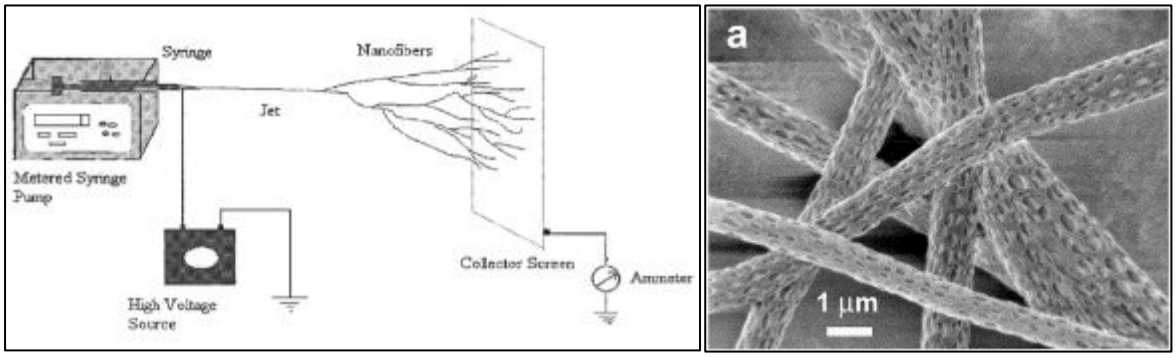

Figure 1.1.3 Schematic diagram of the electrospinning process, and an image of fibres created through electrospinning. Taken from Bognitzki et al. 2001; Subbiah et al. 2005.[5,7]

Photolithography – This technique can be used to pattern proteins and cells through the creation of a reusable "stamp" (Figure 1.1.4). The use of ultra-violet (UV) light can be manipulated to photoablate or bind proteins on a substrate with photosensitive groups.[12] Photolithography has a greater control of parameters such as interconnectivity and pore geometry compared to solvent casting and porogen leaching, to allow the creation of microstructure scaffolds with high resolution and fidelity, with features as small as 1 μm reported.[13] A combination of the high costs associated with the equipment and the need for the use of clean rooms makes this technique less accessible for smaller research groups.

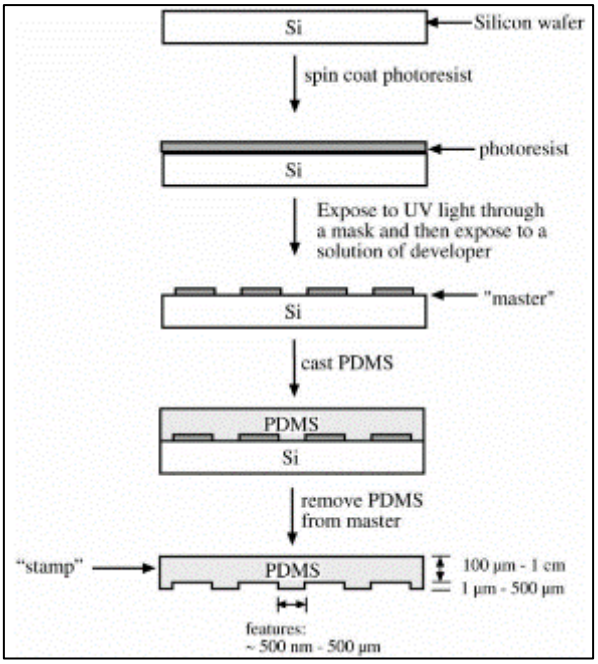

Figure 1.1.4 Schematic diagram of an example of photolithography used to fabricate a PDMS stamp from a master having relief structures in photoresist on its surface. Taken from Kane et al. 1999.[14]

Soft lithography - Soft lithography uses elastomeric stamps by casting and curing an elastomer on a silicon master (Figure 1.1.5), allowing material to be deposited to create patterned environments from ECM proteins, cells and compounds.[14,15]

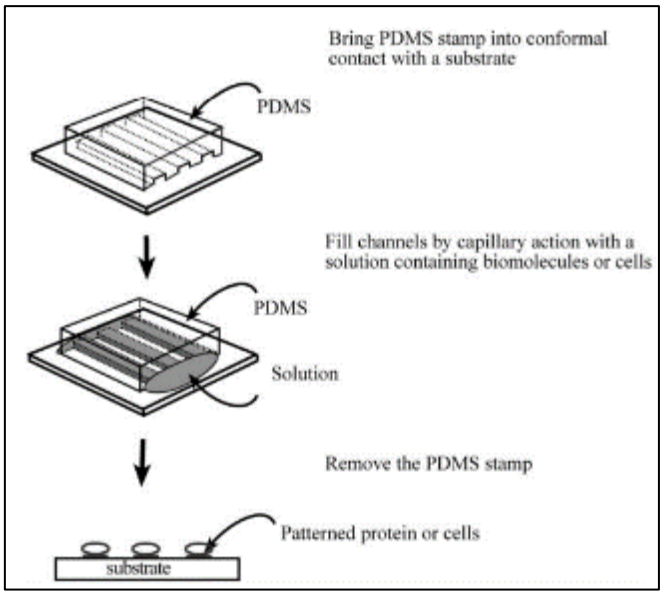

Figure 1.1.5 Illustration of the procedure used to pattern proteins and cells using microfluidic channels. Taken from Kane et al. 1999.[14]

Inkjet Printing - Inkjet printing, with multiple printheads, can create 2D and 3D biologically relevant tissues. The material and cells can be compartmentalised and precisely controlled to the desired shape, with the goal being the creation of anatomically correct structures to mimic actual tissue structure.[16] Inkjet printing will be discussed later in this chapter.

Such methodologies work for the creation of biomaterials and tissue engineered scaffolds because they are able to mimic several factors of native tissue. Such factors include (and are described in more detail in the subsequent paragraphs); physical factors such as the porosity, topography and substrate stiffness characteristics of a scaffold, along with the physiochemical and biological characteristics, and the ability to seed cells into the scaffold.

In summary, there are many different means to engineer biologically relevant tissue, and no one technique is universally superior. The application of the engineered tissue, size required and length of time to be in the patients are important factors to determine which technique is best to create the scaffold. When the engineered scaffold is too different from native tissue, the scaffold can fail mechanically, not integrate with the host, have insufficient cell infiltration, poor vascularisation and have cells differentiate into the wrong cell types if such aspects are not satisfactory.

1.2 Factors that affect viability of Tissue Engineered scaffolds

There are a variety of types of tissues within the human body, that differ greatly e.g. soft tissue such as skin and hard tissue such as bone. For the fabrication of soft tissue, the fabricated tissue needs to match of be compatible with the host tissue. Factors to consider in fabrication include the degree of porosity, stiffness, topography, physiochemical/ biodegradability and biological characteristics [1,17]

1.2.1 Porosity in Tissue Engineering

A solid block of a tissue engineered scaffold would only allow cell attachment on its surface. For a truly viable biological scaffold, cells must integrate inside and populate the whole structure; this can be done through the use of interconnected-porous materials. Interconnected scaffolds are scaffolds with open ended pores within their structure that allows material to freely diffuse through the entire scaffold. The

size of the pores and internal architecture have a great effect on cell viability, structural mechanical properties, flow resistance and cell remodelling of the scaffold.[18] Porosity has been shown to affect cell migration, with cell type and pore size affecting movement of the respected cell.[19,20] Figure 1.2.1 shows an example of a porous scaffold produced by the creation of an alginate scaffold. As can be seen the scaffold has a sponge-like interior which allows cells to penetrate into the bulk. Interconnectivity of porous scaffolds is essential as it allows the free movement of cells and material. If the pores were not connected, they would be termed "closed" pores, and such pore types are not suitable unless used for drug delivery to encapsulate drugs. Scaffolds with closed pores could also be toxic to biological tissue, if the fabrication process used toxic substances for its creation and were trapped within such pores that can break apart /degrade over time.

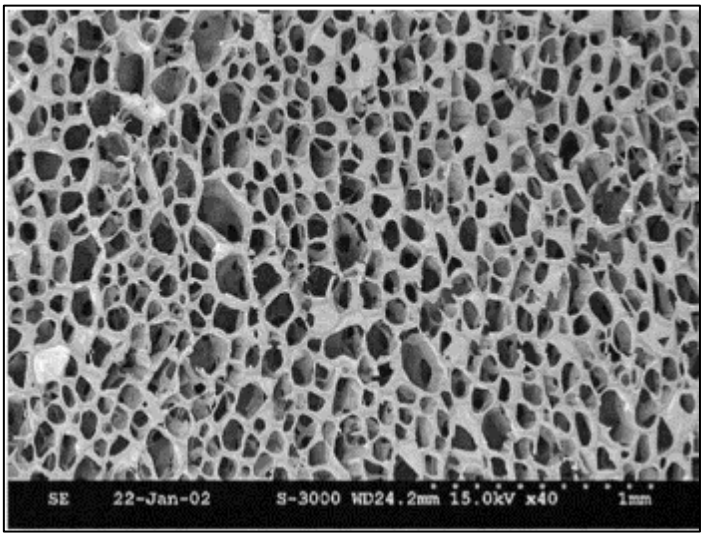

Figure 1.2.1 micrograph of typical top surface morphology of alginate scaffold made with 3% alginate and 0.03 m calcium chloride. Image taken from Lin & Yeh 2004.[21]

Gas-foaming techniques that involve the foaming of fluid precursors, or leaching of pore-generating particles can create large structures quickly, however a percentage of pores generated are not connected together with one another (closed pore), with at most, having 60% open pore structure.[22] It would be expected that newer research within this field would have better open pore percentage in recent years.[23] Interconnectivity, the degree of open pores is important for the flow and penetration of cells within the scaffold, as closed pores (which create dead volume) are isolated and are not engaged with cell seeding

of the structure. If a closed pore breaks down, exposing it to the external environment, there is a risk of harmful agents being released that were not cleaned out properly during its formation.

1.2.2 Substrate stiffness in Tissue Engineering

It wouldn't be suggested to heal a skin wound with a material like glass. If such an individual, subject to this approach, moves and compressive forces are exerted, the glass, being very stiff, would not flex and cause further injury, or detach from the patient. The mechanical strength of a scaffold needs to be similar to the injured area into which it is to be incorporated, otherwise, like the example above, tissue failure can occur to the surrounding environment. Different cell types have preference for adhering to different materials, and misalignment of stiffness characteristics can cause sub-optimal adherence and interaction.

On substrates with unfavourable stiffness, cells showed a rebuilding in cytoskeletal composition through fewer focal adhesion molecules and interactions and less actin filaments (Figure 1.2.2), resulting in a rounded physiology compared to cells on a favourable substrate.[24,25] A rounded morphology was seen with single cells, but once the cells interacted with one other, actin filament growth developed normally as cell-cell interactions guided cell proliferation and substrate stiffness became inconsequential.

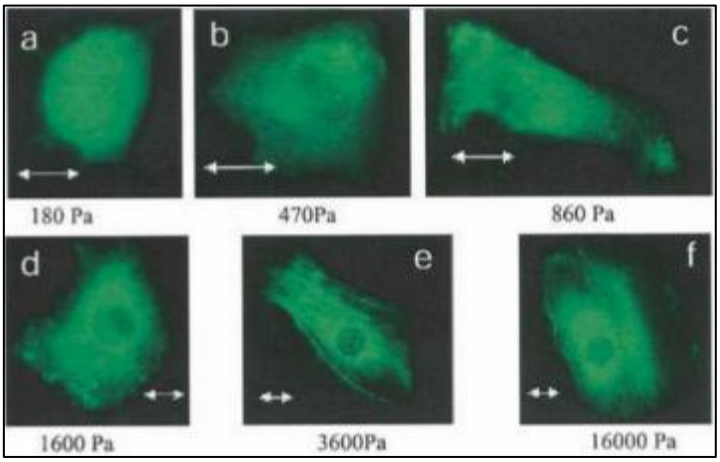

Figure 1.2.2 Effect of substrate mechanical properties on fibroblast actin cytoskeleton on fibroblasts grown polyacrylamide gels with varying stiffness. Fibroblasts on soft materials had no stress fibres compared with fibro-blasts on stiffer materials that do have articulated stress fibres with defined orientations. Scale bar = 10 µm. Image taken from Yeung et al. 2005.[24]

1.2.3 Substrate surface topography

Cells behave differently on different topological structures as it affects their signalling pathways, its morphology, how strongly they bind onto the substrate, rate of proliferation and rate of migration and differentiation. The resolution of the topography can range from micro to nanometres, and can come from the general surface of the substrate, or from the individual extracellular matrix molecules themselves.[26] Figure 1.2.3 shows examples of topographical structures; nanogrates, nanoposts and nanopits, and how epithelial cells can be seen growing in the same direction as the nanograte surface that they have adhered onto.

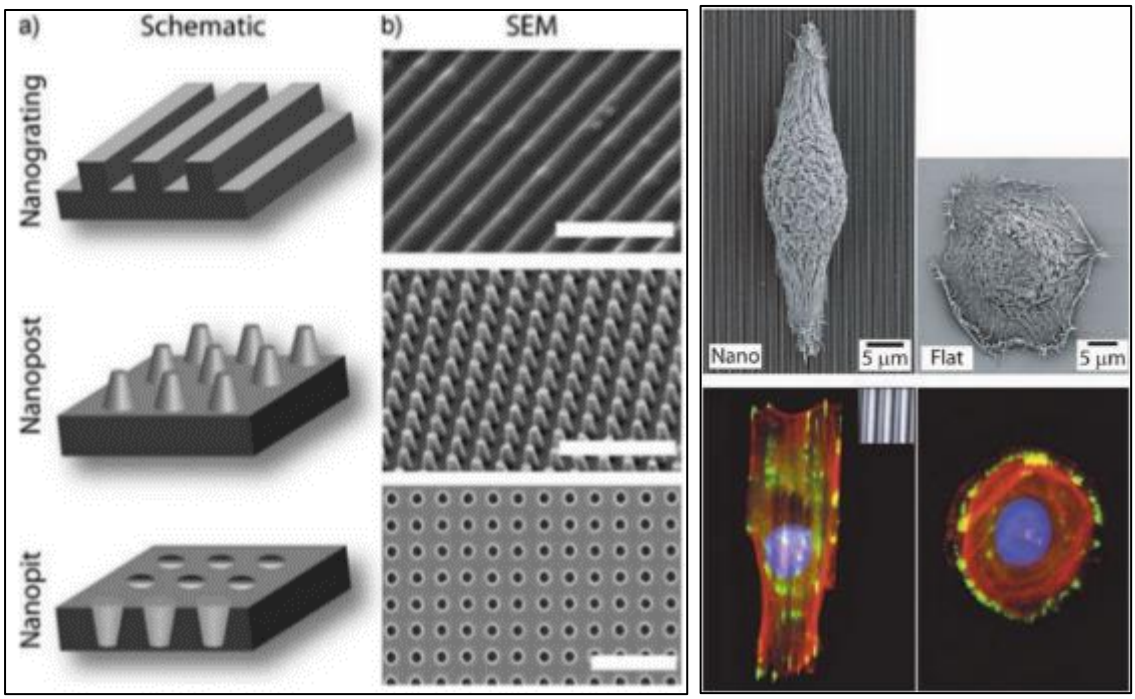

Figure 1.2.3 [Left] Schematic depictions (a) and SEM images (b) of representative nanotopography geometries. Three basic nanotopography geometries include nanograting (458 tilt, scale bar 5 mm), nanopost array(158 tilt, scale bar 5 mm), and nanopit arrays (08 tilt, scale bar 1 mm). [Right] Epithelial cells growing in the direction of the orientation of a nanograted surface, compared to a smooth surface for control, as shown with light and confocal microscopy. Taken from Bettinger et al. 2009 and Company of Biologist.[26]

1.2.4 Physiochemical characteristics in Tissue Engineering

Understanding the physiochemical properties of a tissue is essential to create biocompatible scaffolds, otherwise the scaffold would be more likely to be rejected/unsuitable. Such characteristics include the scaffold's wettability, degradation rate, roughness, crystallinity, charge and functionality. These factors can affect protein-scaffold and cell-scaffold interactions which include protein adsorption, cellular adhesion, proliferation, morphology and selectivity.[27] Ideally, when tissue engineered scaffolds are

used, they dissolve or degrade at the same rate as the native tissue's rate to regrow back into the injured area, resulting in completely natural tissue replacement. With ideal biodegradable scaffolds, they would increase the rate of tissue regeneration and promote the deposition of the correct extracellular matrix, reducing scarring and allowing faster recovery. For hard tissue engineering, the ideal scaffold would have the same mechanical characteristics as the bulk material, be biocompatible and not cause resorption of neighbouring native hard tissue which can cause mechanical failure.

1.2.5 Biological characteristics in Tissue Engineering

Wound healing, morphogenesis, immune response, angiogenesis, nerve regeneration, cell migration, cell adhesion, differentiation, survival and a vast array of cellular functions are controlled through biological stimuli through spatially and temporal patterned endogenous chemical signals. These can comprise of, but not limited to, growth factors, proteins, chemicals, neurotransmitters, hormones, ligands and cytokines. Such biological signals need to be integrated into tissue engineered scaffolds to promote integration into the host body. Collagen, fibronectin, fibrinogen and vitronectin are well documented extracellular matrix proteins that are used in tissue engineering to promote cell interaction.[28]

Bioactive molecules can be fixed onto a substrate so that they are not affected by diffusion or be washed away. They can be adsorbed onto the substrate, linked by covalent bonding through interactions with carboxylic acid or primary amine moieties on the surface of the substrate natively, or added in a sequential step. Hydrogels have been used as a substrate and have been shown to be very useful in being coated with bioactive molecules, with a great extent having been researched with 2D scaffolds, and 3D experimentation increasing. There has been extensive research with signal biological molecules on directed axonal growth through chemotaxis. Through changing the concentration of signal molecules, axon growth from nerve cells could be directed and increased,[29–32] with an example shown in Figure 1.2.4 with different biological coatings affecting nerve regeneration.

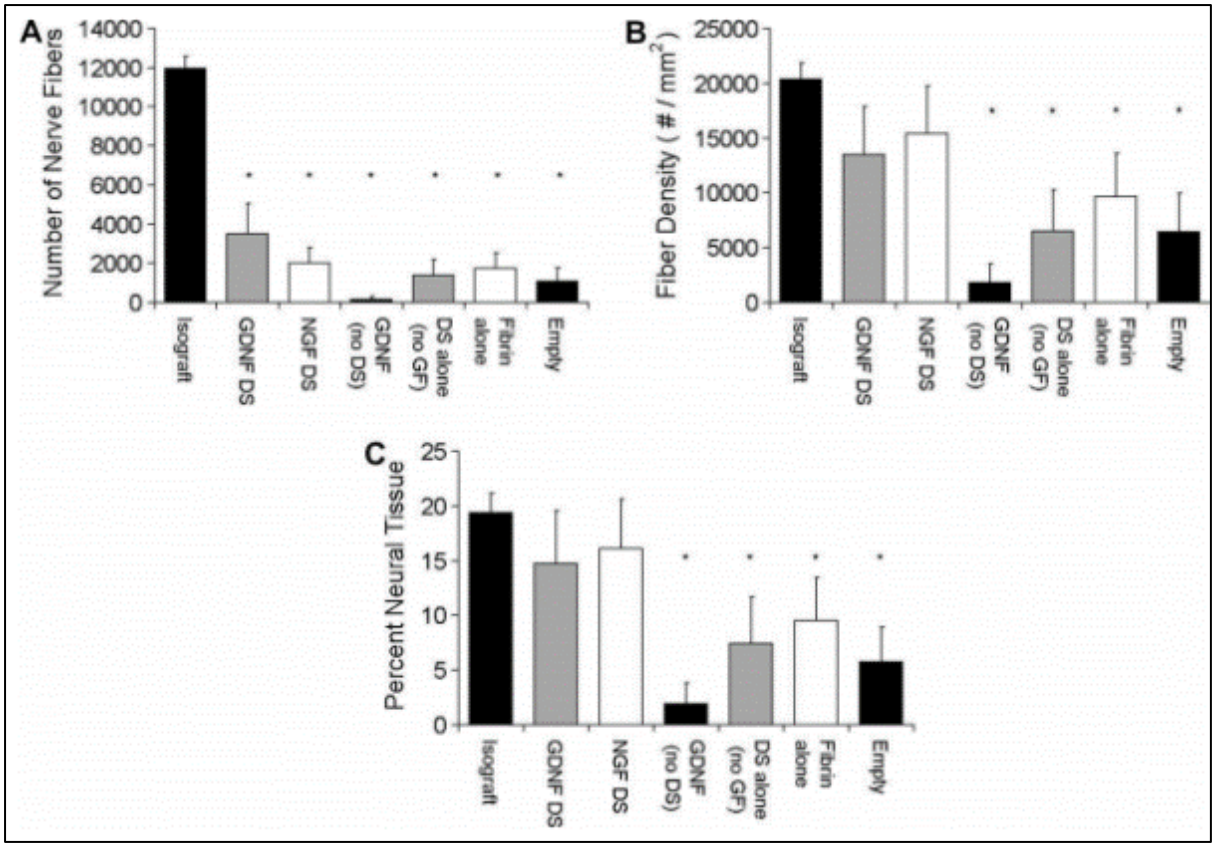

Figure 1.2.4 Histomorphometric analysis of nerves (or graft) that were cultured on different substrate surfaces. Taken from Wood et al. 2009.[32]

1.3 Cell interactions with tissue engineered scaffolds

1.3.1 Cell seeding in Tissue Engineering

For a tissue engineered scaffold to be successful, it must readily accommodate cells within its structure. Without this accommodation, the scaffold would not properly integrate into the patient and would be termed a prosthetic and not organic. Having a population of cells seeded within the scaffold is essential to test compatibility prior to host integration, drug testing and allow long term viability.

There are several static and dynamic cell seeding methods; passive seeding, rotational seeding, vacuum/pressure seeding, magnetic cell seeding, electrostatic cell seeding and immobilisation cell seeding.[33] Once the scaffold is created, the use of bioreactors to help growth is an option to use for the maturation of cell seeded scaffolds, whereby cells proliferate, and deposit extra-cellular matrix in their surrounding environment and to allow the cell cycle to propagate.[34] This can be an ideal springboard prior to the use of animal models, if they are needed at all.

There is an active relation between the cells and the scaffold itself, as when cells proliferate and differentiate, they would occupy more of the scaffold. Therefore, the scaffold needs to have a suitable internal structure and vasculature depending on the volume of the scaffold, otherwise complications can occur. Cell adherence itself can be a problem with tissue engineered constructs, as cells deposited on the periphery of a scaffold eventually act as a barrier to further proliferation and diminish the transport of nutrients and waste.[35] Early research has shown that, without an extensive vasculature network to transport nutrients and waste, cells can survive up to 500 microns deep through diffusion alone. Cartilage tissue regeneration is the exception to this rule, as cartilage is inherently avascular, and cells have been shown to survive deeper in cartilage tissue without vasculature. This is because chondrocytes can survive in lower oxygenated environments.[36]

1.3.2 Tailored Cell Patterning

For many tissue engineering applications, a uniform layer of cells is suitable for cell seeding. However there are cases where more precision is required for cell deposition. Such examples can be the interaction of specialised cells and their supporting cells, such as nerve cells and their supporting glial cells.[37] Others include co-culture of cells that elicit a response that would not be seen in monocultures.[38] The method of depositing cells must also be finely controlled to mimic the complexity seen in native tissue, for example, the skin, kidney and liver have several defined layers each of which have a different proportion of cell types in order to create the architecture of healthy skin. Spatial and temporal control is required, with the ability to deposit multiple cell types to create a suitable environment.

Cell patterning also allows the creation of experimental conditions ideal for analysing individual cells and molecular interactions of cells with neighbouring cells and their environment, and is helping to develop a better understanding of fundamental cellular processes.

There are several cell patterning techniques, which can be split into two categories; 1) modifying the substrate to control cell adherence, and 2) direct cell positioning.

1) Modifying the substrate so cells preferentially adhere/draw them to the desired space (Figure 1.3.1). Within this category, such techniques include photolithography[39,40] and micro-contact printing.[41] Extra-

cellular matrix related proteins and synthetic polymers such as cytokines, fibrin, collagen and PLGA can be deposited at high resolution on a substrate that is unfavourable for cells to grow on, thereby causing selected cells to adhere onto the patterned environments (Figure 1.3.1). Due to the significant costs of unique proteins to different cell types for such techniques to work, it can be very costly and therefore normally no more than two cell types can be patterned without interference with the other cell types.[42]

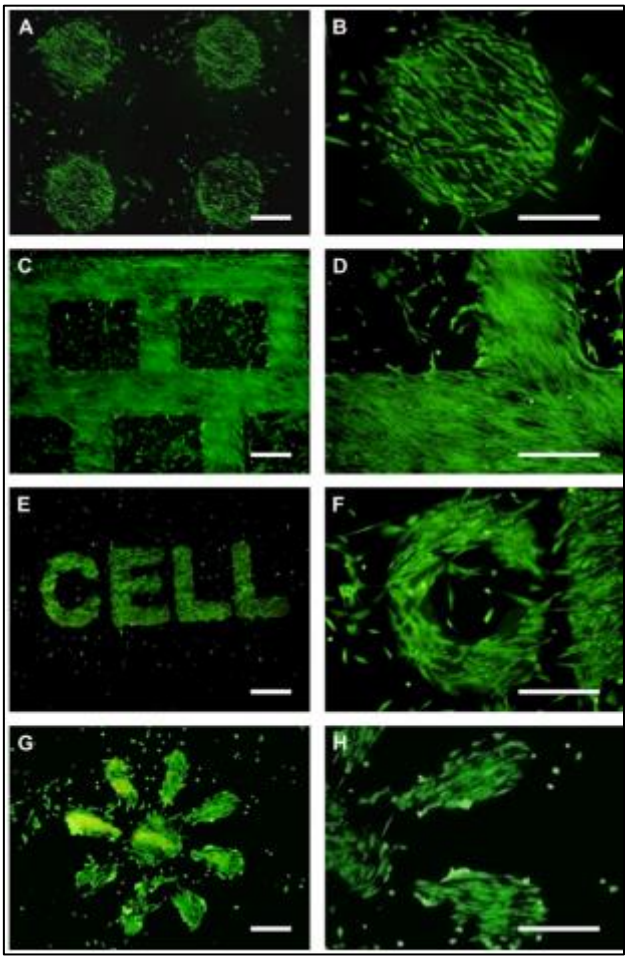

Figure 1.3.1 Inkjet printed PLGA on polystyrene substrates, with stem cells preferentially growing on PLGA. Images taken 5 days after cell seeding. Scale bar = 500 mm. Taken from Kim et al. 2010.[43]

2) An application of a force to actively deposit cells to the desired space. Figure 1.3.2 shows an example of laser-guided direct writing of cells. Within this category, such techniques include dielectrophoresis,[44] optical tweezers, laser-directed cell writing (Figure 1.3.2) and an assortment of magnetic and acoustic trapping techniques that enable cells to be controlled through the manipulation of light, gradient control and magnetism.[45]

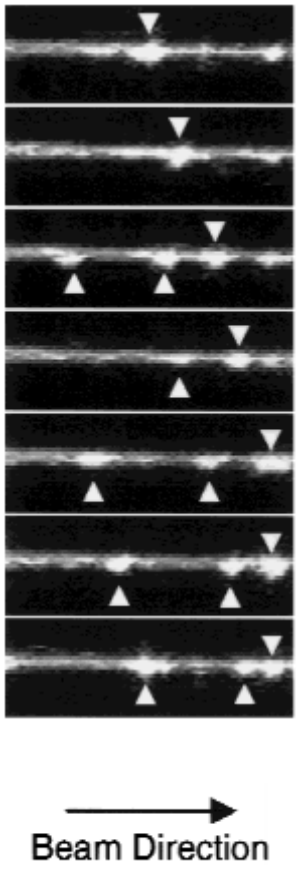

Figure 1.3.2 Laser-guided direct writing of living cells. This example shows embryonic chick spinal cord cells moving on a glass cover slip. Arrow heads mark the position of cells. Image taken from Odde & Renn 2000.[46]

1.3.3 Creation of extracellular matrix by deposited cells

Once cells have integrated with the tissue engineered scaffold, they deposit extracellular matrix around their environment. The extracellular matrix has several purposes, acting as a physical support and physical barrier for given tissues and guiding cell development, providing a temporary scaffold to guide tissue growth and organisation, which enhances cell signalling to retain tissue-specific gene expression. The stiffness, topography and spatio-dimension of the extracellular matrix all significantly govern cell fate and are investigated in more detail elsewhere.[47–49] Cells and the ECM interact in tandem and cells produce tissue-specific ECM proteins that direct the function and structure of the tissue to return to optimal functionality.[50,51]

In summary, the extracellular matrix is not a permanent feature within tissue. It is dynamic and frequently remodelled by all stages of a cell's life cycle, through the excretion of proteases such as

matrix metalloproteases to break down old proteins, and together with the generation of new extracellular matrix in their environment.[52] The extracellular matrix contains a whole plethora of molecules, including integrins, proteoglycans (heparin sulphate, chondroitin sulphate, keratin sulphate), hyaluronic acid, collagen, elastin, glycoproteins, laminin, growth factors and cell receptors, all of which can have an influence in how cells interact with their surrounding environment. Cell behaviour is determined through recognising the specific signals presented to the cell by the extracellular matrix, of which can be unique to each region and type of tissue.[53,54]

1.4 Phantoms for medical applications

There are applications within the medial field which do not require the replacement of tissue. Disease identification and diagnostic applications to determine the health of a patient by using MRI, CAT scan and ultrasound are examples. Within the scope of this thesis, medical phantoms were also studied and prepared. The use of phantoms for medical applications is an area where medical professionals use models to test their diagnostic imaging techniques, plan for surgery and for general training.

With regards to the scope of this thesis, a scaffold that can imitate blood vessels and the effects of an aneurism is termed a phantom. An aneurism is an area of a vessel that has excessive localised swelling, and can rupture to cause life-threatening complications such as strokes and heart attacks. Medical professionals can create *in vitro* models to better understand such abnormalities. Such phantoms have uses with surgeons to better prepare with surgical planning and training to treat aneurisms through application of standard, fenestrate and branched stent-grafts. Typically phantoms are created using silicone rubber, usually PDMS, or epoxy resin (Figure 1.4.1). Phantoms have been used to study the coagulation behaviour within vessels, effectiveness of medical imaging techniques, show the effectiveness of non-invasive thermotherapy for the elevation of tumours, understanding ruptured blood vessels and fluid behaviour.[55–58] What is important with such phantoms is to imitate native tissues realistically, and designing and fabricating realistic vessel structures is currently difficult and have very basic anatomy with very little variance. Manufacturing techniques, such as moulding, assembling and cutting would leave mould lines that can greatly affect the rheological properties of a mould, and such

lines would be difficult to remove due to the scale and internal structure of the phantom. There is a demand from surgeons to acquire a technique that can reliably mimic a patient's tissue, and have a standard for which to validate new endovascular techniques. The use of animals has been tried, however there is no means of repeating and validating results,[59] therefore phantoms can be considered to be more favourable, if they can be reliably made. The use of wax loss technique has been used, whereby the vessel is created in wax, and enveloped by a silicone bath, solidified, and then putting the phantom into a hot bath to extract the wax out of the silicone mould.[58] Additive manufacturing has played a role with creating higher resolution and bespoke phantoms through fused deposition of the sacrificial material. To date, there have not been any publications of inkjet printing of the sacrificial material (wax) to fabricate phantoms.

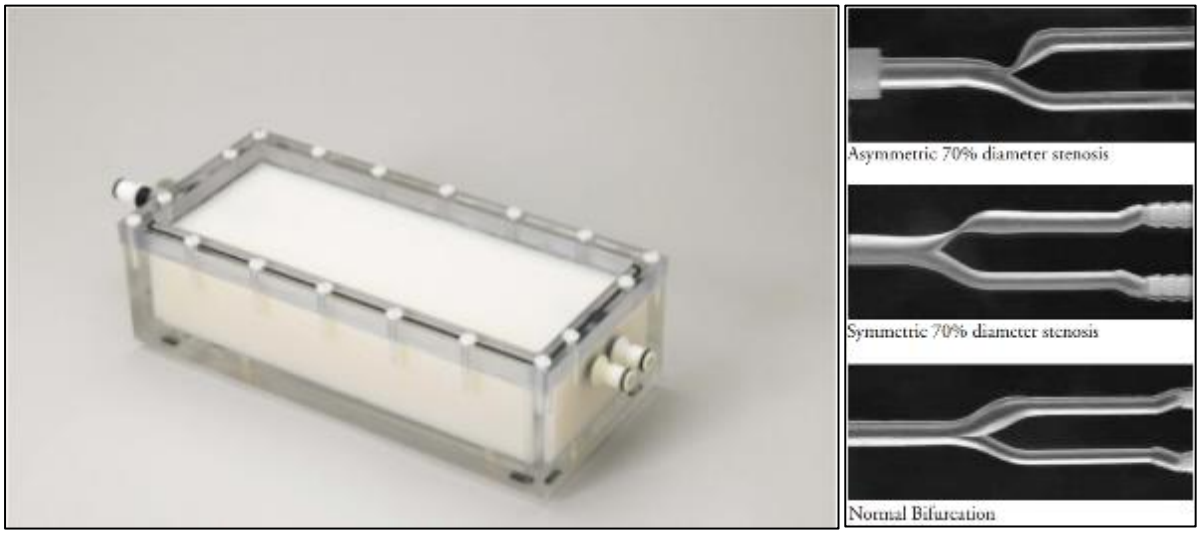

Figure 1.4.1 Example of a commercial product that mimics arterial bifurcation vasculature, with features to mimic different stenosed vessel geometries. Such tools can help medical professionals to better understand the rheological conditions in their patients. Taken from product website; http://www.simutec.com/Docs/Carotid%20Bifurcation%20Doppler%20Flow%20Phantoms%20low-res.pdf.

1.5 Additive Manufacturing

This thesis utilises inkjet printing which is classified by the umbrella term of additive manufacturing. Additive manufacturing, or AM, is an automated process that can fabricate solid objects in a layer-by-layer fashion. These typically use Computer-Aided-Design (CAD) and have been used in industry,

especially for small and medium enterprises for rapid prototyping designs in a cost-effective way. Originally applied to the development of metals, ceramics and thermoplastic polymers within the engineering discipline, the AM set of technologies has now moved to the field of tissue engineering. The creation of objects is performed using the generation of a 3D render with software; in the form of a CAD, STL (stereolithography) or proprietary file type. This file can then be used within the AM machine to translate the digital object into a physical object.

The automated fabrication techniques of AM can make anatomically-correct bespoke implants for medical, preoperative planning, education, surgical simulation and research purposes. Using medical images of the patient (MRI and CT scans), additive manufacturing has allowed the creation of medical implants that suit each individual's needs.[60] AM can potentially provide an unprecedented level of detail that is bespoke to each individual. The conversion of the medical images into a printable file can be difficult at times, as optimisation may be required to reduce noise and to create a better print finish. As such, software development for medical printing applications is important in ensuring that additive manufacturing produces the object defined by medical imaging.[61,62]

AM techniques can be grouped into four different kinds of systems, depending on the precursor material used (Figure 1.5.1);

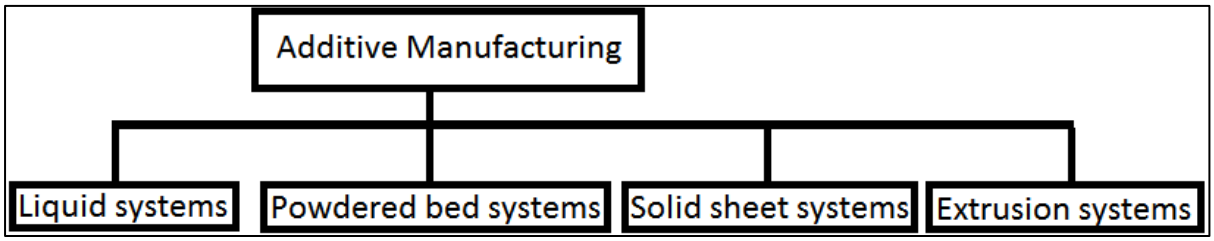

Figure 1.5.1 4 types of additive manufacturing systems.

1. Liquid systems

During the processing step, a liquid raw material is used, and is turned into a solid material, through oxidation, light exposure and/or heat. Stereolithography and phase change inkjet printing are examples.

Stereolithography uses a vat of photosensitive monomer liquid, which when selectively exposed to UV light, polymerises and solidifies. The vat is then moved down and another curing process takes place until it is completed. Stereolithography techniques use thermosets, such as acrylates, epoxies, blends of the two and filled resins. Inkjet printing will be discussed in more detail in Section 1.5*.

2. Powder bed systems

Selective laser sintering (SLS) and binder jetting are examples that use a powder form of a material. SLS typically use powdered metals and polymers. A powdered bed of the respected material is preheated to just below its melting point for crystalline materials, or below its glass transition temperature for amorphous materials. A laser beam traces the geometry of the cross-section of the part, fusing the powder together, before a new layer of powder is deposited whilst the powder bed descends to a height equal to the layer thickness. This process is done in an inert atmosphere (typically nitrogen) to reduce oxidation and reduce warping of the object. Powder that is not fused acts as a supporting material for future layers, and helps to prevent the fused object from warping and shrinking from the stresses experienced through the fusing process.

3. Solid sheet systems

Laminated object manufacturing (LOM) was one of the earliest additive manufacturing techniques. Metals like aluminium sheets would be used and stacked on top of one another, with the sections being drawn by either a cutting knife or selective laser cutting. The underside of each layer has an adhesive, which can be thermally activated. Complex geometries and objects to be created with cavities cannot be made with this technique, as there would be no way to remove the internal material

4. Extrusion systems

Much like toothpaste, extrusion systems apply a force in the reservoir, and the material is squeezed out and onto the substrate. A nozzle is used to direct the extruded material. Extrusion systems can operate at high temperatures to make solid materials at room temperature melt, so they are more easily jetted

out from the system. Typically a coil of material is used, which is fed through the nozzle and heated until it is able to flow. The material is extruded and solidifies after deposition. Figure 1.5.2 is an example of extrusion; here a filament of a slurry loaded with functional material is extruded out of a nozzle, and seeded with cells to show biocompatibility.

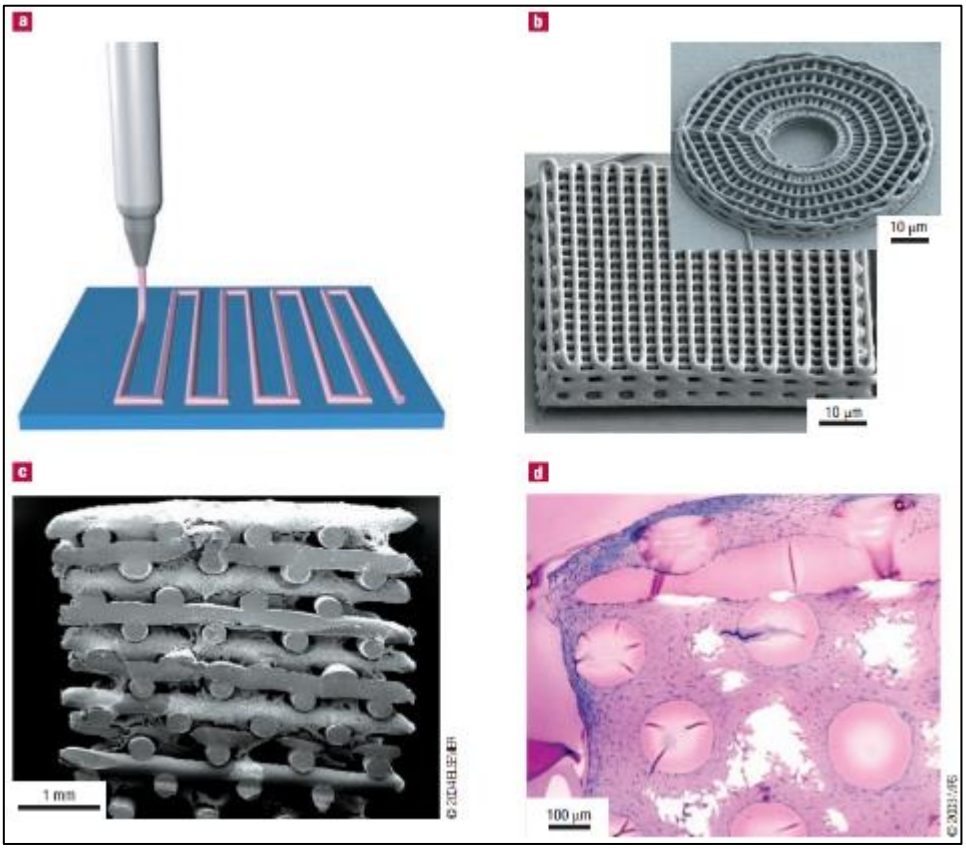

Figure 1.5.2 Examples of structures created with extrusion technology. a) extrusion printing system, b) biologically relevant structures created with extrusion printing, c) scanning electron microscopy of cross-section of scaffold d) shows proliferation of cells in biocompatible porous scaffold created with extrusion technology. Taken from Woodfield et al. 2004; Gratson et al. 2004.[64,65]

Unlike conventional manufacturing techniques, the complexity of an object is not a limiting factor for additive manufacturing, which can create new geometric shapes that were not possible with traditional methods. Additive manufacturing techniques have additional factors that need to be taken into account however; shrinkage through setting/curing of the material, changes in structural integrity, inability to create overhangs, post-production finish (may need to remove supporting structures), toxicity and high temperature during operation all need to be considered, and reassessed with tissue engineering applications.[66,67]

The current leading research interests involve combining cell seeding with additive manufacturing, whereby cells can be incorporated within the computer-aided fabrication of the living construct [68]. Still in its early stages, AM is hoped to become a promising scalable and reproducible technique for the production of tissue engineered structures.[69,70]

With the creation of scaffolds, significant research in cell behaviour had been done extensively with 2D cell cultures. There is greater control over the creation of experimental procedures in 2D cell culture, and characterisation is easier. However the implications of such research do not translate to represent native behaviour of tissues as relevantly as 3D experiments,[71,72] as such models over simplify the cell environment. Therefore, there has been more focus in analysing cell behaviour in 3D in vitro experiments (Figure 1.5.3). Examples of the striking difference between 2D and 3D cell culture are given by Hutchmacher, Benya & Shaffer and Baker & Chen,[73–75] involving cancer analysis, chondrocyte differentiation and elegant opinions from the authors respectively.

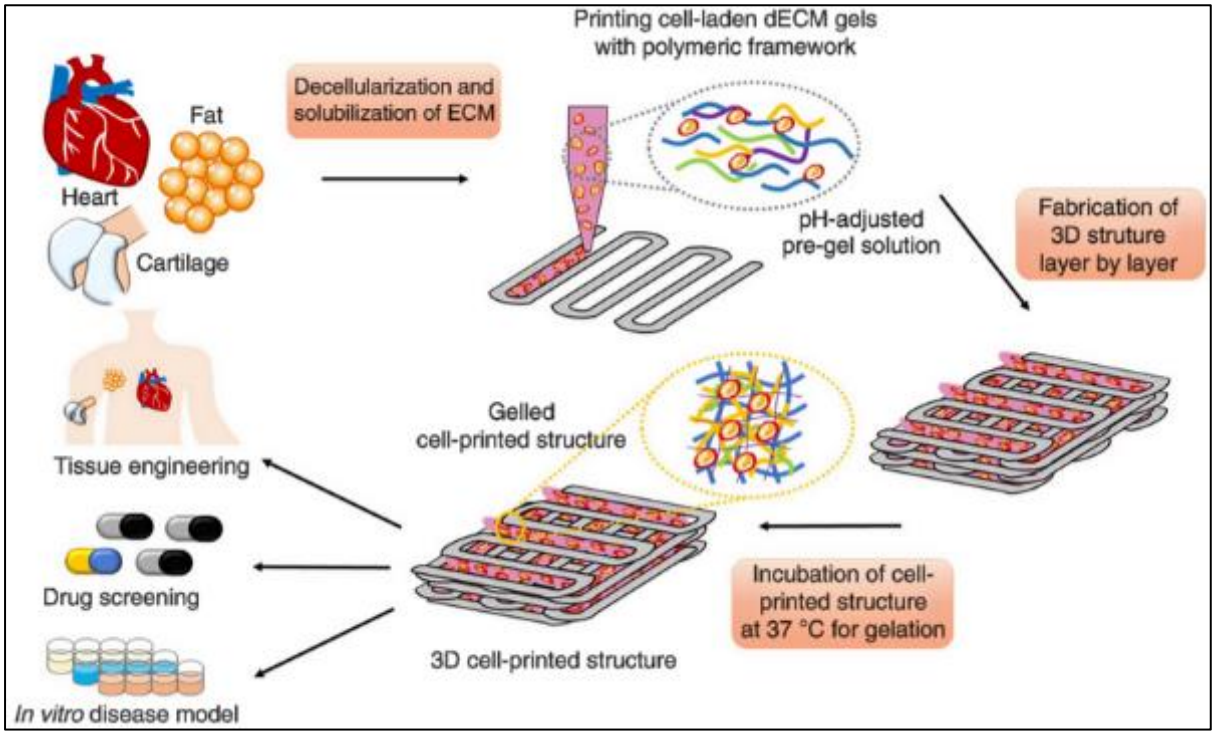

Figure 1.5.3 Schematic elucidating the tissue printing process using an additive manufacturing technique. Taken from Pati et al. 2014.[76]

Fabricated structures have been used in drug testing, implanted into patients and been used to study cell interactions;[77] skin,[78] meniscus,[79] aortic valves,[80] cartilage,[81] bone,[82] and blood vessels[83] are a few examples of what has been created through additive manufacturing techniques.

1.6 Inkjet printing

Inkjet printing has been of great interest for biomedical research. First published written experiments involving the printing of a biological material occurred in 1988 by Klebe,[84] through the deposition of fibronectin. He termed the process cytoscribing.

Thomas Boland and his group pioneered the application of inkjet printing techniques for tissue engineering, initially using a modified desktop to jet cells and proteins.[85]

Inkjet printing offers the following advantages:

- A three-dimensional structure can be produced with a single procedure
- Both the scaffold and the cells can be deposited at the same time using multiple printheads
- Subnanoliter drops can be deposited in a precise and repeatable spatial and temporal manner
- No requirement of the creation of masks and tooling requirements
- It is a non-contact printing process which reduces the risk of contamination
- Easily scalable through the addition of more printheads or through an increase in ejection frequency

The versatility of inkjet printing can be seen in its modern day applications, whereby the technology has advanced significantly within the 60 years of its first inception. The technology can be demonstrated to have commercial uses in fabricating transistor circuits,[86] electroluminescent displays,[87] lab-on-a-chip designs,[88] rapid prototyping,[89] organic sensors,[90] and tissue engineering.[91] This additive manufacturing technique is not limited to the constraints of mold or dies, and is able to create unique one-off designs as easily as copies, allowing the creation of designs with varying input parameters. The resolution that can be produced is an order of magnitude less than similar dispensing techniques; such as micropipetting, syringe and valve displacement dispensing. This is a significant advantage as it allows

the creation of a large variety of scaffolds with a gradient of design characteristics that can be researched to allow optimisation.

There are two main inkjet printing systems: a) continuous inkjet printing (CIJ) and b) drop-on-demand inkjet printing (DOD), with DOD further divided into: 1) thermal and 2) piezoelectric. In this thesis, a piezoelectric DOD inkjet printing system was used. The properties of the ink (discussed in more detail Section 1.6) are key to inkjet printing, which places limitations due to the specific requirements of viscosity and surface tension. Heating of the print head, and the substrate is possible and can be independent from one another.

1.6.1 Continuous Inkjet Printing

Continuous Inkjet Printing and Drop on Demand both are inkjet techniques, with the difference between the two being the state of flow of the ink.

Continuous inkjet printing dispenses a steady flow of ink and has a higher jetting rate than drop-on-demand printing. Droplets are dispensed through being exposed to a charged area under pressure. The ejected droplets' flight can be controlled through movement of the substrate and/or the application of a charge on deflector plates before reaching the substrate to print a desired pattern. The continuous stream cannot be stopped during the printing process and wherever a droplet is not needed on the substrate the deflector plates direct the droplets into a gutter/waste collector. Waste ink that has been collected can be fed back directly to be used again. Depending on the set up used, the recycling nature of this feeding back technique carries a risk of contamination of the ink with the external environment, which can be detrimental to the experimental procedure if it is prone to the risk of infection or the solvent has a very fast evaporation rate, leading to the inability to recycle the jetted ink.

1.6.2 Drop-on-Demand Inkjet Printing

With drop-on-demand, a droplet of ink is only ejected when it is required. As such, there is potentially no waste incurred when jetting. The droplet ejection to the desired position on the substrate is achieved by positioning the nozzle of the jetting printhead above the desired location. There are two types of DOD inkjet printing, thermal and piezo inkjet printing, that will be discussed shortly.

Figure 1.6.1 shows the different methods of inkjet printing. The ejection of the droplet from the printhead can be caused through the generation of an air bubble through heat (thermal) or through wave propagation by a piezoelectric crystal (piezo). Inkjet printing is very versatile, as the size and the velocity of the droplet can be controlled through varying the pressure pulse propagation.

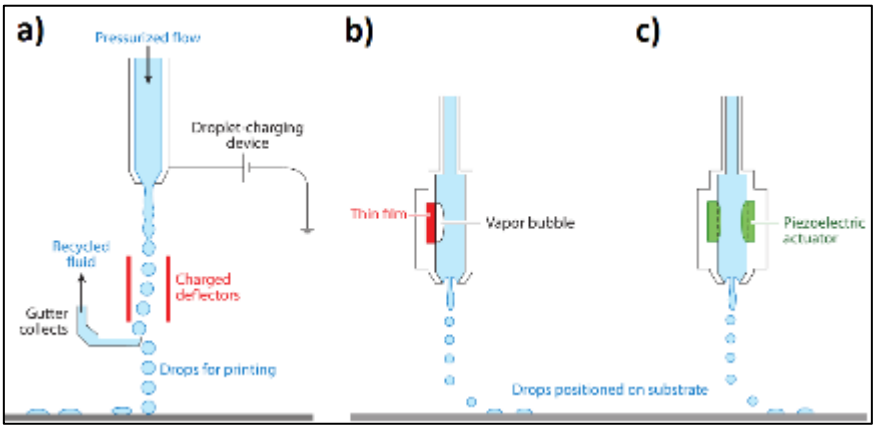

Figure 1.6.1 Schematic diagram showing the principles of operation of a) continuous inkjet (CIJ) printer b) thermal drop on demand (DOD) c) piezoelectric DOD. Image taken from Derby 2010.[93]

1.6.2.1 Thermal DOD

Thermal DOD requires the use of heat to generate the jetting of ink from the printing system. Within the printing component, a resistor heats up a thin film that is in contact with the ink, causing a localised area to increase in temperature. This rapid rise in temperature causes a bubble of gas to form, which generates a pressure difference through the rapid expansion and collapse of the bubble, creating a large enough energy difference to eject a droplet out of the printhead.[94] The rheology of inks suitable for thermal DOD is more limited than piezo DOD inks, due to the principle that suitable inks need to have a high vapour pressure under ambient conditions to successfully generate a bubble when heat is applied.

Biochemical gradients,[95] proteins,[96] bacteria,[97] hydrogels,[98] cells with no sizeable differences in survivability compared to controls in experiments with neural cells,[99] smooth muscle cells,[100] Chinese hamster ovary cells[101] and embryonic motorneurone cells[102] have been shown to print successfully using thermal DOD.

1.7 Understanding factors involved in Inkjet Printing

Piezo DOD employs a piezo crystal in the printhead (a typical example is shown in Figure 1.7.1) that actuates in response to an applied voltage, causing a change in the pressure within the reservoir that leads to droplet formation.

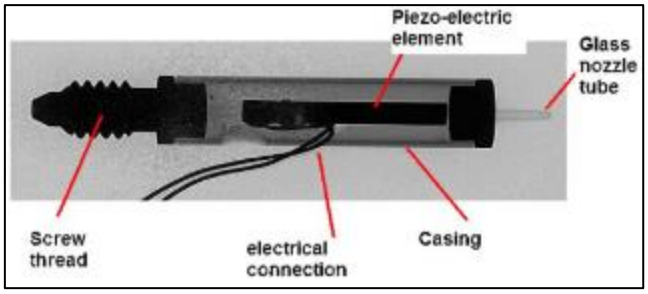

Figure 1.7.1 X-ray image of the printhead used within this document. The image illustrates a glass nozzle tube with 50µm inner diameter which is sleeved with a tube-type piezoelectric element. Taken from Gan et al. 2009.[103]

In the following section, a description of inkjet printing parameters is discussed. There are three stages within inkjet printing that characterise the technology: the generation and jetting of the droplet, the deposition/ interaction between the droplet and the substrate, and post printing behaviours such as drying and coffee staining;

1.7.1 Generation and jetting of the droplet

Within this section, the creation of an acoustic wave is discussed, which leads to the generation of a droplet from the piezoelectric printer.

A piezo crystal converts electrical energy into kinetic energy and vice versa. Upon applying a voltage, the piezoelectric actuator moves, causing the volume within the printhead to move and the pressure changes which can allow the jetting of a droplet.

Figure 1.7.2 highlights the generation of an acoustic wave in a piezoelectric printhead when a voltage is applied to the piezoelectric actuator that surrounds the glass nozzle. Upon actuation, the piezo crystal moves radially outwards, causing a negative pressure to form within the nozzle (Figure 1.7.2(B)). The negative pressure propagates in opposite directions from the middle towards both ends of the channel (with half the amplitude each) (Figure 1.7.2(C)). The nozzle end is considered a “closed end” in acoustic

wave theory, due to the small channel opening compared to the cross-sectional area of the channel, whilst the channel end leading to the reservoir is considered an "open end" as the reservoir's cross-section is larger than the channel.[104] The wave that reaches the "open end", i.e. the reservoir, is reflected back with its phase reversed, whilst the wave that returns from the "closed end", i.e. the nozzle, retains its phase (Figure 1.7.2(D)). As the waves return back to where they originally propagated, the piezoelectric actuator returns back to its resting position and radially contracts, causing a positive wave to propagate (Figure 1.7.2(E)). This new wave coincides with the return of the reflected waves, and they interact with one another (Figure 1.7.2(F)); the wave travelling to the reservoir is cancelled out, and the wave that travels to the nozzle combines to become a large positive wave (Figure 1.7.2(G)).[104]

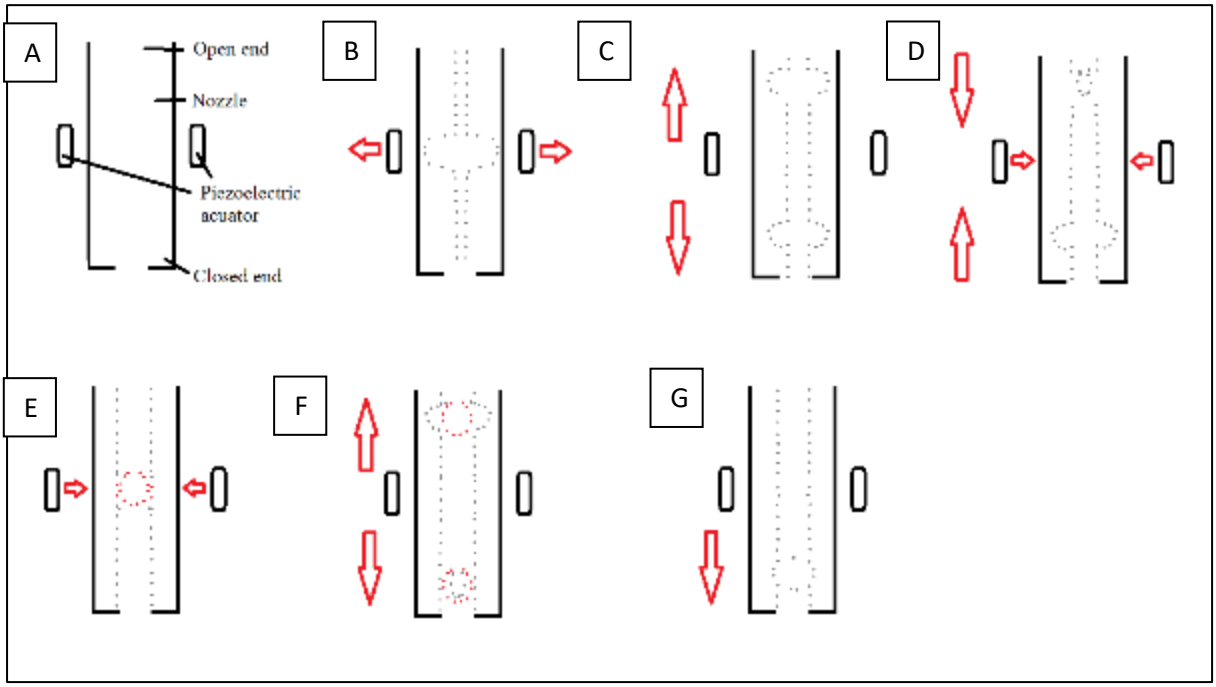

Figure 1.7.2 Diagrams depicting each stage of droplet formation caused by the actuation of the piezoelectric crystal in the printhead. A) showing the identification of each section of the diagram. B) upon the application of voltage into the piezoelectric actuator, the piezo actuators move radially outward, creating a negative pressure within the chamber. C) this negative pressure moves to both ends of the chamber, with half the amplitude. D) The negative pressure reaches the nozzle tip (closed end) and returns with the same phase, whilst the negative pressure returning from the open end has its phase reversed. In live experiments, steps (B-D) can be seen clearly as the liquid within the nozzle can be seen to be sucked into the nozzle; caused by the build-up of negative pressure within the chamber. E) all this occurs and the piezoelectric actuator returns back to position and causes a positive pressure to be produced. F) the acoustic waves formed by the piezoelectric actuator moving radially outward and inward combine together. G) the two waves moving towards the open end cancel each other out (positive+negative wave), and the waves traveling to the nozzle stack together (positive+positive wave). The overall product is a large positive acoustic wave being produced that moves to the nozzle.

A droplet is jetted from the inkjet nozzle when the kinetic energy in the droplet is greater than that of the surface energy needed to form a droplet. The greater the difference, the larger the velocity of the droplet.[105] The voltage and viscosity are important factors that determine the success of jetting the ink.

The rheological nature of the ink needs to be considered for droplet formation. More kinetic energy is required to break the surface energy of the droplet if the viscosity is high. If the viscosity of an ink is too high, droplets cannot be formed due to the dampening of the pressure wave[106] created by the piezoelectric crystal.

The voltage that is applied to the printer is an important factor for the generation of droplets. If the voltage is too high, the acoustic waves will not dissipate completely before the next wave is formed. These waves cause a chaotic droplet ejection environment as unwanted interactions take place in successive droplets. de Gans et al gave four different droplet regimes:[107]

1. successful single droplet formation
2. secondary generation of tail droplets
3. secondary generation of satellite droplets
4. failed formation.

Physical properties of fluids can be expressed with the Ohnesorge number, Reynolds number and Weber numbers. These dimensionless numbers relate liquid density, surface tension, droplet diameter and liquid viscosity to give a measure of the ability to print the ink, formation of droplets and fluid flow situations.

The viscosity, density and surface tension of printable fluids are the most important physical parameters to consider,[92] with $1 \leq Z \leq 10$ (Ohnesorge Number) being ideal printing values (Equation 1). When Z is less than 1, droplets tend to form the second type of droplet regime of de Gans[107] and form long filaments that breaks to form satellites and takes longer for singlet-droplet generation. This degrades the positional accuracy and printing resolution. Fluids with a high Z value have the inability to form a single droplet and satellites accompany the main droplet. Other significant parameters to create inkjet

behaviour include optimising single-droplet formability, distance from substrate to printhead, positional accuracy, and maximum allowable jetting frequency.

$$z = \frac{\mathrm{Re}}{\sqrt{\mathrm{We}}} = \frac{1}{\mathrm{Oh}} = \frac{\sqrt{\rho\gamma l}}{\mu}$$

z	Z number
Re	Reynolds number
We	Weber number
Oh	Ohnesorge number
ρ	Liquid density (mg/mm^3)
γ	Surface tension (dyne/cm)
l	Drop diameter (mm)
μ	Liquid viscosity (cP)

Equation 1 shows formula for z value, with key on the right

There are methods to assist the creation of an ink that has a suitable Z number, and that is through the addition of solutions such as isopropyl alcohol or acetophenone, which are able to bring down the Z number of a solution to the desired values. Although the viscosity of an ink can be modified by the addition of co-solvents and viscosity modifiers, such additions may negatively affect the final function of the printed feature. In terms of tissue engineered scaffolds, such additives may be toxic or reduce mechanical stiffness.

1.7.2 Drop/substrate interaction

After contact with the substrate, the behaviour of the deposited droplet strongly determines the final print quality. With molten, temperature and chemical sensitive “inks”, phase change can occur with the deposited droplet solidifying/drying. The completion of the phase change, which can be time dependent, can be the final desired product, or another processing step could be introduced to further develop the deposited ink (i.e. sintering a metal ink). This change, from liquid to solid, can be caused by a single or combination of several causes: solvent evaporation, temperature dependent changes or a chemical reaction causing the solidification/gelling of the substance.

1.7.3 Controlling the final shape

The width of the deposited droplet on a substrate is influenced by the contact angle formed by the ink on the substrate, the volume that is dispensed and the interaction of neighbouring drops.[92] The overlapping of dispensed droplets may not necessarily lead to spreading of the ink, but can lead to flow reversals as the droplets are pulled towards the bulk solute. The combined properties of the rate of solvent evaporation and the rate of ink droplet deposition are also factors that can change the shape of the final pattern. With respect to the creation of water-based hydrogels, several other factors affect the final shape; gelation time, swelling or contraction, stability and the substance's printability. Overall shape can be classified into five categories; individual drops, scalloped line, uniform line, bulging line, and stacked coins (Figure 1.7.3).[108] In all aspects of inkjet printing, the printed line behaviour is very important to the final finish of the scaffold. Ideally, a uniform line should be created, which would allow the successful stacking of progressive printing to occur. Such behaviour characteristics are governed by the droplet spacing between each droplet and the time allowed for the droplet to dry before the proceeding droplet is deposited Figure 1.7.4.

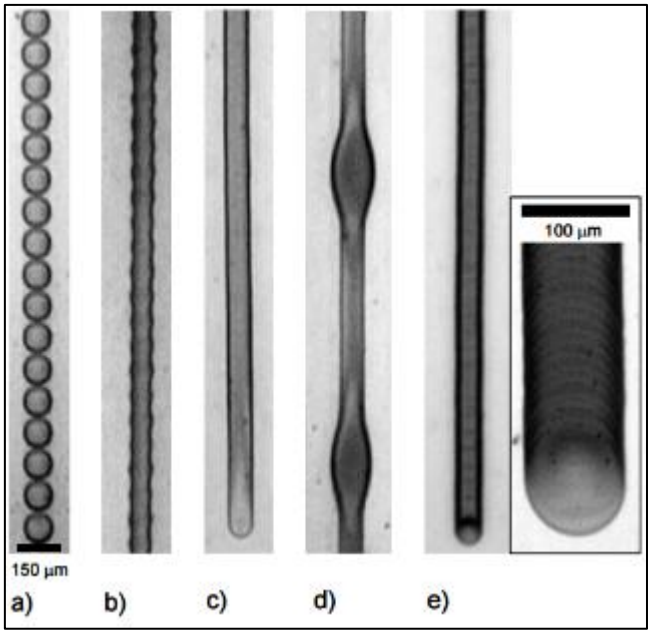

Figure 1.7.3 Examples of principle printed-line behaviours: a) individual drops; b) scalloped; c) uniform; d) bulging; e) stacked coins. Morphology is dependent on droplet spacing and inter-droplet drying, Drop spacing decreases from left to right. Image taken Soltman 2011.[108]

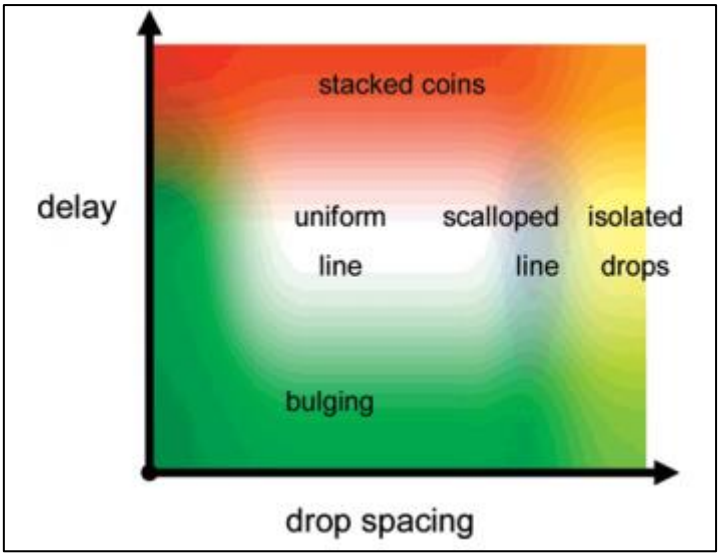

Figure 1.7.4 Graphical representation of the formation of different line behaviours proportional to inter-droplet spacing and inter-droplet drying. Image taken from Soltman & Subramanian 2008.[109]

1.7.4 Coffee Staining

Once the contact line has been pinned onto the substrate, an ink with nanoparticle suspension can form the so-called coffee-ring effect. This phenomenon, and more specifically its cause, continues to generate discussion. Coffee staining is affected by the disparity of the evaporation rate across the breadth of the ink feature: the evaporation rate is higher at the edges of the droplet, which drives a replenishing flow from the droplet's centre towards the pinned contact line, which in turn leads to the accumulation of solute at the droplet's edge forming a ring shape.[110] Deegan stated three conditions for coffee staining: a pinned contact line, a volatile solvent and a higher evaporation rate at the edge compared to the rate at the centre, as shown in Figure 1.7.5. A basic description of coffee staining is as follows. Once a droplet of ink has been deposited on a substrate, the leading edge of the droplet becomes fixed and is termed as a pinned contact line. Over time, the volatile liquid evaporates, and the volume of liquid decreases. On a very smooth surface, this evaporation would cause the contact line to retract from its original position. However, because the contact line is pinned (i.e. it cannot move), the height of the droplet decreases, as does the contact angle. The loss of solvent at the contact line must be compensated, which sets up a replenishing flow from the droplet's centre, causing nanoparticles to move radially outward towards the contact line. This flow causes an accumulation of nanoparticles at the edges of the droplet.

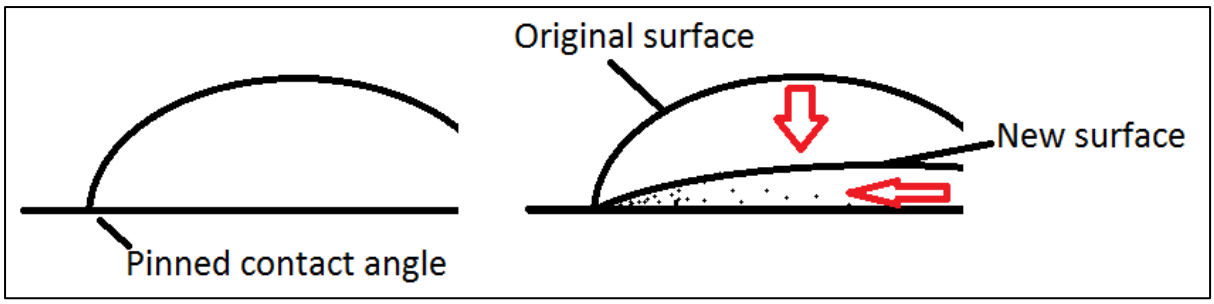

Figure 1.7.5 Generation of coffee staining. With a volatile liquid with nanoparticles, the rate of evaporation is larger at the edges compared to the centre, leading to the nanoparticles being transported to the pinned contact angle.

Coffee staining has been exploited to create higher resolution individual wells that have the potential to be used as miniature well plates,[111] as shown in Figure 1.7.6. This was created as the nanoparticles were controlled to be positioned at the outer edges of the droplet to form high peaks at the periphery that could act as a well. This was possible through the use of a more volatile solvent which caused a movement of the nanoparticles very quickly to accumulate at a concentrated region. Less volatile solvents would create a more evenly distributed coffee stain effect as the evaporation of a less volatile solvent occurs more slowly and therefore reduces the momentum to move nanoparticles in suspension.

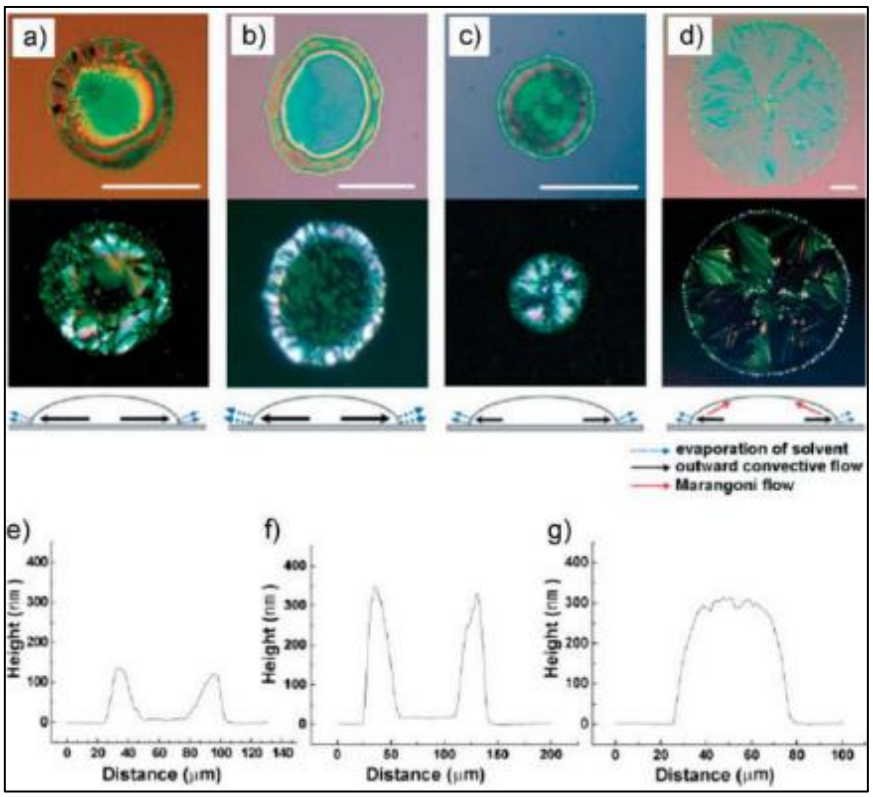

Figure 1.7.6 Through the use of difference solvents, the deposition of nanoparticles can be controlled to create varying steepness of valleys within coffee stained structures. Taken from Lim et al. 2008.[112]

1.8 Current state of the art of Inkjet Printing

Bioprinting describes the use of an inkjet printer to deposit cells, proteins, extracellular matrix components (ECM) onto 2D surfaces. There has been a steady interest in 3D bioprinting as more evidence shows that the printing process does not affect the efficacy of biological substances[90] and does not harm cells through the jetting process.[113] Ideally, the fabrication of scaffolds needs to be cost effective and easy to perform. The fabricated scaffolds should be biologically compatible with the host, able to break down into non-toxic substances and able to resorb at the same rate as tissue regenerates inside the wound.[114] Brian Derby[115] reviewed the use of bio-printing, in which an inkjet printer directly deposits proteins and living cells and Delaney[116] considered several other applications of using inkjet printing to print proteins, such as in the preparation of sensors and diagnostic devices. Inkjet printing builds structures droplet by droplet, allowing the fabrication of scaffolds with ideal internal structures for tissue engineering.[117] In this section, the different kinds of inks that can be printed are discussed, such as proteins, cells. The fabrication of 3D structures is also considered.

A broad range of bio-material applications has been studied with piezo inkjet printing; chondrocytes,[118] a combination of stem cells, smooth muscle cells, endothelial cells in a calcium chloride hydrogel,[119] bone constructs,[120] differentiation of stem cells,[121] silk-based biosensors,[122] artificial cells,[123] ganglion and glial cells,[124] proteins (BMP-2),[125] cellular tubes[126] and 3D tissue constructs[127,128] have all been printed. With such research under investigation, Figure 1.8.1 depicts examples of bioprinting techniques that have been investigated, involving both submerged and non-submerged printing, depending if the process has a chance of drying out bioinks with cells inside.

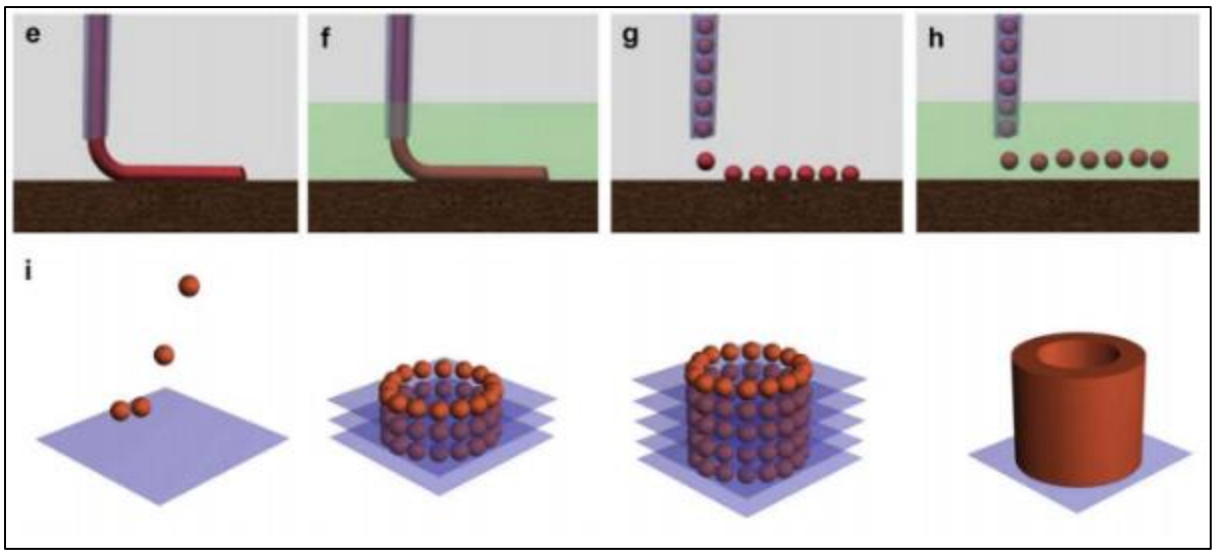

Figure 1.8.1 Images depicting different principles of extrusion bioprinting technology: e) extrusion in air; f) extrusion dispensing in fluid; g) dispensing spheroids of cells in air; h) dispensing spheroids of cells in fluid; i) a step-by-step process of a self-assembled tubular structure through bioprinting of spheroids. Taken from Mironov et al. 2011.[70]

In summary, it is possible to create complex 3D scaffolds that mimic the function of native tissue. However more research is required to understand the fundamental mechanisms of bioprinting, cell-substrate interactions and how bioprinted tissues would mature and how to cultivate bioprinted tissue. Figure 1.8.2 depicts the steady level of progression which bioprinting scientists wish to achieve as the technology matures. The simplest bioprinted tissue are described in Step 1 (Figure 1.8.2); cells of the same type are printed together to form sheets, and multiple layers can be printed to create 3D structures. Step 2 involved the creation of 3D scaffolds that require multiple cell types and biomaterials i.e. to create vasculature and different layers within tissue. Currently, research has achieved step 2 within this diagram, with private companies such as Organovo and Cyfuse making commercial bioprinted tissues for drug testing. It is hoped that in the near future, scientists would be able to print whole organs.

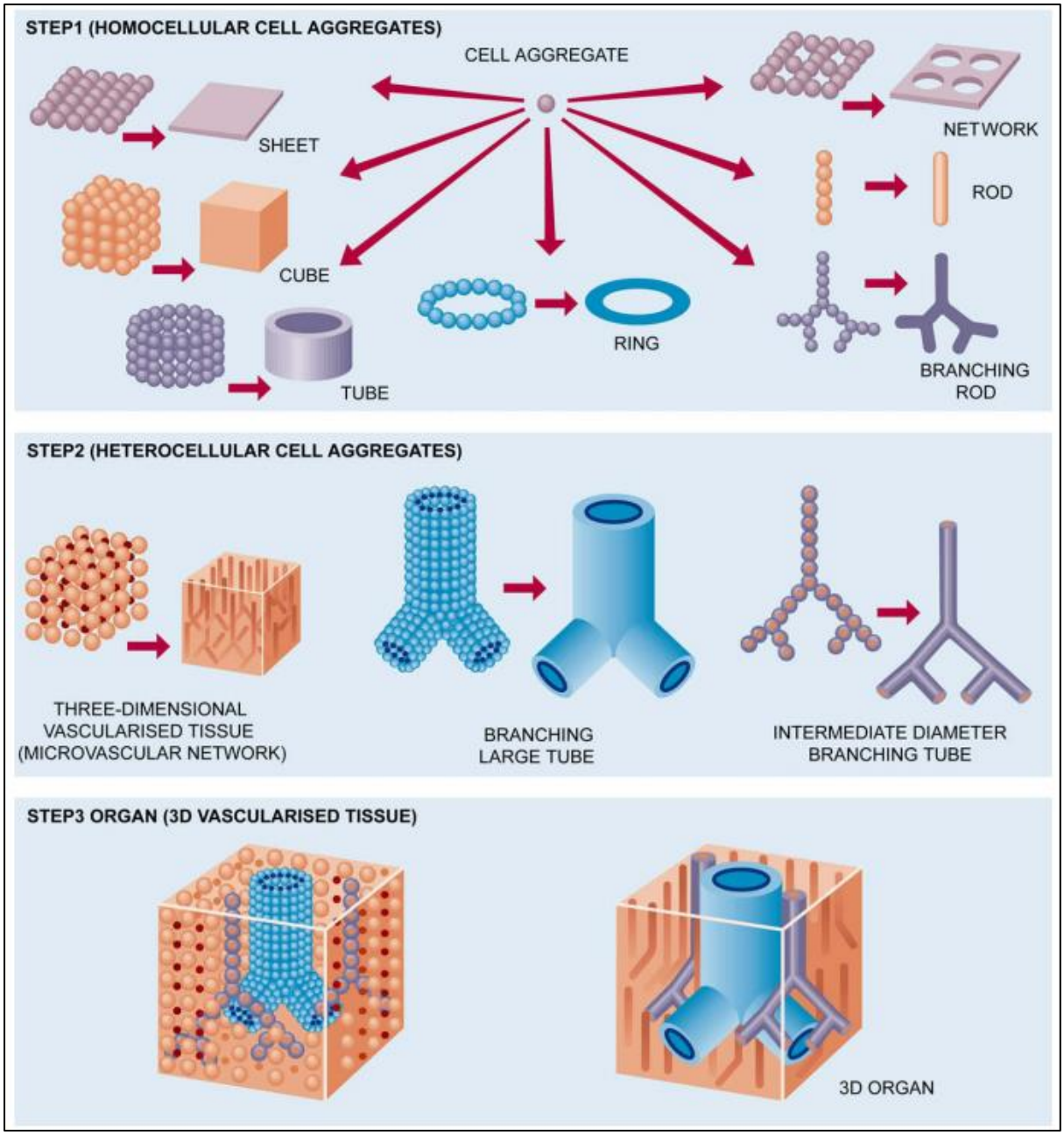

Figure 1.8.2 Theoretical eveolution of bioprinting. Taken from Mironov et al. 2011.[70]

1.8.1 Printing non-cellular materials

Inkjet printing has been used to enhance the interactions of cells and engineered biological scaffolds. By depositing solutions of proteins and ECM components, it is simple to print low concentrations onto a wide range of substrates using inkjet printing. The ease of printing is because of the ideal printing rheological properties of low concentrations of substances, which lie within the printing parameters of the printing system, and printing low concentrations of proteins and ECM components has been widely applied in research.[117] Due to the non-contact nature of inkjet printing, inks can be deposited on hard

and soft surfaces such as on tissue culture plastic, glass and spongy materials without difficulty.[129] Nishioka showed that inkjet printing does not significantly affect enzymatic activity through the process of printing and that the addition of sugar molecules can act as carbohydrate chaperones that protect proteins/enzymes from excess damage.[130] Typically a substrate can be coated in three ways with inkjet printing; 1) even coating 2) gradients and 3) selective deposition.

1) When using inkjet printing to coat a large surface with a uniform thin film, the layer thickness is less than dip coating, but thicker than spin coating.[131] Dip coating can be performed by immersing the substrate into the relevant solution and taking the substrate out again, which leaves a film of the solution around the substrate. Spin coating can be performed by spinning the substrate at very high speeds on a spin coater and applying a drop of material at the centre which spins off the edges of the substrate due to centrifugal forces, leaving a uniform thin film. There is less interest with this method of applying inkjet printing, as this doesn't focus on the key strengths of inkjet printing, which is its ability to print at high resolution with picolitre volumes. Several layers of spin coating would offer a simpler and quicker method of creating a thin layer.

2) A gradient can be described as an environment whereby a concentration of a substance is linearly increasing from one area to another. Creating a gradient can be done with inkjet printing, as inkjet allows highly controlled deposition of materials and the desired gradient scales, with which cells would interact with and respond to such gradients. Campbell's group showed that they had printed a gradient of FGF-2 on a fibrin substrate, with which fibroblasts responded differently dependent on the concentration of the hormone present.[132] The printed patterns lasted up to 10 days in cell culture conditions. Such control allows basic studies in developmental biology (i.e. efficacy of ECM components) and in-vitro drug testing to test cell behaviour in the presence of different proteins, growth factors and drugs, examples include laminin, fibroblast growth factor-2 (FGF2), insulin-like growth factor-II (IGF-II) and bone morphogenetic protein-2 (BMP-2).[133–136]

3) Selective deposition at discrete areas offers the most versatile application of inkjet printing. Printing proteins and other biologically relevant materials at discrete positions allows the selective deposition of

cells that will be seeded at a later stage. Figure 1.8.3 shows an example of how cell patterning of smooth muscle cells can be achieved through printing collagen at the desired areas, and Figure 1.8.4 with dorsal root ganglion cells respectively.

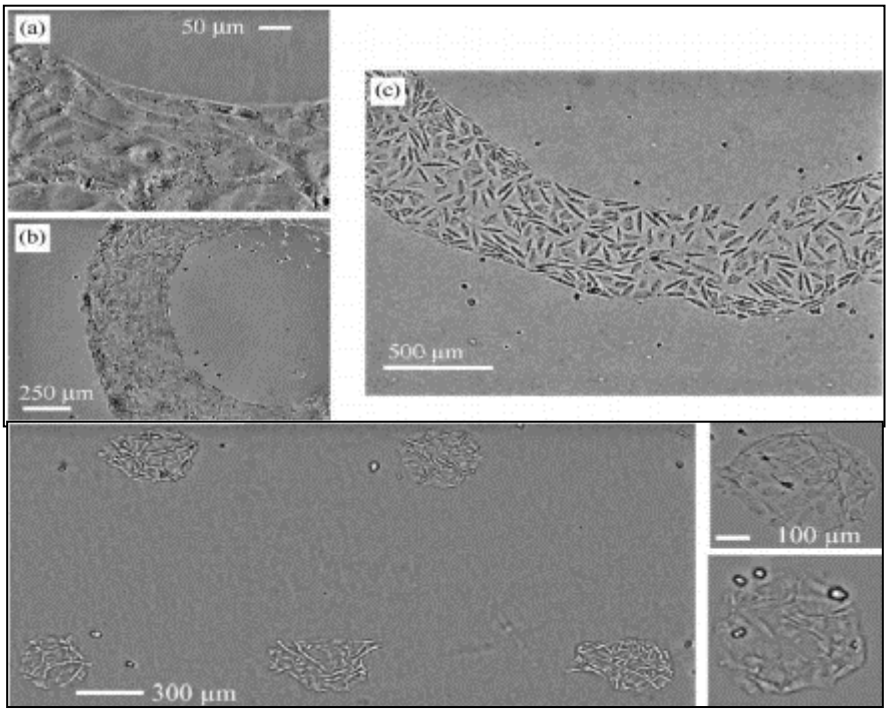

Figure 1.8.3 Inkjet printing was used to print collagen onto agarose coated glass slides that allowed directed cell positioning. Image taken from E. A. Roth et al. 2004.[137]

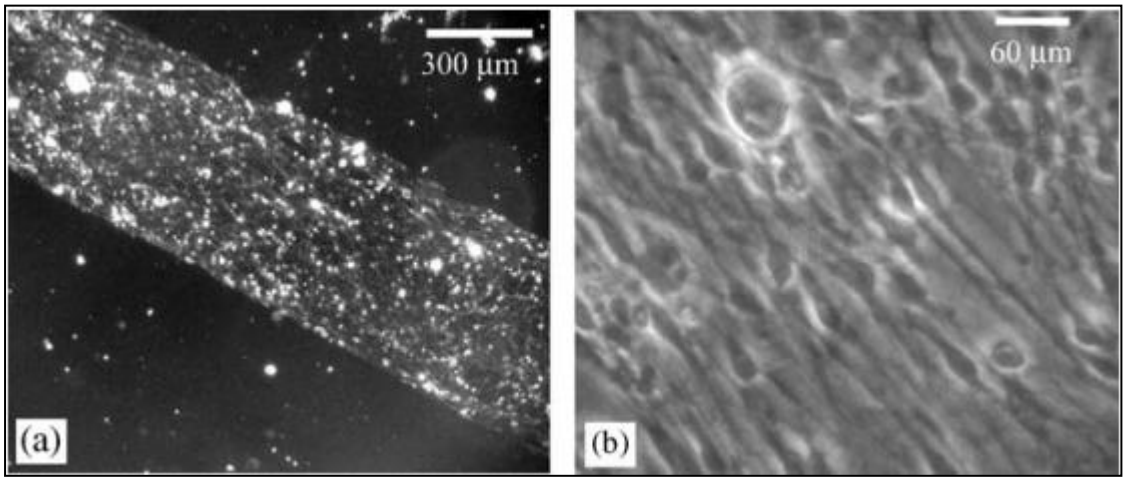

Figure 1.8.4 Neurons growing on inkjet patterned collagen substrates. Taken from E. A. Roth et al. 2004.

Additionally, selective deposition of materials like wax (Figure 1.8.5) and silver nanoparticles can be used in tissue engineering to create lab-on-a-chip devices and bioelectronics. Traditional methods to create biosensors and biodevices consist of high device manufacturing costs and are very efficient at creating devices of the same specifications. The advantage of inkjet printing is the flexibility to prototype numerous designs without the need to create additional masks and templates; inkjet printing patterning is a digital-to-fabrication technique. The electronics field is evolving towards a more flexible and planar production of organic and hybrid devices, with the focus on silicon-based semiconductor electronics being shifted. The use of inkjet printing allows high resolution production of devices with highly complex patterns being fabricated with a reduction of steps and at high yields.[16,138]

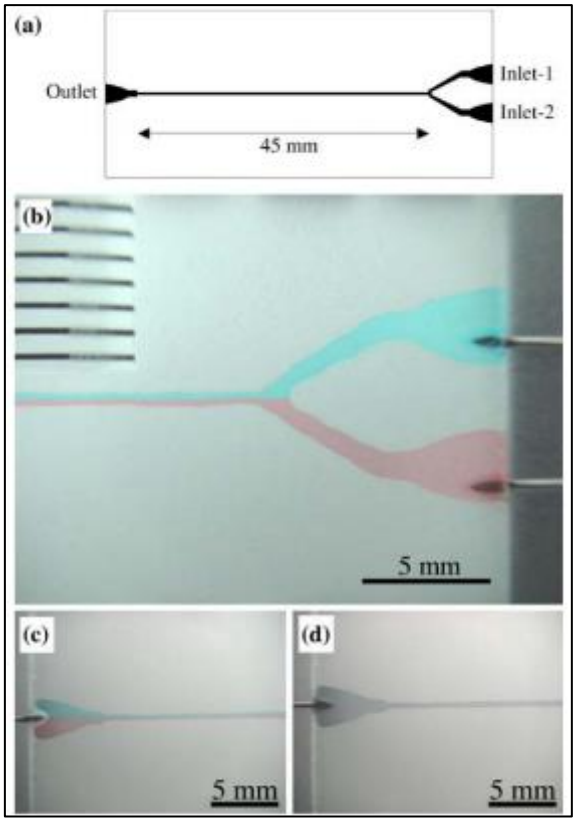

Figure 1.8.5 Hydrophobic inks were printed to create the desired channels in between the spacing of two hydrophobic coated glass slides. a) Y-shaped figure printed on the slide. Photographs of the Y-shaped channel, b) near the inlets, c) near the outlet when the injection rate was 5 ml/min, and d) near the outlet when the rate was 0.5 ml/min. Taken from Watanabe 2010.[138]

1.8.2 Printing of cells

Conventional methods involve manually seeding cells onto scaffolds [1]. Cell and organ printing has been shown to have great potential for applications in tissue engineering, due to inkjet printing's ability to

combine high-throughput capability with high precision of placement of material that can include cells.[68] Printing cells allows the ability to position cells on a scaffold, which can be beneficial when creating co-culture environments. Such environments can be neuronal (with glial and nerve cells) and organs.

Cells have also been directly deposited using inkjet printing. Saunders et al[113] successfully printed human fibroblast (HT1080 fibrosarcoma) suspensions using piezoelectric DOD and found that survivability reached 98%, compared to controls (Figure 1.8.6). In 2005, Boland et al used thermal DOD to print a Chinese Hamster Ovary cells suspension and found that cell viability was 97%.[102] These data indicate that mammalian cells can be delivered via inkjet printing without significant damage to the vast majority of cells. Further, fibrin was printed with neural cells the following year to build a 3D structure in a layer-by-layer process.[99] Cells have also been printed to promote cartilage repair.[139]

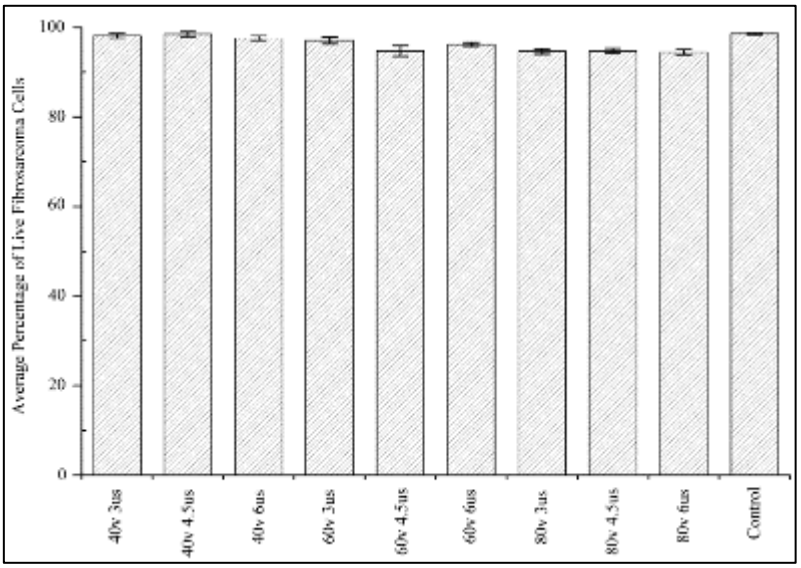

Figure 1.8.6 Viability of HT1080 cells as determined by a live–dead assay after inkjet printing different printing parameters. Taken from Saunders et al. 2008.[140]

After printing, cells seem to have a transient increase in the density of nanopores, which is ideal for transfection with genetically modified vectors containing genes or markers. This consequence has been manipulated to transfect cells with plasmids with potential to lead to a new branch in gene therapy, as transfected cells are able to produce the proteins encoded within the plasmid.[141] An example that could implement this method include the printing of cells for drug testing, with a vector for drug resistance

and/or fluorescent markers to better detect changes within a cell caused by drug testing. Further work with Chinese hamster ovary cells showed cells having pore sizes generated by inkjet printing to be on average 105Å, decreasing to 37Å after 60 minutes, 22Å after 90 minutes and behave normally after 120 minutes.[101]

With respect to cell printing, there are reports which show that when cells experience high frequencies in their environment, cell lysis can occur at ranges above 15kHz.[142] This has to be taken into consideration, and all experimental procedures using piezo DOD to eject cells were undertaken at frequencies that were significantly lower than this value.

With cell printing work, a droplet of ink would contain the respective cells and be suspended in cell media. After deposition onto a substrate, the cell media would evaporate over time, leaving the cells to dry out. The rate of evaporation depends on the volume of ink deposited and environmental factors such as ambient temperature. Typically, cell loaded inks would be printed, and left for half an hour to an hour for cell attachment to occur, before more cell culture media was added for incubation. The reliability of printing cells can be improved through the use of biocompatible surfactants; it was shown[143] that stirring and the addition of Pluronic as a surfactant improved the reliability of droplet formation.

It has been shown that an increase in cell concentration in the ink does not necessarily correlate with an increase in the number of printed cells.[101] With high cell concentrations, it becomes more likely that cells aggregate and clump together within the ink, causing blockages and making it difficult for aggregates to be ejected from the printhead (Figure 1.8.7)

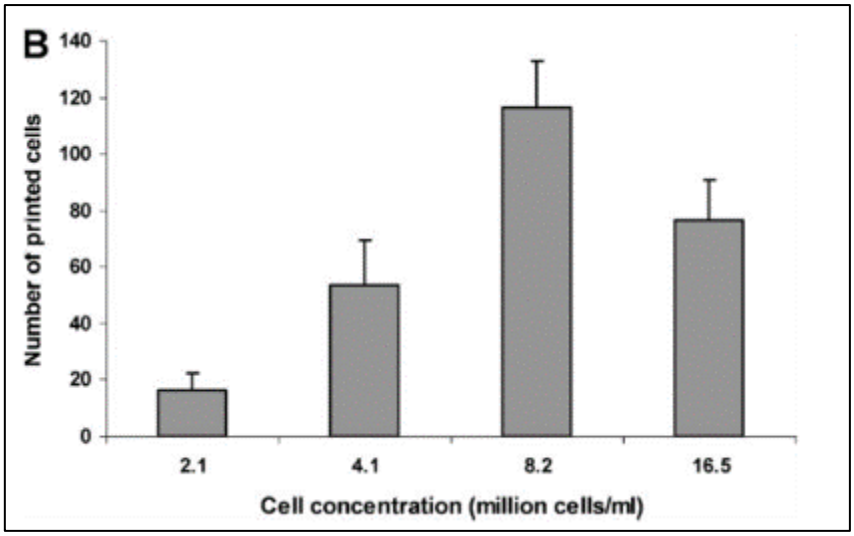

Figure 1.8.7. Quantitative cell printing showed percentage of drops containing cells varied linearly except for the highest concentration. Taken from Cui et al. 2010.[101]

The period of time that cells in suspension can be printed is also limited due to their preference to adhere to their surroundings, and it has been shown that, without additional influence, cells will begin to agglomerate and affect printing after 20 minutes.[113] To alleviate this restrictive time limit, the cells in suspension could be stirred in the printer to keep them stable for longer.

1.8.3 Three dimensional structures

Through controlling the dot spacing of the printed material, the final shape can be controlled to form lines, arrays and other two-dimensional structures. Placing multiple droplets on top of one another can cause a rise in height of the structure and stacking to occur to form three-dimensional structures, although, obviously some form of morphological control is needed. Typically, this control is achieved by using a phase change approach. Paraffin wax is a good example which is molten at high temperatures (>60°C) and quickly solidifies upon contact with a room temperature substrate. There have been examples of bioceramics successfully printed for biological applications, such as hydroxyapatite and related calcium phosphate substances have been used for bone regeneration applications.[144] For fabricating 3D soft tissue, there has been research into the creation of hydrogels, with substances like fibrin and collagen. A fibrin scaffold has been successfully printed for the fabrication of microvasculature.[145] Human microvascular endothelial cells (HMVEC) in cell media, supplemented

with thrombin (100 unit/ml) was printed into a microvasculature pattern on a fibrinogen (60 mg/ml) covered microscope cover slip.

1.8.4 Reactive printing

When depositing different inks together at a single location on a substrate, it is possible to create a compound directly on the substrate, as opposed to pre-making it prior to printing. In some experimental procedures, certain reactants, once reacted, are not able to be jetted out; as the final product can have unfavourable viscosity or oxidises easily, making it unprintable. Reactive printing reactants can be very efficient as reactions can take place at a nanolitre scale.[146] This method can decrease the total steps in creating the final product. However, if a washing step is required to remove unwanted side-products, there is a chance of washing away the desired product also from the substrate.

Reactive printing is mentioned as it will be carried out with experimental procedures with crosslinking gelatin through inkjet printing a crosslinking agent (glutaraldehyde), which will be discussed in more detail in the relevant experimental chapter.

1.8.5 Limitations of inkjet printing

Due to the nature of inkjet printing using a layer-by-layer process to form 3D structures, it is difficult to create a new layer of material above an empty cavity. This problem can be alleviated directly through the printing of supporting material to fill the voids of the internal structure with sacrificial materials that can be easily removed post printing.[147] The use of a sacrificial material can be further complicated however by the difference in setting characteristics of the sacrificial material and the desired material. If printing a single layer was taken as an example, the setting properties of both materials can be different and the resultant film will not be uniform, but rather uneven, which will affect the positioning of proceeding layers. Printing several layers would require an algorithm that understands the expansion/shrinkage of the sacrificial material in relation to the desired material, and adjustments taken to counter this variable.

Another limitation to inkjet printing is that the inkjet printer can only print inks that are low in viscosity; typically inks with viscosities of between 1-20 mPa/s. Inks that have a lower viscosity than 1 mPa/s

would not be very stable for prolonged printing, as the energy required to form an ink droplet would be so small that miniscule fluctuations in the printing system would cause significant disruption of the jetting of the ink. Inks with viscosities of more than 20 mPa/s would be difficult to print, as the printing system may not provide enough energy to overcome the surface tension of the ink at the nozzle to create a jetted droplet. Inks that have a higher viscosity can have their viscosity lowered to more favourable units through increasing the printing temperature and decreasing the ink's concentration by adding more solvent.

1.9 Materials used in thesis

Many materials have been made as a consequence of the field of tissue engineering, while other materials had other purposes when it was conceived, but later proved to be an ideal biological scaffold material. Synthetic polymers have proved to be versatile, being used as space filling agents, for drug delivery and creation of three-dimensional structures. Such substances could be made with easier purification and processing than the more complicated natural methodologies. Some synthetic polymers may be bioinert, but can be readily functionalised with the desired traits. There are already products and research into more desirable scaffolds that are easier to manage and handle, from injectable, expanding and shape-memory materials that can respond to photo, chemical and/or physiological stimulation that allow the material to be easily managed and handled.[148–150]

Looking at nature as a guide to creating scaffolds is useful, as it gives an informed understanding of how tissues naturally interact, and can become a basis to develop materials that mimic such interactions. The main materials that were used to create biologically relevant structures within this document were gelatin and paraffin wax.

1.9.1 Gelatin

It would be ideal to create a scaffold that had controlled degradation rates that could be used for time-dependent drug delivery, and to be in sync with host wound healing. Gelatin is one of the most commonly used hydrogels for mammalian cell growth[151] and biomedical applications. Such biomedical applications include drug delivery through hard and soft capsules, wound dressings, cell encapsulation

and in vitro tissues (Kuinkjet printingers et al. 2000; Esposito et al. 1996; Wissemann & Jacobson 1985). Being a hydrogel, gelatin hydrogels can maintain a physiologically moist environment. Its precursor prior to chemical modification – collagen, is an essential a major component of the extracellular matrix, and through its similarities to collagen, mammalian cells grow very well in the presence of gelatin. Gelatin is a biocompatible denatured protein of collagen that is biodegradable, non-immunogenic and can be controlled at a desired rate by altering the cross-linking to suit its purpose. Cross-linking of the biopolymer is required as virgin gelatin turns into its sol state at biological temperatures (37°C), which upon cooling returns to a thermoreversible hydrogel. Proteolytic enzymes released by adhered cells help facilitate the virgin gelatin to dissolve and break down the gelatin into the cell culture media. There are many ways to cross-link gelatin; through using UV-light [155], a cross-linking enzyme [156–158] and chemical crosslinkers. Such chemical crosslinkers include carbodiimide, diphenylphosphoryl azide, and glutaraldehyde [151]. However glutaraldehyde provides the most stable crosslinking agent compared to others mentioned.

Crosslinking allows gelatin to remain as a hydrogel at biological conditions, whilst also improving the thermal and its mechanical stability. Glutaraldehyde crosslinking involves the reaction of free amino groups of lysine or hydroxylysine (lysine oxidised by lysyl hydroxylase enzymes) amino acid residues of gelatin and collagen with the aldehyde groups of glutaraldehyde.[159] High concentrations have proved to be toxic as residual glutaraldehyde is toxic to cells in cell culture. As a rule of thumb, glutaraldehyde concentrations of less than 2.5% are suitable for biomedical applications. 1 wt% glutaraldehyde is sufficient to cross-link 100% of exposed gelatin and increase its Young's modulus by 20 times. Once concentrations are above 2.5%, cell toxicity becomes a significant problem as glutaraldehyde can be slowly released from the gelatin over time.[160] Gelatin has been used in tissue engineering in bone,[161] cartilage,[162] wound healing of skin[163] and adipose.[164]

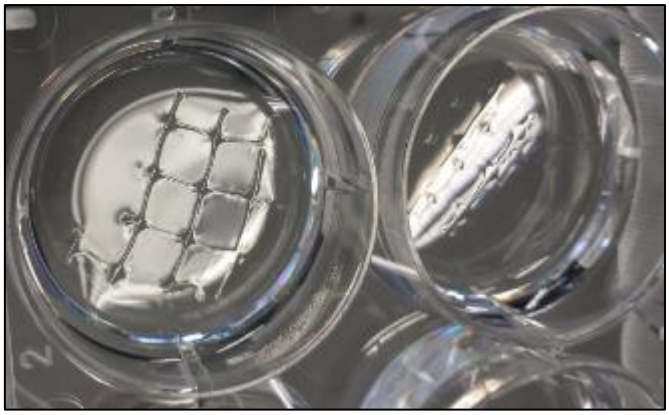

Figure 1.9.1 Gelatin scaffolds used for tissue engineering cultured in well plates

1.9.2 Paraffin wax

Paraffin wax is not usually associated with tissue engineering applications. The exceptions are using wax for histology to preserve embedded samples, creation of moulds, lab-on-a-chip applications (Figure 1.9.3) and wax-loss manufacturing to make solid and porous structures.[165–168] Solid at biological temperatures, having a melting point of around 70°C, insoluble in water, they are long chained nonpolar lipids. Paraffin wax is a synthetic wax derived from petroleum and refined by vacuum distillation. Being biocompatible, biological tissue and its constituents can interact with wax without harm. The combination of being a solid at biological temperatures, biocompatible, cost-effective and easy to print with an inkjet printer made this material an ideal candidate for tissue engineering applications (Figure 1.9.2). There is limited literature with the use of paraffin wax apart from the applications mentioned above, however it had been postulated that wax would be an ideal material for the creation of cell guidance structures and cell patterning.

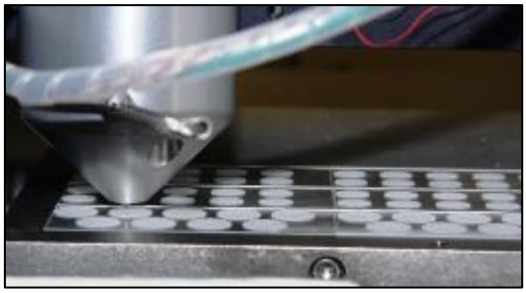

Figure 1.9.2 Printing setup during the printing paraffin wax scaffolds

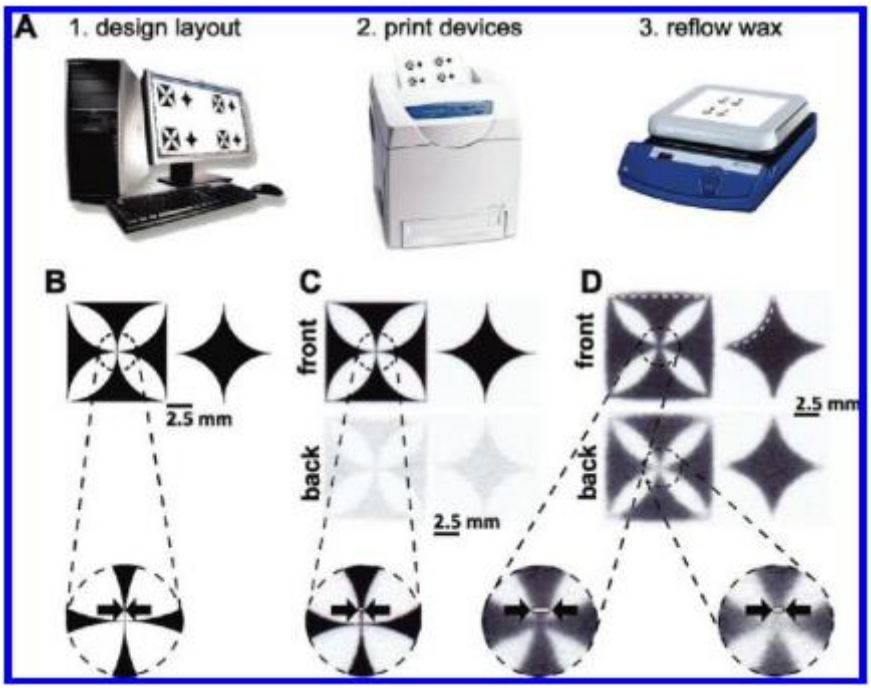

Figure 1.9.3 Patterning hydrophobic barriers in paper by wax printing. Taken from Carrilho et al. 2009.[168]

1.10 Objective of thesis

With the advantages provided by inkjet printing, several novel uses of this technology were explored;

- With the ability to print at precise locations at picolitre volumes, cell deposition quality was studied by seeding cells onto wax patterned environments to allow the control of orientation and patterning of cells in culture.
- Using reactive printing to create 3D scaffolds of cross-linked gelatin arrays, cell biocompatibility was studied to evaluate viability of cells in crosslinked gelatin created by inkjet-printing.
- Cell viability was studied for neuronal cells (Schwann cells and NG108s) inkjet-printed at varying experimental conditions.

2 Materials and Methodology

2.1 Inkjet Printing System

A single nozzle piezoelectric inkjet device (MicroFab, Texas, USA) was used to print each cell type (Figure 2.1.1). Specifically, this was a Jetlab 4 xl-A tabletop-printing platform with positional accuracy and repeatability of 25 µm and 5 µm, respectively, equipped with drop-on-demand PH-46 printheads (MicroFab, Texas, USA). Independent polypropylene fluid reservoirs kept the printing inks isolated prior to jetting, and the dispensing devices were connected together through PTFE fittings and tubings. A CT-PT4 four channel pressure controller was used (MicroFab, Texas, USA) to maintain a slight negative pressure within the system to control a nozzle meniscus level for optimal jetting. A JetDrive III was used to control the generation of a waveform and tailor the jetting parameters to the printheads. Prior to jetting, all tubing, reservoirs and printheads were flushed with 1% (v/v) Micro-90 cleaning solution (10 mL for 10 minutes), distilled de-ionised water (20 mL for 30 minutes) and subsequently with cell culture medium (DMEM / 10% foetal calf serum (FCS)). Unless otherwise stated, the inkjet printer was calibrated to print at 2 kHz, 80 V, rise time 36 µs, dwell time 42 µs, fall time 50 µs and printed within 3 mm from the surface of the substrate. Viability experiments used voltages from 70 V with increasing increments of 20 V to a maximum of 230 V. This setup proved most stable for producing droplets. All samples were jetted into 12 well flat bottom cell culture plates (Costar) at room temperature. Approximately 300 µL was jetted into each well at a concentration of $2x10^5$ cells/mL with their respected variables. Inkjet printing was performed within 30 minutes of loading a cell suspension into the print reservoir. It was established from initial work by other research groups[124] and myself that both fibroblasts and neuronal cells could be printed for up to 40 minutes without significant loss of cell number.

Figure 2.1.1 Photograph showing the Microfab piezoelectric printer used for this study, with magnified images of the CCD camera, printhead holding platform, and printhead during jetting.

2.2 Cell types, culture methods and handling

2.2.1 Cell types

Different cell types were used within the context of this thesis; dermal fibroblasts, RN22 Schwann cells, NG108-15 cells and Porcine Schwann cells.

2.2.1.1 Dermal fibroblasts

Human dermal fibroblasts were obtained from abdominoplasty or breast reduction operations according to local ethically approved guidelines (under an HTA Research Tissue Bank license number 12179).

2.2.1.2 RN22 Schwann cells

Rat RN22 Schwann cells were purchased from the European Collection of Cell Cultures (ECACC) (Health Protection Agency, Porton Down, Wiltshire, UK).

2.2.1.3 NG108-15 neuronal cells

NG108-15 neuronal cells were obtained from the European Collection of Cell Cultures (ECACC Health Protection Agency Culture Collections, Porton Down, UK).

2.2.2 Porcine Schwann Cells

Primary porcine Schwann cells were isolated from both tibial and fibular nerve tissue under the Animal (Scientific Procedures) Act 1986. The term "Schwann cells" mentioned hereafter refers to primary porcine Schwann cells, and not to be mistaken for RN22 Schwann cells.

2.2.3 Cell culture

Cells were cultured in a humidified 37°C/5% CO_2/95% air (v/v) environment in Dulbecco's modified Eagle's medium (DMEM; Sigma) containing 10% (v/v) FCS (Gibco, UK), 1% (v/v) L-glutamine (Gibco, UK), 1% (v/v) penicillin/streptomycin (Gibco, UK), and 0.5% (w/v) amphotericin B (Gibco, UK). Porcine Schwann cells had 0.150% (v/v) bovine pituitary extract (BPE) (Sigma, UK) and 0.02% (v/v) forskolin (Sigma, UK) added to their cell media. Cells were cultured in a humidified 37°C/5% CO_2/95% air (v/v) environment.

2.2.3.1 Induce differentiation to NG108-15 neuronal cells

With respect to NG108-15 neuronal cells, when the experimental procedure required, FCS was removed from the medium on neuronal cells to induce cell differentiation and neurite formation when optimal cell density was achieved.

2.2.3.2 Well plate modification for Schwann cell culture after Inkjet Printing

Previous experiments showed Poly-L-lysine and fibronectin to support Schwann cell growth,[169,170] and therefore these coatings were implemented. The 12-well plates were coated with 0.5 mg/mL poly-L-lysine and 0.5 mg/mL fibronectin respectively for 10 minutes at room temperature on a platform rocker (STR6, Bibby Stuart). After discarding the used poly-L-Lysine and fibronectin, the well plates were dried at room temperature for 2 hours before being washed with warm PBS twice. TCP 12-well plates were used as controls.

2.2.4 Cell seeding

Cells were grown to near confluence, and detached with 0.05% trypsin/EDTA (GIBCO, Invitrogen, Karlsruhe, Germany). A Neubauer chamber was used to count the cells. Passages 16-19, 20-22, 2-3, 9-12 were used for dermal fibroblasts, RN22 Schwann cells, porcine Schwann cells and NG108-15 neuronal cells respectively.

When cells were required to be seeded onto a scaffold, unless otherwise stated, cells were seeded at 4 x 10^4 cells per sample in 1 mL, and left in the incubator for 60 minutes. After this time, the sample was topped off with cell medium to cover the entire substrate.

When cells were required to be seeded in wax scaffolds (discussed later in the thesis), the sample was placed in a petri dish and cells were seeded at 2 x 10^4 cells per sample in 1 mL, and left in the incubator for 60 minutes. After this time, the sample was supplemented with 10 mL.

2.2.5 Cell analysis

2.2.5.1 Trypan blue staining for cell viability immediately after inkjet printing

Cell suspensions were mixed and stained with equal volumes of Trypan blue and analysed by light microscopy. Cells staining positive for blue dye uptake indicated loss of membrane integrity and were counted as dead (or damaged). In contrast, cells excluding Trypan blue dye appearing bright coloured were counted as live. A live/dead percentage was calculated to give population cell viability immediately after inkjet printing. Thirty randomly selected microscope fields of view per experimental condition were selected.

2.2.5.2 MTT metabolic activity for assessing cell viability 1, 3 and 7 days post printing

To investigate the longer term effects of inkjet printing on cells (discussed later in the thesis), samples were analysed for metabolic viability by MTT (3, 4, 5-dimethylthiazol-2,5-diphenyl tetrazolium bromide) assay at each time point. Fibroblasts and NG108 neuronal cells were cultured on TCP, and Schwann cells were cultured on TCP, poly-L-lysine and fibronectin. Non-printed cells were used as a reference control. After deposition, cells were re-suspended at a density of 4x10^4/mL cells and seeded into a 24 well plate in triplicate. Culture medium was removed and the samples were gently washed with PBS x1 and 1 mL of 0.5 mg/mL MTT (in PBS) solution was added. The rate of formazan crystal formation through MTT reduction is proportional to the metabolic activity of the cells. After incubation for 90 minutes at 37°C, unreacted MTT solution was aspirated and replaced with 200 µL acidified isopropanol (0.1% (v/v) HCl in isopropanol), dissolving the purple crystals. 200 µL of solution was then transferred into 96-well plates, and read in a BIO-TEK ELx 800 microplate reader at 540 nm and referenced at 630 nm.

2.2.5.3 Neurite analysis of NG108-15 neuronal cells 1, 3 and 7 days after inkjet printing

Neuronal cells were prepared as described above, but cultured in DMEM without foetal calf serum, to stimulate neuronal differentiation.[171] These are reported to be morphologically different to cells cultured with serum.[172] Figure 2.2.1 shows experimental examples of the physical differences between cells that were cultured with and without serum. Those cultured without serum showed more spindle-like dendritic protrusions.

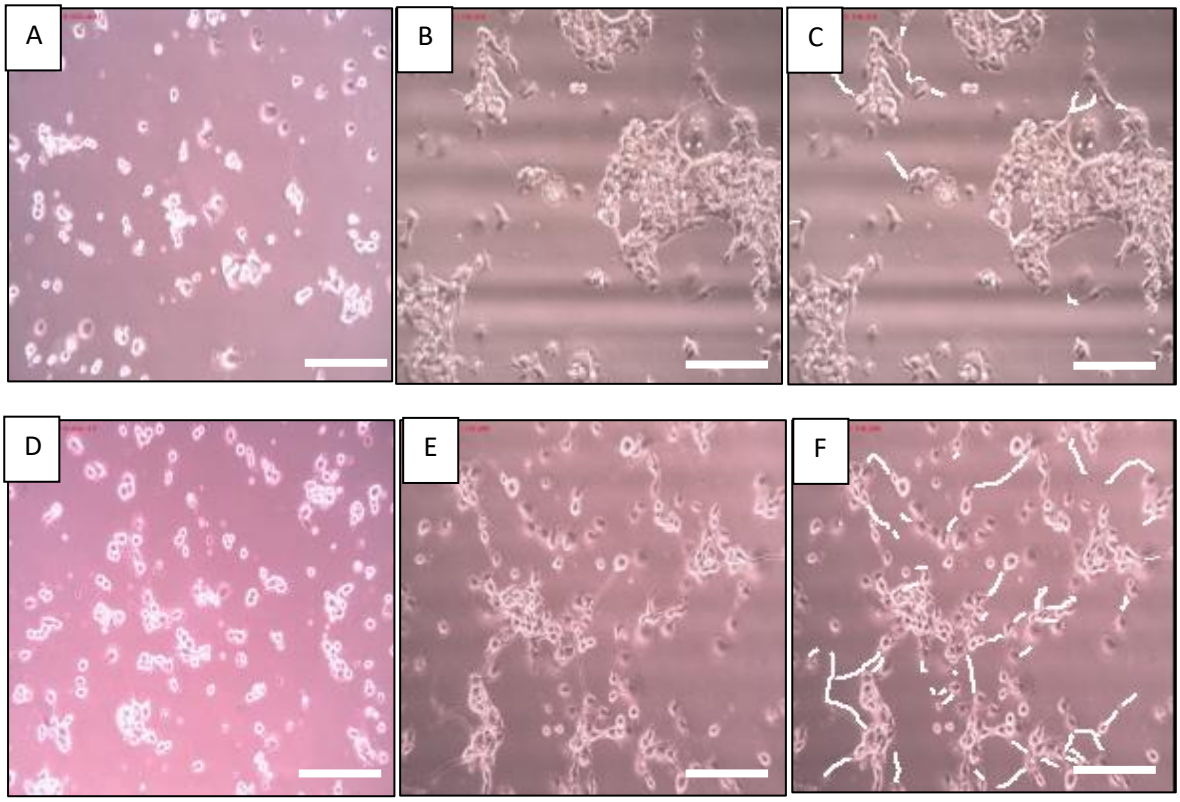

Figure 2.2.1 Light microscopy images of NG108s cultured with foetal calf serum on day 1 (A) and day 3 (B), and an overlay of highlighting the spindle-like dendritic protrusions in white (C). NG108s cultured without foetal calf serum on day 1 (D) and day 3 (E) and an overlay of highlighting the spindle-like dendritic protrusions in white (F). Scale bar = 200 µm.

Five images were sampled from randomly selected fields of view. 10 cells were analysed in each image from the top left corner. This approach was followed consistently to prevent bias. This gave a total of fifty cells being analysed for each measured variable.

Morphological characterisation techniques employed were adapted from previously published work.[169] Cells were only analysed if their cell body was not touching another cell and if the whole of the cell, including neurites, was visible in the image and the neurite length was measured. A neuritic process

twice as long as the length of the cell body was counted as a neurite. The number of neurites per neuronal cell was quantified, together with the percentage of neuronal cells bearing neurites.

2.2.5.4 S-100β, immunolabelling for identification of Schwann cells

Immunolabelling of S-100β protein was used to determine the overall purity of the cell culture of Schwann cells on different well surfaces. Cells were labelled on days 1, 3 and 7. At each time point, Schwann cell growth medium was discarded and cells washed 3 times with PBS (5 min each wash). 500 μL per well of 3.7% (vol/vol) formaldehyde solution was added for 20 min at 4 °C to fix Schwann cells and then washed with PBS (3×5 min). Cells were permeabilised with 500 μL of 0.1% (vol/vol) Triton-X100 for 20 min at room temperature and washed three times with PBS for 5 min. At room temperature, 500 μL of 7.5% BSA per well was added and incubated at room temperature for 60 min, followed by 1% BSA wash once. Primary antibody (rabbit polyclonal anti-S100β antibody (1:250)) (Dako, Denmark) was prepared in 1% BSA and incubated with the samples at 4°C overnight. Primary antibody was removed and followed by 3x PBS washes (10 min each). Samples were then incubated with goat anti-rabbit IgG H&L FITC secondary antibody (1:100 in 1% (vol/vol) BSA) (Vector Labs, USA) at room temperature in the dark for 1 h.

2.2.5.5 FITC-Phalloidin and DAPI Immunolabelling for F-actin and nucleus of cells

For confocal fluorescence imaging, cells were seeded on the scaffolds at $2x10^4$ cells per sample, stained with phalloidin-fluorescein isothiocyanate (FITC) for F-actin filaments and 4',6-diamidino-2-phenylindole dihydrochloride (DAPI) for nuclear staining.

Samples were fixed with 3.7% formaldehyde in PBS for 30 minutes at room temperature and permeabilised with 0.1% (v/v) Triton X-100 in PBS for 30 minutes. Phalloidin:FITC was added at 1:1000 in PBS in combination with DAPI at 1:1000 (300 nM) for 30 minutes, washed and stored in PBS at 4°C until imaging. Cells were washed with PBS (x3) for 5 minutes between each step.

2.2.6 Confocal microscopy

Samples were imaged using an inverted Zeiss LSM 510 META confocal microscope, using an argon 30 mW ion laser (488 nm) for FITC excitation λex = 495 nm / λem = 521 nm. Nuclei were visualized by two photon excitation using a Chameleon Ti-Sapphire tuneable laser λex = 800 nm / λem = 461 nm.

5 images were sampled from randomly selected fields of view and Schwann cells were identified if DAPI labelled nuclei were co-labelled with an S-100β positively labelled cytoplasm. Cells were counted and a percentage of positively labelled Schwann cells were compared to the whole sample population. A confocal scanning microscope (Carl Zeiss LSM510-META, Germany) long-range water-dipping lenses were used. FITC channel (λ_{ex} = 485 nm; λ_{em} = 520 nm). DAPI (λ_{ex} 400 nm; λ_{em} = 460 nm). Image acquisition and analysis were carried out with Carl Zeiss Laser Scanning Systems LSM 510 software.

2.2.7 Aggregation of cells during inkjet printing

Experiments were done to determine cell aggregation in the inkjet printer over time (discussed later in the thesis). Cells were inkjet printed into a 96 well plate for one minute each well, at a frequency of 100 Hz, and a total of 96 minutes was examined. The total cell number for each minute was counted for each well and tallied to produce a graph determining the cell count over time.

After inkjet printing, each section of the printing system was uninstalled and flushed with 0.05% (w/v) trypsin/EDTA (GIBCO, Invitrogen, Karlsruhe, Germany) to remove cells within the system. A log was kept to determine which parts of the printing system had most cells within them, and could be concluded why cell count decreases over time.

2.3 Creating crosslinked gelatin scaffolds

2.3.1 Gelatin hydrogels

Gelatin type B (Bovine skin, G-9382, Sigma, UK) was mixed with either warm distilled water or warm Dulbecco's Modified Eagle Medium (DMEM) (depending on experimental setup), and mixed with a magnetic bead on a magnetic stirrer until all the gelatin was dissolved. The hydrogel was pipetted into the desired wells (e.g. well plates, petri dishes) and allowed to cool. Gelatin was deposited in 6-well plates, or petri dishes (depending on experimental setup).

2.3.2 Glutaraldehyde

Glutaraldehyde (25% in water, G6257, Sigma, UK). Distilled water was used to dilute the glutaraldehyde.

2.3.3 Crosslinked gelatin washing

When the experiment required gelatin to be crosslinked with glutaraldehyde, the crosslinked gelatin would be washed with hot de-ionised water (50°C) three times, and left soaking for 1 hour prior to cell seeding. This washing would remove uncrosslinked gelatin and remove excess residual glutaraldehyde.

2.4 Printing patterned wax environments

Using a combination of Microsoft Paint and MS Windows-based computer aided design software environment (Jetlab4, Microfab), varying shapes and designs were created with varying channel widths and complexity. All patterned environments created within this thesis related to printing wax; for the fabrication of cell-guidance structures, microdevices and phantoms (discussed later in the thesis). The Jetlab4 software is able to read bitmap images and translate the image into a printable structure. Using a black and white bitmap image, a droplet spacing is set, and each pixel represented the droplet spacing, with a white pixel indicating where the printer should jet a droplet, and black pixels being areas to not jet.

The writing of the script is relatively simple, with the addition of the Bitmap description (Figure 2.4.1), with Figure 2.4.2 describing how the Bitmap script works.

```
moveto 0 0
set frequency 200 1
set fly on 20 3
bitmap 0.040 0.040  0 0 0 C:\jetlab4\Scripts\Chris\2012_06_08a\x5a.BMP
```

Figure 2.4.1 A typical script that is used for Bitmap applications.

```
bitmap <dx> <dy> <angle> <topbottom> <bidir&rt; <filename>

dx - Spacing of pixels in x direction (i.e, rows, before rotation), floating point number>=0.0, required.
Note that any size information in the file other than numbers of pixels is not used.
```

dy - Spacing of pixels in y direction (before rotation), floating point number =0.0, required. Note that any size information in the file other than numbers of pixels is not used.

angle - Angle in degrees by which to rotate the bitmap around the starting point. Required.

topbottom - Flag indicating if the rows are stored top-to-bottom (topbottom=1) or bottom-to-top (0); the latter seems to be the default used by Microsoft Paint. Required.

bidir - Flag to indicate if rows are to be printed forth and back (1) or not (0). Required.

filename - Name of the bitmap file to be printed. Because the current directory cannot be reliably predicted, it is highly recommended to specify the full path. If there are spaces in the path or file name, enclose the full name in double quotes. Required.

i.e. bitmap 0.040 0.040 0 0 0 C:\jetlab4\Scripts\Chris\2012_06_08a\x5a.BMP
drop spacing of 0.04 mm on both x and y axis, 0' change in angle, bottom to top printing and not printed forth and back, with the file in the directory C:\jetlab4\Scripts\Chris\2012_06_08a\x5a.BMP

Figure 2.4.2 Key to understanding the Bitmap script

Inkjet printing parameters were optimised to create a single droplet per ejection, with initial experiments to determine the ideal droplet spacing to create the ideal geometries. The volume of ink that was ejected from the piezoelectric printhead could be manipulated through the fine tuning of its printing parameters, such as the voltage, rise and echo time which alters the size and velocity of the droplet to create optimum conditions to print on varying surfaces and resolutions.

When starting a new experiment, the ideal droplet spacing must first be identified through an incremental step-by-step process. A script was created that could be repeatedly used with any ink that was tested, that would automatically print the ink with various droplet spacings, and then a microscope could be used to examine each of them to determine the ideal droplet spacing. Due to environmental changes that potentially affects the jetting of the ink, the ideal printing parameters from one day may

not result in a successful printing behaviour when repeated on another day of use, and therefore the standard practice was developed to accommodate to this variance.

2.4.1 Wax removal

Wax scaffolds that were printed onto glass slides, and had cells seeded into these devices, were able to be removed. This was done by physical removal with a sharp scalpel to peel it off the surface, with care not to damage the adhered cells.

2.5 Creating phantoms

2.5.1 Paraffin wax

Paraffin wax was printed onto a microscope slide to mimic a healthy blood vessel. By printing the paraffin wax, a higher resolution scaffold could be created compared to pipetting the wax. Paraffin wax was placed inside the printing system's reservoir and the printing system was heated up to 75°C for printing. A simple "C" shape was printed with paraffin wax (Figure 2.5.1A), and a total of 10 layers of wax was used to add height to the negative scaffold. Using a 5 mL syringe, molten wax was pipetted onto the wax vessel to create a rough form of an aneurism (Figure 2.5.1B). The slide was placed inside a petri dish ready for PDMS treatment.

2.5.2 PDMS

PDMS mixture; SYLGARD® 184 Silicone Elastomer and curing agent. This is supplied in a matched kit consisting of the elastomer and the curing agent in separate containers. The two components were thoroughly mixed using a weight ratio of 10:1 elastomer: curing agent.

After pouring the PDMS mixture into a petri dish with the sample and later put in a vacuum oven for 15 min to remove any bubbles. The sample was left overnight to cure completely (Figure 2.5.1C).

2.5.3 Making the phantom samples

The next day, the phantom was cut out from the petri dish for further processing (Figure 2.5.1D). Two holes were pierced into the PDMS/wax mould with blunt ended needles of internal diameter of 0.8 mm

(Intertronics, UK) (Figure 2.5.1E), put into an oven at 80°C for 15 minutes to melt the wax. The molten wax was removed with 5 mL syringes from the holes created previously (Figure 2.5.1F).

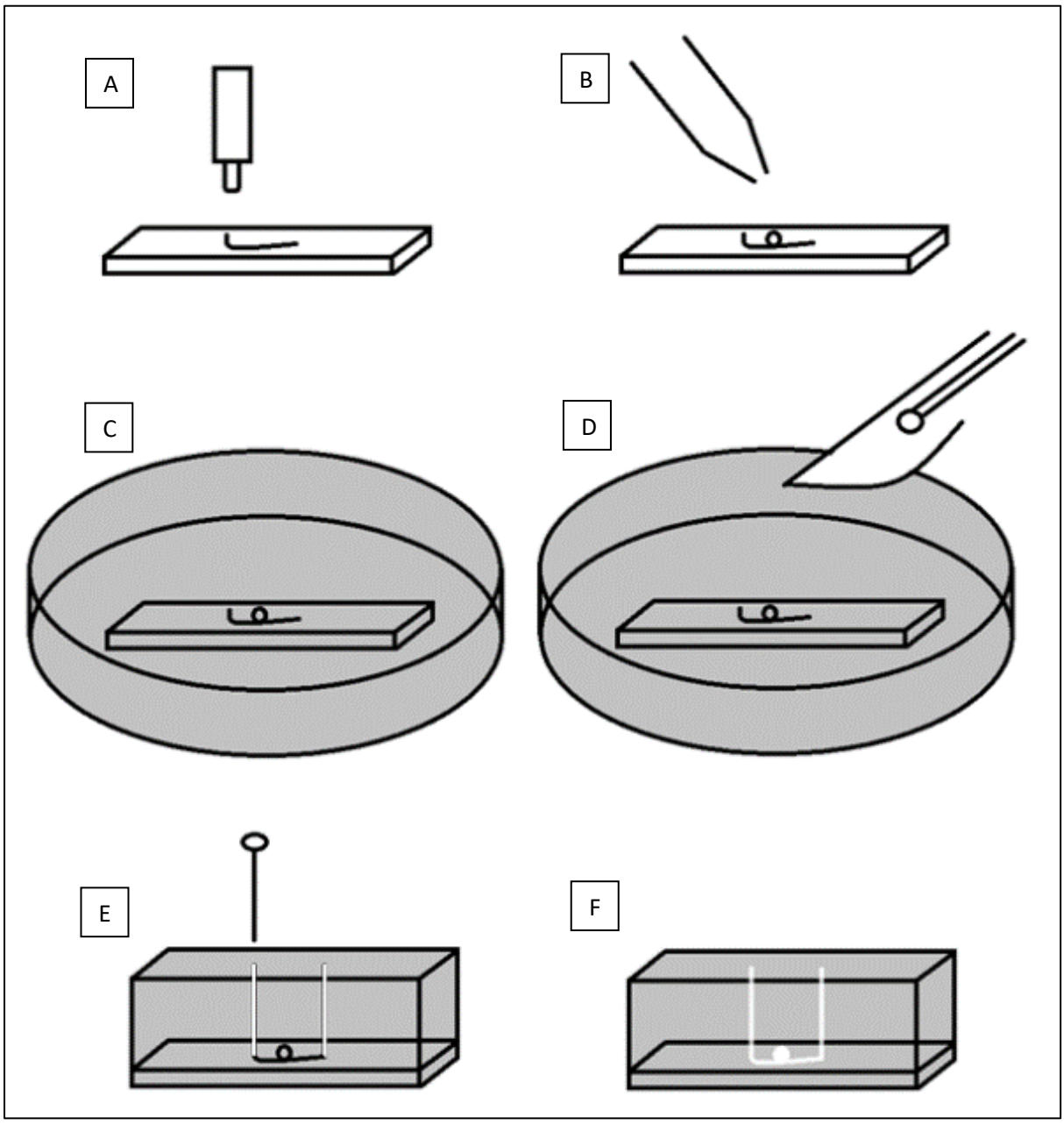

Figure 2.5.1Schematic diagram of how the phantoms were made; A) Molten paraffin wax, heated to 75°C in the inkjet printer, is printed onto a glass slide to create a channel. B) A pipette is used to pipette out a droplet of paraffin wax on top of the printed wax, which will later become the aneurism. C) Sample is placed in a petri dish, PDMS is poured into the petri dish, placed under vacuum to remove bubbles and left overnight. D) Once the PDMS has fully cured, a scalpel knife is used to cut out the sample. E) Blunt ended needles were used to pierce through the PDMS and make contact with the wax and air at both ends of the phantom. F) The sample is heated to 80°C and a syringe pump is used to remove the wax from inside the phantom, creating a hollow cavity within the PDMS scaffold.

Figure 2.5.2 shows experimental results of the finished wax printed vessels with the addition of a wax droplet on top (which will become the aneurism within the phantom). With respect to the schematic

diagram shown in Figure 2.5.1, the photographs represent steps E-F. This is a method to creating a 3D aneurism as it simulates the resultant shape of a ruptured blood vessel and the movement of fluid through this phantom compared to a real aneurism are similar.

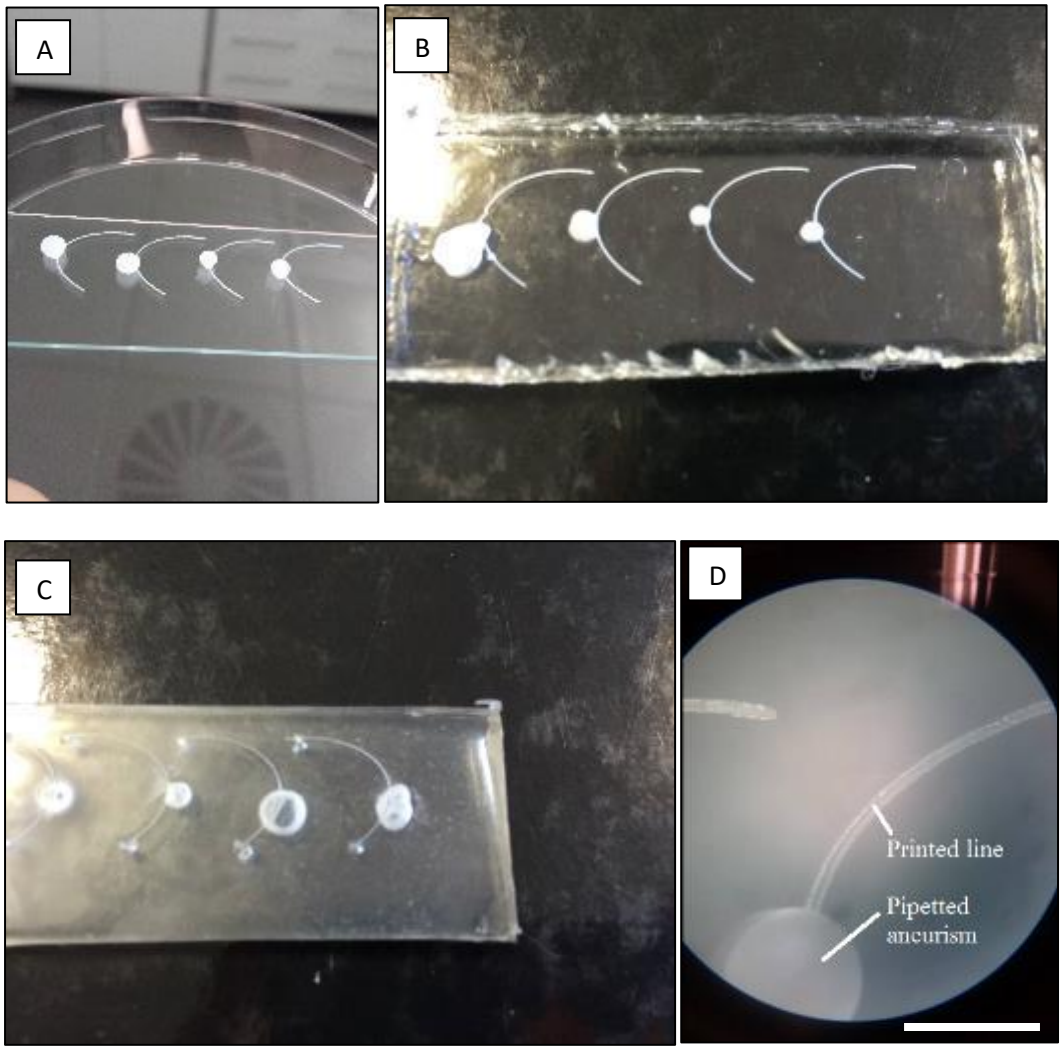

Figure 2.5.2 Images of fabricated negative phantoms using paraffin wax. A) Wax samples ready for PDMS moulding. B) After the PDMS has set, a scalpel was used to cut the sample out of the petri dish. C) Piercing the ends of the channel, the sample was placed in an oven at 80°C and the wax was sucked out. D) Microscope image of printed line (channel) and pipetted aneurism that combine together to form the phantom. Scale bar = 2 mm

2.5.4 Analysis of phantoms

Fluorescent microbeads (15 µm, FluoSpheres Polystyrene Microsphere, Thermofisher Scientific, UK) at 1.0 x 10^6 beads/mL was flushed through the vessel at a steady rate at 600 µL/h with a syringe pump (Genie Plus, Kent Scientific, Torrington, CT, USA). Images were captured every 50 ms.

An Image Express epifluorescent microscope (Axon Instruments/Molecular Devices, Union City, CA, USA) was used to record the flow of the microbeads through the phantoms. ImageJ was used to analyse

the data; through compiling the video into a stack of images, ImageJ was used to select a substack for analysis. Using the software plugin Manual Tracking, individual beads could be tracked within the flow of the vessels. Microsoft Paint was used to create flow velocity diagrams and vortex characteristic diagrams.

Note: the term “aneurism” will be used within the results section to describe the cavity created by the pipetted wax droplet (which becomes a cavity through wax-loss within the PDMS structure). The term “channel” and “vessel” will be used to describe the channel that enters and exits the aneurism, created by the inkjet printed wax (which becomes a channel through wax-loss within the PDMS structure). The term “phantom” will be used to describe the whole sample; aneurism + vessel (Figure 2.5.3 for clarity).

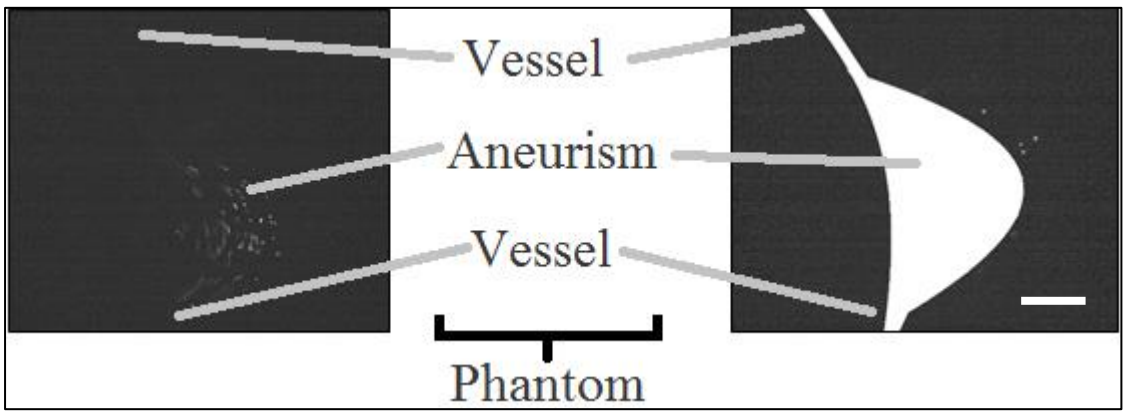

Figure 2.5.3 Identifying each section of the phantom Left) raw image captured of microbeads flowing through a phantom Right) the same image edited to show contract between fluid cavity (white) and surrounding PDMS (black). The dimensions of the phantom are more clearly seen when fluorescent beads are passing through. Scale bar = 1000 µm

3 Creating crosslinked gelatin scaffolds for cell seeding

3.1 Overview

This chapter discusses the work that was undertaken to investigate how glutaraldehyde could be inkjet printed onto a bed of gelatin to create crosslinked-gelatin-patterned-environments suitable for cell seeding. Crosslinking was required on gelatin hydrogels as virgin gelatin melts at biological temperatures (37°C), and therefore a method was required to increase its melting temperature to be more suitable for tissue engineering applications.

Transglutaminase,[173,174] genipin,[157,175] formaldehyde,[176] carbodiimides,[177] and glutaraldehyde[178,179] have been researched extensively as crosslinking agents for gelatin. Also to note, riboflavin had been investigated to successfully crosslink collagen, and collagen is what gelatin is prior to denaturing.[180] All crosslinking agents offer a degree of toxicity, and although glutaraldehyde has been shown to cause the most cell death as a crosslinking agent, glutaraldehyde provided the best mechanical strength and was selected for the experiments documented in this chapter. The cause of toxicity for glutaraldehyde is caused by residual glutaraldehyde leaching out and causing cell death. To minimise toxicity of glutaraldehyde, the research was focused on using lower concentrations to prevent toxicity to cells.

Glutaraldehyde was inkjet printed at various concentrations onto a bed of gelatin to allow crosslinking to occur. The concept of printing glutaraldehyde onto a bed of gelatin was performed, as printing gelatin proved to be too unstable for practicality. Due to solvent evaporation, printing gelatin, even at low concentrations, led to an accumulation of gelatin at the tip of the printhead, which eventually caused the printing system to block. Unblocking the printhead required the printing to reset, and no structures could be printed for more than 15 minutes before droplet generation failure due to clogging. No such problems occurred when printing with glutaraldehyde.

Crosslinking of gelatin by glutaraldehyde occurs through the aldehyde groups reacting to the free amino groups of lysine or hydroxylysine amino acid residues on gelatin molecules.[181] Primary amines and secondary amines react with the aldehyde group in glutaraldehyde through nucleophilic addition to form

carbinolamines, which can then dehydrate to give substituted imines and enamines respectively. A range of possible resultant products are outlined in Figure 3.1.1. This diagram shows collagen reacting with glutaraldehyde. Many of the reactions involve the formation of a Schiff base intermediate (Structure III) that is able to form a plethora of products. It is through this reaction that the mechanical properties of gelatin and its mechanical properties increase; through the generation of bigger complex compounds within the gelatin.

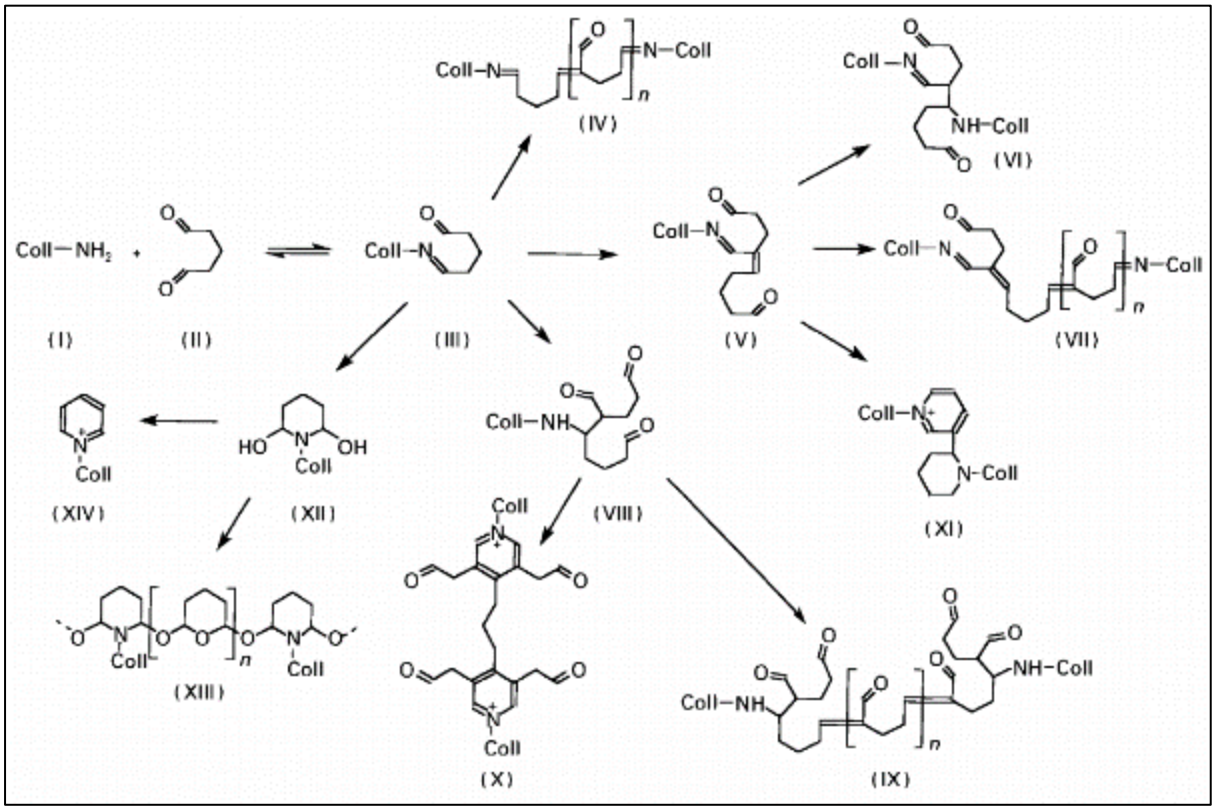

Figure 3.1.1 Gelatin is denatured collagen, and the various reactions pathways shown here can be related to the crosslinking of gelatin (i.e. Coll-NH_2 = Collagen-amine group). Taken from Damink et al. 1995.[182]

A local deposition of glutaraldehyde will, over time, diffuse out and spread through the gelatin substrate. This is a time-dependant diffusion process which is caused through the imbalance of the distribution of particles.

3.1.1 Brief of work carried out for Chapter three

There were several main points that were identified, which were investigated and are discussed in this chapter;

1. Cytotoxicity of glutaraldehyde-crosslinked gelatin

2. Optimal printing conditions for glutaraldehyde printing
3. Optimal parameters to create patterned-crosslinked gelatin with inkjet printed glutaraldehyde

   Cell seeding on gelatin crosslinked by inkjet printed glutaraldehyde scaffolds

3.2 Seeding fibroblasts onto glutaraldehyde-crosslinked-gelatin.

3.2.1 Introduction

Three variables were considered; gelatin concentration, glutaraldehyde concentration, and time for crosslinking. Using these variables, the minimum concentration of glutaraldehyde was determined, which would crosslink the gelatin, and not be toxic to cells. Previous work on seeding cells on gelatin scaffolds of 8% or more showed a decrease in cell viability, indicating an upper limit to gelatin concentration. This phenomenon was reported from another research group, that used 5%, 10% and 15% gelatin crosslinked with methacrylate as a crosslinking agent with 3T3 fibroblasts,[183] and showed viabilities of 90%, 80% and 75% respectively (estimated) (Date can be found in Appendix One)

Variables;

Parameter	Value/s
Volume of Glutaraldehyde	2 ml
Glutaraldehyde Concentration	0.125%, 0.25%, 0.50%, 1.0%, 5.0%, 10%, 15%, 20%
Gelatin Concentration	0.5%, 1%, 2%, 4%
Time	5 minutes, 30 minutes, 1 hour, 2 hours, 5 hours, 24 hours
N	1

Normally in literature, 4% is the typical concentration of gelatin that is used for tissue engineering. Previous experiments had shown that higher gelatin concentrations would inhibit cell attachment onto

the surface of the gelatin and therefore higher concentrations were not considered. Lower concentrations were tested as it was speculated that these may become viable if higher concentrations of the crosslinking agent were used, with also 4% and 8% gelatin to cover a broader spectrum of variables.

A range of glutaraldehyde concentrations were tested, ranging from 0-2% through a serial dilution. Through previous experiments, higher concentrations showed toxicity to cells, and therefore lower concentrations were investigated.

The time allowed for the gelatin and glutaraldehyde to react was also controlled, as it was shown previously that the reaction rate was also dependent on time.

Using a petri dish, the respective concentrations of gelatin were warmed up and 10 ml were pipetted into each petri dish. A 13 mm bore was used to cut out the scaffolds and they were each placed in 6 well plate wells. Next, 2 ml of the respective concentrations of glutaraldehyde were pipetted onto the gelatin for the respective amount of time. Once the time was complete, the wells were washed with distilled water twice, and then soaked overnight. Prior to cell seeding (of 40,000 fibroblasts), the samples were soaked in cell media (DMEM) for an hour to remove excess glutaraldehyde and distilled water. Cells were seeded with 1 mL of 40,000 cells/ml in DMEM, and an extra 2 mL of DMEM was added on top. MTT analysis was used to determine metabolic activity of cells at day 1 and day 3. It was concluded that day 7 analysis would not be required as the condition of cells on day 3 would give a sufficiently accurate indication to cell viability with the respected glutaraldehyde concentration.

3.2.2 Results

Some of the higher concentrations of glutaraldehyde were omitted from further analysis, as they were seen to be unsuitable for cell seeding, indicated by the change in DMEM colour from pink to brown. The colour change was caused by free glutaraldehyde being released into the cell media and shows that the hydrogel was toxic to cells (Figure 3.2.1).

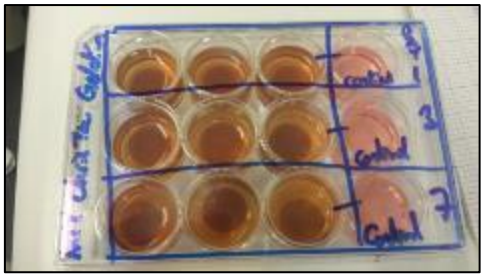

Figure 3.2.1 Photograph showing gelatin scaffolds that were soaked in 8% glutaraldehyde in 5 hours. This concentration and amount of time for crosslinking was too much, and when cells and cell media was added, the media and the scaffold turned brown, indicating that the crosslinked gelatin was toxic and was not a viable scaffold.

During cell seeding, images were taken to examine the physical characteristics of the cells to give an indication of viability. It could be seen that the higher the glutaraldehyde concentration the more toxic the crosslinked gelatin hydrogel was. An example can be seen in Figure 3.2.2, whereby cells were viable on 2% gelatin crosslinked with 0.125% glutaraldehyde, but cells were unhealthy when grown on gelatin crosslinked with 0.50% glutaraldehyde. This can be understood by the ability for cells to adhere onto the scaffold if the scaffold is non-toxic.

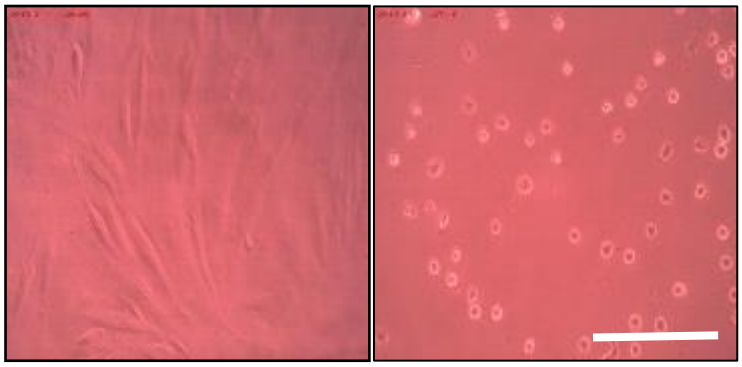

Figure 3.2.2 Visual analysis of fibroblasts. (Left) fibroblasts grown on 2% gelatin, 30 minutes of 0.125% glutaraldehyde, day 1. (Right) fibroblasts grown on 2% gelatin, 30 minutes of 0.50% glutaraldehyde, day 1. Scale bar = 200 µm

The results were put into graph form and separated by gelatin hydrogel concentration, with metabolic activity (MTT results measured by optical density) over glutaraldehyde concentration (Figure 3.2.3). The readings are proportional to cell density, as it can be correlated that a higher reading is caused by higher metabolic activity, and this has to be caused by an increase in cell population in the sample. If readings are comparatively low, then it would signify a decrease in cell population.

Through examining the data, it was shown that the higher the glutaraldehyde concentration, the lower the survival rate of cells, with concentrations of glutaraldehyde of 0.50% showing significant

detrimental effects to cell metabolic activity. Upon inspection with a microscope of such samples, it was clear cells did not attach onto the crosslinked samples as strongly, as cells looked spherical, indicating poor attachment. Concentrations of more than 1% glutaraldehyde became toxic to cells, which must be due to residual glutaraldehyde molecules present in the gelatin hydrogel that were released into the cell media. The best concentration for glutaraldehyde was the lowest concentration (0.125%) and the shorter the time it reacted with gelatin the more viable the scaffold was for cell attachment. 5 minutes of crosslinking was the best duration, with 0.125% glutaraldehyde on 4% gelatin.

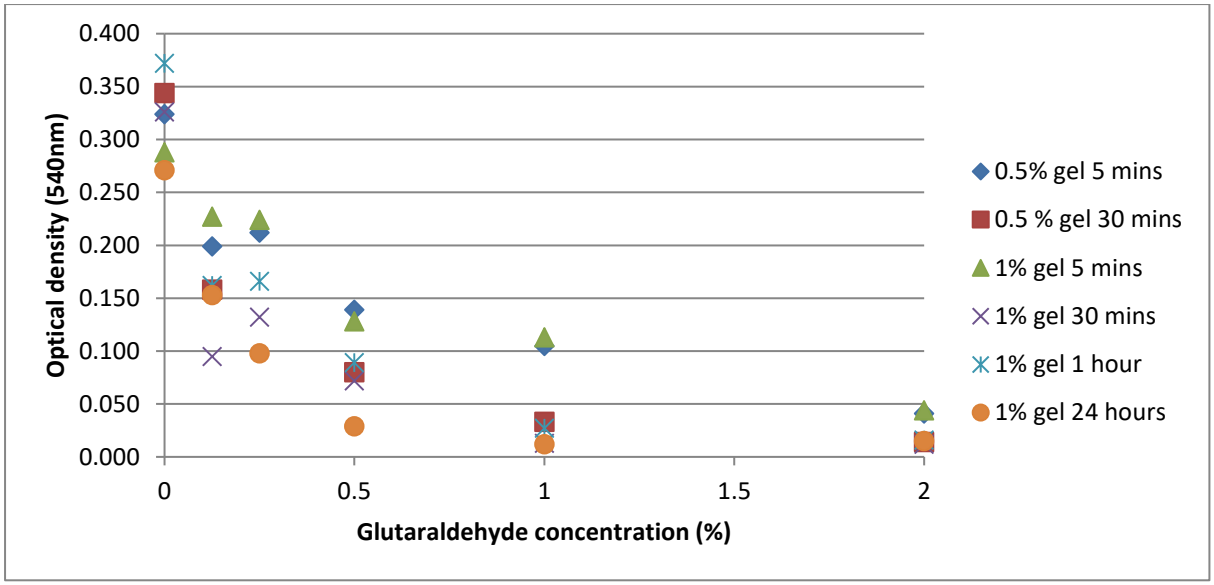
0.400
0.350
0.300
0.250
0.200
0.150
0.100
0.050
0.000
Optical density (540nm)
0
0.5
1
1.5
2
Glutaraldehyde concentration (%)
0.5% gel 5 mins
0.5 % gel 30 mins
1% gel 5 mins
1% gel 30 mins
1% gel 1 hour
1% gel 24 hours

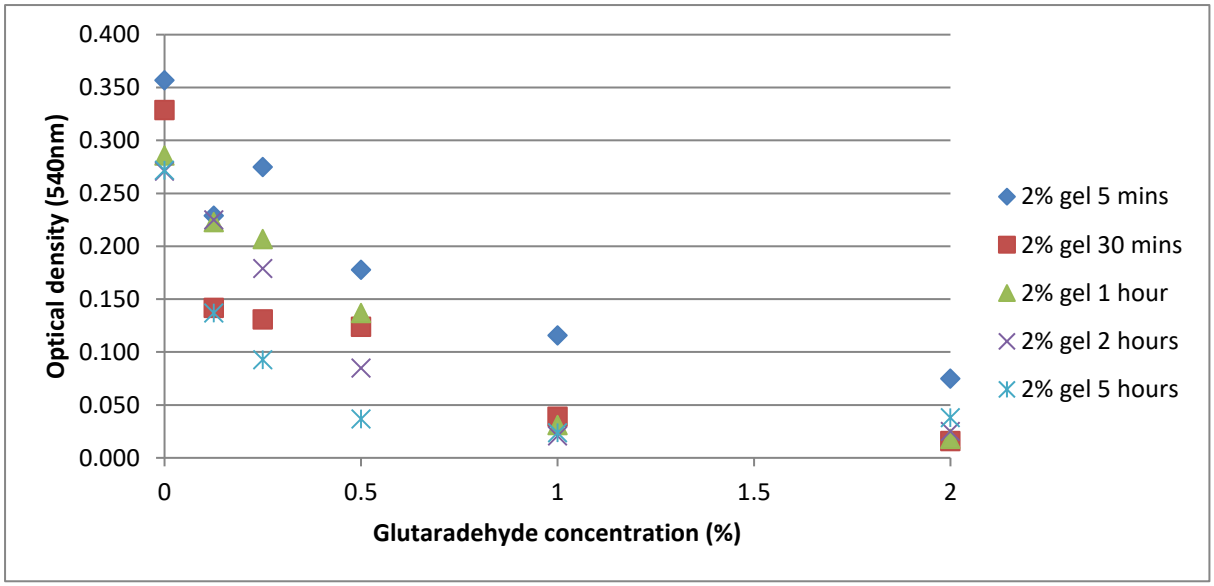
0.400
0.350
0.300
0.250
0.200
0.150
0.100
0.050
0.000
Optical density (540nm)
0
0.5
1
1.5
2
Glutaradehyde concentration (%)
2% gel 5 mins
2% gel 30 mins
2% gel 1 hour
2% gel 2 hours
2% gel 5 hours

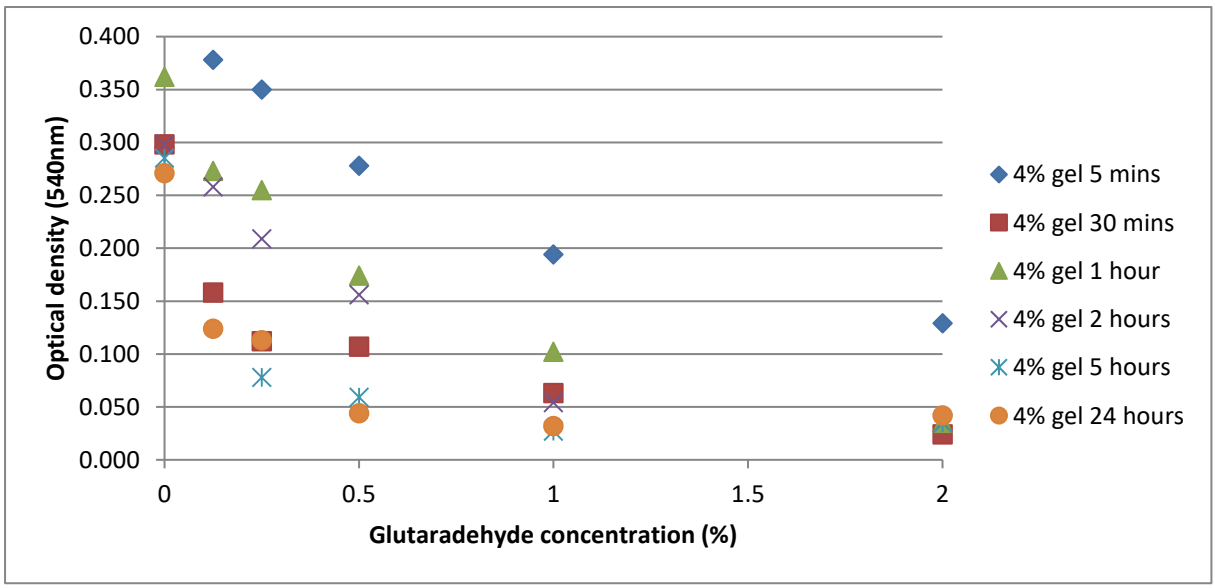
0.400
0.350
0.300
0.250
0.200
0.150
0.100
0.050
0.000
Optical density (540nm)
0
0.5
1
1.5
2
Glutaradehyde concentration (%)
4% gel 5 mins
4% gel 30 mins
4% gel 1 hour
4% gel 2 hours
4% gel 5 hours
4% gel 24 hours

Figure 3.2.3 A set of three graphs showing the optical density reading of fibroblasts on gelatin hydrogels crosslinked with glutaraldehyde, 1 day after seeding 40,000 cells. Key indicates the experimental parameters i.e. "4% gel 1 hour" = on 4% gelatin and crosslinked for 1 hour. Optical density readings are MTT assays that give an indication of metabolic activity of cells in culture. Concentrations of 0% glutaraldehyde are controls. n = 1

A chart was created noting the phenotypic changes of each sample. This was displayed as the % of live to dead cells in a random area of the scaffold (100%, <80%, 50%, >20, 0% healthy) and not displayed in the main body of text due to the large data set, but which can be found in Appendix One.

Day 3 MTT analysis was performed on all parameters used for Day 1 analysis. The resultant metabolic activities were quite poor on most parameters. Figure 3.2.4 shows the experimental settings that had an optical density reading of more than 0.1. It was considered that any readings that were less than 0.1 had significant cell death within the sample, and would not be appropriate as a biological scaffold. The parameters are shown in Figure 3.2.4 would be ideal to use for inkjet printing, specifically 2% and 4% gelatin with 0.125% glutaraldehyde (lowest concentration tested) for 5 minutes, as they were able to crosslink the gelatin and have fibroblasts proliferate after 3 days in culture on crosslinked gelatin.

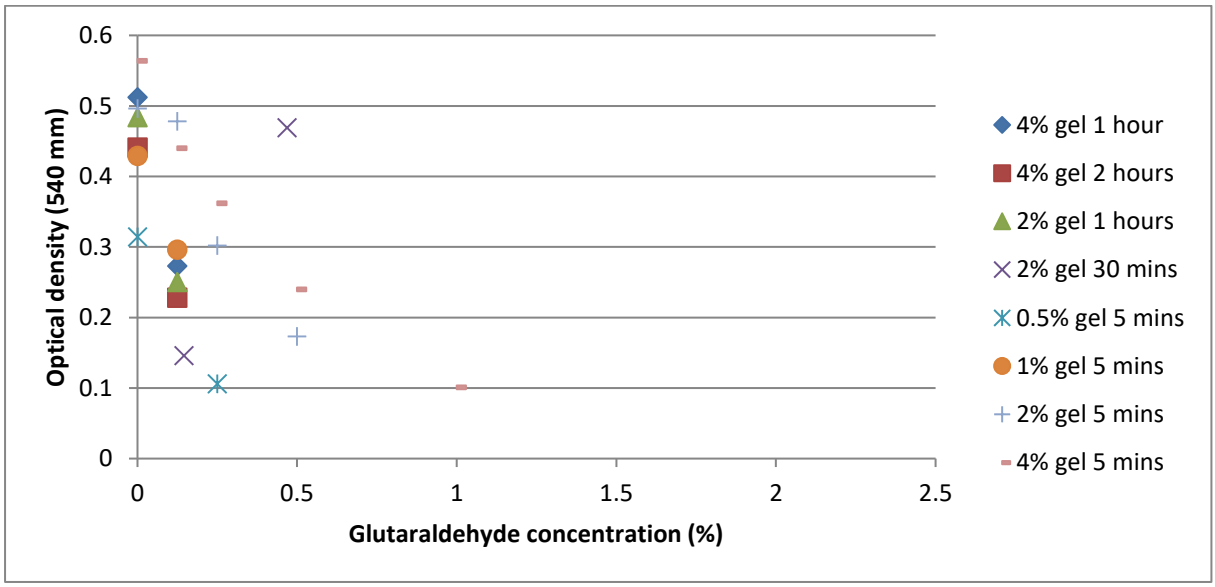

Figure 3.2.4 Optical density reading of fibroblasts on gelatin hydrogels crosslinked with glutaraldehyde, after 3 days after seeding 40,000 cells. Only reading above 0.1 were plotted, as any value below 0.1 were considered not sufficiently viable. Key indicates the experimental parameters i.e. "4% gel 1 hour" = on 4% gelatin and crosslinked for 1 hour. Optical density readings are MTT assays that give an indication of metabolic activity of cells in culture. Concentrations of 0% glutaraldehyde are controls. n=1

What can also be seen when comparing all the data from day 1 and day 3, is that they all have a decrease in viability, except the lowest concentration of glutaraldehyde in the experiment; 0.125%, with which,

some had a slight increase. The biggest increase occurred with 4% gelatin with 5 minute crosslinking time in the presence of 0.125% glutaraldehyde; increasing from 0.378 to 0.44 in optical density reading for MTT analysis.

The results of viability analysis suggest that cells may not be able to survive very well for longer periods of time of more than 3 days. The reason would be caused by the leaching of glutaraldehyde out from the scaffold. The protocol of washing the scaffolds with distilled water twice and then soaking the samples overnight should be sufficient to remove residual glutaraldehyde, as other groups have washing routines that are less thorough, but still create cell-friendly gelatin hydrogels; Yang et al washed their glutaraldehyde-crosslinked-gelatin with warm water,[184] Zhang et al used a temperature to remove residual glutaraldehyde,[185] and Ai et al washed their glutaraldehyde-crosslinked scaffolds with cell culture medium.[186]

Matsuda et al had the most complicated washing steps; their washing routine involved washing with distilled water, air drying, submersion with glycine at different concentrations and sodium borohydride.[187] This method was not considered as it was speculated this process would damage the micron-scale scaffolds when they were created with the inkjet printer.

In summary, when comparing the data for each of the parameters, it could be concluded that the concentration of glutaraldehyde (the lower the better for cell viability) was the most significant factor in affecting cell viability, followed by time (the lower the better), and then gelatin concentration (ideally 2-4%). Large droplets have shown to crosslink a large area, however there is an accumulation of residual glutaraldehyde which becomes toxic to cells. Inkjet printing has the potential to jet nanolitre volumes and in a controlled manner so that no residual glutaraldehyde would remain, and create viable patterned tissue scaffolds for cell growth.

3.3 Optimal printing conditions of glutaraldehyde printing

To create inkjet printed scaffolds, the optimal printing conditions were required to be identified for the successful creation of biologically relevant cell-friendly scaffolds.

Viscosity measurements were taken to determine the ideal printing conditions, as stated by the manufacturer (Microfab). Ideally, the viscosity of the ink should lie between 1 – 20 centipoise. Table 1 shows that within the range of temperatures tested, glutaraldehyde would be printable within 0-40°C. This is ideal as this means that printing at room temperature would not cause a problem with printing glutaraldehyde, as room temperature would be suitable for printing (this range of temperatures would lie within 1-20 centipoise for suitable inkjet printing).

Table 1 viscosity behaviour of 25% glutaraldehyde (w/w in water) at different temperatures. Data taken from manufacturer's website; http://www4.mpbio.com/ecom/docs/proddata.nsf/(webtds2)/198595.

Glutaraldehyde Conc. (%)	Temperature (°C)	Viscosity (centipoise)
25	0	8.4
25	20	3.4
25	40	1.7

Knowing that the viscosity of water at 20°C is around 1 centipoise, it was safely assumed that the viscosity of glutaraldehyde concentrations between 0-25% would be within the range of 1-3.4 centipoise respectively.

A range of printing parameters were tested and used when printing glutaraldehyde. Table 2 and Figure 3.3.1 shows an example of one of the printing parameters used. The average droplet diameter was calculated as 40 µm, and through using the volume of a sphere equation, the volume of each droplet was calculated to equate to 33.51pL

Table 2 detailing printing parameters of printing 1% glutaraldehyde. When printing other concentrations of glutaraldehyde, the printing parameters were tweaked to compensate for the difference in rheology

Printing parameters	(ms)
Rise Time	39
Dwell Time	42
Fall Time	8
Echo Time	90
Rise Time 2	5
Voltage (V)	55
Average droplet diameter	40 µm
Volume of jetted droplet	33.51pL

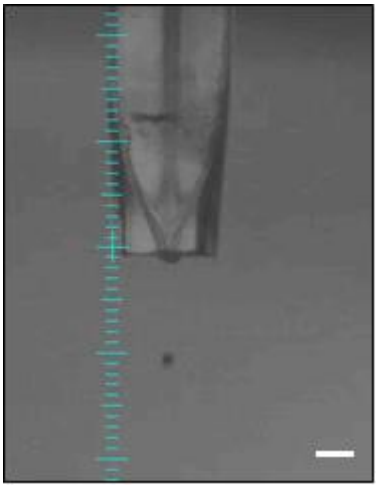

Figure 3.3.1 Screen-capture of a successful jetting of a droplet of 1% glutaraldehyde (w/w in water), scale bar = 100 µm

$$V = 4/3\pi r^3$$

Equation 2 volume of a sphere; used to estimate the volume of jetted glutaraldehyde from the printing system

The stability of printing glutaraldehyde was very good, as changes to the printing parameters did not cause significant deviation to successful jetting. When using different concentrations of glutaraldehyde, the parameters did not deviate significantly, and successful jetting could be created with deviations of $\pm$ 5 ms with "rise time" and "dwell time" settings.

3.4 Inkjet printing glutaraldehyde to crosslink gelatin

3.4.1 Introduction

To determine the best glutaraldehyde concentration to print onto a bed of gelatin, several concentrations were tested to evaluate the fidelity of resultant patterns. Initially, glutaraldehyde concentrations proposed by the work done previously were used (0.125% - 1%). Glutaraldehyde concentrations of 0.125% - 1% had been shown to crosslink gelatin and cells were able to grow sufficiently when seeded. However when these were created with droplet spacings of 100 µm and washed with 50°C water, it was clear that the scaffolds were too weak to handle with tweezers. If the scaffolds were too difficult to handle, then they would not be suitable as they would most likely break during the cell seeding and handling of the scaffolds during analysis. Decreasing the droplet spacing of 100 µm was considered, however this would have changed the resolution of the selected pattern. Instead it was decided that higher concentrations of glutaraldehyde were tried out, whilst maintaining the 100 µm droplet spacing, which were originally predicted would be too toxic for cell seeding; from 10%, 15% and 25%.

3 mL of warm (>25°C), 4% gelatin solution (w/v, in water) was pipetted onto glass slides to cover the whole surface area. The surface tension of the glass slide prevented the gelatin from flowing off the glass slide, and this was put into a fridge to cool prior to printing. Once the gelatin became solid, the samples were loaded into the printing system. The glutaraldehyde ink (of the selected concentration) was loaded into the printer, and the parameters optimised. A droplet spacing of 100 µm was used, and a cross-hatch pattern was printed to emulate a connected network (Figure 3.4.1).

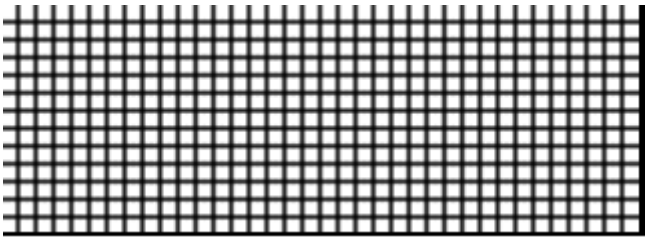

Figure 3.4.1 Image showing the hatch pattern designed for printing onto gelatin. A droplet spacing of 100 µm was used, and the distance between each connection within the pattern would be 2.5 mm across.

After printing, the samples were left for different periods of time to allow crosslinking to occur, ranging from 5 minutes to 24 hours (overnight).

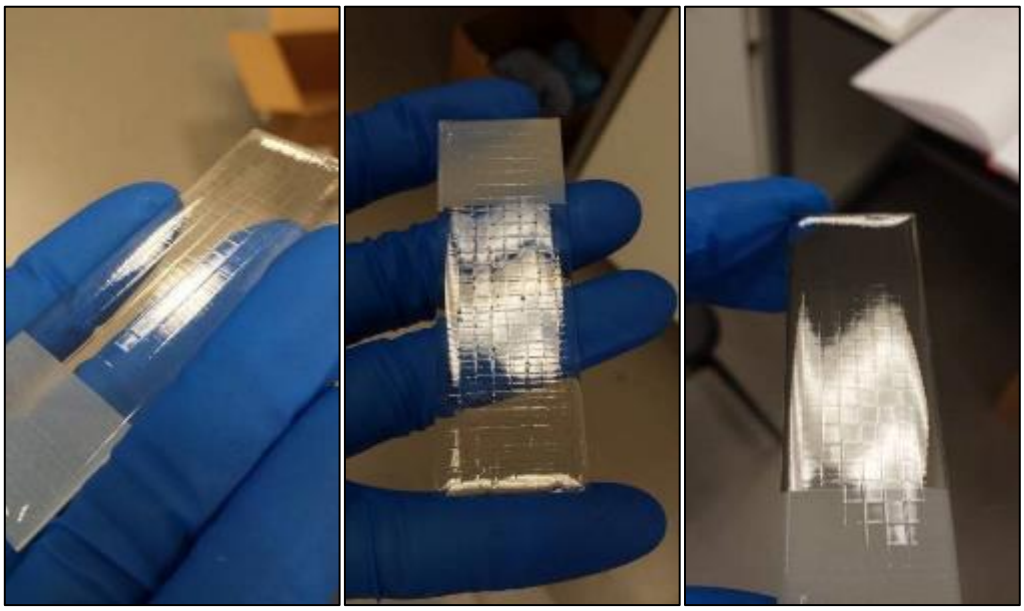

Figure 3.4.2 Photographs of inkjet printed glutaraldehyde onto a bed of 4% gelatin on a glass slide. The samples were cut out into segments that would fit into a well in a 6-well plate, using a scalpel.

After the allocated time, a scalpel was used to cut the scaffold into smaller segments and placed into each well of a 6 well plate (Figure 3.4.3). Hot water (around 50°C) was gently pipetted into each well to wash off uncrosslinked gelatin, five times. Scaffolds were inspected and assessed to determine the most suitable scaffolds for cell seeding.

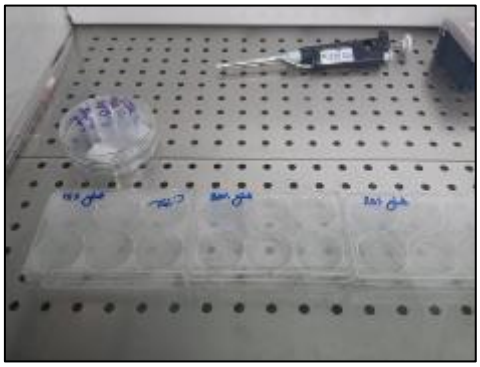

Figure 3.4.3 Image showing an experimental procedure where the crosslinked samples were put into labelled 6 well plates prior to washing away the uncrosslinked gelatin.

3.4.2 Results

Initially concentrations of 0.125% - 1% glutaraldehyde were selected to crosslink 4% gelatin, however when the uncrosslinked gelatin was removed, glutaraldehyde concentrations of less than 2% created scaffolds that were structurally too weak and were prone to tearing. Most scaffolds that were created with the inkjet printer were too delicate to manipulate with tweezers, as the scaffolds would curl up and collapse on themselves due to surface tension when being manipulated. The only viable scaffolds that were deemed sufficiently strong and were considered for cell seeding (in the following experiment) were gelatin scaffolds that were crosslinked with 10%, 15% and 25% glutaraldehyde for 24 hours. Figure 3.4.4 shows examples of the successful samples created.

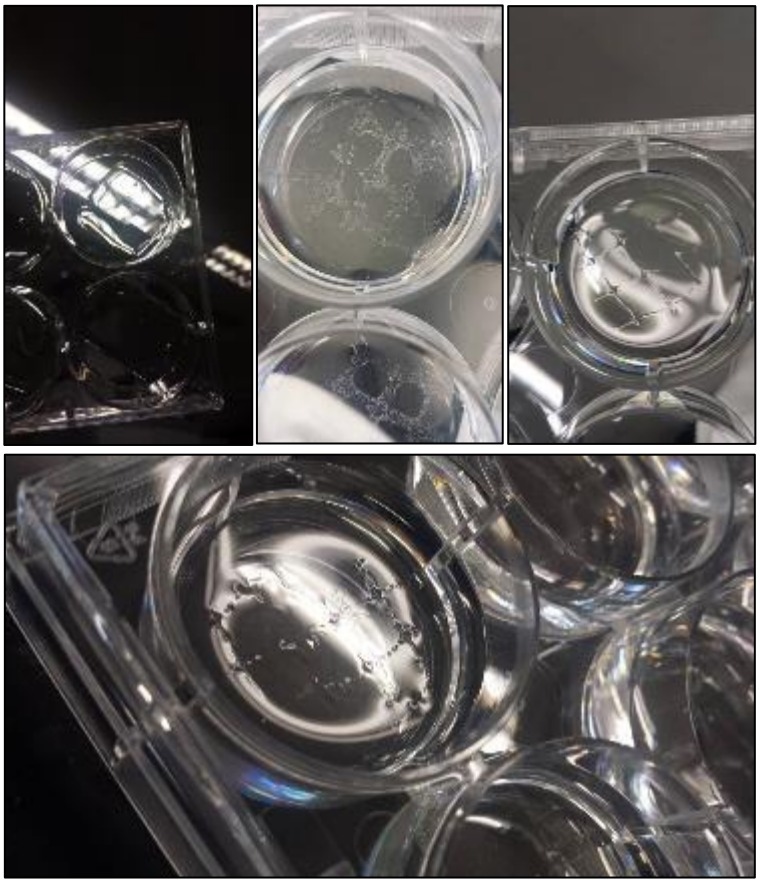

Figure 3.4.4 A collection of images showing crosslinked gelatin scaffolds being washed with hot water in well plates. The samples shown here are samples that were crosslinked with 25% glutaraldehyde and left overnight for 24 hours. Only samples that were crosslinked with 10-25% glutaraldehyde and allowed to crosslink for 24 hours created sufficiently mechanically strong scaffolds. All other samples that were created were too flimsy and collapsed on their own structure during the washing and cell seeding stages.

The other scaffolds that were created were too fragile and this was caused by several reasons; lower glutaraldehyde concentrations, shorter time for crosslinking, and the pattern used for created the

scaffold. With work shown in previous sections, lower glutaraldehyde concentrations and shorter crosslinking times crosslinked gelatin less, and therefore the resultant scaffolds were thinner and less structurally strong. The pattern that was selected to be printed out was a cross-hatch pattern with each beam being 25 mm long. If a single thin sheet or a cross-hatch pattern with smaller spacing of gelatin was printed, it could be expected that more of the printing parameters that were tested would have created a viable scaffold for cell seeding; as the mechanical properties of such scaffolds would be stronger than patterns that appear "stretched".

Another alternative that could have increased the rigidity of the scaffolds would have been to print several layers of gelatin, to add more glutaraldehyde onto the gelatin; thereby making the crosslinked beams thicker. Ten layers of 1% glutaraldehyde would equate to the same as one layer of 10% glutaraldehyde, and for the sake of experimental efficiency, one layer of 10% glutaraldehyde was printed instead of ten layers of 1% glutaraldehyde.

The experimental results acquired prior to inkjet printing glutaraldehyde had shown that gelatin that was crosslinked by glutaraldehyde with concentrations of more than 1% would be detrimental to cell viability. However it can be stated that the experimental procedure outlined with this set of experiments was different. With the volume of glutaraldehyde that was deposited onto the gelatin (through inkjet printing), the volume was so small (picolitres), that there were no diffusion restrictions for the glutaraldehyde to diffuse through the z-axis and therefore there would be minimal residual glutaraldehyde present in the scaffold. When diffusion of glutaraldehyde is blocked (i.e. limitations caused by the thickness of the gelatin), the local area aggregates residual glutaraldehyde which can make the hydrogel toxic (Figure 3.4.5). When there are no restrictions to the diffusion of glutaraldehyde (i.e. when glutaraldehyde was allowed to crosslink gelatin in a tub), crosslinking occurs uniformly throughout the gelatin, without accumulation.

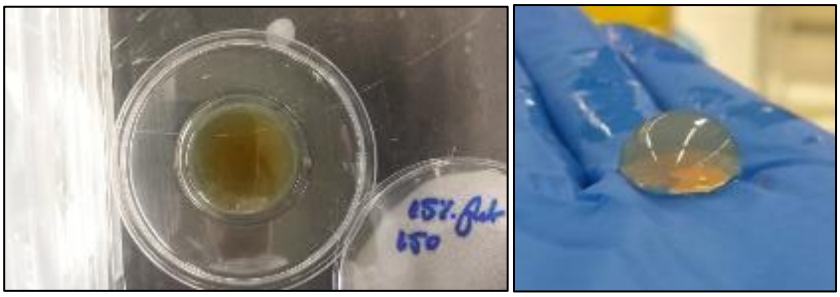

Figure 3.4.5 Washed samples of 25% glutaraldehyde-crosslinked gelatin on (Left) a petri dish and (Right) when reacted in a tub of gelatin. Because of the restrictions of not being able to diffuse further in the z-axis when pipetted onto a bed of gelatin on a petri dish, the residual glutaraldehyde in the crosslinked gelatin is highly concentration in the centre, and is highly toxic to cells. When there is no restriction to glutaraldehyde diffusion, there is no concentric accumulated of residual glutaraldehyde, and would not pose the same toxicity.

Having determined that 10%, 15% and 25% glutaraldehyde for 24 hours on 4% gelatin would be suitable to create sufficiently robust scaffolds, these were selected for cell seeding.

3.5 Cell seeding onto inkjet-printed-glutaraldehyde-crosslinked-gelatin

3.5.1 Introduction

The scaffolds used for cell seeding were made by printing 25% glutaraldehyde in a cross hatch pattern onto 4% gelatin on glass slides and reacted for 24 hours before the removal of uncrosslinked gelatin. The scaffolds were washed five times with 50°C water to remove uncrosslinked gelatin and residual glutaraldehyde (Figure 3.5.1). Although gelatin that was crosslinked with 10% and 15% glutaraldehyde did create suitable scaffolds, 25% glutaraldehyde was selected as it produced the most structurally stable scaffolds.

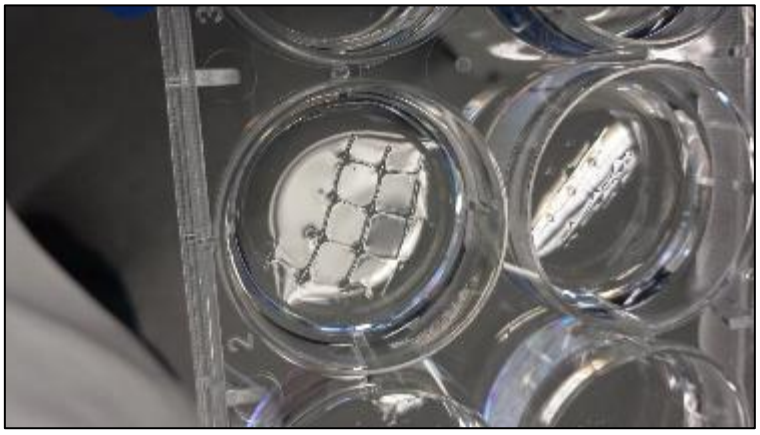

Figure 3.5.1 Crosslinked gelatin pattern created with an inkjet printer. 25% glutaraldehyde was printed onto a bed of 4% gelatin with a droplet spacing of 100 µL, left for 24 hours for crosslinking to take place, and then compartmentalised in well plates prior to washing with 50°C distilled water 5 times to remove uncrosslinked gelatin and residual glutaraldehyde.

1 mL of fibroblasts were seeded at 40,000 cells/mL into each well, and topped off with 2 mL of cell media, before being stored in an incubator. The samples were experimented in triplicate, with light and confocal images taken on day 1, 2 and 3. Confocal images were stained with FITC-phalloidin and DAPI, with the aim to determine cell viability of these scaffolds.

[*the term scaffold/hydrogel/gelatin lines will be used interchangeably to describe the crosslinked gelatin patterns]

3.5.2 Results

Gelatin scaffolds made with 25% glutaraldehyde were handled successfully and cells were able to grow on the patterned environments on all days that they were observed (day 1, 2 and 3 after cell seeding).

Figure 3.5.2 shows an example of images taken near an intersection where several gelatin beams join together. The structure appears "furry" due to the surface of the hydrogel being populated by fibroblasts growing on the surface of the crosslinked gelatin scaffolds. The scaffolds did not show any signs of toxicity, and cells proliferated at a rate that is typical for healthy cells, as can be seen under the microscope. If the scaffolds did release glutaraldehyde, or it was detrimental to cell health, the population of cells would have decreased on the scaffold, or more cells would adopt a spherical shape to indicate unfavourable culture conditions. These types of physical cues were not seen in all samples examined.

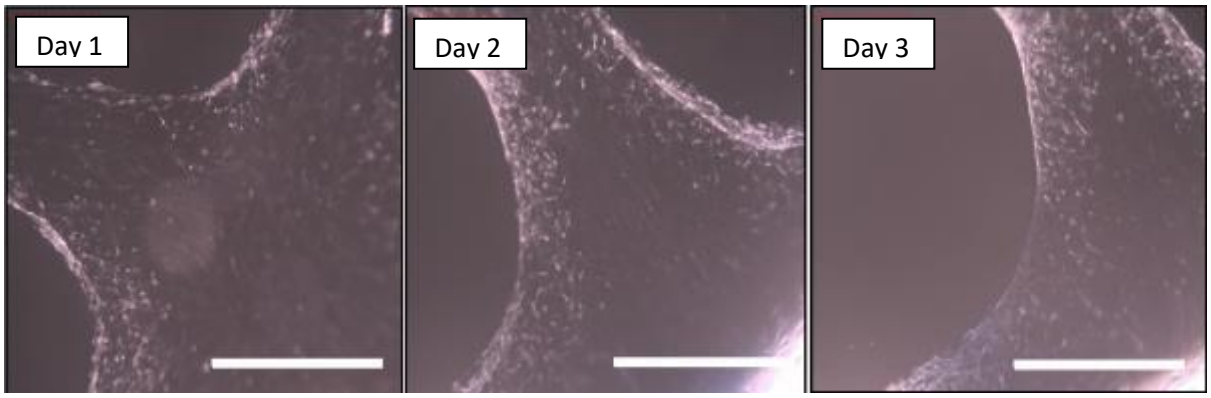

Figure 3.5.2 Microscopy images of fibroblasts seeded onto crosslinked gelatin through inkjet printing glutaraldehyde onto a bed of gelatin. Images taken 1, 2 and 3 days after cell seeding respectively. Enlarged images can be found in Figure 3.5.4. Scale bar = 300 µm

This showed that cells were able to grow on gelatin that had been crosslinked with up to 25% glutaraldehyde. No residual glutaraldehyde was expected to be released into the cell culture because there was no aggregation of glutaraldehyde during the crosslinking process; this was because the glutaraldehyde was able to diffuse freely in all 3 axis and was added in picolitre amounts.

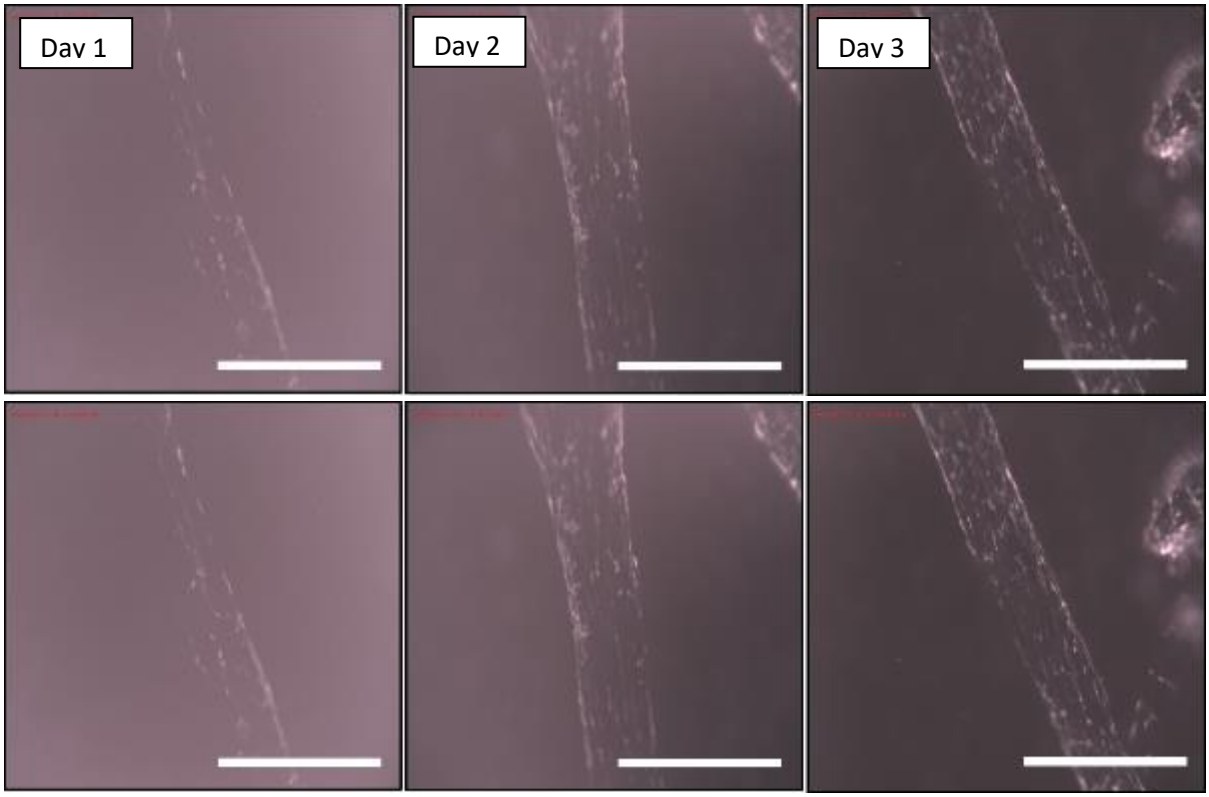

Figure 3.5.3 Microscopy images of fibroblasts seeded onto crosslinked gelatin created with inkjet printing. Images taken 1, 2 and 3 days after cell seeding respectively. Scale bar = 300 µm

The gelatin scaffolds that were created had a range of thicknesses, ranging from 250-100 µm, being thickest at the intersections. The beams resembled a more cylindrical shape, which was caused by the way in which the glutaraldehyde diffused uniformly from the area of deposition. Through the use of inkjet printing, of creating crosslinked gelatin scaffolds, it would not be possible to create sharp edged scaffolds, unless the diffusion of the glutaraldehyde were to be inhibited by restricting its movement with a physical barrier. If this were to be done, care would need to be considered about excess glutaraldehyde within the scaffold which would leak out over time and make the scaffold more toxic.

Figure 3.5.4 shows enlarged light microscopy images of the cell seeded gelatin scaffolds. On day 1 after cell seeding, cells manage to adhere and begin to proliferate on the scaffold. There is a larger population of cells proliferating on the side of the scaffold that was facing the cell seeding process, but it is interesting to see cells have also managed to grow on the periphery and underside of the scaffold. This will be discussed more thoroughly later on.

By day 2 and 3, as shown in Figure 3.5.4, there are no detrimental effects of crosslinking with glutaraldehyde, as the gelatin scaffold has not melted under biological temperatures, and cells have proliferated along the whole structure. More alignment of the cells can be seen on day 2, that are running in the same direction as the beams. The alignment was lost once the population of fibroblasts become overconfluent growing on the scaffold.

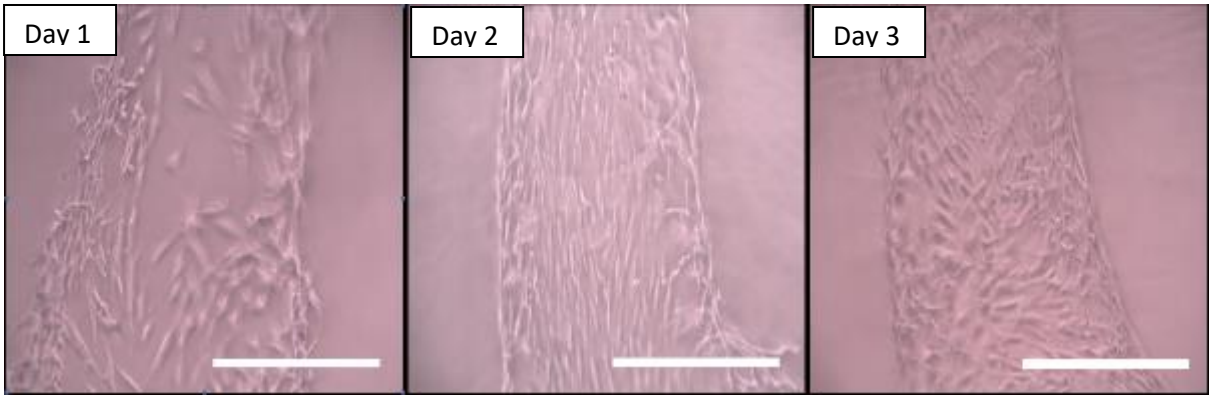

Figure 3.5.4 Enlarged microscopy images of fibroblasts seeded onto crosslinked gelatin through inkjet printing. Images taken 1, 2 and 3 days after cell seeding respectively. Scale bar = 150 µm

Confocal images were recorded to analyse the cell seeded gelatin scaffolds. Due to the 3D nature of the scaffold, the confocal images capturing a plane of the scaffold show a limited amount of data. However, the details that can be seen by analysing each pane individually makes it clear that fibroblasts were able to infiltrate into the scaffold and proliferate within. Figure 3.5.5 shows a cross-section of a gelatin scaffold seeded with fibroblasts after 3 days of cell seeding. The periphery of the image shows a shell of cells on the surface of the gelatin scaffold; stained for actin (red; phalloidin-TRITC) and nuclei (blue; DAPI), and also note the cells situated in the middle of the image. These cells are proliferating within the gelatin scaffold, and it must be assumed that the fibroblasts were able to not just proliferate on the surface of the gelatin, but also infiltrate the hydrogel and grow within it.

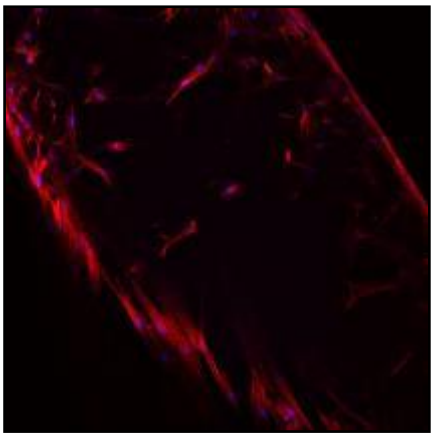

Figure 3.5.5 Confocal image of a cross-section of the middle of a gelatin scaffold beam stained for actin (red; phalloidin-TRITC) and nuclei (blue; DAPI)

Several areas were analysed, and a z-stack was created of each area. By combining the z-stack images with the Zeiss LSM Image Browser software, a 3D model of the scaffold was created. Figure 3.5.6 to Figure 3.5.7 are such models, and a series of images are shown, with each image being rotated by 30°.

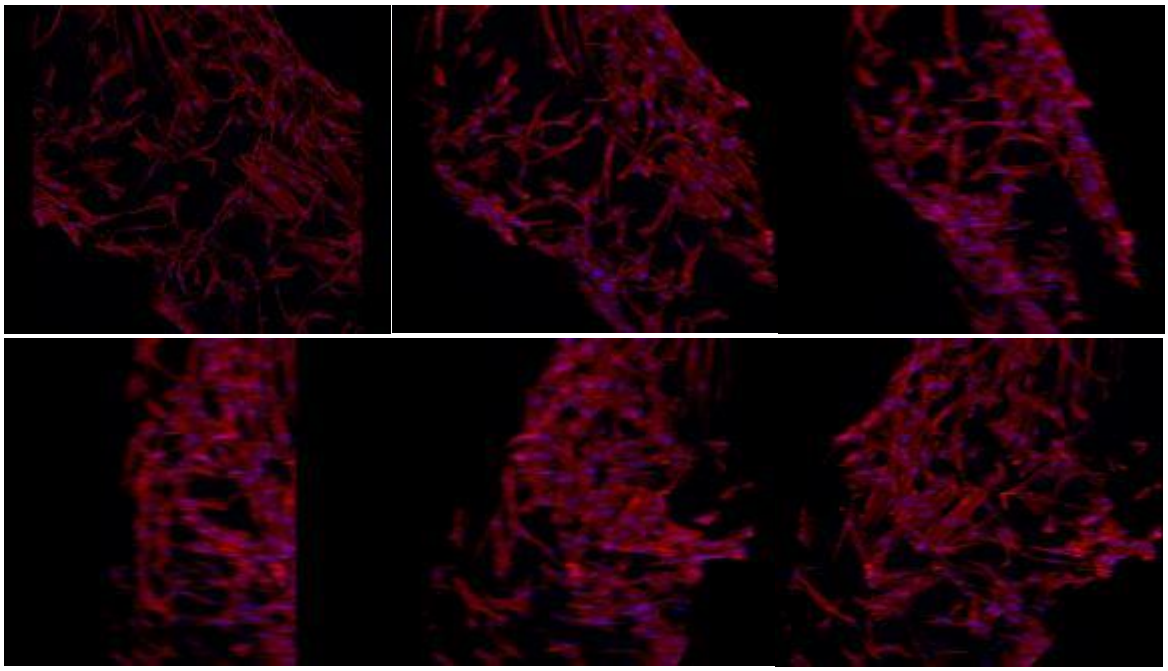

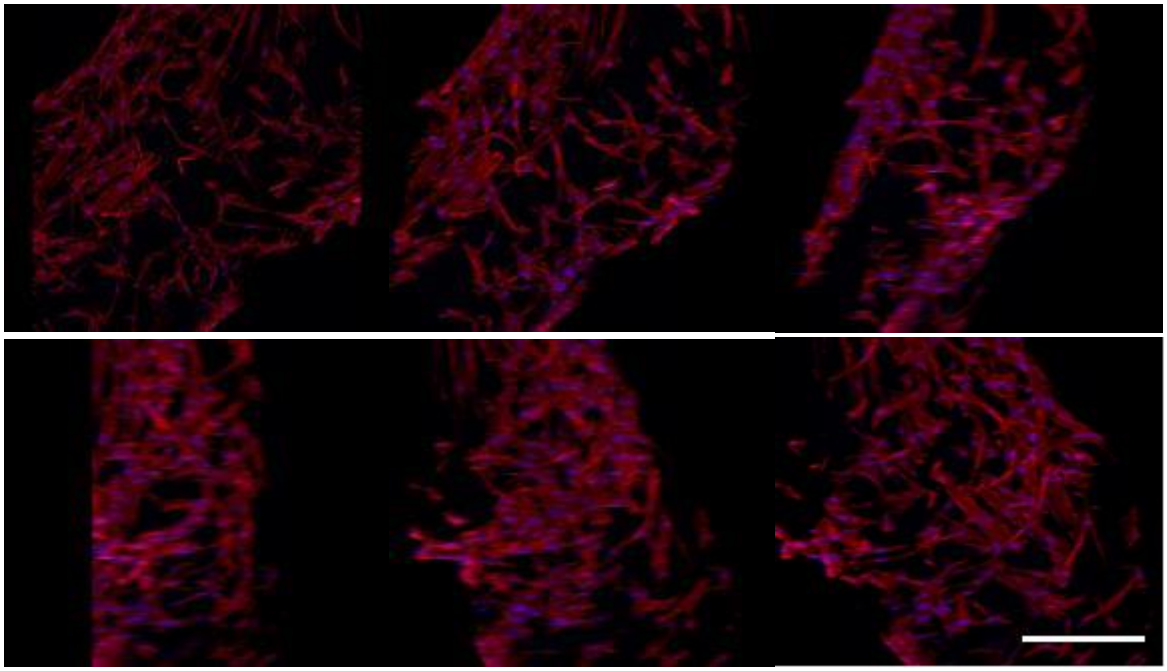

Figure 3.5.6 A sequence of 2D images of a 3D projected crosslinked gelatin scaffold with seeded fibroblasts after 1 day, stained for actin (red; phalloidin-TRITC) and nuclei (blue; DAPI). Scale bar = 250 µm

The majority of cells that proliferate on the scaffolds were proliferating on the surface. Only a small percentage of the cells are growing within the gelatin hydrogel, and this population increased over time, most likely caused by the cells preferentially differentiating to areas with the least resistance. It could be seen that there were more cells infiltrating the hydrogel during the second and third day after cell seeding, as the surface of the gelatin become more populated, the action of proliferating through the gelatin hydrogel became a better alternative than competing for space on the outer surface.

The morphology of the gelatin scaffolds varied over time; as originally, the branches were typically cylindrical in shape. With the addition of cells, they are able to eat away at the gelatin slowly, and when the cell population on the gelatin become confluent, the gelatin scaffolds became more elongated and flat. Figure 3.5.7 shows the flattening of the gelatin occurring after 3 days after cell seeding. In the target area, cells had fully covered the surface facing the cell seeding side, and cells had begun migrating into and enveloping the scaffold. The shape of the gelatin scaffold can be determined through the outlines given by the population of cells adhering onto and into the scaffold. More cells can be seen proliferating within the hydrogel compared to samples analysed on day 1 after cell seeding.

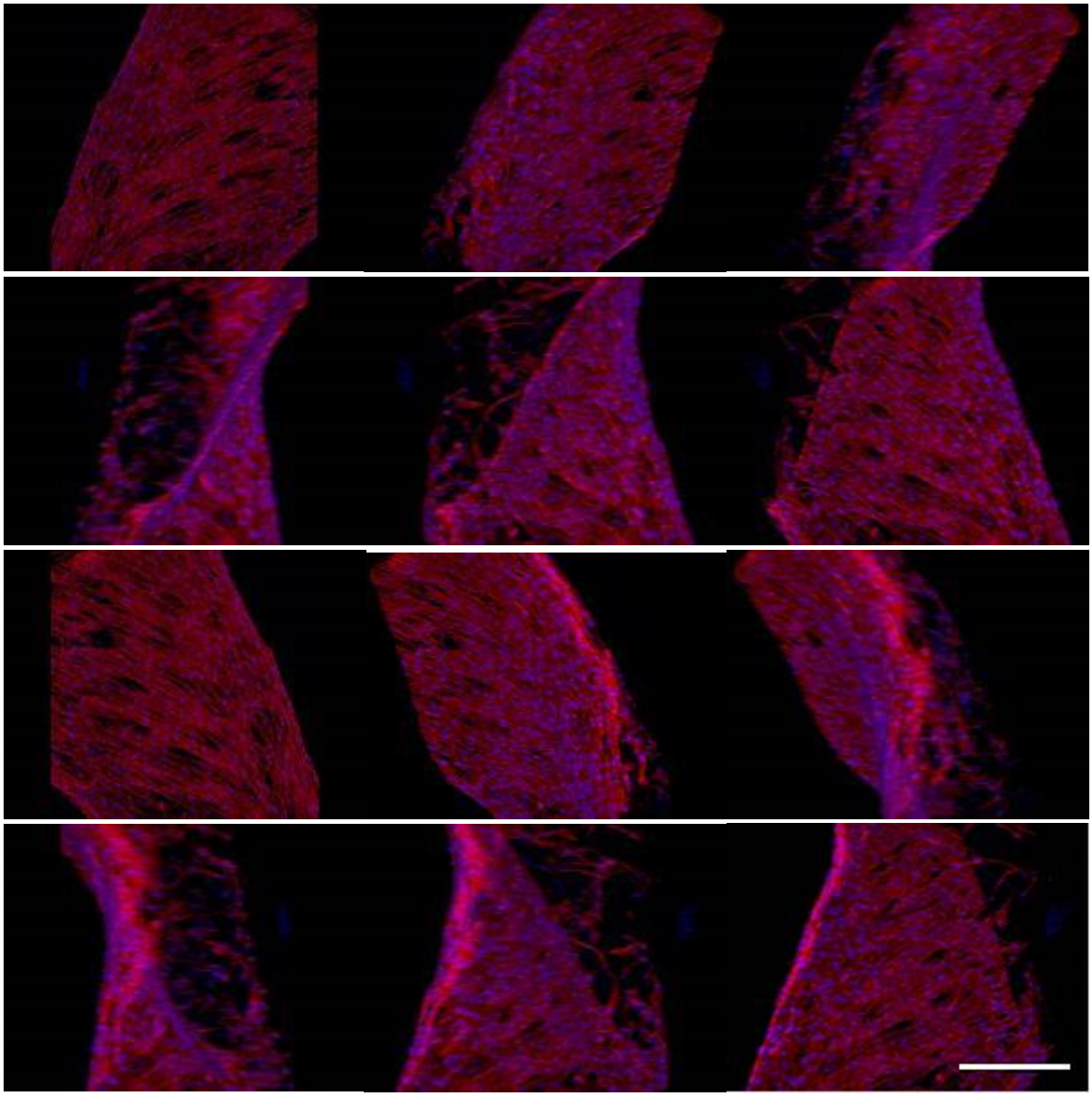

Figure 3.5.7 A sequence of 2D images of a 3D scaffold that shows fibroblasts grown on glutaraldehyde-crosslinked gelatin. A 3D image was generated through the stacking of multiple confocal images to create a z-stack. Stained for actin (red; phalloidin-TRITC) and nuclei (blue; DAPI), day 3 after cell seeding. Cells proliferated significantly more on the surface side where cell seeding took place. Cells can be seen to infiltrate within the gelatin and grow within the scaffold. Scale bar = 250 µm.

3.6 Conclusion

With the crosslinked gelatin being a hydrogel (being mostly water), cells were able to adhere and survive within the gelatin scaffold. The high concentration of glutaraldehyde that was used did not cause the gelatin scaffold to become toxic, as it can be assumed that all glutaraldehyde molecules were either fully reacted with the gelatin, and/or all residual glutaraldehyde was removed during the washing process. Inkjet printing is able to create scaffolds and have cells successfully seeding onto and into it.

Thinner scaffolds could be created with a lower concertation of glutaraldehyde, however to prevent damage to such scaffolds, the design and handling of the scaffolds needs attention. Thicker scaffolds cold be created by the printing of multiple layers of glutaraldehyde onto the bed of gelatin; however like all other tissue engineered scaffolds, all scaffolds that do not exceed a few millimetres in thickness can have cells proliferate on/in them, as simple diffusion is a sufficient method to transport nutrients into cells from the cell media and remove waste. A limit to inkjet printing would be that scaffolds may not be more than a few millimetres thick, unless a vasculature network is designed within the scaffold to allow directed transport of nutrients and cell waste throughout the scaffold. It could be postulated that with the simple cross hatch pattern that was used to create these scaffolds, once cells have been seeded, the scaffold could be collapsed and rolled together to form a larger, thicker scaffold of significant size, and with the porosity of the design of the scaffold, cells would survive at a better rate than a solid block of hydrogel of the same material.

4 CELL GUIDANCE STRUCTURES FABRICATED WITH INKJET PRINTED WAX

4.1 Overview

Organs such as bone, the cornea and skin are relatively simple tissues, as they have well-defined layers which can be recreated with tissue engineering techniques.[188,189] There are more complex tissues, such as the kidneys and liver, which have a complex inner structure of cell positioning and cell types. The ability to create tissues with multiple cell types and to control their deposition behaviour is essential when wanting to create complex tissues. This chapter describes how inkjet printing wax can help create microenvironments to direct cell deposition. The scope of applying this technique would not be suitable for *in vivo* applications, but would be ideal for the creation of complex organoids for drug testing and the creation of tissue models for research.

Research into cell patterning and spatial coordination are growing fields, as new technologies enable researchers to accurately position populations of cells and promote the design of better biological systems.[190,191] When considering the design of cell patterning experiments, geometry and topology are important factors that affect anchorage-dependent cells,[192–194] as living cells actively investigate their surroundings, which can influence function and morphology.[195] The wealth of knowledge that can be generated through studying cell-to-cell behaviour and cell-to-substrate interactions can allow scientists to better understand the dynamic mechanism that affects cell architecture, polarity, morphology, survival and division within their surrounding environments.[192,196,197]

Much has been learnt recently about cell behaviour in a micro-environment and the creation of microstructures, that are essential in the understanding of fabricating micro-devices to control cell-substrate interactions.[198–201] The importance of such research was highlighted in a special themed issue of *Soft Matter* in 2014 on cells in patterned environments.[202] Being able to control the deposition and location of cells onto a surface allows the creation of scaffolds suitable for tissue engineering, biosensors, the formation of neuronal networks, cell-based assays and for the study of cell-cell interactions.

One popular "gold standard" for preparing patterned environments for cells uses PDMS (polydimethylsiloxane) during the construction of lab-on-a-chip devices and micropatterning [203]. PDMS is a versatile material, with the ability to modify its mechanical, optical and chemical properties and typically used on glass[204] or silicon.[205] An essential requirement when using PDMS is the creation of a master mould, into which PDMS can be poured, cured and removed to create the desired construct. There has been research in reducing and making the process easier, as the pattern design can be created on the master mould through soft-lithography, or through etching into silicon. The photomask can be created using high resolution printers[204] or photoplotters,[206] but a clean-room environment is required for fabrication. Solid object printers have been used to create the initial patterns for the master mould,[207] with resolutions of >250 μm. Other techniques have also been investigated by researchers, which deposit a cell attractive or repelling agent onto a substrate typically involving depositing a biologically active molecule such as fibronectin, collagen and/or polymers to selectively adhere cells at specific places on a substrate[208,209] (as mentioned in literature review; 1.7.1 Printing non-cellular materials), or physically restrained to grow within the confines.[210,211] Such approaches, however, do not allow the user to remove such a physical confine at a later time.

The use of PDMS is advantageous if several copies of the master pattern are required. However, when prototyping, when the user requires a large range of variances in their design, a typical need exists to create tens, or hundreds of master moulds. In contrast, the direct patterning of a design using wax printed on a substrate bypasses the conventional process of using PDMS. Potential applications of our proposed method are found in the field of simulation studies and optimising microdevice prototypes.[195,209] Additionally, the ability to remove the wax after cell seeding can lead to studies of cell differentiation, from a restricted environment to a non-restricted environment.

Using inkjet printing to produce patterned environments offers fewer limitations compared to previously mentioned techniques that have to use UV exposure, photomasks, organic and toxic solvents, long processing times, complicated machinery, etching and the requirement of multiple steps. Avoiding these drawbacks would aid in the fabrication of microfluidic devices in research and industry settings,

as the turnaround times inherent in these techniques can be reduced, from around 24 hrs (with the majority of this time being used for mold preparation), to hours.

The use of wax for the creation of microfluidic devices has been used to create paper and glass-based devices as a simple and inexpensive method using commercially available materials.[167,168,212] This ability to create biosensors has been investigated to an extent with inkjet printing technology.[213–216]

4.2 Printing paraffin wax

4.2.1 Introduction

Prior to creating wax scaffolds, understanding the behaviour of wax during inkjet printing and the topological finish after printing was studied. Outside of optimising the printing behaviour of the wax, the droplet spacing between each wax droplet needed to be optimised to create smooth uniform lines when printed in one axis.

Paraffin wax was placed inside the cartridge reservoir and the printing system was heated up to 75°C for printing, while the printing platform was heated to 30°C to improve the topography of the printed structures. Wax viscosity was measured with a rheometer (AR 2000, TA Instruments) at different temperatures (Figure 4.2.1). When the temperature reached above 60°C, the viscosity was less than 10 mPa.s (10 centipoise) Specification guidelines from Microfab stated that inks should have a viscosity below 20 mPa.s (20 centipoise) for successful droplet formation during inkjet printing. At the temperature of printing (75°C) the viscosity was 6.02 mPa.s (6 centipoise), which was within optimal printing limits.

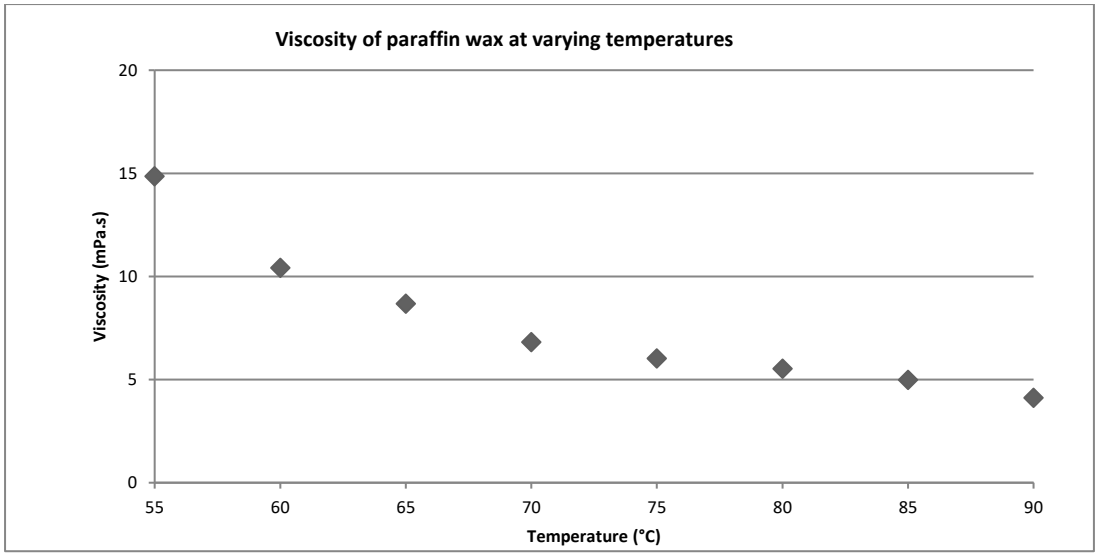

Figure 4.2.1 Viscosity values of paraffin wax over a range of temperatures, which was Newtonian when molten. Printing parameters below 20 mPa.s was optimal for printing.

4.2.2 Results

Table 3 shows examples of printing parameters that were used within this chapter for the successful droplet formation of paraffin wax. Several printing parameters are shown because optimal jetting parameters changed during the period of several months during the experimentation within the scope of this chapter. These changes were required due to the external environmental fluctuations that would occur through each season that affects the jetting behaviour of the inks jetted. The final size of droplets varied slightly through the different parameters, and the most significant changes were seen through varying the voltage during the jetting, causing the volume jetted to be proportional to voltage strength. Figure 4.2.2 shows images of the jetting printhead with different printing parameters, jetting different volumes of wax.

Table 3 main printing parameters used when printing paraffin wax, at 70-80°C

Paraffin Wax	Setting 1	Setting 2	Setting 3	Setting 4	Setting 5	
Rise Time (1)	15	8	15	11	3	µs
Dwell Time	10	9	10	22	12	µs
Fall Time	5	5	5	14	4	µs
Echo Time	10	10	10	10	15	µs

Rise Time (2)	2	2	5	5	4	µs
Voltage	28	15	36	26	68	V

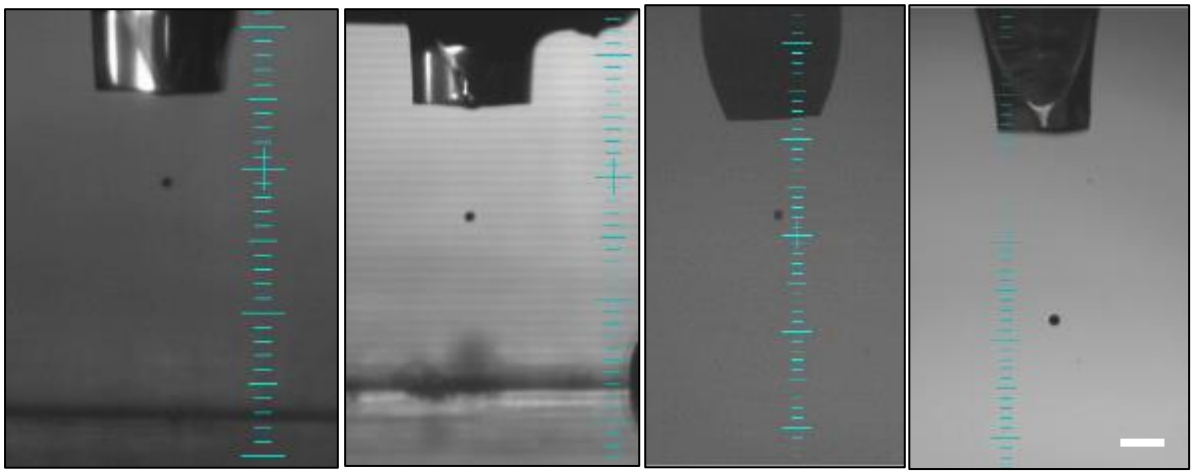

Figure 4.2.2 A collection of images showing the jetting molten wax with carrying jetting parameters, noting the variance in droplet size, from 45-17 µm. Note that conventional research had pointed out that, as a rule of thumb, the droplet size deposited onto the substrate would be roughly twice the diameter of the nozzle used. Droplets of 35 µm were easily created with a 50um diameter nozzle, through optimising the jetting parameters and the ease of forming single droplets with paraffin wax. Scale bar = 200 µm.

The diameter of the droplets were calculated through measuring the droplet sizes after micrograph images were taken of the samples; as shown in Figure 4.2.3, with average diameters of 32.5 µm.

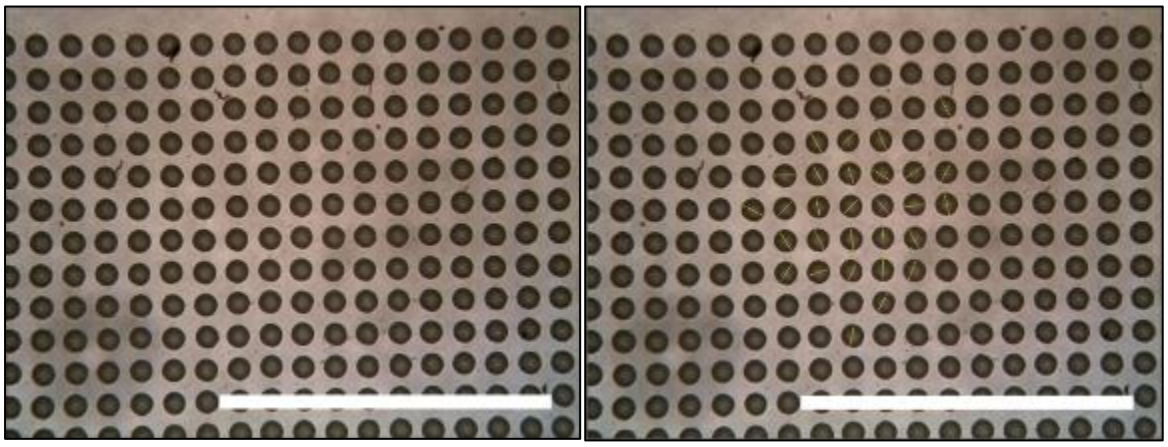

Figure 4.2.3 Inkjet printing an array of paraffin wax at 70°C, with droplet spacing of 140um between each droplet. Left; showing an example of successful droplet jetting with parameters outlined in Table 1. Right; using ImageJ and setting the appropriate scale bar, the diameter of the droplets could be measured. Wax diameter = 32.5 µm, SD± 1.53 µm. Sample size= 10. Scale bar = 500 µm

Single droplets can be deposited easily once the optimal printing parameters were identified. To create solid objects that were then used for tissue engineering applications, the single droplets were required to merge together to create uniform objects. To perform this, the droplet spacing between each jetted droplet was decreased, until the preceding droplet merged with the jetting droplet. As mentioned previously, there are different line behaviours as outlined by Soltman,[108] and the ideal droplet spacing would create uniform lines; Figure 4.2.4 is an example of testing different droplet spacings; the largest droplet spacing tested was 120 µm, and with Figure 4.2.4, it is clear that each droplet is isolated from neighbouring droplets and are not merged together. As the droplet spacing becomes closer, the droplets on the substrate become closer also. When the droplet spacing was set at 70 µm, the droplets are close enough together to begin merging with one another to create an unbroken chain of droplets. With a droplet spacing of 70 µm, the lines are still considered bumpy, as the droplet spacing is not sufficiently close enough to create a smooth topographical feature. At a droplet spacing of 40 µm, a sufficiently smooth topography can be seen to be fabricated as there is a consistent volume of wax being deposited in the given volume of space. The diameter of the droplet as it was jetted was, on average, 35 µm, and the deposited droplet diameter on the substrate was on average 70 µm, indicating that the diameter of the droplet in flight doubles once it has landed on a substrate. When the droplet spacing was 30 µm and 20 µm, bulging and scalloping occurred, whereby the droplets began to land on previously jetted wax droplets and created a “staircase” of droplets. This feature can be clearly seen in Figure 4.2.4, and with a droplet spacing of 20 µm, the structure is not completely focused in the picture, as the lower section of the wax pattern was lifted off the substrate, as the droplets stacked on top of one another.

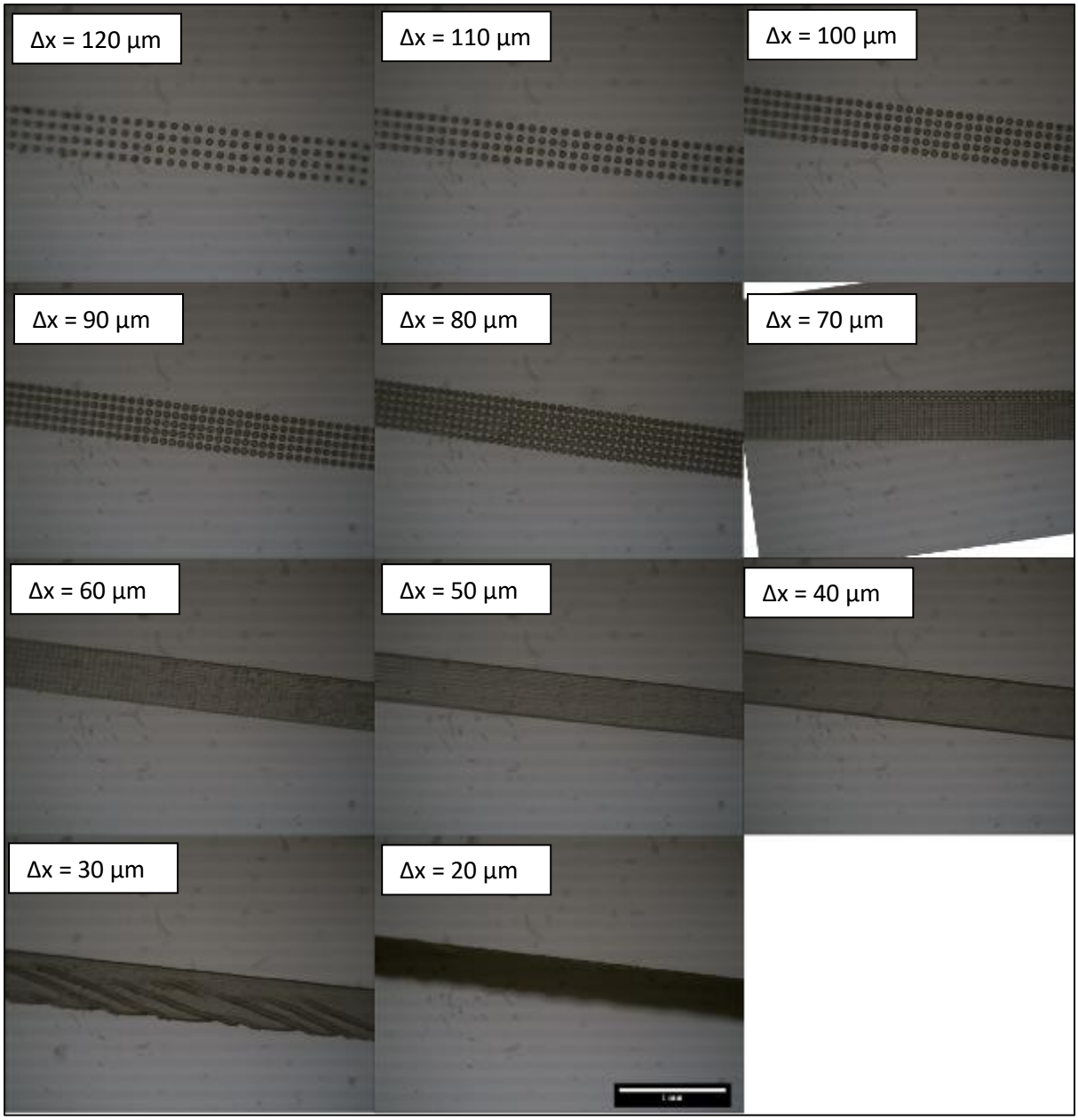

Figure 4.2.4 Decreasing the droplet spacing allows individual droplets to merge together to form a solid single line. Left to right; droplet spacing starts at 120 µm, and decreasing 10 µm per image, until a final droplet spacing of 20 µm can be seen in the last image. Bulging can be seen with a droplet spacing of 30 µm, and with 20 µm, the droplets begin staking on top of one another, creating a sloped wall with height. Scale bar = 1 mm

4.3 Creation of microfluidic devices

4.3.1 Introduction

Wax has been used to create paper-based microfluidics[168] and wax-loss methods with PDMS.[217] The function of a microfluidic device is to direct fluids at the micro-scale, through channels into different segments of the device, with each compartment offering a function to validate the fluid. The combination of wax and glass to create the skeleton of a microfluidic device offers a cheap and effective way to create microfluidic devices on-the-fly. Such applications can be found when researchers need to prototype microdevices quickly, creating many different variations, which would be very labour and time intensive with PDMS-related fabrication techniques.

4.3.2 Results

Through using the combination of Microsoft Paint and the Jetlab software, different patterns were created ranging from simple lines and curves to complex scaffolds and tissue engineered inspired patterns, such as an example of a more organic feature that was printed, showing that curves and angled shapes are just as easily fabricated (Figure 4.3.1).

Figure 4.3.1 More organic printed scaffolds could be created that were just as easy to print, as shown here with a wax patterned tree on a glass slide.

By directly printing wax, fabrication costs associated with producing microfluidic devices could be reduced. Through using inkjet printing to fabricate wax microfluidic devices (Figure 4.3.2), it can eliminate the use of other conventional equipment typically used in their creation, such as mask aligners, spinners, photoresist etc. and can be tailored on-the-fly within a remote environment, in academia and industrial settings.

Once the ejection parameters were optimised, creating the microfluidic patterns was straight forward. In Figure 4.3.2, an example of a microfluidic device is shown, with magnified images to show the resolution of inkjet printing.

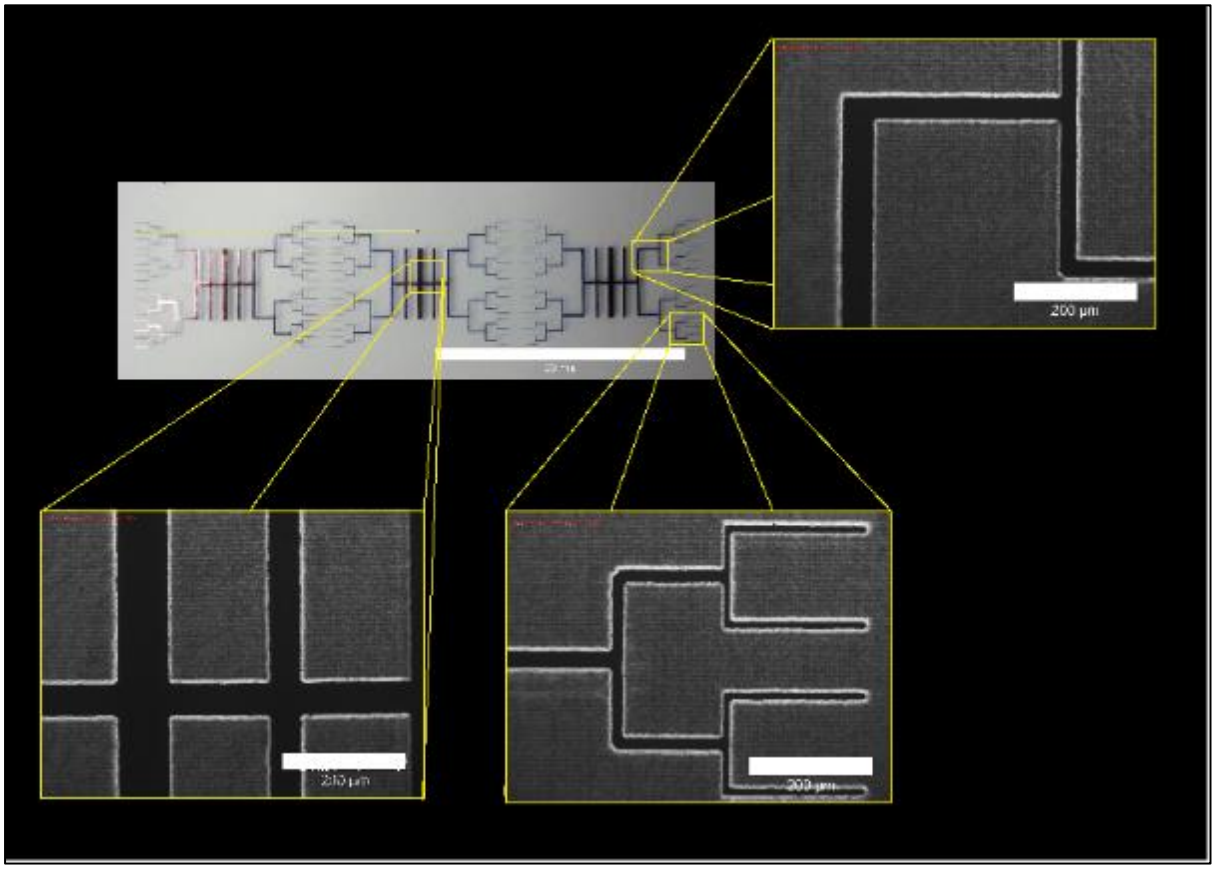

Figure 4.3.2 Scaled-up versions of the original printed circuitry pattern, to show scaling is not an issue with the inkjet printing technique. The wax was submerged in blue ink to show contrast between the glass and wax. The thickest channels measured to be 80 µm, and decreased to 50, 34, 37, 20 and 11.5 µm to the smallest channel respectively. Scale bar of unexpanded image = 20 mm, scale bar of expanded images = 200 µm.

During the creation of microdevices using paraffin wax, it was considered possible that finer resolution microfluidics could be made by decreasing the droplet spacing further. The limit of channel width was investigated.

With samples that were created that resemble a microprocessor (Figure 4.3.3, Figure 4.3.4), these samples can be used as a microfluidic tool to isolate, analyse and test developing neurites of nerve related cells. The ability to scale up or down a pattern can be done through resizing the image with the appropriate software (Microsoft Paint, Photoshop CS3 etc.), an example can be seen with Figure 4.3.3 with the circuit pattern.

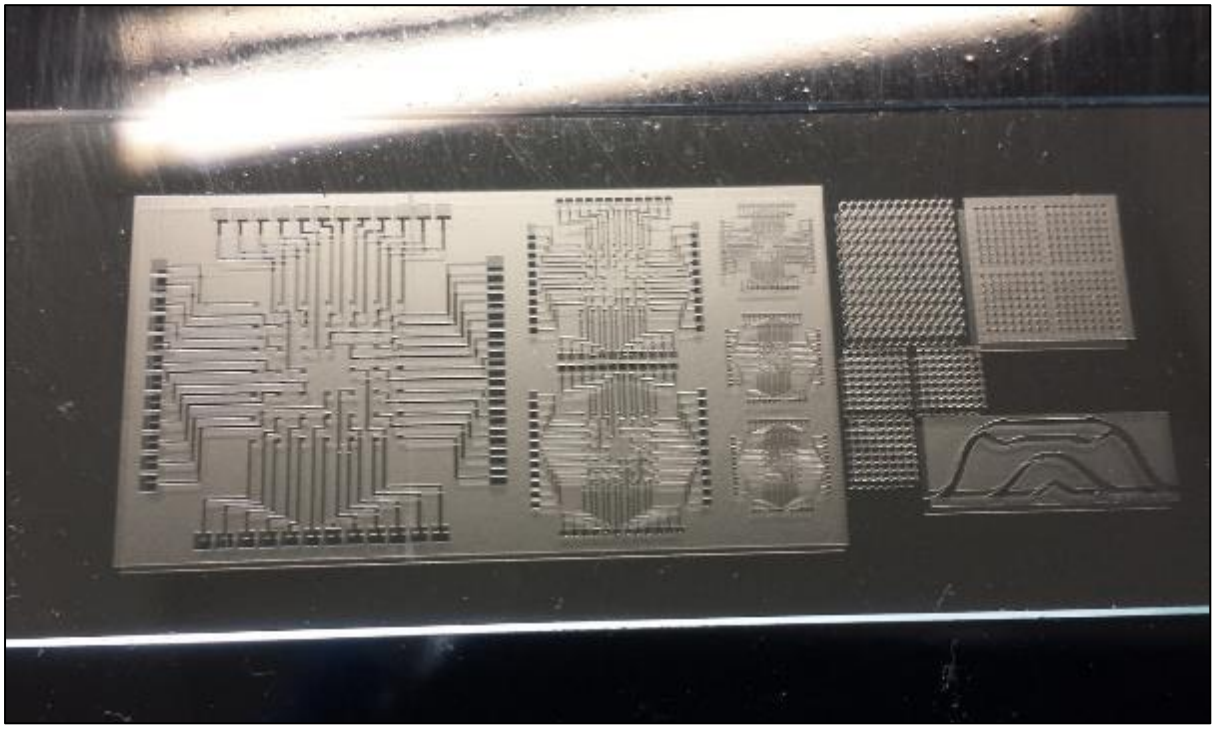

Figure 4.3.3 Glass slide with a variety of inkjet printed patterns

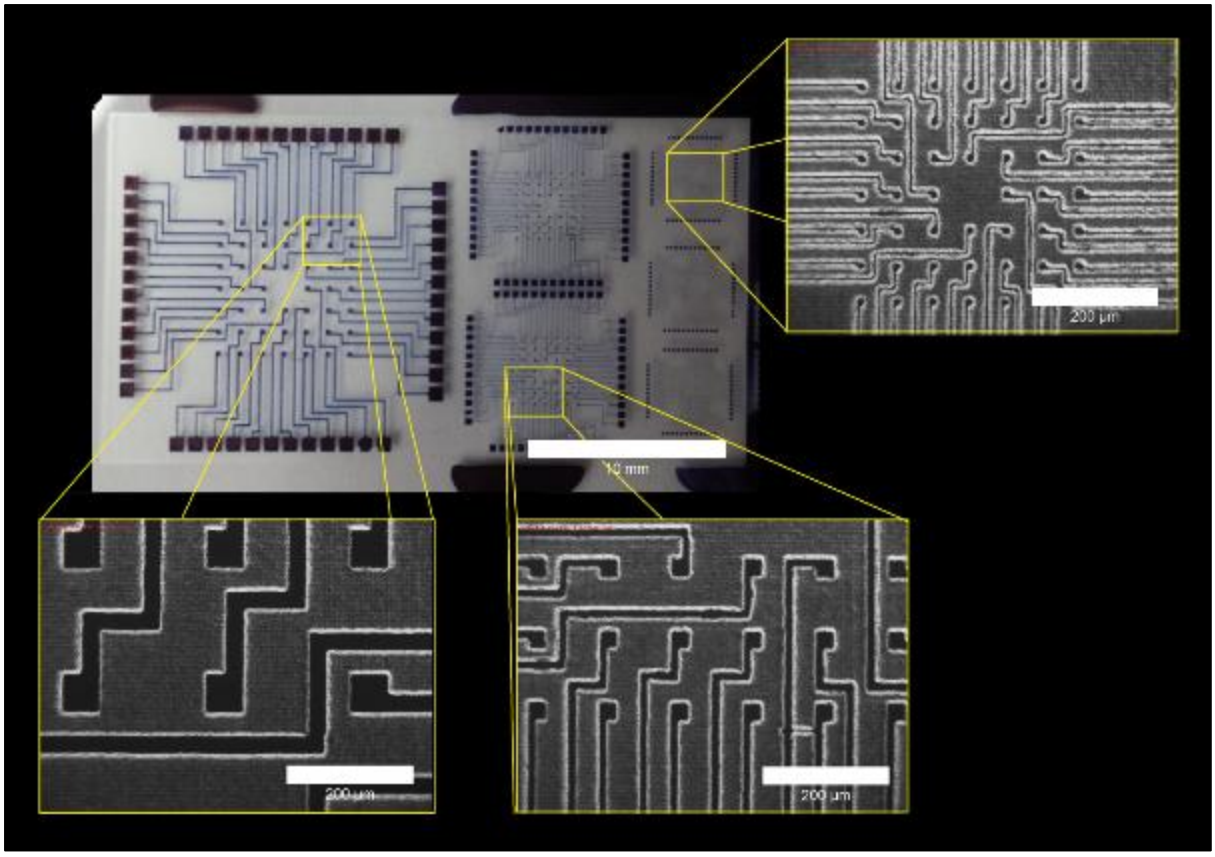

Figure 4.3.4 Scaled-up versions of the original printed circuitry pattern, to show scaling is not an issue with the inkjet printing technique. The smallest resolution channels that were produced were 3.5 µm, as shown in the top right enlarged image, with 10 µm inlets. Scaled-up versions had 14 µm, 31 µm and 31 µm and 71 µm for channel widths and inlets respectively. The wax was submerged in blue ink to show contrast between the glass and wax. Scale bar of unexpanded image = 10 mm, scale bar of expanded images = 200 µm.

To complete the microdevice, a heated glass slide (just below the melting point of paraffin wax) was placed on top to sandwich the patterned wax design between two glass layers. The high temperature melted the top layer of wax, to create a tight seal. To make an orifice for solutes to enter the microfluidic device, open channels were created at the edges of the glass substrate, so when the second layer of glass was positioned on top, the open channel created an opening.

As it can be seen in Figure 4.3.4 and Figure 4.3.5, the smallest width channels that were produced were 3.5 µm for the smallest scaled microprocessor patterns. At such resolutions it can be ideal for microfluidics of solutes, as cells are too large to pass through such narrow channels. To the author's knowledge this is the smallest width channel that has been produced with using paraffin wax. Previous research groups had generated widths of 25 µm[168] and 70 µm with wax-loss casting with PDMS.[218]

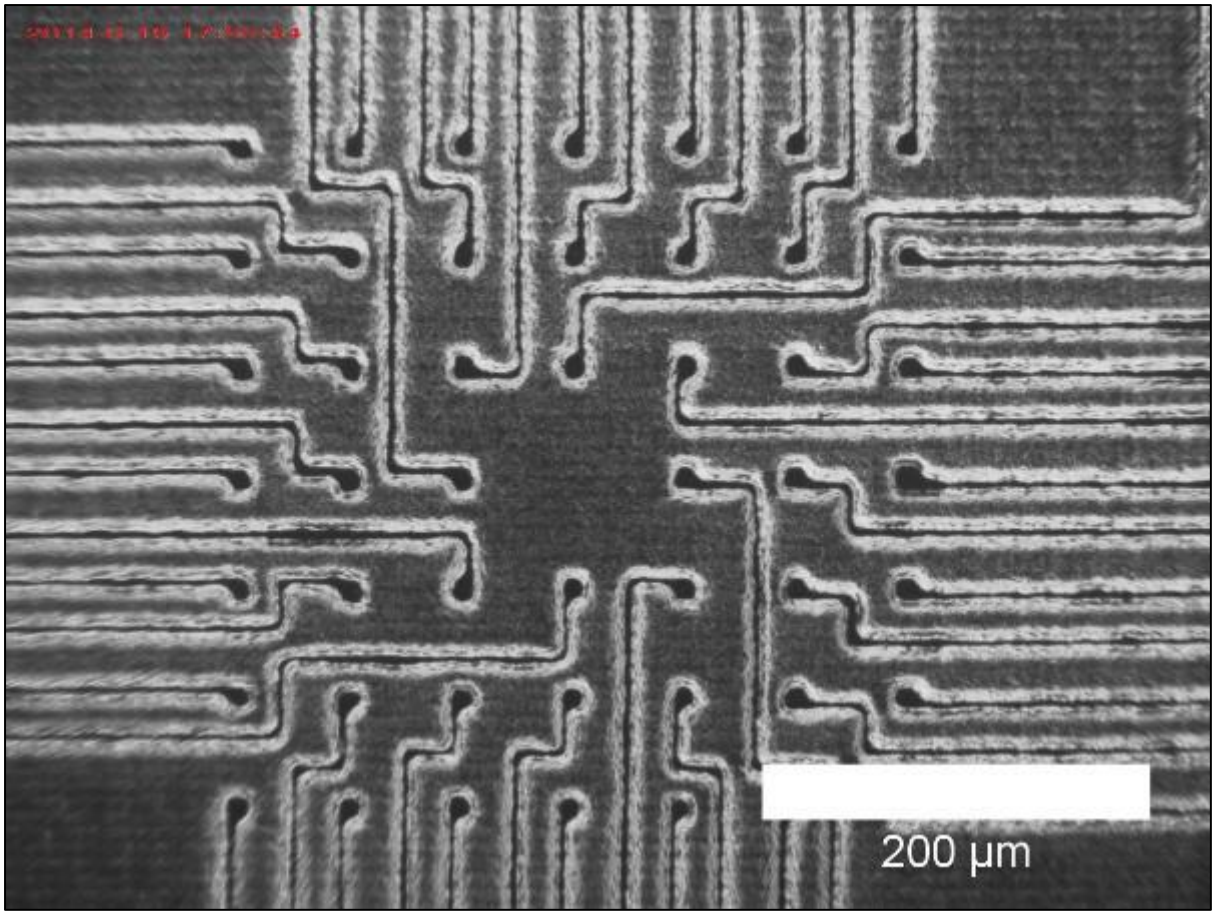

Figure 4.3.5 Enlarged image of microprocessor pattern to show 3.5 µm width channels. Scale bar = 200 µm

There are other techniques such as direct laser writing that can create nanofluidics with channel widths of less than 50 nm, which are too small for cell research, but are optimal for DNA analysis.[219] However, compared to direct laser writing, the inkjet printing is simpler, easier to optimise and less expensive.

Figure 4.3.6 shows a number of printed patterns on cover slips in a petri dish, with an enlarged version of the pattern and the BITMAP file that was used to create the pattern. A single microprocessor pattern can be inkjet printed onto a cover slip in less than 10 minutes.

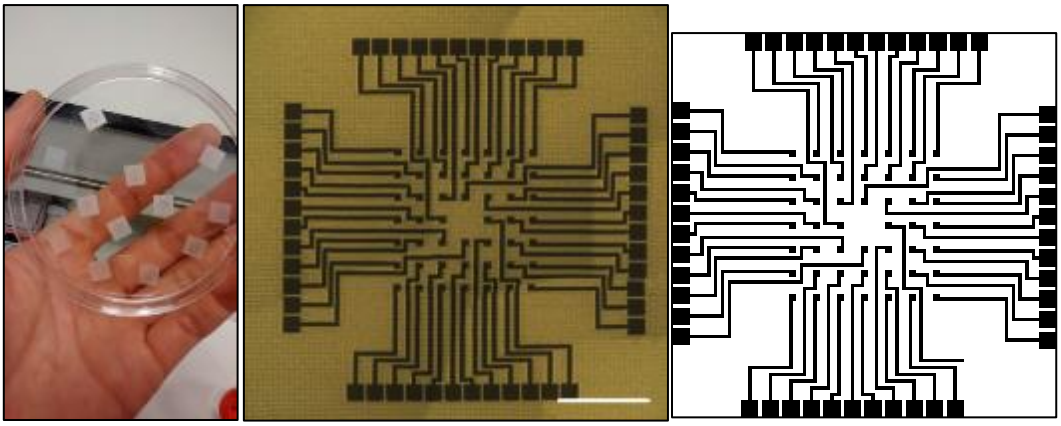

Figure 4.3.6 Inkjet printed microdevices using wax. Left: showing samples created with the inkjet printer with the circuitry pattern on cover slips placed inside a petri dish. Middle: Enlarged image of the inkjet printed wax circuitry pattern on a glass cover slip. Several imaged were merged with Photoshop CS3 to create a large enough image of the whole pattern. Scale bar = 1 mm Right: Black and white bitmap image used to create the circuitry pattern.

An advantage of inkjet printing is its ability to create complicated patterns just as easily as simple ones. The creation of patterns is not limited by its complexity, unlike traditional techniques such as stamps and stencils. Inkjet printing offers a technique that builds the pattern through a raster and row-upon-row creation as the material is only applied to where it is needed. Compared to standard photolithography techniques, the topology of a printed wax microfluidics device does not have as smooth a finish, due to the variability of cooling of molten wax after it has been deposited during the creation of the device. This means that inkjet printing has a minimum resolution within the scale of 1-10 microns, whilst there are commercial stereolithography machines that have a minimum resolution of 10-100 nanometres. This makes inkjet printing more suitable to the creation of certain types of microdevices that benefit from its ability to create tailored devices without the need of multiple types of machinery and that do not require nanometre resolution. Such examples include a variety of diagnostic applications; ideal for prototyping and creating devices with frequent layout changes, or devices with low production quantities and disposable due to its low cost in manufacture. With the ability to create smaller devices, it would make inkjet printed microdevices highly portable; ideal for rapid medical diagnostic applications in remote regions of the world.

In feasibility studies, it can be assessed that printing paraffin wax for the creation of microfluidic devices, with channel width resolution of 4-100 µm are most ideal, as at such resolutions, inkjet printing

can use its strengths to create such devices; ease of fabricating complex structures, resolution, speed, inexpensiveness of materials and inexpensiveness of start-up costs.

Microdevices can be fabricated through printing patterned paraffin wax onto glass, and adding a heated glass substrate on top to enclose the wax like a sandwich. The smallest channels created were 3.5 µm, which is, to the author's knowledge during the time of writing, the smallest that has been created with an inkjet printer and paraffin wax. Such high resolution is useful in the application of lab-on-a-chip applications as significantly less solutes are required for tests, and also through the technique of additive manufacturing, smaller devices take less time to fabricate, and more can be transported given a single weight.

4.4 Creating 2.5D structures

4.4.1 Introduction

When creating microdevices, the channel's width and height of the channel can be varied. As shown in Figure 4.4.1, two layers of wax can make a diagnostic device with very shallow channels (with a high width-to-height ratio), or if many layers of wax are printed together, deep channels can be created (with a low width-to-height ratio). There are no ideal dimensions for creating microdevices, however the final width-to-height ratio will affect the fluid movement through each channel.

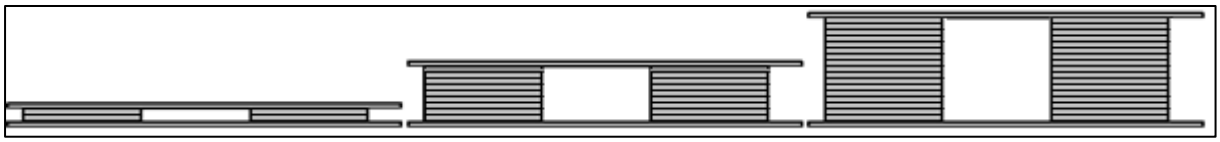

Figure 4.4.1 A cross section of a design of a microdevice. Wax (grey) is sandwiched between two pieces of glass. The need for multiple layers of wax to create appropriate dimensions for fluid flow needs to be balanced by the number of layers. (Left) if one layer was printed, the width would be large, and the height too low. (middle) has similar unsuitable width/height ratio. (Right) this design would be best, whereby the width and height are similar.

There are other needs to be able to print consecutive layers on top of one another. Such examples include the ability to create tailored isolated culture environments. This saves the use of space (with more cell isolates that can be cultured in a set volume) and cell culture media used. Digital BITMAP patterns such as the ones shown in Figure 4.4.2 were created, with the example showing multiple honeycomb

designs, as inspired by Claeyssens et al which show that honeycomb structures could help with repairing nerve damage [220].

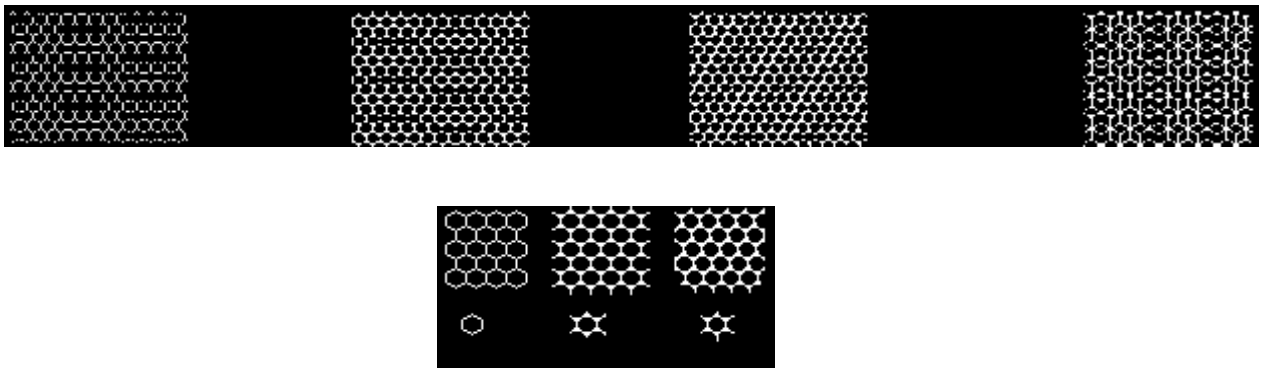

Figure 4.4.2 Examples of Bitmaps used for printing 2.5D structures. These patterns were printed successively on top of each other to create height within the structures that created separate channels for cell isolates

The patterns that were created could not be considered full 3D structures, but 2.5D. A pattern could be printed several times on top of itself on a single microscope glass slide, and the z-axis raised to compensate for the gain in height as the structure built up and repeated to create a 2.5D scaffold.

4.4.2 Results

With the ability to print accurately with a repeatability of $\pm$ 5 µm, stacking wax on top of the previous layer was possible to create wax scaffolds with height (Figure 4.4.3).

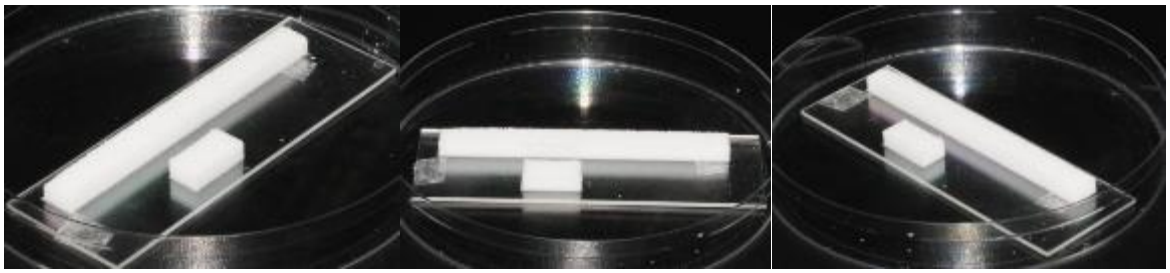

Figure 4.4.3 Images showing the creation of 2.5D structures for the creation of microdevices. Several hundred layers was printed on a glass substrate. The sample has a height of 4 mm.

Figure Figure 4.4.3 and Figure 4.4.4 show the final structures that were created through printing multiple layers on top of each other, with varying number of layers to control the height, using the BITMAP as shown in Figure 4.4.2.

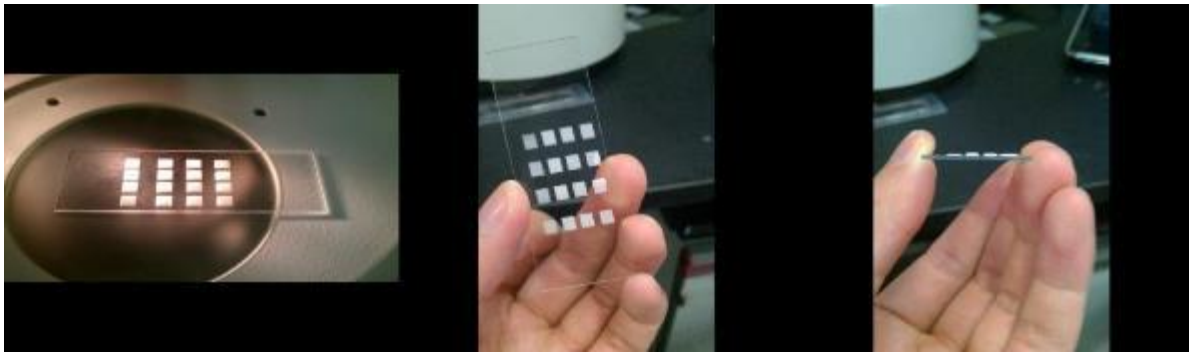

Figure 4.4.4 The resultant 2.5D print on glass substrate. A regular pattern was printed four separate times, and from top to bottom, was printed with 10, 30, 60 and 100 repeats respectively.

This ability to create any shape and size of compartmentalised volume can have a wide range of applications in culturing cells and tissue. As it can be seen in Figure 4.4.5, each honeycomb structure is an independent compartment that it isolated from each other. An immediate use for such designs and creations can help the most recognised bioprinting companies – Organovo (US) and Cyfuse (Japan), as material can be printed into such compartments, which would allow greater precision and scalability that is not possible with standard pipetting techniques.

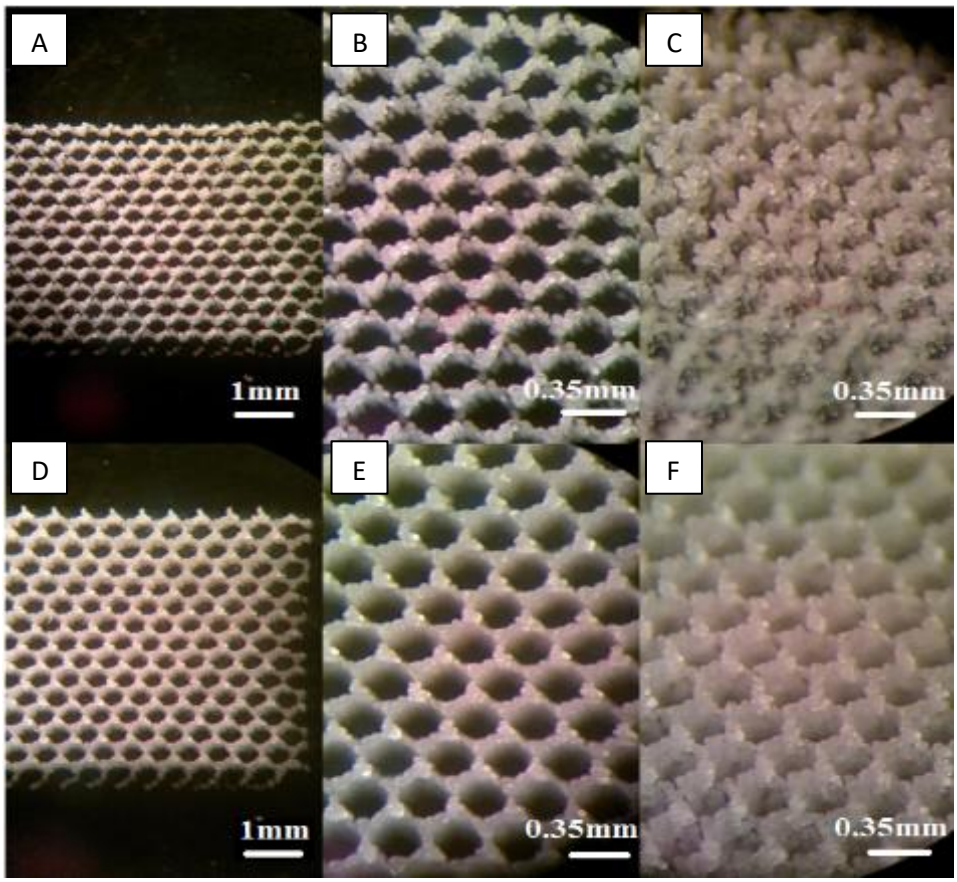

Figure 4.4.5 Microscopic images of the honeycomb structured paraffin wax. A-C were repeated 30 times, D-F were repeated 60 times. D and F were imaged captured at an angle to show the dimensions of the structures.

Both these companies have developed scaffold-free bioprinters; NovoGen Bioprinter and Regenova respectively that can create soft tissue without the need of an extracellular matrix support or hydrogel. Their bioprinters position and utilise spherical aggregates of cells of a controlled shape and size, using robots to load the spheres into the bioprinter. To create these aggregates of cells, they need to be cultured until maturation, and typically cultured in well-plates, before being selected for use; the smallest being 96 well-plates (3.6 mm in diameter). As shown in Figure 4.4.6, the standard 96 well plate is unnecessarily large for the aggregation of the cells to create a spheroid. Through the use of this design and with wax, wells of less than 0.35 mm in diameter could be created, and can accommodate for the population of cells required to create the cellular spheroids for bioprinting. This would allow more spheroids to be created in a single plate, saving on costs of consumables such as the well plates used and cell media, as more is used than required.

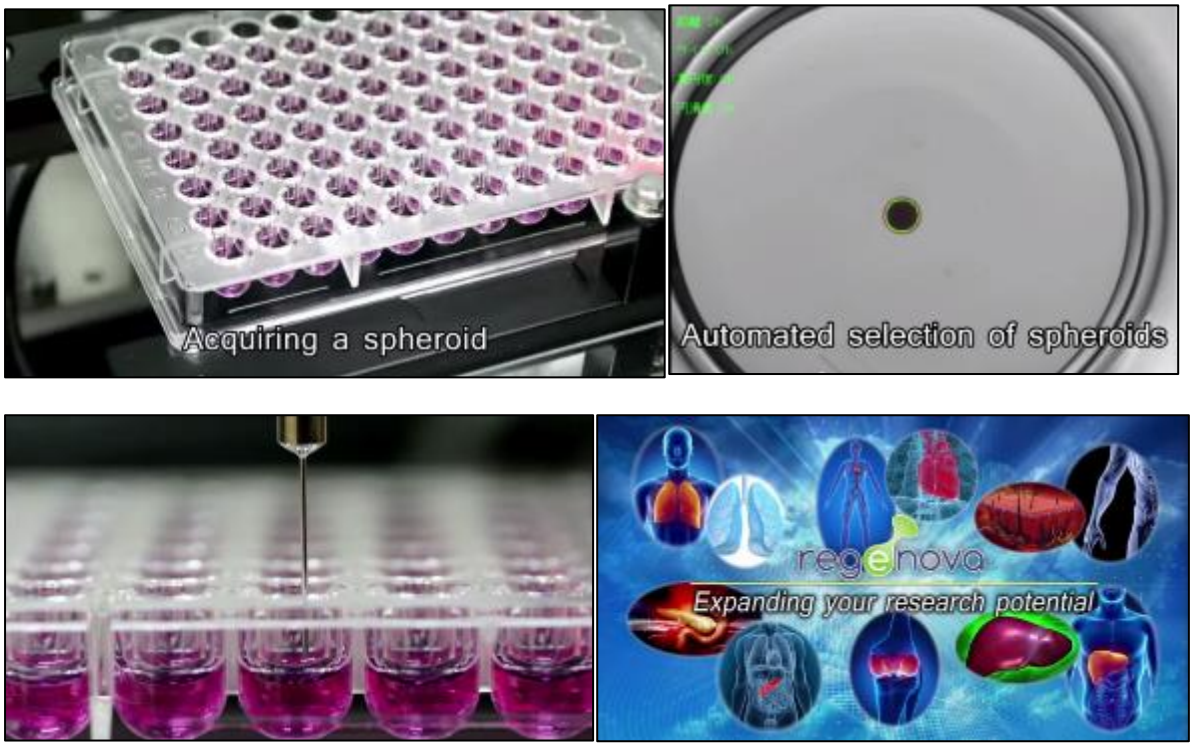

Figure 4.4.6 With respect to Cyfuse's proprietary bioprinting; Regenova, spheroids are acquired through an automated process of detecting the suitable size of the cell aggregate and then being manipulated by a robotic syringe. Images compiled from acquired from Regenova's promotional video; https://www.youtube.com/watch?v=6SMiCgli8TQ

To summarise, printing layer-by-layer of paraffin wax on top of a previous pattern is possible to create solid structures with height, and is useful to tailor the creation of microdevices and microwells. The droplet volume should be modified to jet larger volumes, to increase the speed of fabricating scaffolds with height, as several hundred layers were required to be printed to create samples of over 4 mm in height, which can be too time consuming.

4.5 Wax patterning for neurite analysis

4.5.1 Introduction

With respect to the study of dynamic behaviour of dendrites and axons, traditional outgrowth experiments typically generate random and overlapping neurite extensions, or use expensive microdevices containing wells, channels and a set of microgrooves. Such commercial microfluidic devices can be purchased to empower scientists within this field (i.e. Axon Isolation Devices) that have rigid specifications with their products. It was postulated that an alternative could be created through the use of printing wax to create a device which performs in a similar manner as commercial isolation devices, with more tailored fabrication ideal for each experimental setting. Such devices have relatively simple components to create an isolation device; defined areas to position cells, channels for neurite outgrowth and a transparent substrate for microscopy analysis.

4.5.2 Results

Using standard glass slides, wax was inkjet printed with different patterns to create suitable designs for neurite analysis. The pattern shown in Figure 4.5.1 required 1 minute to create once the printing parameters were optimised and shows individual wax droplets positioned on a glass slide at 40 µm intervals. Droplet diameters were on average 17 µm, with high regularity of the positioning of each droplet with a standard deviation of $\pm$ 0.07 µm. Such designs show the ease of fabrication of microdevices, and a heated glass slide can be placed on top to sandwich device together to create a closed system.

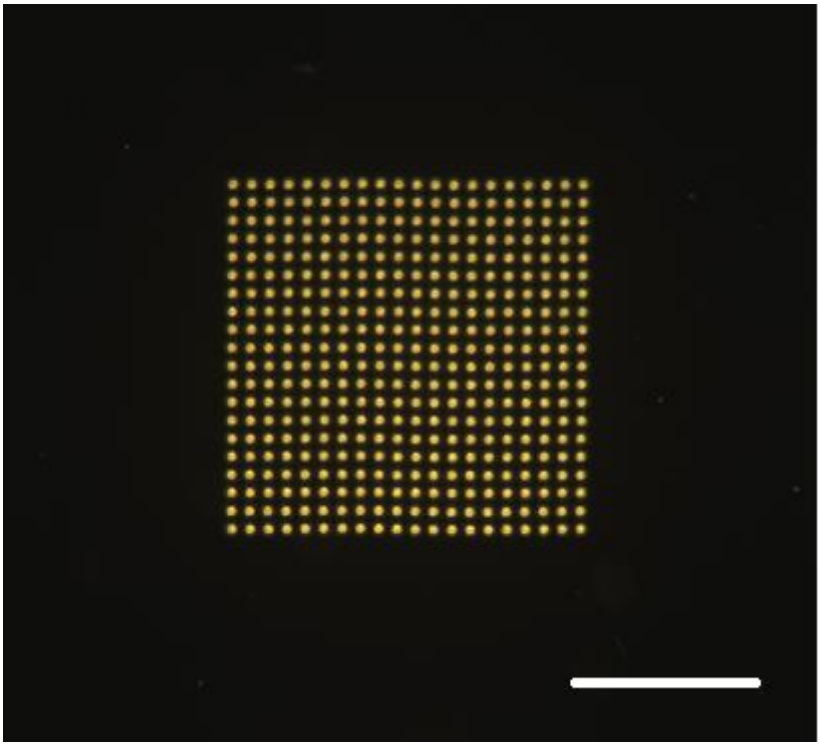

Figure 4.5.1 A 20x20 array of wax droplets on glass, with a droplet spacing of 40 µm between the centre of each droplet. Droplet diameter averages 17 µm. Scale bar = 400 µm

Initial experiments identified an appropriate range of dimensions that were biologically relevant to the creation of microdevices, which were simple channels and honeycomb-like structures. A range of arrays with different droplet spacings were created, with fibroblasts, and later, RN22s seeded into them,

Once the wax designs were fabricated on a glass slide, cells from culture were grown to confluence, seeded at 2 x 10^4 cells per sample in 1 mL and left in an incubator, with more cell culture media added to the petri dish containing the scaffold after 60 minutes (to prevent evaporation of cell media). The droplet spacings used, ranged from 100 µm to 40 µm. Figure 4.5.2 shows two examples of the behaviour of cells in an array with 100 µm and 60 µm droplet spacings. With these examples, the droplet spacing proved to be too large to be an effective method of spatially arranging cells. The wax droplets did not provide any cues for cells to arrange in an ordered way.

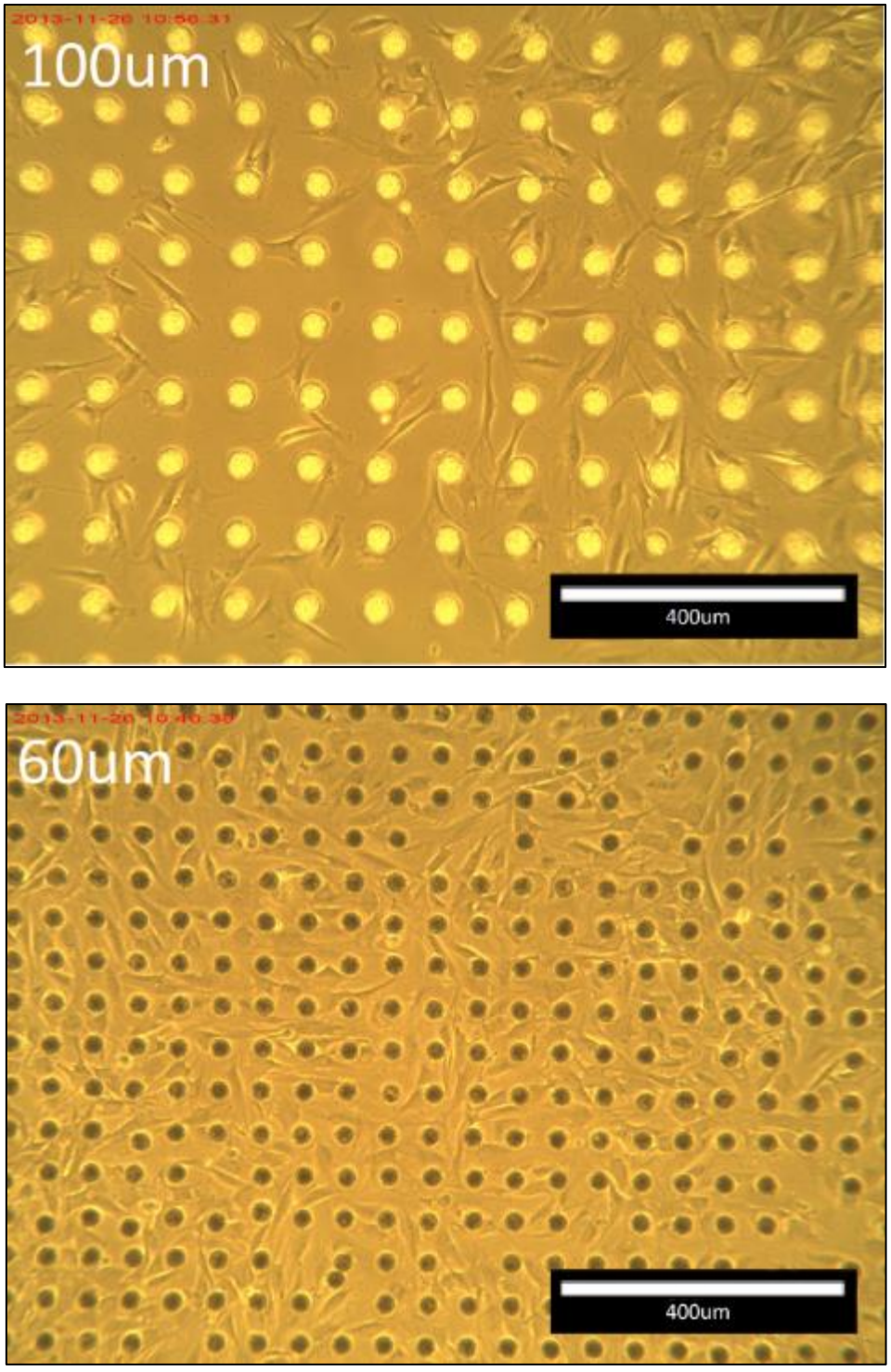

Figure 4.5.2 Microscopy images of fibroblasts seeded onto wax arrays after 3 days in culture. (100 μm and 60 um droplet spacings)

Fibroblasts were used initially, and were later replaced with neuronal RN22 cells to allow the study of neurite orientation behaviour in the presence of the wax arrays.

A smaller wax droplet spacing of 50 µm was shown to be too large (Figure 4.5.3), and cells were not organised effectively within the array.

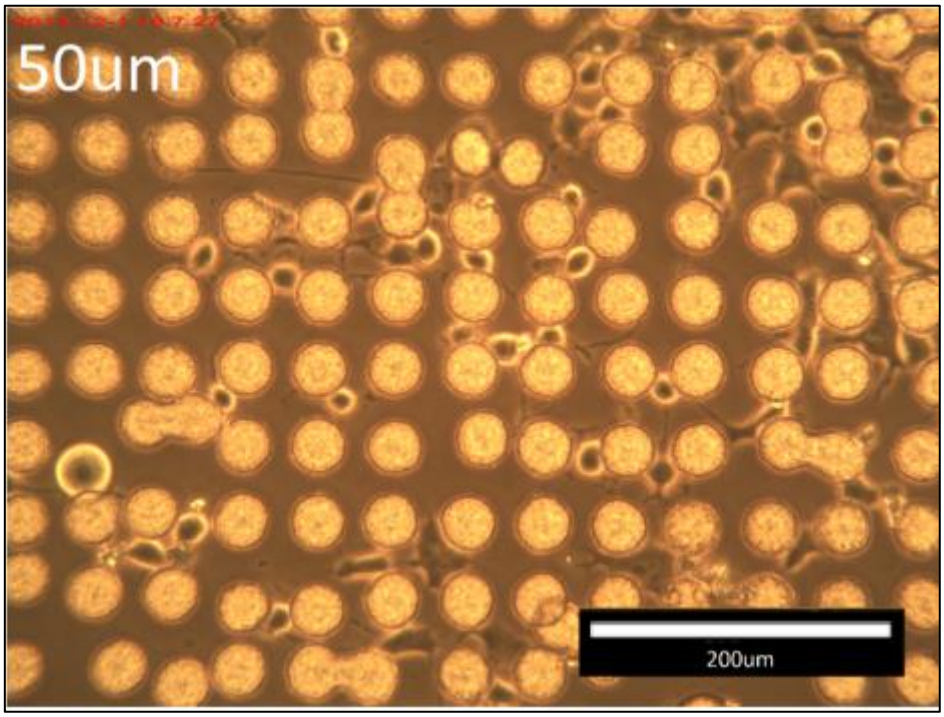

Figure 4.5.3 Microscopy image of RN22s after 1 day of culture on wax arrays with 50um droplet spacing. There is a minimum of 16um channel between each leading edge of a droplet to the adjacent droplet. This channel length was too large, and cells were not organised within the arrays as ordered as 40 µm array scaffolds. Scale bar= 200 µm

The arrays that had droplet spacings of less than 40 µm created a single solid scaffold as adjacent droplets merged together. As shown in Figure 4.5.4, paraffin wax droplets of 34 µm in diameter were jetted, and were jetted with spacings of 40 µm from the centre of each droplet. This meant that there was a 6 µm distance of separation from each leading edge to its neighbouring droplet.

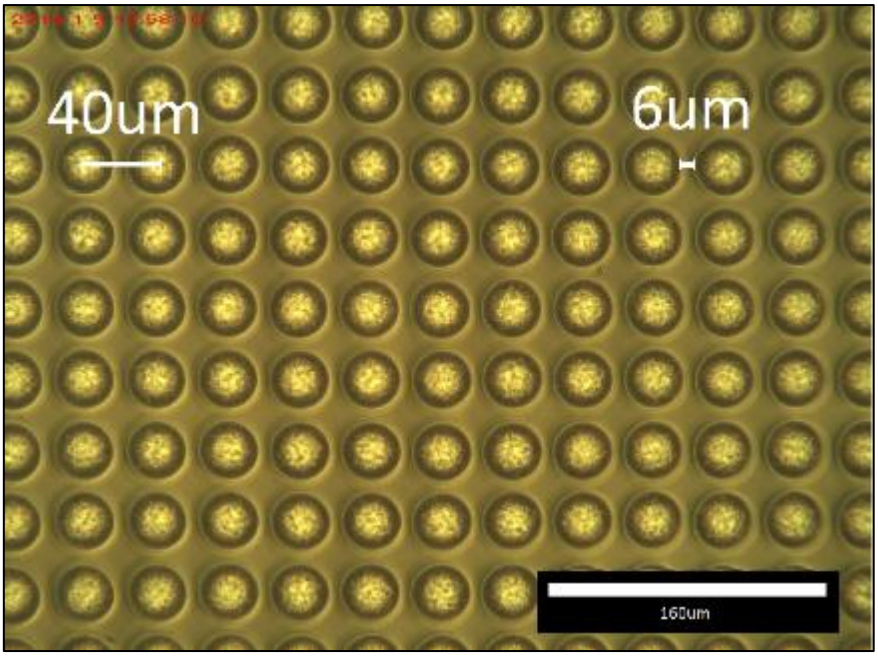

Figure 4.5.4 Enlarged image of the array in Figure 4.5.1. Wax droplets with droplet spacing of 40um, and each dot being separated by 16 µm at their leading edge to adjacent dots. Average diameter = 34.08 µm, with SD= 0.729, x=10. Scale bar = 160 µm.

Once the optimal droplet spacing was discovered, RN22 Schwannoma cells were seeded into the arrays and left to differentiate over several days. Figure 4.5.5 shows a microscopy image of cells that have adhered onto the glass and growing around the wax dots after 1 day of culture.

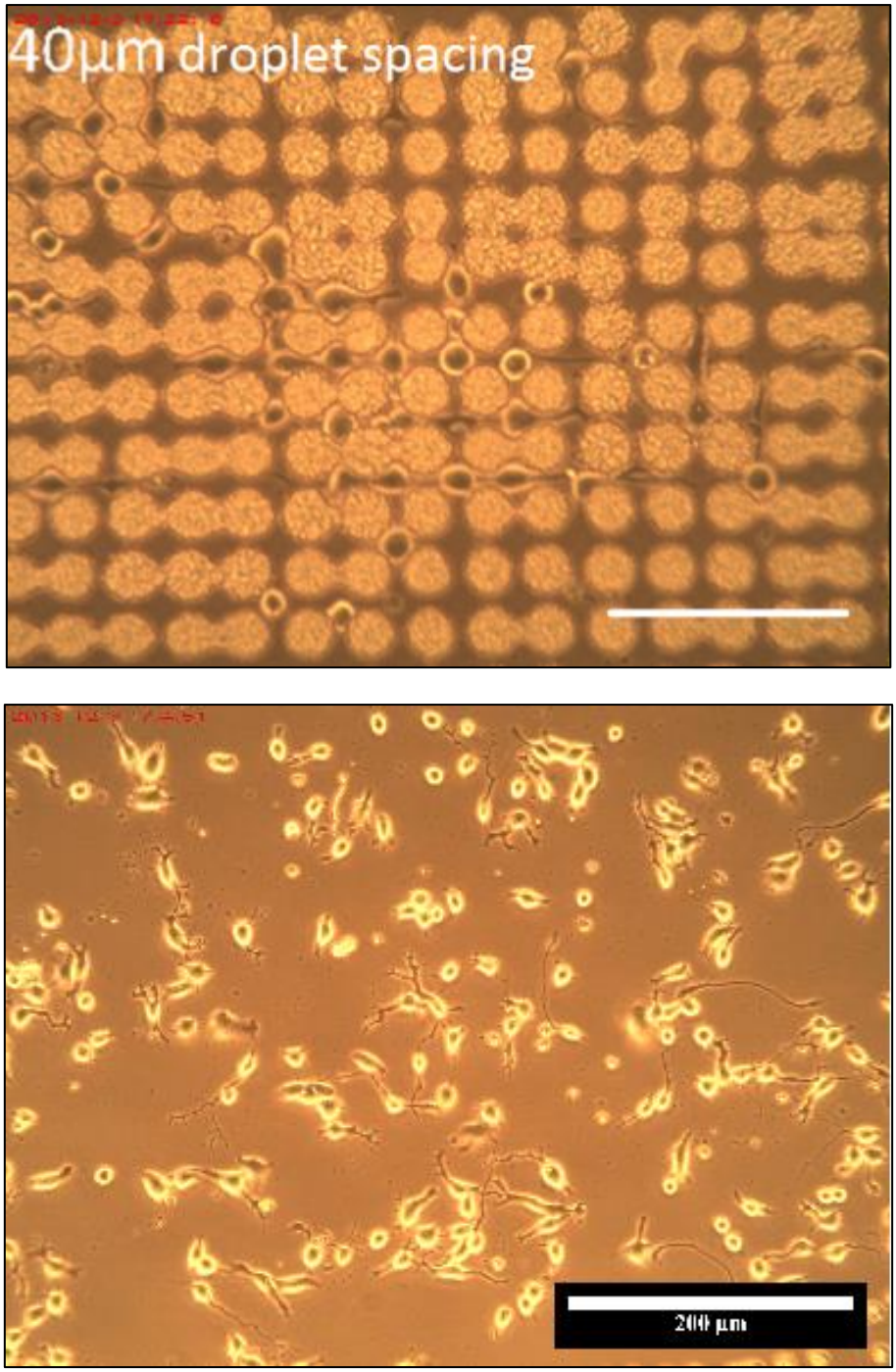

Figure 4.5.5 Cell alignment caused by wax guidance. Top) showing wax arrays 40 µm apart, with RN22s seeded onto the glass substrate after 1 day of culture. Bottom) showing a control sample with RN22s growing on a plain glass slide to show disorder of orientation with respect to the neuritic protrusions. Scale bar = 160 µm and 200 µm

Note with a droplet spacing of 40 µm, cells were situated between the wax, as shown by the cluster of cells in the centre of the image. Due to the presence of the wax dots, the cells extended neuritic protrusions that moved up, down, left and right of the respected cell. No protrusions were seen to extend over and across diagonally of the wax dots, limiting the direction of the growth of protrusions (more

examples can be found in Appendix One). An ideal droplet spacing of 40um was identified that allowed neuronal RN22s to be trapped between the droplets, and having enough room to only allow their neurites to protrude to adjacent channels.

Having shown that nerve cells can be seeded and can be grown with aligned neurites with physical cues, without the use of additional chemical and biological factors, inkjet printing wax has the potential to be used to create ordered neuronal circuits in vivo and be used for the study of synapse generation, cell-cell interaction and neural cell development. The ability to remove the wax scaffold after cell seeding is not available with this technique, due to the non-connected array of wax droplets.

The specifications of the wax patterns can be tailored to requirement and with the printer having a repeatability resolution of 0.8 µm, scaffolds can be finely tailored to have a theoretical channel width resolution of a minimum of 0.8 µm. As shown in Figure 4.5.6, a minimum of 6 µm channels were produced between each leading edge of a droplet. At this resolution, neurites are able to freely traverse the channels, whilst the cell body is too large and will be restricted to larger areas of the chip. With the control of fabricating the design of the wax, cells can be deposited at pre-defined distances apart, with thin channels that only neurites can grow into so cell behaviour can be studied.

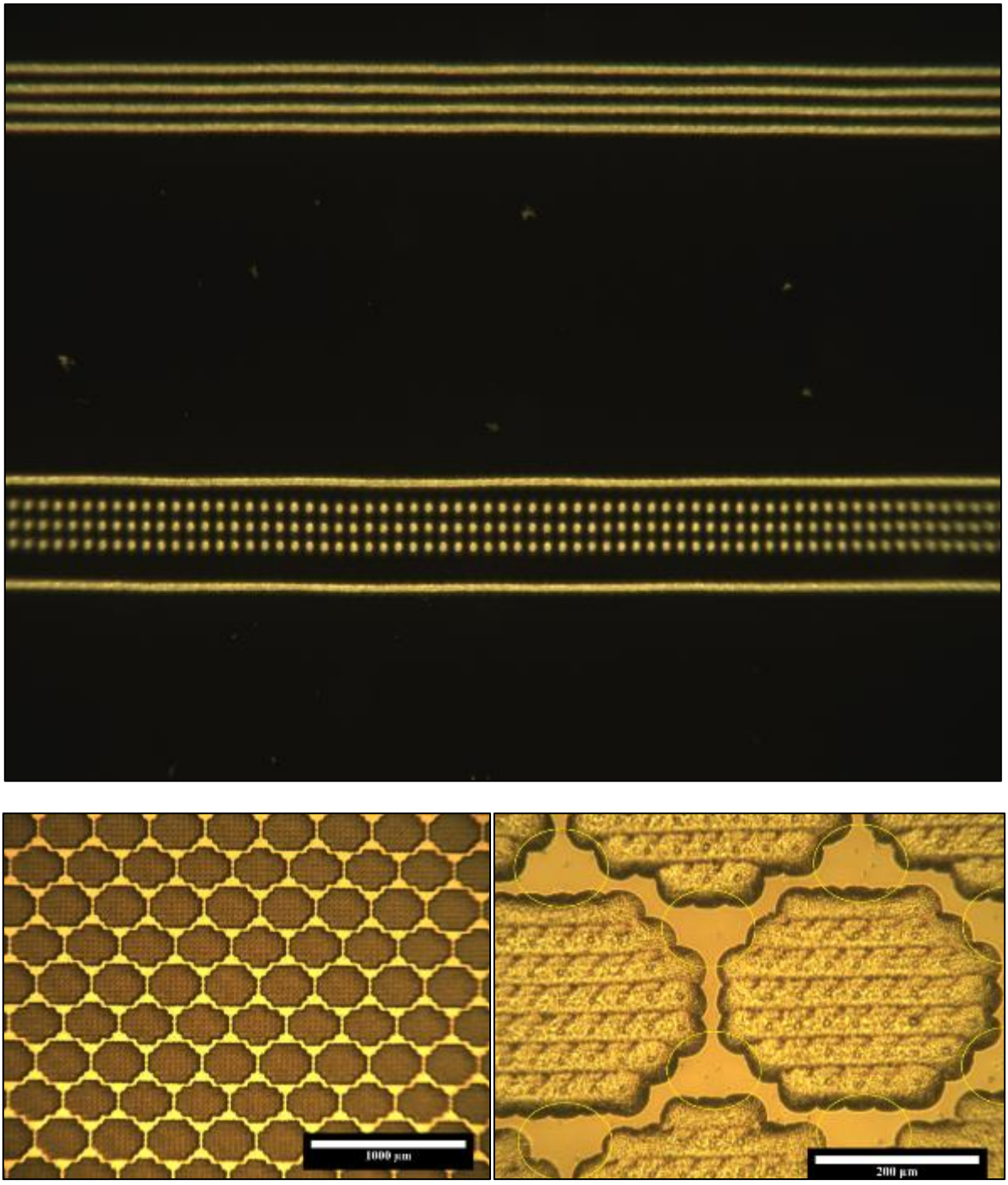

Figure 4.5.6 Inkjet printed wax patterns. Top) showing an example of possible microfluidic patterns that can be created, which can allow nerve cells to be seeded and different topological features to be tested under the same environment i.e. straight lines, no features (control) and dot arrays features. Bottom left) an example of a different version of a custom axon isolation device, Bottom right) enlarged image. Neuronal cells would be seeded in areas with the yellow circles, and their neurites could traverse through the channels to join with neighbouring cell bodies.

In summary, cells can be grown in an environment surrounded by paraffin wax. Typically lab-on-a-chip research is fabricated with PDMS and requires at least 24 hours preparation overnight for the PDMS to set, limiting the speed of prototyping research. Alternatively, a cell-attractive substance can be applied onto the substrate that cells preferentially adhere onto, however such proteins and extra-cellular matrix components are magnitudes costlier to purchase. Inkjet printing wax allows quick

prototyping, and is very easy to change the printing settings on-the-fly, to tailor the structures accordingly with minimal down-time. The handling of the wax and equipment are easy to use, and a large number of possibilities are available for creating different array geometries.

4.6 Inkjet printing of wax guides/ orientation/ cell study experiments

4.6.1 Introduction

This section shows that cells can be seeded into wax patterned environments and allowed to differentiate to study their mobility behaviour. The ability to create cell-appropriate wax scaffolds was investigated, and later seeded with cells, with the option to remove the wax for free cell differentiation afterwards.

4.6.2 Results: Formation of wax guides

Figure 4.6.1 shows an example of creating channels of 80 µm width. Such patterns do not take long to create, and inkjet printing offers high variability to tailor the design of the microfluidic channels/ cell culture environment.

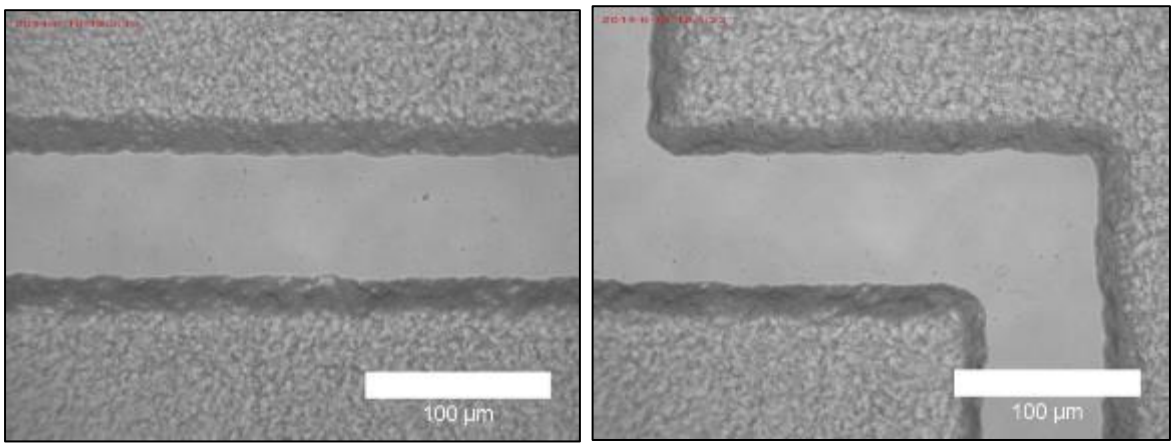

Figure 4.6.1 Micrographs of simple patterns that were created using the inkjet printer

A variety of designs were created that were suitable for isolating and connecting islands of cells on glass slides [Figure 4.6.2 (a-c)]. The scalloping behaviour was due to the droplets being cooled quicker than optimal during jetted flight, after landing on the substrate, merging with the previous deposited droplet and partially retained their individual rounded contact lines.[221]

Under high magnification, as exemplified in Figure 4.6.2 (a) single wax rows of droplets appeared to have a slightly uneven topography due to scalloping behaviour. The final shape and surface texture of the resultant printed structure was dependent on conditions that include the wettability of the substrate and its temperature, printhead temperature, gap distance from the printhead to the substrate and droplet

material.[222–224] Printing wax allowed the creation of a range of different complexities and channel widths that allowed the creation of thick impermeable blocks.

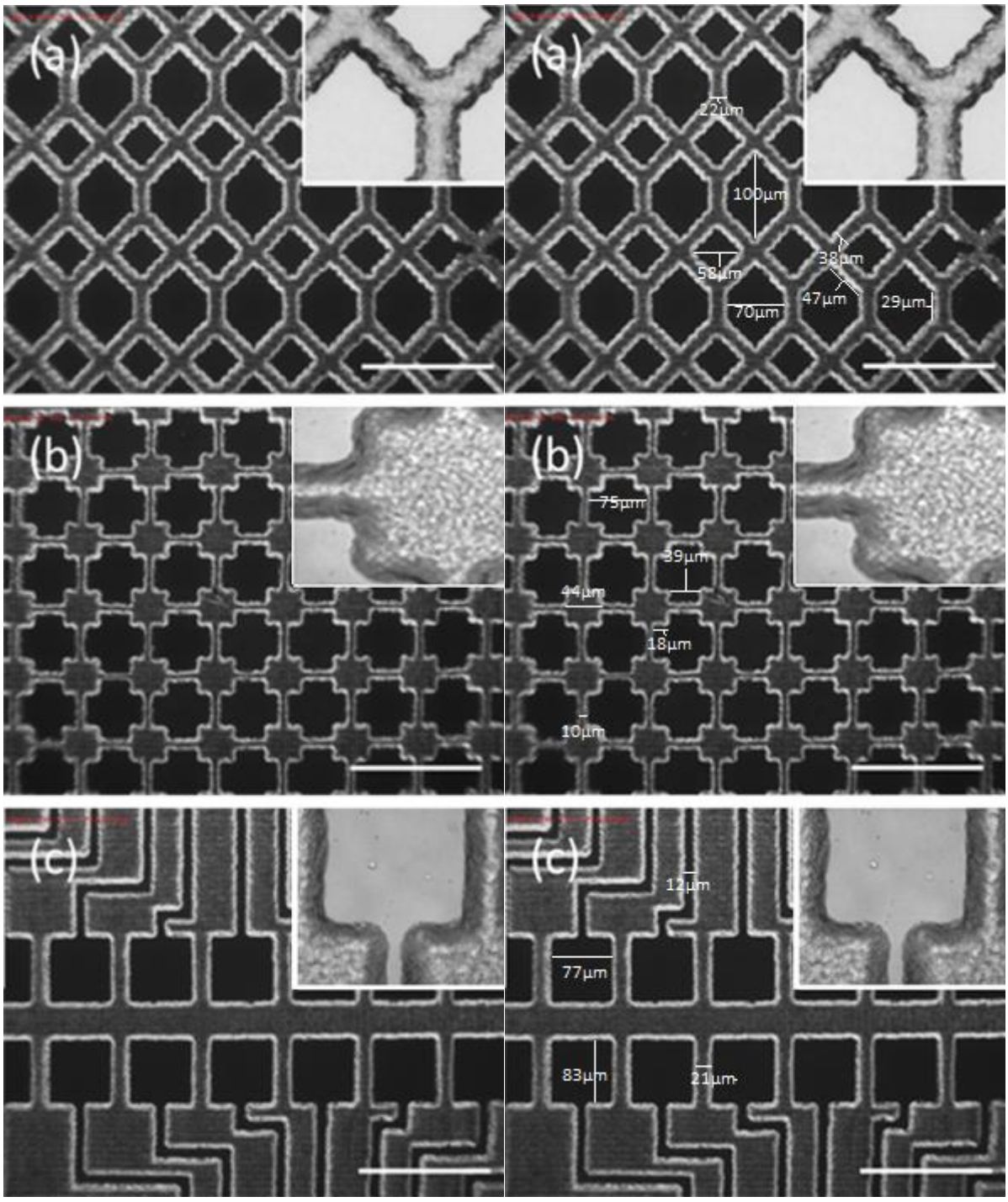

Figure 4.6.2 Analysis of printed wax patterns. Left) Micrographs of printed wax on glass. Right) same image with additional measurements. Magnified light microscopy images are shown in the small frame. Bar = 200 µm.

Initial scalloping behaviour that was present with initial designs, as shown in Figure 4.6.2a, were reduced through optimising the printing conditions. The scalloping behaviour was caused because of the jetted droplets were larger than optimal, meaning that when they were deposited at a droplet spacing of 30 µm, the droplet landed and increased its surface area. Through changing the droplet behaviour (by decreasing the rise time and echo time in the printing parameters of the printing system), the droplet diameter (and therefore the volume) was decreased and when it was used to fabricate the patterns, a smoother finish was created. Figure 4.6.2 shows the print quality of the printed wax patterns after optimisation, which shows features that are smoother and with a higher resolution than previous patterns such as Figure 4.6.2a and Figure 4.6.2b.

4.6.3 Results: Cell orientation studies

Cell adherence to the substrate, shape and orientation have been shown to affect cell behaviour.[225,226] Within Schwarz and Gardel's paper, they describe how cell adherence affects the direction of cell adhesion, their interaction with the environment and neighbouring cells. During normal cell culturing, cells adhere and proliferate randomly within a cell culture environment (normally in a T75 flask). To create cell culture in an orientated environment, additional factors are required to be added to the substrate to allow alignment. Such factors can include biological or physical cues that cells detect and align respectively.[225,227]

Paraffin wax is an inexpensive material that can be used to facilitate cell alignment, which is significantly cheaper than biological factors that could be added to a substrate to promote alignment. Paraffin wax combined with inkjet printing allows a user to create cell culture environments for the study of effects of cell orientation. Initial studies had shown that the width of the area allowed for cell culture greatly influenced their ability to generate orientated cell sheets, and therefore inkjet printed wax environments were investigated.

Initially, cells were added to patterned environments such as those seen previously in Figure 4.6.2. It was shown that cells orientated themselves when cultured in linear channels. Human dermal fibroblasts and RN22 rat Schwann cells were seeded and imaged to show cell compartmentalisation and connection within the wax structures. Figure 4.6.3(a) and Figure 4.6.3(b) show images taken after 24 hours of cell

culture with fibroblasts and Schwann cells, respectively. Cells were too scattered, and with no dominant plane of orientation to align and therefore their orientation remained random. No cells were observed growing across and over the wax structures, showing how this technique was effective at impeding the cell interactions between individual compartments and creating separate environments for collections of cells to grow.

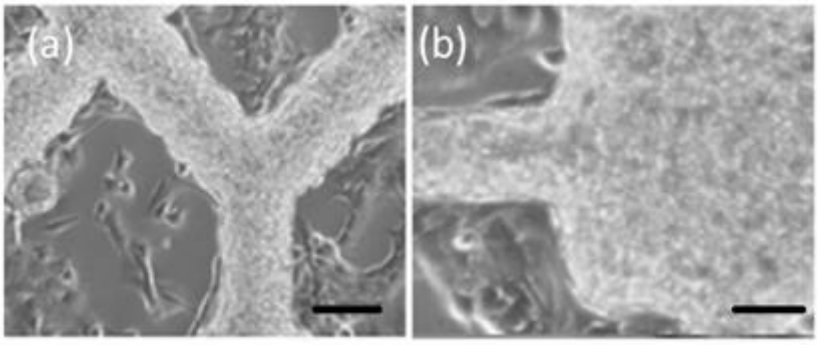

Figure 4.6.3 Micrographs of (a) fibroblasts after 24 hours, (b) Schwann cells after 24 hours. Bars = 50μm and 40μm respectively.

With isolated arrays, cells differentiated in random shapes with no obvious direction (Figure 4.6.3 (a-b)), but when a linear patterned structure was created, cells aligned in the direction of the structure (Figure 4.6.4).

Figure 4.6.4 shows cells aligning to the same orientation as the channel, and through the use of ImageJ software, the orientation of cells could be clearly observed following the direction of the channel. Cell alignment could be investigated with this methodology as in research reported by Duclos et al. (2014), who described how NIH-3T3 mouse embryo fibroblasts aligned on confined strips from 30 μm to 1.5 mm.

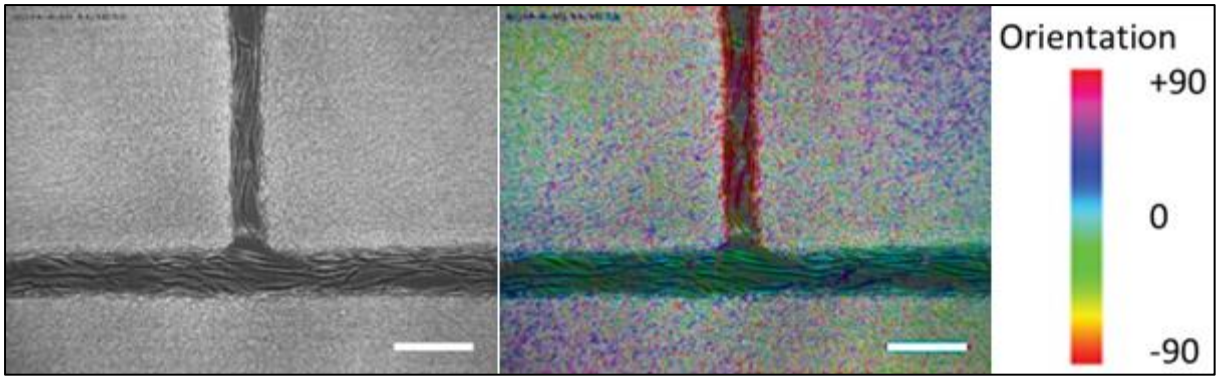

Figure 4.6.4 Microscopy images of cells proliferating in wax patterned environments. Left) a wax pattern where fibroblasts are proliferating and orientating along the channel after 2 days in culture. Right) the same picture after processing with OrientationJ to highlight the alignment of cells within the channel. Channel widths are 40 µm and 60 µm and bar = 100 µm.

Analysis of data had showed cells initially adhered and aligned randomly within the confines of the wax channels with little cell-to-cell interaction. After one or two days, cell population increases due to proliferation, and cells begin to align, from the edges towards the centre.

Figure 4.6.5 shows cells in culture after 3 days, whereby the cells have orientated and aligned with the shape of the wax pattern.

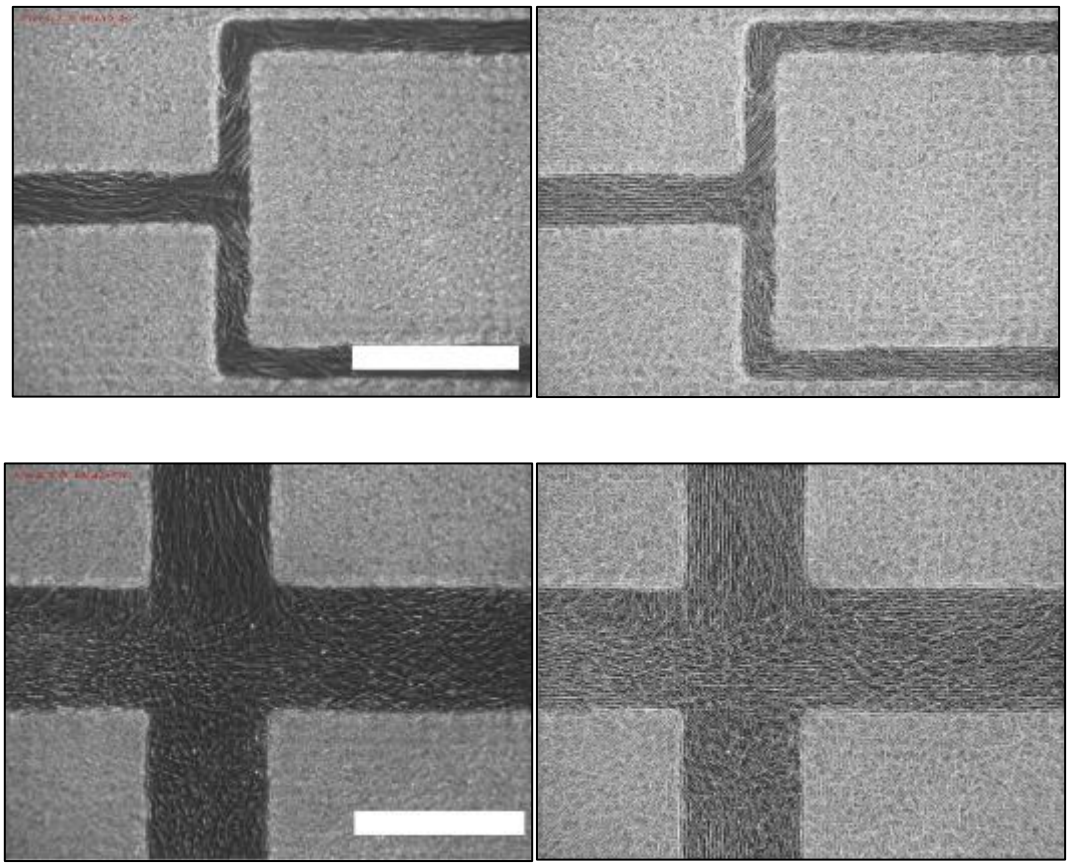

Figure 4.6.5 Microscopy images of cells proliferating in wax patterned environments. Left) fibroblasts grown between wax patterns after 3 days of culture. Right) The orientation of fibroblasts cells are better visualised using OrientationJ Direction. Top) The widths of the channels were 60um and 36um, Bottom) 145um and 135um, respectively. Scale bar = 200um

Previous work from Duclos had also reported cells growing in a constrained environment showed alignment, which became ineffective after a certain width was reached. Figure 4.6.6 gives an example of his work, showing the width of the channels affected the alignment of adhered cells, as it could be seen that channel widths of more than 800 µm did not align cells as effectively. The dynamics of the critical width at which this emergence of order begins to lose itself can be easily studied through the generation of a variety of wax scaffolds for which cells can be seeded into. Using inkjet printing to create variable channel widths from wax is an ideal technology to use, as the prototyping of each device can be done without the creation of a master-mould for each variable, which is a significant disadvantage to non-additive manufacturing techniques that saves resources and time.

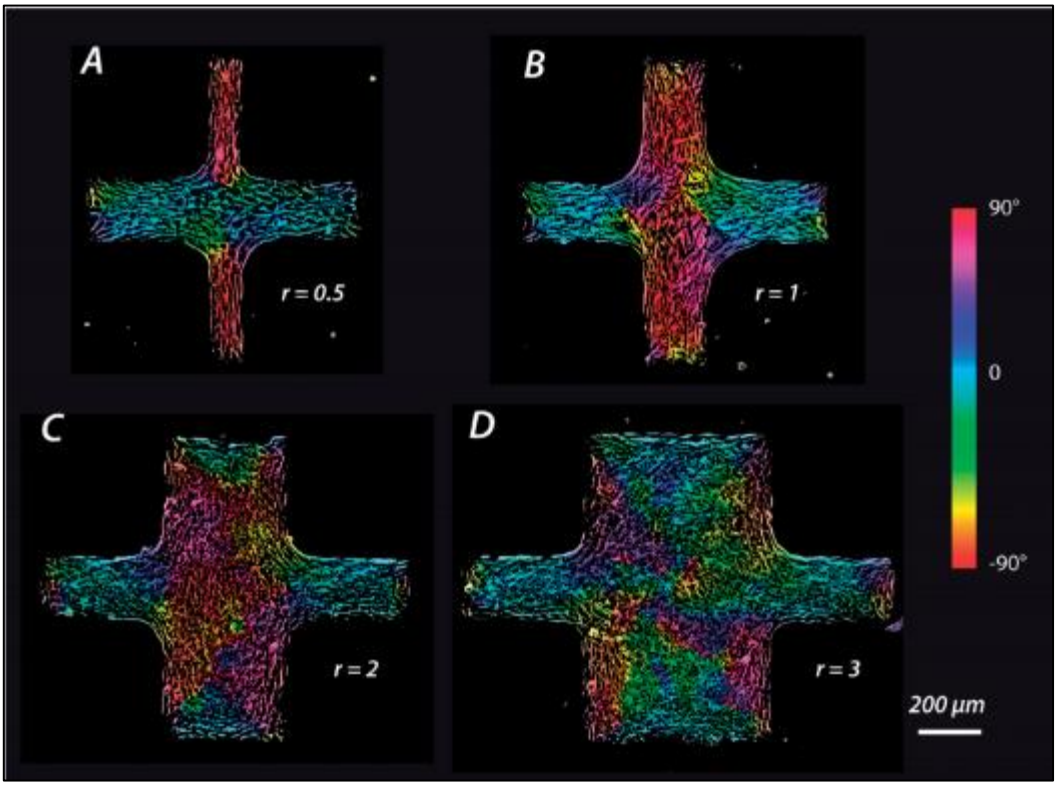

Figure 4.6.6 Cells confined in a cross-shaped pattern. The width of the horizontal arm is kept constant at 200 mm while the width of the vertical arm varies from 100 mm to 600 mm. (Colour codes show the cellular orientation). r is the ratio of the width of the vertical arm to that of the horizontal one. The central part of the pattern is perfectly oriented in the first three situations. Depending on r, it is either the vertical or the horizontal arm that imposes its orientation. In situation B, the orientation is dominated by the horizontal or vertical (as illustrated here) arm with equal probabilities. Image taken from Duclos.[197]

After fibroblasts or Schwann cells were seeded, they adhered, spread and thereafter differentiated into the desired positions and orientation. Figure 4.6.7 shows light and confocal images of the fabricated wax structures, patterned cells. Cells maintained their position and orientation for at least 7 days after seeding as shown. Figure 4.6.7a shows an area of the glass substrate where wax was inkjet printed. Figure 4.6.7b shows confocal microscopy after 2 days of cell culture. Figure 4.6.7c shows cell culture after 7 days in a wax patterned environment and Figure 4.6.7d shows the same sample under a confocal microscope.

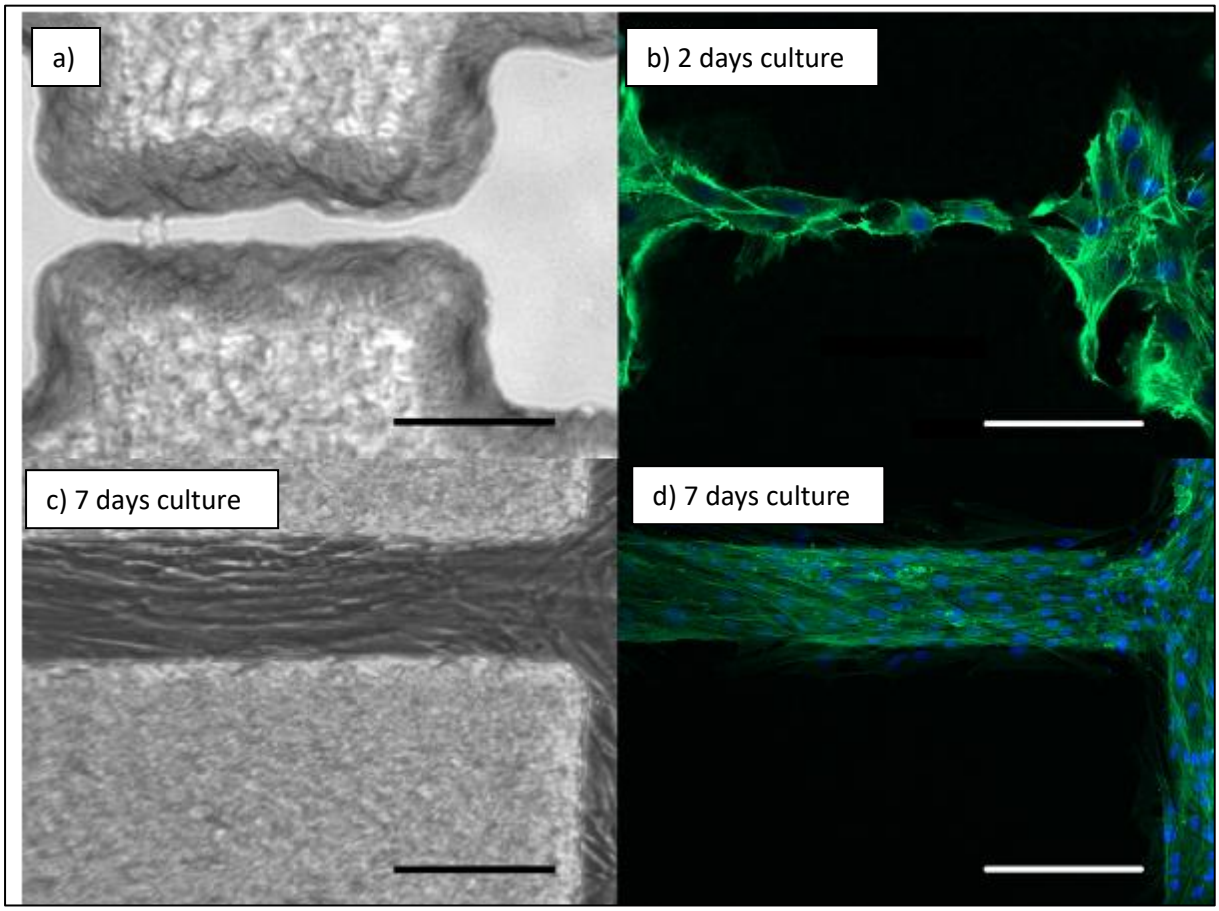

Figure 4.6.7 Light microscopy and confocal micrograph images that showed Schwann cells differentiated and aligned between two compartments through an open channel (bar a-b = 100 µm, c-d = 200 µm); (a) printed paraffin wax on glass; (b) confocal image after 2 days of Schwann cells cultured on wax structures, stained for actin (green; phalloidin-FITC) and nuclei (blue; DAPI) and with the wax removed; (c) Schwann cells differentiated and remained within the confines of the wax structures, with the channel width that spanned several cell widths; (d) confocal image of Schwann cells after 7 days of culture, cells were seen firmly adhered and aligned with the orientation of the channel. Stained for actin (green; phalloidin-FITC) and nuclei (blue; DAPI). Channel widths averaged 30 µm (i.e. the confines of the wax).

To summarise, initial seeding of low numbers of cells show that they adhere and differentiate in the confines between the wax patterns. They align randomly when they have little contact with neighbouring cells, with some align to the orientation of the edges of the wax. Over time, cells differentiate, increasing the cell density in the sample, and cells begin to align, from the edges towards the centre.

This dynamic reorientation, not seen in control samples with non-confined environments, can be postulated to be caused by the restriction of differentiation caused by the wax as a physical constraint. When channel widths are wide (>800 μm), alignment degrades and is most evident in the centre of such patterns, as the propagation signals for alignment are weakest further away from the leading edge of the wax confines. In summary, narrow width channels produce highly ordered and aligned cell patterns, whilst broad channels produce a steadily degraded order of alignment which is most apparent at the centre of such channels.

4.7 Removal of Wax Structures

4.7.1 Introduction

As shown in the previous section, cells are able to orientate themselves within confined environments. The ability to remove the restrictions imposed by the patterned wax allows for the study of cell behaviour, from a restricted environment, to a non-restricted environment. Cell motility, behaviour and their alignment can be studied. Such experiments can enable better understanding of cells proliferating into a new space from their native environment i.e. in wound healing of skin and the relation between cell elongation and their effects on developmental studies in tissue morphogenesis.[228] The skin has an ordered structure, and when the skin is damaged, cells and tissue is lost. The body is able to repair the skin through reepithelization whereby cells proliferate into the wound and is able to remodel the damaged tissue.[229] This is just one example of how the study of cells proliferating from a restricted environment and into a non-restricted environment is useful.

Cells were cultured to varying confluences inside the wax patterned samples, and had the wax removed and the cells analysed at different time points, with accompanying light and confocal images for

analysis. The percentage of cells that remained after wax removal was calculated by counting the cells before and after wax removal.

4.7.2 Results: Varying channel widths

A range of wax channels were fabricated, with fibroblasts adhered and grown into the desired density prior to wax removal. Channel widths ranged from 50-200 µm, and cell density varied from 0-800 cells/mm^2. Cell density was calculated through counting the total number of cells in a set area, from light microscopy images taken during the analysis of samples. Figure 4.7.1 shows how cells behaved when the wax was removed. In Figure 4.7.1, a channel width of 115 µm was created, and had cells grown to a cell density of 200 cells/mm^2. Upon wax removal, 85% of the cells remained attached onto the glass substrate. It can be seen that the cells that were closest to the wax were removed.

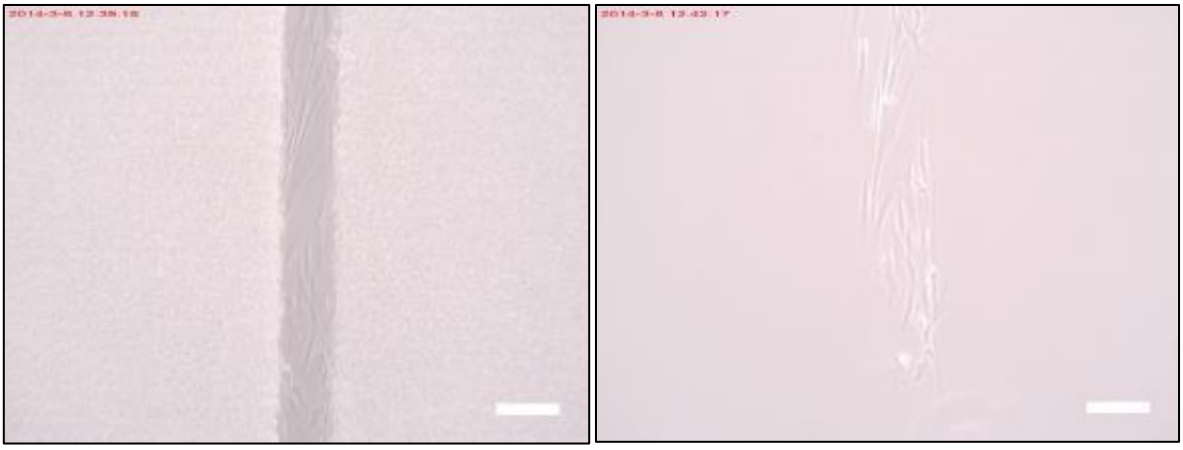

Figure 4.7.1 Cells proliferating within the confines made with patterned wax. Area = 0.1 mm^2, width 115 µm, total cells remaining after wax removal = 85%. Showing example of when wax removal displaces very little cells (fibroblasts), due to the cell concentration on the surface being around 200 cells/mm^2, and having a channel width of 115 µm. Scale bar = 100 µm

In Figure 4.7.2, this idea that cells closest to the wax were removed is amplified, as the majority of cells are removed when the channel width is very narrow. The results showed that the majority of wax structures with channel widths of less than 90 µm would have <20% of cells remaining adhered on the glass surface upon wax removal. Figure 4.7.2 shows an example of wax removal with a wax structure with channel widths of 55 µm and having a cell density of 441 cells/mm^2.

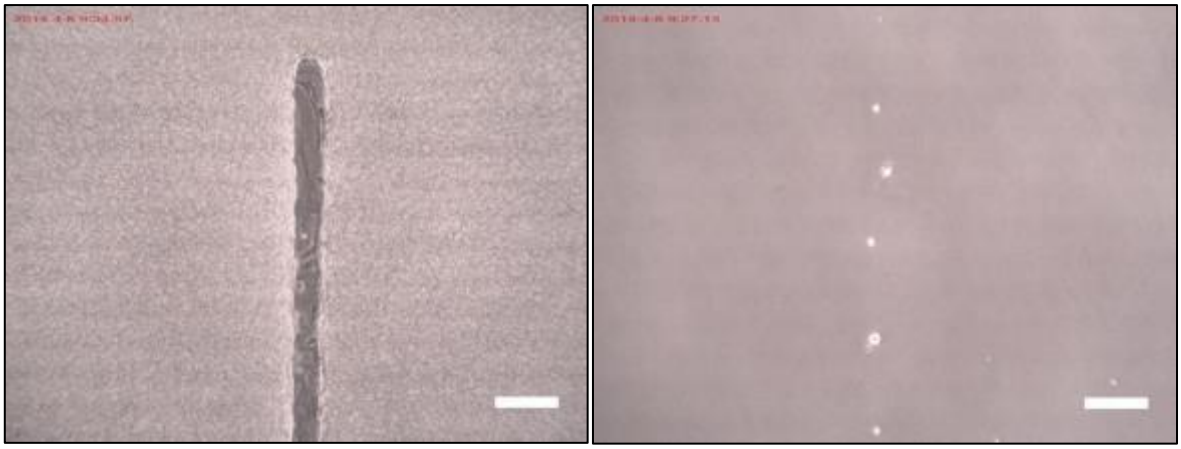

Figure 4.7.2 Light microscopy image showing a 55 µm wax channel with fibroblasts seeded into the substrate. The majority of cells detached when the wax was lifted off. Around 441 cells/mm^2. Scale bar = 100 µm

Given that a typical cell (fibroblast) can be 20-30 µm in diameter, around 3 cells could adhere side-by-side to one another, of which cells at the periphery would adhere to the wax. During wax removal, the peripheral cells have the tendency to also be detached along with the wax. When the width of the channel is comparatively wider, the proportion of cells adjacent to the wax is fewer and more cells will remain after wax removal. Given the variation of cell size, shape and adhesion strength to different substrates and to neighbouring cells, only a general trend can be determined; decreasing the channel width causes an increases in cell removal during wax removal.

4.7.3 Results: Varying cell concentration prior to wax removal

Given the width of the channel which cells proliferate in can affect the number of cells removed when the wax is removed, the cell population was also studied. Cell concentration plays a significant role in the proportion of cells that are removed during wax removal. When cell concentrations were below confluency cells not at the periphery near the wax structures would remain attached on the substrate during wax removal, and cells at the periphery would be removed if they adhered onto the wax.

An interesting finding occurred when cell density reached and went above confluency (>400 cells/mm^2). Under normal light microscopy, it is not possible to view what is underneath the wax, as the wax blocks light and therefore the details underneath it. Confocal microscopy was employed, and shows that when cell density was high, it could be seen that cells grew underneath the wax patterns (Figure 4.7.3). Figure 4.7.3 shows an image, whereby the brightest areas were where wax was not

present. There are fibroblasts seen to be in a darker shade than neighbouring cells, which are underneath the wax.

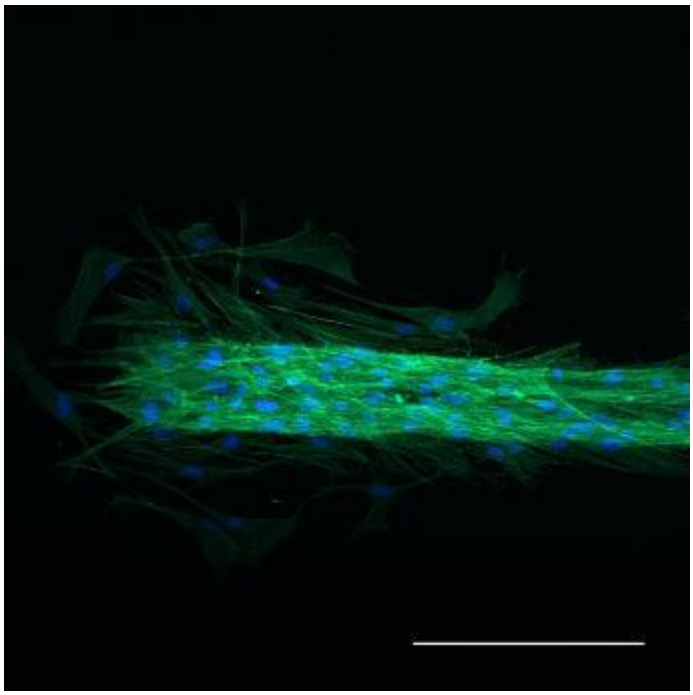

Figure 4.7.3 Confocal micrograph image that shows fibroblasts cultured on a glass substrate. Stained for actin (green; phalloidin-FITC) and nuclei (blue; DAPI). Channel widths averaged 30 µm (i.e. the confines of the wax), with cell density of around 850 cells/mm^2. Scale bar = 100 µm

Further experiments were carried out to determine the ability for cells to grow underneath the wax, and the effects of wax removal with respect to the adhered cells. Figure 4.7.4 shows an extreme example of culturing cells for 10 days, increasing the cell density to >900 cells/mm^2. All cells that were confined into the open space made by the wax were removed. This is an example of a very high cell concentration with a width of 175 µm, the cells were attached to one another to create a uniform film together and when the wax is removed, the whole layer of cells also detach. What remained were cells that had infiltrated between the wax and glass substrate. These results show the ability for fibroblasts to be able to overcome the strength of the wax-glass interaction and proliferate throughout underneath the glass.

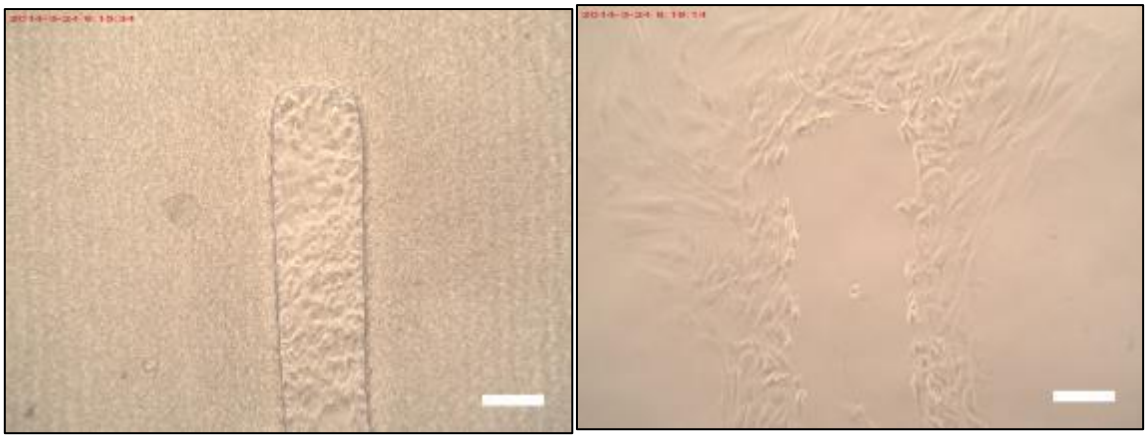

Figure 4.7.4 Cells (fibroblasts) growing on a glass substrate being restricted by a wax structure. Upon removal of the wax, the layer of visible cells within the 175 µm channel are also lifted off, but what remains are cells that have differentiated between the glass and wax. Scale bar 100 µm

When cells were sufficiently confluent (approx. 800 cells/mm^2), upon wax removal, it was possible to create an outline of where the cells used to be cultured, with cells remained adhered at the edges of where the wax used to be (Figure 4.7.5). This has the potential to be an alternative method to create very high resolution micropatterned cell constructs for complex co-culture (when combined with another layer of seeded cells) and cell-cell studies.

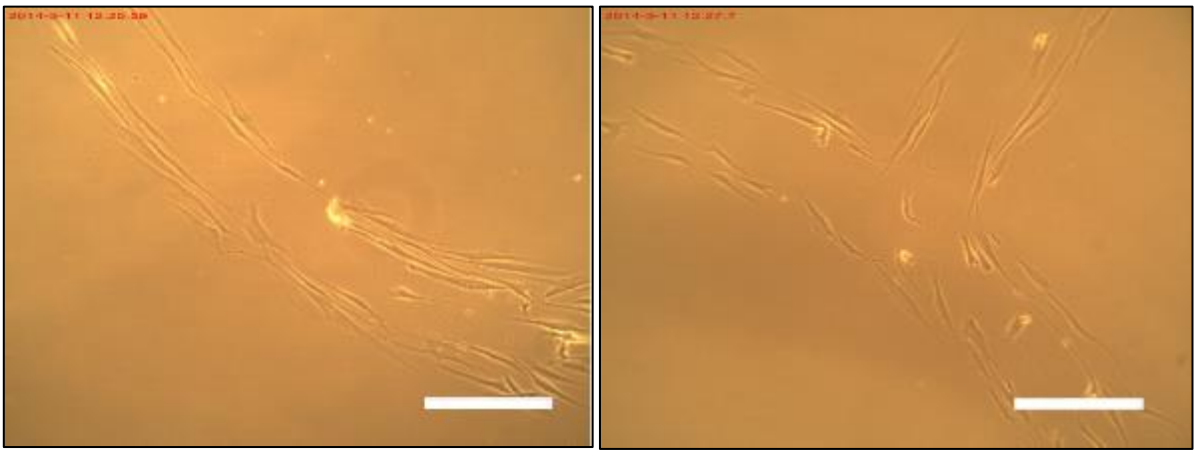

Figure 4.7.5 Images of remaining cells after removal of wax on samples that had overconfluent cells on the surface. The outline of the wax can be clearly seen. Left: curved wax structure from top left leading to bottom right. Right: three channels joined at the centre, with channels coming from top right, left and bottom right. Scale bar=100 µm.

This phenomenon of cells detaching upon wax removal was speculated to happen due to the deposition of extracellular matrix (ECM) over time by adhered cells. Adherent cells steadily produce ECM in their surroundings, making it more favourable for cells to grow and differentiate. Over time, this ECM can

grow and allow neighbouring cells to connect together, and on the wax, forming a cell-friendly layer which allows the cells and wax to interact. When samples were overconfluent, cells have a very strong interaction between each other, the ECM they had produced, and the wax. Therefore, upon wax removal, the whole sheet of cells also detach along with the wax. Due to the confines of the wax and the constant steady differentiation of cells on a restricted environment, there comes a point whereby all available space gets taken up. Cells are then forced to grow between the glass and wax, and deposit ECM in the process.

Upon wax removal, cells that have grown on the ECM attached to the wax are also removed. This can have a cascading effect and cause more cells to be removed that were also interacting with the ECM and adhered cells. Cells that have grown underneath the wax do not get removed and remain attached to the glass (Figure 4.7.4 and Figure 4.7.5), as the underlying cells are not bound to the wax through the ECM.

Just under 100 samples were recorded and analysed in total, and their data plotted in a form of a chart to visualise how cell density and channel width affected the number of cells that were detached during wax removal (Table 4). Channel widths of 111-200 mm showed the most number of cells remaining after wax removal, when cell concentrations were below 500 cells/mm^2. Within these parameters, cells could be seen to align with the orientation of the wax, and they were not all connected with neighbouring cells; upon wax removal, no "daisy-chain" effect occurred and isolated areas of cells around the periphery would be removed and not the whole population of cells. When the channel width was less than 90 mm, there were a greater proportion of cells around the periphery, and therefore it was found that $\geq$60% of cells were removed along with the wax when the wax was removed. Generally, when the cell population reached above 500 cells/mm^2, there were significant cell-to-cell interactions with all neighbouring cells, that upon wax removal, all cells were removed, regardless of channel width. Within the table, cell densities of 701-800 cells/mm^2 shows a negative imprint of the wax as a means to describe how cells are completely removed within the confines of the wax structure, however cells remain where they have proliferated underneath the wax (as shown in Figure 4.7.4).

Table 4 shows how the percentage of cells remaining after wax removal is different depending on the width of the channel and concentration of cells. Note: Negative = all cells in the open space created between the wax pattern were removed, and what was left were cells that differentiated underneath the patterned environment (i.e. Figure 4.7.4 and Figure 4.7.5).

Density (cells per mm^2)

Width (mm)	<100	101-200	201-300	301-400	401-500	501-600	601-700	701-800
51-60								
61-70								
71-80								
81-90								
91-110								
111-140								
141-170								
171-200								

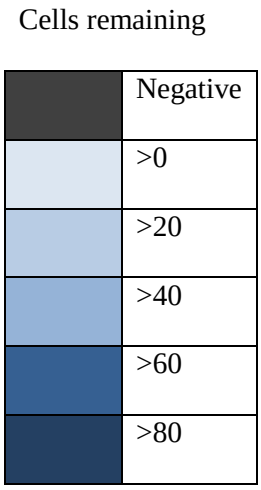

Cells were able to remain attached onto the substrate even after wax removal. An exception to this occurred when cell concentration exceeded confluence. From this study, when cell density began to reach confluency (typically more than 300 cells/mm^2) an increased proportion of cells detached. All cells within the scaffold were removed when cell density reached above 700 cells/mm^2. It is important to note that cells deposited in this way show a high level of alignment to the direction of the channels.

The width of channels affects the proportion of cells that are in contact with the wax substrate; the smaller the width, the more cells are in contact with the wax per unit volume. Cells near the wax start to produce extracellular matrix components over time, that can interact with the wax, making the surface of the wax adherent to the cells, leading to cells attaching onto the walls of the wax, and becoming detached from the glass substrate upon the removal of wax. High cell concentrations through longer incubation times with the wax substrate on a glass surface allowed us to measure the effects of varying the cell concentration during the removal of wax. At low concentrations, the majority of cells that adhere

to the substrate have weak or no cell-cell interactions with one another due to limited cell-to-cell interactions with one another (Figure 4.7.1).

The least amount of cells that are removed is from a concentration of 400 cells/mm^2 and with widths of more than 90 µm. Cell counts that were more than 700 cells/mm^2 showed that over this cell concentration, cells began to grow underneath the substrate and when the wax was removed, only these cells remained on the sample. These findings show another method of cell patterning is possible, whereby the wax can be used to create the positive image of the pattern required, and have the wax removed after the cell population has reached >800 cells/mm^2. When cells become over confluent, with nowhere else to differentiate, they are able to edge their way between the glass and wax to continue to differentiate over time. This could be considered a limitation of this study; as the extracellular matrix deposited caused the cells to adhere on the wax.

4.8 Cell migration after removal of wax

4.8.1 Introduction

After wax was removed, the cells were seen to continue to differentiate, and encroach on the newly available open space, which gave environmental conditions that allowed the study of how cells behave as they transition from a restricted enclosed space, to an open environment.

Cells were cultured in wax channels to the desired cell density in wax channels until cells grew and aligned with the wax patterns. The wax was removed to leave adhered, ordered cells on the glass substrate. These cells were then analysed over several days to determine cell differentiation.

Wax scaffolds with channel widths of 40 µm and 30 µm connected together at one end were created and fibroblasts were seeded into the wax structure and cultured (Figure 4.8.1). The wax was removed with a scalpel and the same area was captured with a light microscope over a period of 3 days.

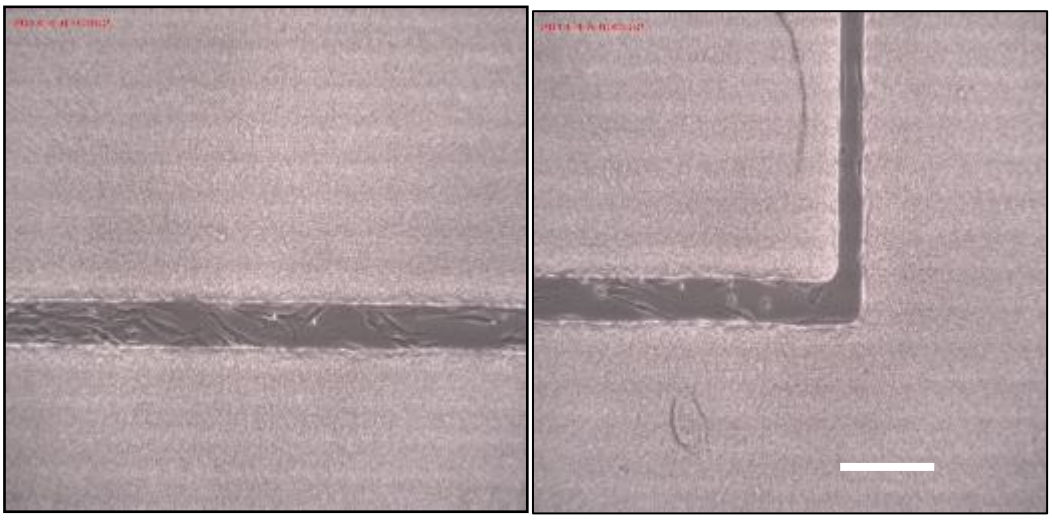

Figure 4.8.1 Wax scaffolds that were made for experiments regarding how cells behaved after wax removal. Scale bar = 100 µm.

4.8.2 Results

Figure 4.8.2 shows what happens when patterned cells were allowed to differentiate on bare glass, after the confines of the patterned wax were removed. Quantitative data was difficult to collect as the field of interest could be difficult to relocate after each day of culture. Qualitatively, it is clear that cells grow steadily, until a critical cell density is reached, and after which, cell density quickly exponentially

increases. This is caused by the gradual improvement of the culture environment as cells interact more with neighbouring cells and deposit more ECM, which are key signals that promote cell differentiation. With respect to the culture of fibroblasts, the orientation and pattern originally formed by the cells is steadily lost over time, as cells differentiate in more and more random directions, with no dominant orientation.

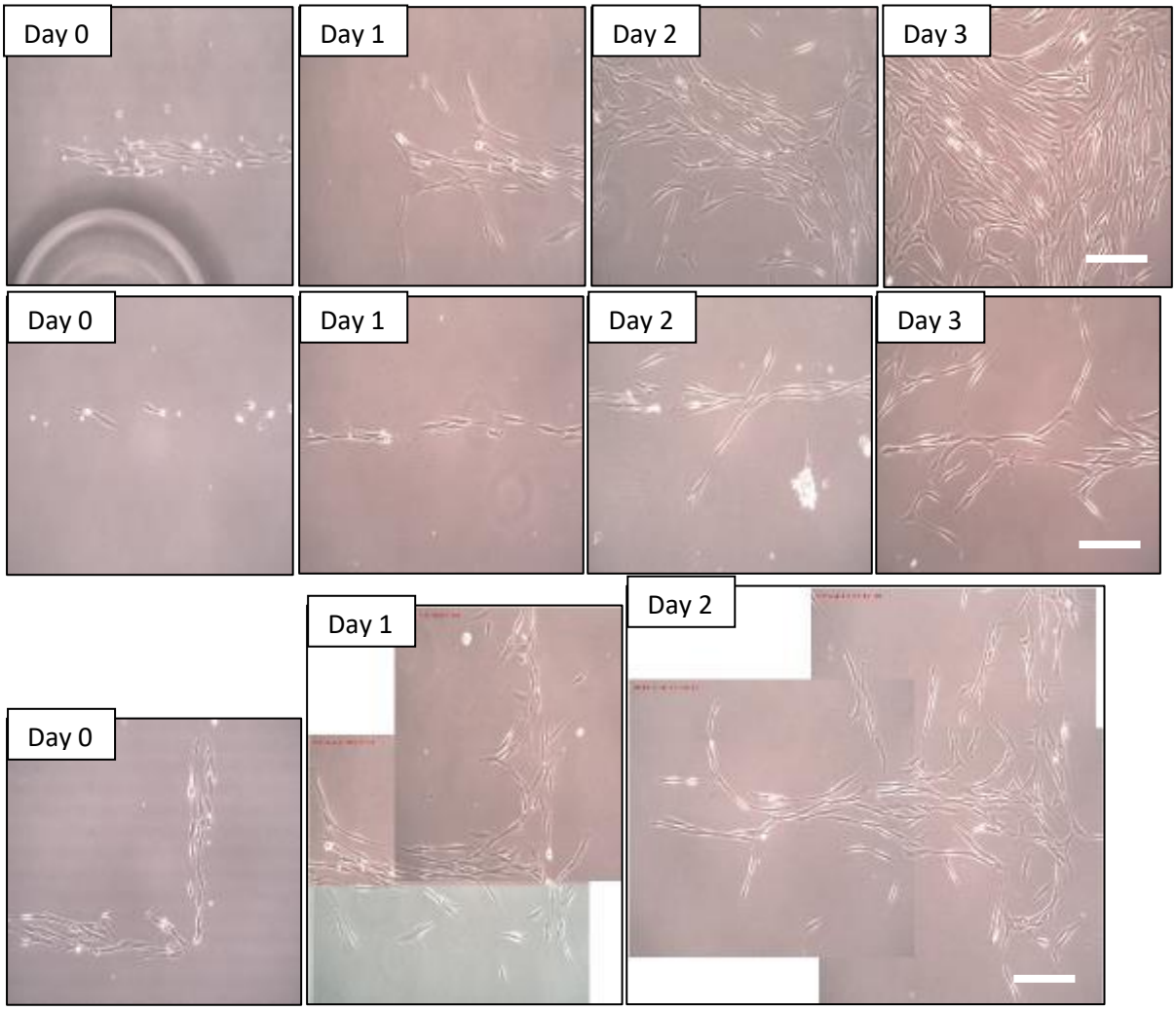

Figure 4.8.2 Three sets of microscopy images of fibroblast cell patterns after wax removal. First image shows cell patterns immediately after wax removal, and each subsequent image were taken 24hrs after the preceding image. Scale bar = 100 µm

The quantitative data can be better visualised through adding a filter to colour-code the orientation of the cells. Figure 4.8.3 shows microscopy images after being processed with OrientationJ. After the wax was removed, there were no more physical restrictions to the growth of cells, and they differentiated randomly to their surrounding area. Through analysing the behaviour of individual cells, it can be seen that each have a different differentiation rate. This is most obvious in Figure 4.8.3 (c) with cells

highlighted in yellow and red projecting distinctly away from the main body of cells. If all cells had the same cell cycle and differentiation rate, it would be seen that the migration of cells would be spread across the surface of the glass evenly. However it can be seen that there are certain spear-like protrusions that develop after each progressive day. This shows that certain clusters of fibroblasts grow at different rates, which supports the idea that cells differentiate more readily when there are more cell-to-cell interactions available. The increased cell-to-cell interactions allow cells to receive more stimulatory extracellular signals from neighbouring cells and thus stimulates cell proliferation.[228]

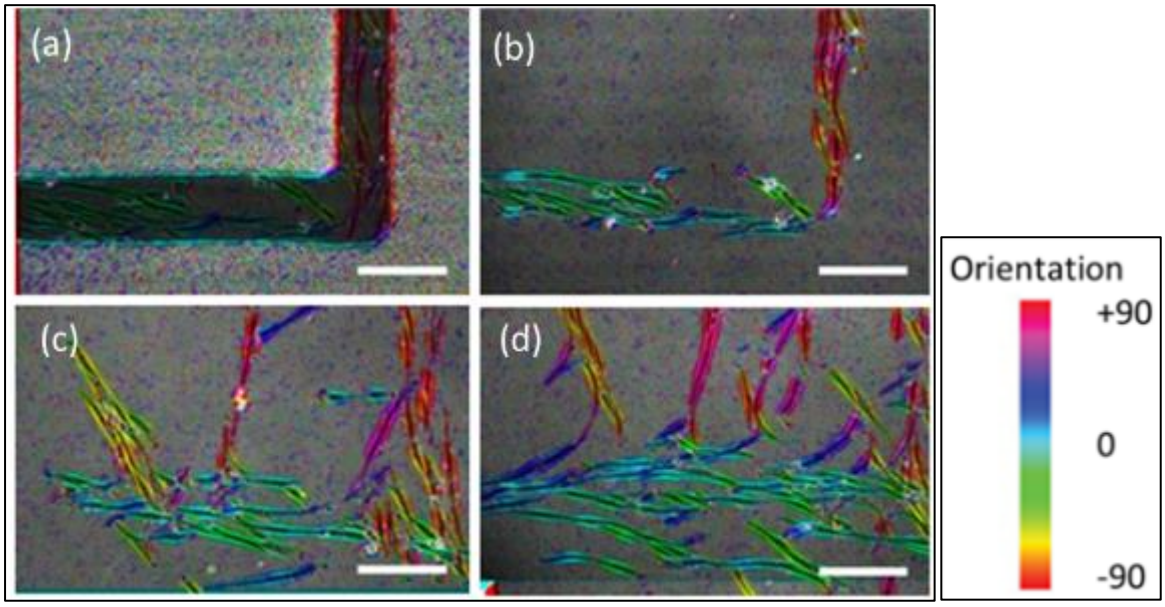

Figure 4.8.3 Micrographs having being processed with OrientationJ to highlight the alignment of cells. (a) fibroblasts aligning within wax structures, (b) immediately after wax removal, (c) 24 hours and (d) 48 hrs after wax removal taken in the same sample regiona of interest. Bar = 50 µm.

Cells that were patterned to predetermined shapes gradually lost their conformity over time, if there are no physical restrictions surrounding them. The removal of the paraffin wax was easy to accomplish using a sharp scalpel, although a percentage of cells were lost during this process (as discussed in the previous section). Different patterned aligned cells were examined, and showed that the restrictions created from the wax were lifted, cells differentiated and spread away. This differentiation is not an even distribution, and areas with more cell-to-cell interactions differentiated at a quicker rate than more

isolated clusters of cells. Carefully patterned cell shapes were lost within a few days after wax removal, as cells differentiate and spread into the available space on the glass substrate.

4.9 Conclusion

The use of paraffin wax for biologically relevant applications were studied. Wax behaviour under printing conditions was analysed and the optimal parameters were identified that allowed the creation of very fine resolution scaffolds. Upon optimisation, channel widths of 3.5 µm could be created with the inkjet printing system. This resolution has not been achieved before without the use of additional factors such as adding a hydrophobic coating through lithographical techniques combined with inkjet printing.[230] The flexibility of being able to create different structures through using inkjet printing (an additive manufacturing technique) without the use of moulds is beneficial to reduce waste.

Microfluidic devices have been shown to be successfully created with the use of printed wax, and can be made to fabricate different structures "on-the-fly". Such devices, when combined with biological markers, would be ideal for diagnostic applications; they would be readily disposable and an extremely small volume of fluid would be required for testing.

The ability to print progressive layers on top of one another allowed the creation of 2.5D structures. The possibility of creating micro-wells was studied, and with the addition of using a biocompatible material (wax) cell aggregates can be cultured in such environments. For private companies such as Cyfuse and Organovo, this would allow more spheroids to be created in a single well plate substrate, saving on costs of consumables such as the well plates used and cell media.

Paraffin wax was used to act as a physical barrier that guided neurite growth by restricting where the neurites could expand to within a given culture environment. When the wax droplets were merged together to create a uniform structure, cells could proliferate in the negative spaces between the wax. The confluency of the adhered cells and the width of the channels created by the wax determined the level of alignment of the cells with respect to the orientation of the wax.

When the wax was removed during cell culture, a proportion of cells would detach with the wax. A concentration of 400 cells/mm^2 and with widths of more than 90 µm showed the least amount of cells being detached during wax removal. Cell counts that were more than 700 cells/mm^2 showed that over this cell concentration, cells began to grow underneath the substrate and when the wax was removed, only these cells remained.

Cells proliferated normally after wax removal, and proliferated from a highly arranged pattern, to a disordered culture environment. The original pattern which the cells maintained within the wax pattern was quickly lost within 48 hours of cell culture. It was identified that pockets of cells were able to proliferate quicker than others, and it was suspected that this was due to more cell-to-cell interactions with one another that enhanced proliferation.

5 CREATION OF PHANTOMS

5.1 Overview

Understanding blood flow through vessels within the body is an important aspect to understanding rheological flow. Through replicating medical conditions with *in vitro* systems, we can study and analyse blood flow behaviour for healthy individuals as well as for medical conditions such as strokes and aneurisms. The flow behaviour is different between smooth vessels and expanded vessels caused by ruptures and understanding such differences can promote better care. A stroke can occur when there is a blockage within a blood vessel in the brain that causes the brain tissue to become oxygen deprived further down the vessel as the blockage prevents oxygenated blood to travel to where it is needed. An aneurism is a condition termed for the ballooning of a blood vessel, which can lead to the rupture of the blood vessel.

Currently there are a lot of computational simulations to study blood flow, and there have been experimental models for the study of ultrasound techniques, stent and haemorrhagic simulations.[231,232]

Computational simulations have provided very useful data within the research of medical phantoms.[233] With the biggest advantage of performing a simulation being the reduction in cost. Through the use of simulations, the retesting and changing of variables can be done cheaper and faster than real life tests. Compared to traditional real life experiments, simulations allow unprecedented ease to simulate an infinite amount of versions of aneurisms through manipulating the virtual model on software such as SOLIDWORKS. Variables can be changed with ease i.e. flow rate, viscosity of fluid, size of aneurism, diameter of vessels, elasticity of vessels.

The second advantage of simulations is that the data generated can be more detailed than real life experiments; as some factors may not be readily measurable in real life (e.g. the probe, or the means to measure the result, can skew the data). With respect to medical phantom simulations, such data can include the ease of generating data points at all areas within an aneurism (i.e. wall shear stress), the

analysis of pressure, the miniscule detail to track each particle through the aneurism is a factor which cannot be done with fluid in real life.

However, simulations are only as good as the knowledge of the experiment the user has. This means that simulation errors can be significant if not all factors that can affect the experiment have been considered and applied. In order to give simulation results credibility, a control experiment is required to confirm that the results generated in the simulations are comparable to real life. The control experiment would be required to be real life experiments, which leads to the second disadvantage of simulations; that they are simulations. Simulations require real life experiments for validation, but not vice versa; therefore some consider simulations as unnecessary.

A method of studying aneurisms, and other rupturing of bodily vessels can be achieved through the use of flow phantoms; a type of medical phantom that is specifically designed for the study of rheology. Flow phantoms offer a range of advantages not available with *in vitro* studies, such as repeatability and control.

However, the cost of flow phantoms can be very expensive, with commercial Doppler flow phantoms costing approximately US $6,000 and rheologically similar blood-alternatives costing US $500 per litre in 2010.[234] There have been many experimental alternatives, which cost a fraction of commercial product; investment casting techniques,[235] silicone elastomers and stereolithography are popular with the fabrication of phantoms.[236,237] Within the range of flow phantoms, the more the phantom resembles its native counterpart, the more effective the study is in replicating function and reaction. There have been more interests with more "organic" aneurisms[238] compared to traditional geometrical approximations of vessels.[239,240] Both stereolithographic and 3D printing techniques are well suited for the creation of native vessel geometries. Stereolithography and 3D printing allow the creation of scaffolds with the appropriate resolution and size, having been used to create an opaque portal vein pattern that could be used with ultrasound to study rheological flow.[241]

The method that is proposed within this chapter allows the user to create flow phantoms by printing patterned wax resembling vasculature for a wax-loss method (a form of investment casting using wax)

combined with polydimethylsiloxane (PDMS). This is a multi-step process, but does not require a skilled user and there is minimal use of wax due to the volume of casting wax required. This method is most suitable for the study of vessels within the scale of 1,000-100 μm, with any size of aneurism. When the vessel size is smaller than 100 μm, the roughness of the interior of the vessels become a significant factor, in which case other fabrication techniques such as stereolithography[242] would be more suitable as they produce a smoother interior finish. The aim of this work is to devise a cost effective and efficient framework for developing native-like vasculature flow phantoms with a range of sizes for aneurisms anywhere along the vessel.

In the first step, a negative model of the vessel is fabricated by inkjet printing wax on a glass substrate. Polydimethylsiloxane (PDMS) was used to cover the negative model and left overnight to cure. The next day, two holes were pierced into the PDMS mould, which would then be placed into an oven at 80°C and the wax was removed. Afterwards, a solution with fluorescent micro beads was aspirated into the phantom with a steady flow provided by a syringe pump and a confocal microscope was used to analyse the flow of microbeads.

5.2 Results

Figure 5.2.1 shows the placement of the molten droplet of wax on top of the printed line, prior to the creation of a phantom. Different shapes were made and were created by how quickly the wax solidified and how the wax was pipetted; by gently pipetting the wax on top of the wax line, the amount of merging with the wax line and wax droplet can be controlled to create large and small aneurisms.

The vessels were printed and measured around 250 μm in diameter, whilst the aneurisms had varying diameters, ranging from 3-6 mm. To complete the phantom, the samples were submerged in PDMS, cured overnight, cut out using a scalpel and the wax removed through heating the sample to 80°C for 15 minutes and the molten wax was extracted by a syringe.

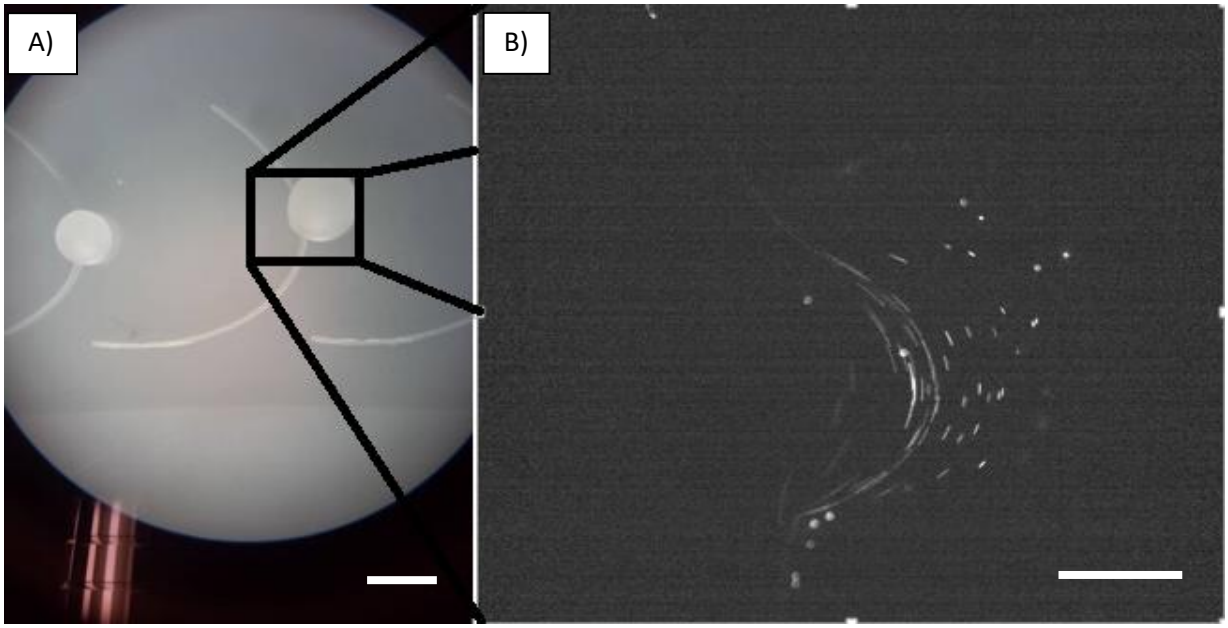

Figure 5.2.1 A 3D representation of how the shapes shown in Figure 5.2.2 were created. A) The molten wax droplet was pipetted on top of the wax line, and depending on how fast the molten wax solidified determined the final shape investigated. B) Flow of fluorescent micro beads through the phantoms created in part by inkjet printing. Flow is faster in the inner curve of the phantom compared to the outer curve, as shown by the speed distortion from the fluorescent microbeads travelling at the inner curve of the phantom. Scale bar = 3 mm and 1 mm respectively

Different sized phantoms were created and analysed, as shown in Figure 5.2.2; ranging from slightly inflated, to a more prominent distention of the aneurism. These distensions were caused by how the molten wax was pipetted onto the printed wax line (Figure 5.2.2A). If the molten wax was pipetted with more pressure, the molten wax would move across the substrate more and interact with more of the wax line and the flat surface of the substrate, creating a more distorted final shape (Figure 5.2.2C). It is hard to ascertain the size and shape of the phantoms with just still 2D images alone. The shapes determined in Figure 5.2.2 were calculated from examining several hundred consecutive images to resolve the paths the fluorescent micro beads travelled and plotting the vessel dimensions (Images can be found in the Appendix Two).

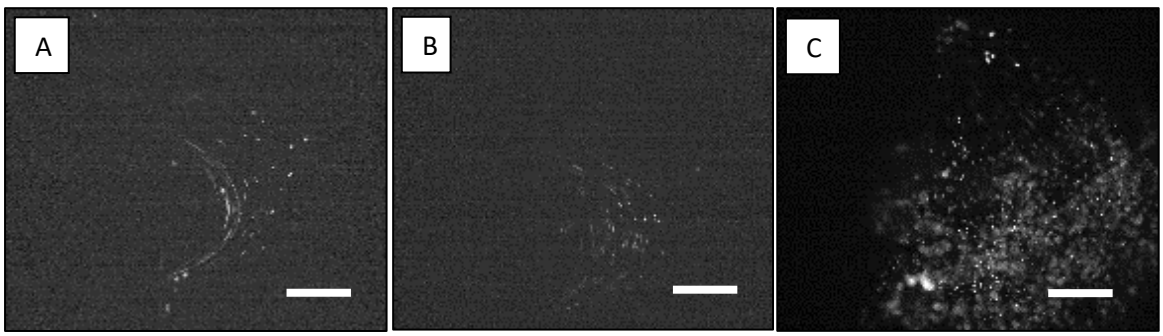

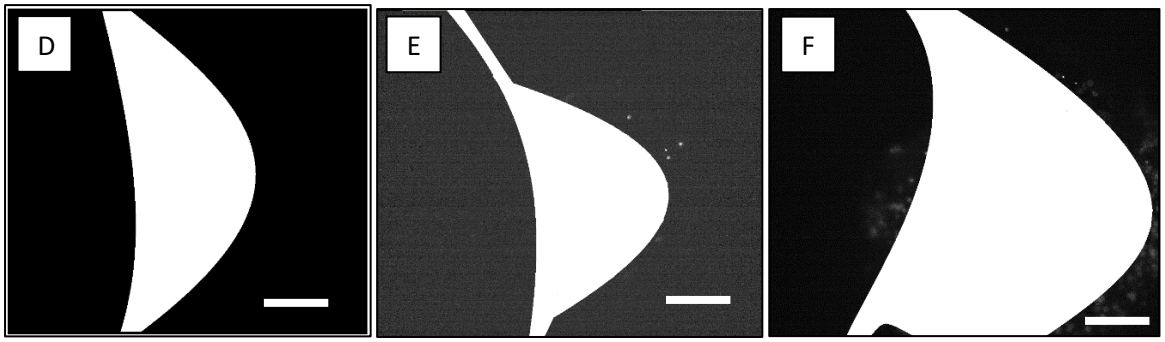

Figure 5.2.2 Phantoms created with inkjet printing and wax-loss method in PDMS. (A-C) showing epifluorescent images of phantoms created using inkjet printed wax and pipetted wax. (D-F) Showing the depiction of different channel shapes that were tested fabricated with inkjet printed wax-loss with PDMS. The original image was edited with Paint to make the contrast between the open area and PDMS clearer. Scale bar = 1000 µm

The different resulting phantoms that were fabricated created interesting fluid behaviour. Using the Manual Tracker Plugin from ImageJ, individual beads could be tracked through the video set that was captured for each phantom created to give an indication of flow and behaviour; as shown in Figure 5.2.3 (original set of images) and Figure 5.2.4 (images + overlay with Manual Tracker). A general trend can be seen with the phantoms that were tested; the fluid containing the florescent microbeads travelled through the phantom quickest through the shortest distance and travelling from the vessel to aneurism decreased the velocity of the beads the most travelling at the outer areas of the phantom. Microbeads flowing through the inner diameter of the channel travelled the quickest through the phantom, and microbeads traveling through the outer diameter of the phantom showed to travel the longest through the phantom. As shown from Figure 5.2.4, the fluorescent microbeads traveling at the inner curve of the phantom took on average 200 ms to travel through the area analysed within the phantom, compared to 350 ms of the microbeads that travelled along the outer curve of the phantom. If the constant flow was changed to a pulsatile flow that would better mimick the flow behaviour of the cardiovascular system, the analysis of rheological flow would be more accurate to native behaviour, along with matching the viscosity and density to that of blood.

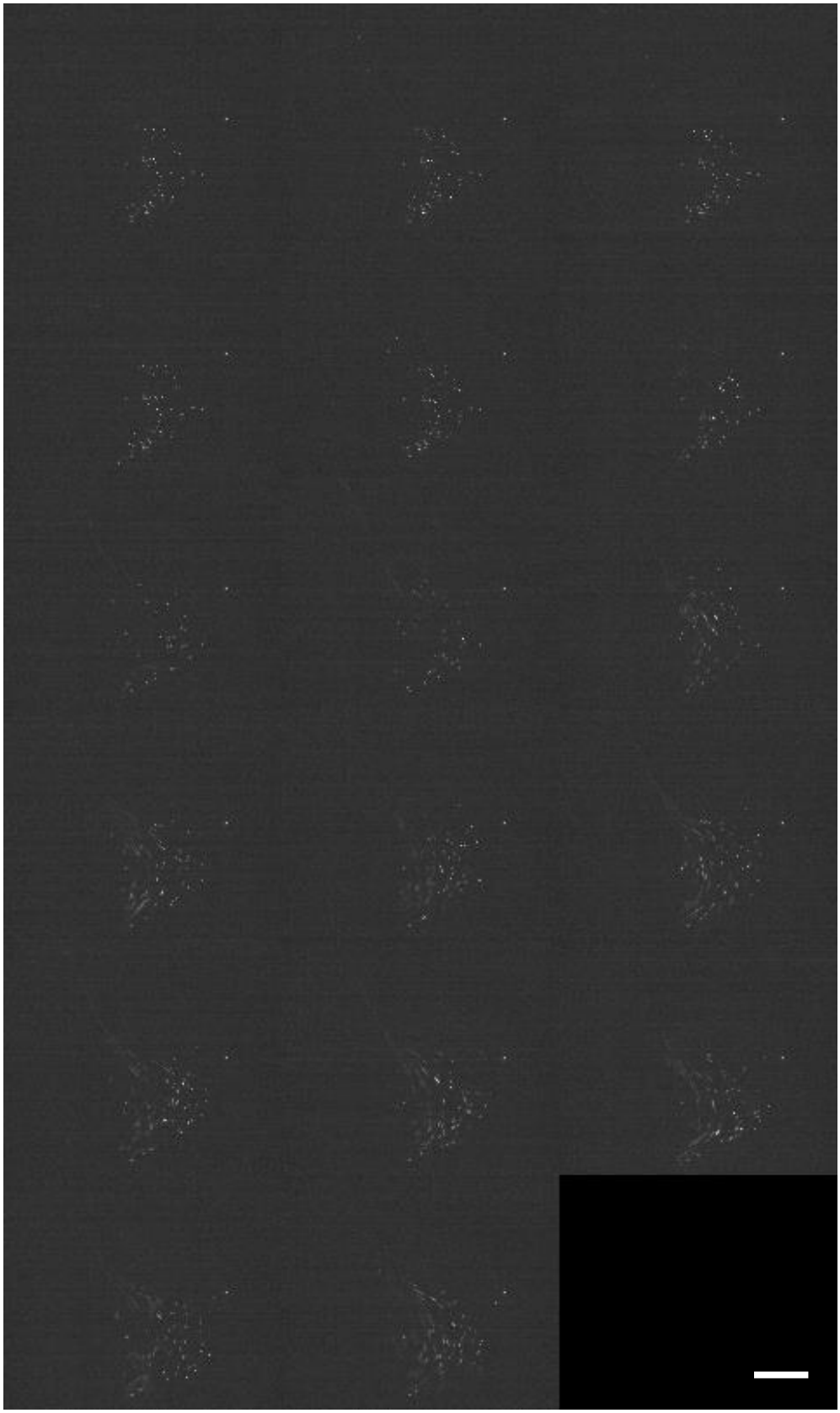

Figure 5.2.3 A set of consecutive images of microbeads flowing through a phantom, created with wax-loss PDMS fabrication. Due to the 3D nature of the phantom, many of the fluorescent beads move out of focus and back into focus over time. Each image was taken 50 ms apart. Scale bar = 1000 µm.

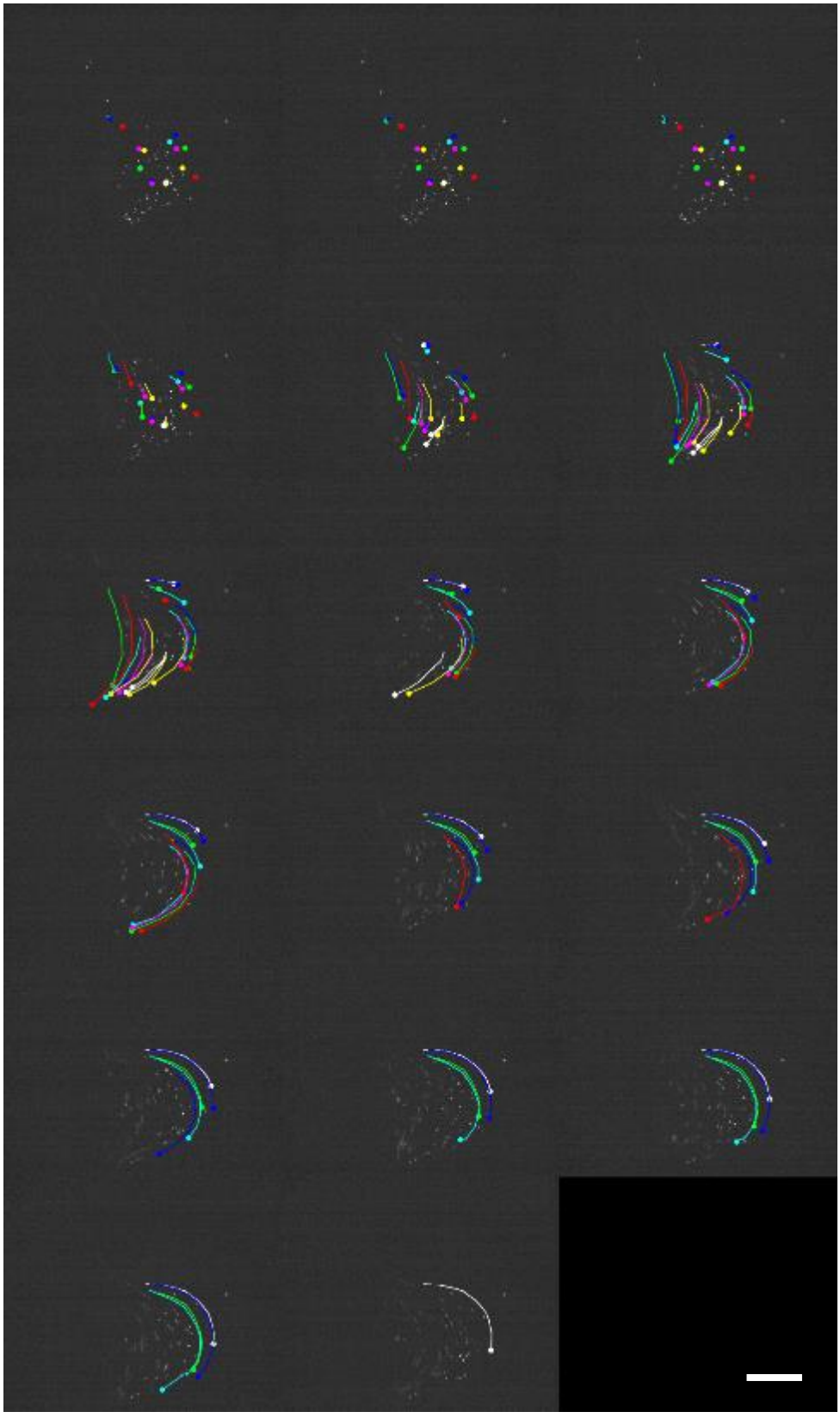

Figure 5.2.4 shows the images shown in Figure 5.2.3, with an overlay of a set of fluorescent beads that were tracked through each frame by using the Manual Tracker plugin in ImageJ. Scale bar = 1000 µm

It was not possible to analyse the microbeads and fluid flow within the bubble created by the pipetted wax, as the experimental setup could only focus on one z-plane, and therefore it was unable to analyse the movement of the microbeads in a 3D environment. The most important finding that flow phantoms can be created with inkjet printing can be seen sufficiently with epiflorescent microscopy and florescent beads to show proof of concept that inkjet printing can support the creation of phantoms. By using the method of fabricating phantoms through using inkjet printing of wax, this method could compete with other methods that create high resolution phantoms such as 2-photon polymerisation and traditional mould casting. Inkjet printing would allow the creation of more complex vasculature at a higher resolution compared to traditional mould casting, and it would not require the use of lasers such as that used in 2-photon polymerisation.

Figure 5.2.5 shows a representation of the flow of fluid within each phantom tested, with red lines representing the fastest flows and yellow lines highlighting the slowest flows. These representations were derived from analysing epifluorescent images of microbeads in water flowing through the phantoms. It was established that the fluid slows down within the larger cavity from the smaller cavity as the fluid experiences the change in vessel diameter.

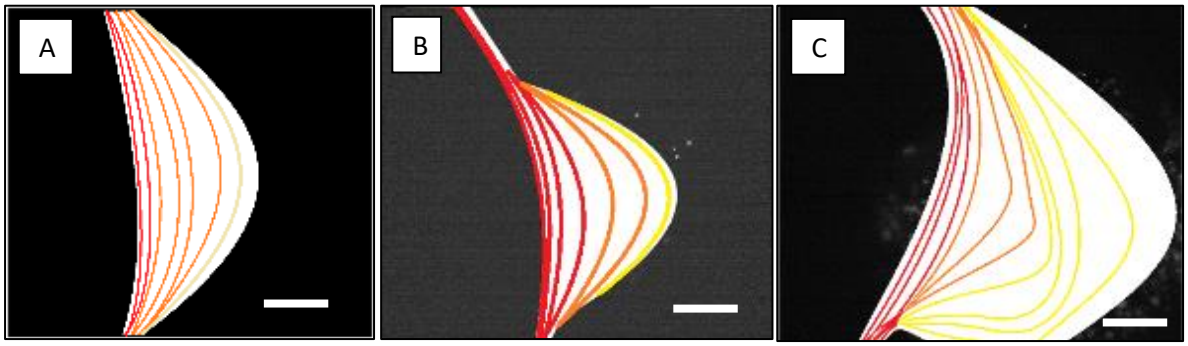

Figure 5.2.5 Fluid flow within different flow phantoms created with wax-loss PDMS fabrication. Analysing the flow of fluorescent microbeads through the phantom at a steady flow rate, a general consensus of fluid flow rate can be created; red lines indicate flows which were fastest, with yellow lines showing the slowest flows with the phantom. Scale bar = 1000 µm

The flow of the last phantom (Figure 5.2.5C) is slightly more chaotic, and was speculated to be caused by the steeper angles at which the fluid enters and exits the larger cavity (created by removing the bulbous wax that was originally there from pipetting onto the line of printed wax). This notion can be better explained with the support of Figure 5.2.6; where it is illustrated how the vessel aligns itself with

the aneurism with each phantom created. As shown in Figure 5.2.6C, the angle at which the vessel enters and exits the aneurism is steeper compared to the other phantoms, and with a strong enough fluid flow generated by the syringe pump, vortices were created.

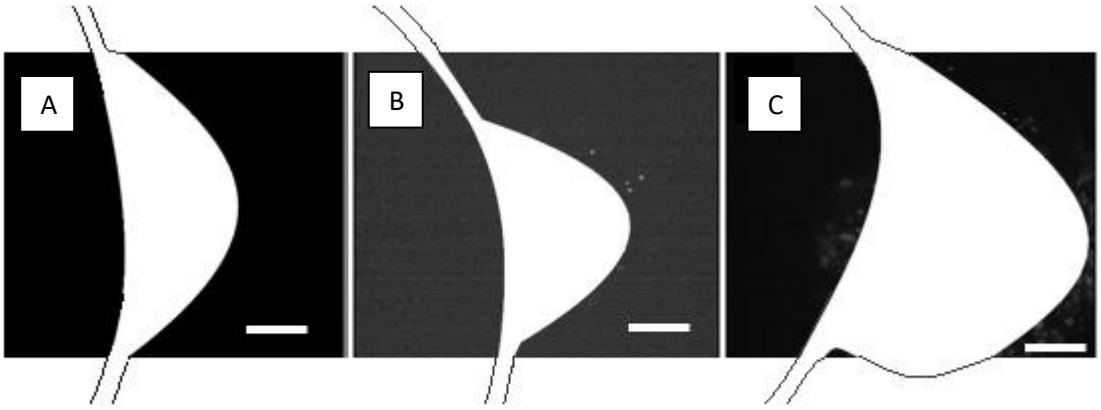

Figure 5.2.6 Representative images of how the phantoms looked like if the analysed area was zoomed out slightly; showing more of the narrow channel created through wax-loss of inkjet printed wax and their angles of entry. Note that the fluid flow direction travelled from top to bottom. Also note the angle at which the fluid enters the aneurism is steepest with C), which is explained later why vortex behaviours can be seen with this phantom and not seen in the other phantoms created. The angles of entry and exit can be compared as around 165°, 150° and 100° respectively to each image. Scale bar = 1000 µm.

Figure 5.2.7 is a representative image of turbulent flow within each of the phantoms tested. Figure 5.2.7A and Figure 5.2.7B shows most of the turbulence occurred on the outer diameter of the aneurism, as the micro beads slowed down upon entering the aneurism. Figure 5.2.7C shows most turbulence near the entry point of the aneurism. Turbulence occurred because the flow was significantly large, the fluid was not deemed viscous and the fluid entered a larger cavity. With these factors, it can be considered that effect generated a high Reynolds number and supports the creation of eddies within the fluid.[243] Compared to the laminar flow seen with the other phantoms, it can be assumed that the Reynolds number for phantoms as shown in Figure 5.2.7A and Figure 5.2.7B had a dimensionless value of less than 2,300; which would generate laminar flow, whilst Figure 5.2.7C had a Re value of more than 2,300.

.

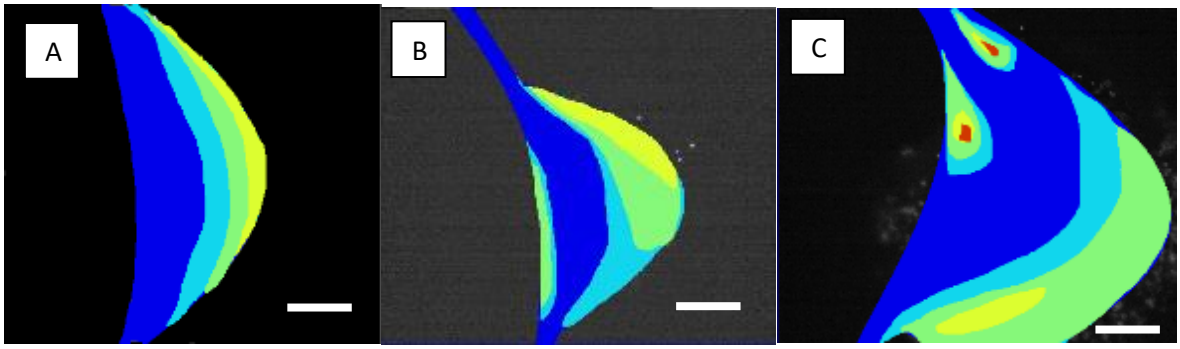

Figure 5.2.7 Approximation of turbulent flow within the respected phantoms, simulated by examining consecutive images of fluorescent micro bead movement in the fluid. Scale bar = 1000 µm.

The rate of change of diameter was the variable that determined if the flow was laminar or turbulent when the fluid passed through the phantom. When the angle of entry and exit of the vessel into the aneurism was steep (Figure 5.2.7C), the diameter of the cavity increased at a larger rate compared to phantoms with a shallower angle of entry and exit through the aneurism (Figure 5.2.7A). An increased rate in the change of diameter was not significant enough to generate turbulence within the vessels, according to Reynold's Number, and therefore the flow behaviour were considered laminar but formed eddies within the phantom.

As with all additive manufacturing techniques, inkjet printing is able to create complex models and patterns from a variety of materials. With this example in creating fluid phantoms for the study of fluid behaviour, vessels of all relevant sizes can be created. Ideally, the larger the vessel the better (>1 mm), as the significance of the surface roughness of the wax is reduced with larger diameter vessels.

The creation of the aneurism (bulging within a vessel) can be created through inkjet printing also, with fine control of its size, however given that the purpose of these experiments were to analyse the suitability of using inkjet printing for the creation of phantoms, the aneurisms were created by using a pipette to save time and to prove the principle. A typical printing time of a phantom was between 15-20 minutes.

The method of using inkjet printing to create negative moulds allows the user to create fluid phantoms of suitable sizes (100 µm- several cm). Combined with PDMS, inkjet printed wax can be removed from a PDMS mould through wax loss methods to create an easy prototyping technique.

However, when creating phantoms, the calibration of jetting is essential to creating smooth-inner-lining phantoms; if the droplet spacing and/or jetting parameters is sub-optimal, the vessels that are created can generate uneven inner surfaces after the removal of the wax. With the experiments carried out within this chapter, the surface of the inkjet printed wax was not uniform, as individual molten wax droplets merged together and a scalloping effect could be seen under a light microscope. Figure 5.2.8 shows a light microscopy image of a wax channel created with inkjet printing. Another disadvantage of the inkjet printing process is the final finish of the sample. Since inkjet printing allows the user to directly print out the object from a digital file, if the sample is at the minimal resolution the printer can create, the digitisation can be seen clearly, especially around the curving segments of the scaffold (Figure 5.2.8).

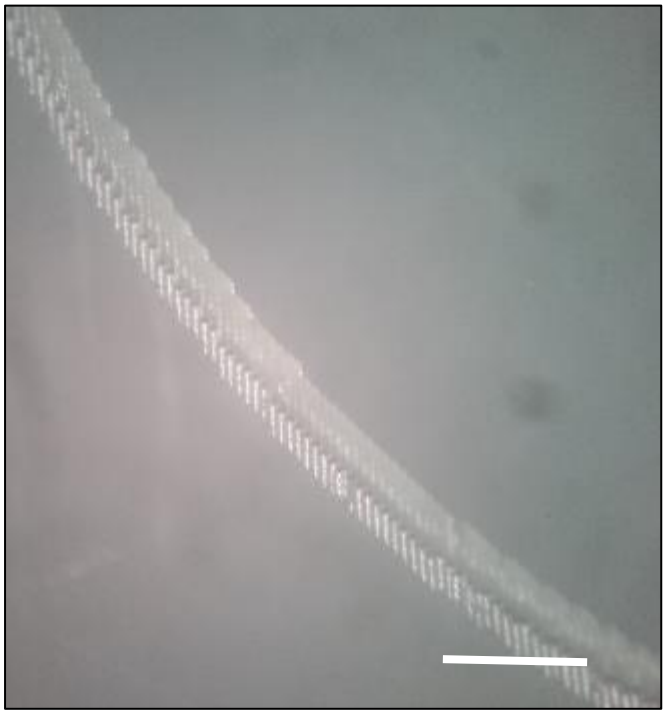

Figure 5.2.8 Magnified image of inkjet printed negative mould of a channel. Note the roughness and how curved areas are digitised, leaving indentations within the structure to mimic curvature. Scale bar = 500 µm

Figure 5.2.9 shows an extreme case of how sub-optimal printing parameters can hugely influence the flow of the fluid travelling through the phantom. If the wax topology is scalloped due to sub-optimal printing, then when the wax is removed, the inner lining of the vessel will also be rough. This roughness can be so significant that laminar flow is not possible and chaotic flow is created throughout the phantom, which would not be representative of native vessels.

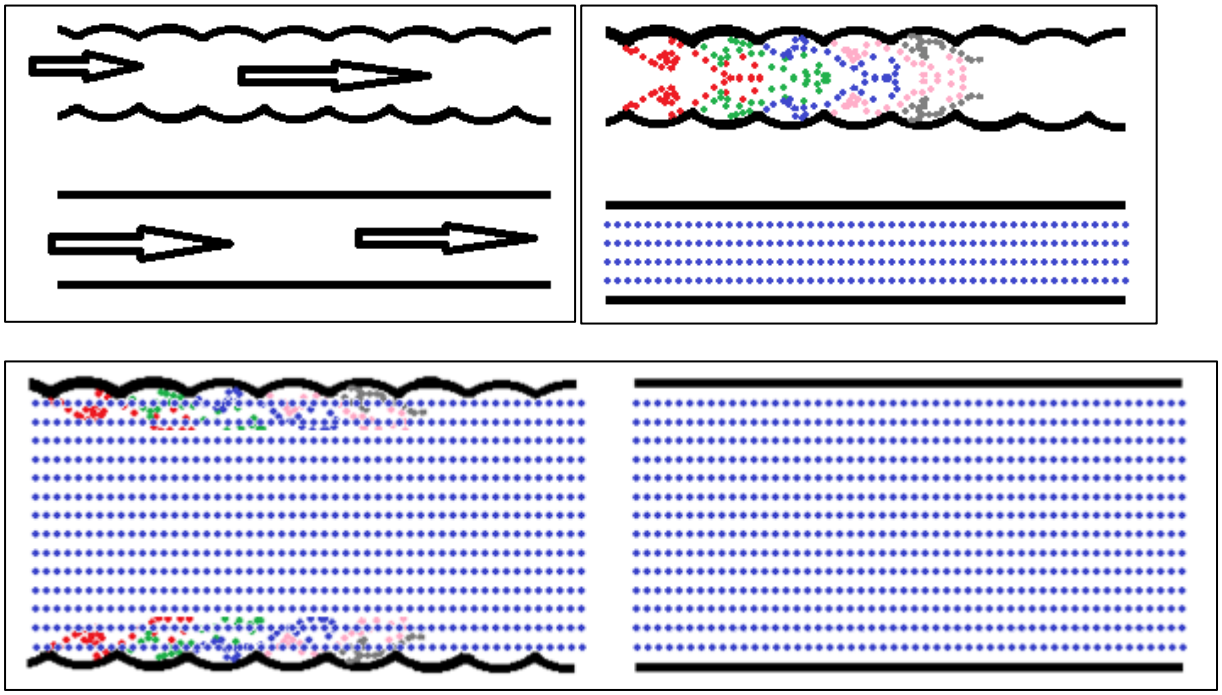

Figure 5.2.9 Diagrams of understanding fluid flow. Top) Topology of inkjet printed wax, and the ideal finish which would be smooth. Arrows represent the flow of fluid. Top right) Coloured dots are representations of the turbulence (vorticity distribution) of a non-smooth channel, compared to a smooth channel. Bottom) With wider channels, the turbulent effects of the surface topography of the wax used would be reduced when fluid flows through the vessel.

However, during the process of the wax-loss technique, it can be assumed that not all the wax is fully removed from the interior of the PDMS. During the removal process, residual wax would coat the roughness of the surface of the vessel, making it smoother Figure 5.2.10. Fortunately, paraffin wax is biocompatible and non-toxic to cells, therefore this method can be used with biologically relevant fluids like blood and diagnostic fluids. This way, vessels created with paraffin wax, and then later removed with wax-loss would be coated with a layer of wax that would smooth the interior wall of the vessels.

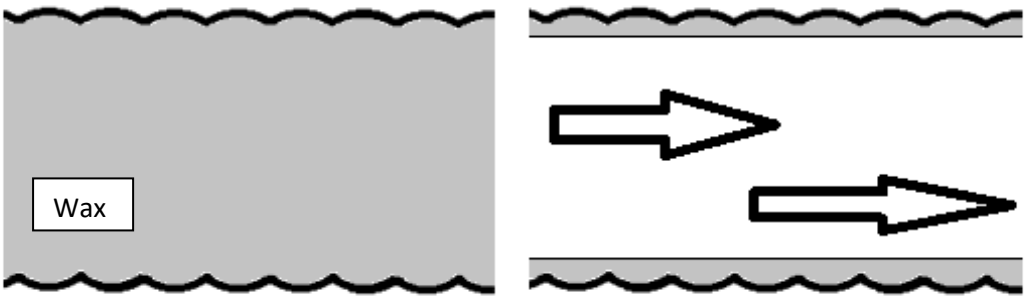

Figure 5.2.10 Representation of printed wax in PDMS mould (left). When the sample is heated up to 80°C and the wax flushed out of the PDMS mould, it was expected that not all the wax would be extracted out (right). A thin layer of wax

would line the interior of the vessel, smoothening the perceived roughness that was originally caused by the scalloping effect of printed lines.

Other ways of removing the wax such as flushing the sample with xylene could be used to completely remove the wax. However, given the understanding of having a thin coating of wax to line the interior of the vessel would make the channels smoother, the use of xylene would not be advantageous.

The ability to analyse the movement of fluid within the fluid phantoms was limited, as the analysis techniques used could only detect fluorescent micro beads in a single z-plane. The plane that was selected for analysis was along the z-plane where the vessel and aneurism could be seen together. Ideally the whole volume of the phantom should be analysed and measured when fluid flowed through. Typically, phantoms are created for the application of non-invasive diagnostic methods such as ultrasound, and therefore the use of ultrasound techniques would be an ideal means for analysis of phantoms created with inkjet printing.[244]

5.3 Conclusion

Phantoms were created, with the use of an inkjet printer to create the negative mould of the vessel. This process is easily performed, with flexibility to change the structure in any way due to the additive manufacturing technique that allows changes to take place immediately as it converts the digital data into a physical scaffold. The use of PDMS is required to create the scaffold, and using the wax-loss method, the printed paraffin wax can be removed to create the negative space where the fluid flows through to make the fluid phantom. It was theorised that the interior of the phantom would be smoother than the perceived printed topology prior to the application of PDMS, as upon the removal of the wax in the PDMS, a thin layer of residual wax would remain and fill in the roughness to create a smoother channel.

6 CELL PRINTING

6.1 Overview

Conventional methods of tissue engineering involve manually seeding cells onto scaffolds [245]. However, cell printing, which is the ability to deposit cells through a printing technique (inkjet, thermal, extrusion printing) onto a substrate, has potential for applications in tissue engineering.[117,246] The ability of inkjet printing to combine a high-throughput deposition capability with high precision placement of biomaterials[68,85] allows it to be employed for *in vitro* tissue engineered models, especially if one can print eukaryotic cells which are undamaged and able to proliferate and differentiate as required post printing.

Saunders et al(2008) reported on the ability to print human HT1080 fibrosarcoma cell suspensions using a drop-on-demand piezoelectric system and found that viability after printing reached 98%, compared to controls. Similarly, Boland *et al* reported on thermal drop-on-demand printing to print Chinese Hamster Ovary (CHO) cell suspensions, and found that cell viability was >90% after printing.[102] The findings of Boland and others indicate that adherent eukaryotic cells can be delivered by inkjet printing without substantial damage. Embryonic neuronal cells (including hippocampal, cortical and motor neurones), stem cells, muscle cells and chondrocytes have all been inkjet printed with resultant survival and growth.[101,119,124,139,247,248] This accumulating research brings closer a viable strategy for making *in vitro* 3D lab devices and for treating damage to the nervous system.[249,250]

A general limitation had been found by several research groups that cell printing could only be done within a limited amount of time (Lorber et al. 2013; Pepper et al. 2011; Saunders et al. 2008). Such studies showed a decrease in cell number after 40 minutes and it was speculated that this was caused by sedimentation of cells to the bottom of the print reservoir and also through the adherence of cells to the tubing and glass capillary of the printhead.

The ability to deposit cells at predefined positions over a relatively short period of time allows better experimental design for the study of intercellular interactions. Accurate positioning of cells can lead to the creation of spatially dependent cell-containing devices to promote the advancement of tissue engineered constructs and the creation of fine neuronal networks.[199,202] This can also help with the understanding of how cells behave in relation to the topography of the substrate.[225] Ongoing research in the field of bioengineering with inkjet printing aims at creating tissues with multiple cell types within a scaffold for mimicking native tissue, which is a progressive step towards organ printing.[77,252] The ability to create tailored tissues quickly and reproducibly will offer scientists a very powerful tool in regenerative medicine and *in vitro* research. The creation of 3D tissue structures have been shown to better mimic natural responses to drug testing conditions.[253] With the demand for organ donors being very high, the most viable alternative to organ donors is using tissue engineering to create such organs. An ideal replacement substitute would be to harvest stem cells at birth, and it is currently not practical to grow and keep spare organs for everyone since birth.[254] The field of bioprinting has grown steadily in the past ten years, with researchers originally printing fibroblasts from a desktop printer,[255] to having successfully created small sections of tissue through additive manufacturing techniques for drug testing and toxicology,[256–258] with more complex cell combinations to better mimic native tissue to be created in the near future.

Within this chapter, bioprinting for neuronal applications were investigated. Neuronal cells and their supporting cells were printed to determine viability after inkjet printing because the co-interaction between them and their surrounding environment are essential for nerve function within the peripheral nervous system. A current challenge in peripheral nervous system injury is to find an alternative to autologous nerve grafting; a technique mentioned in Chapter 1 that a medical professional extracts a patient's own nerve from an undamaged area and replaces damaged/lost nerve at an injured site.

This chapter describes a method for inkjet printing NG108-15 neuronal cells and Schwann cells with phenotypic analysis over 7 days, with cell viability assessed immediately and 7 days post printing, and the extent of neurite outgrowth of printed neuronal cells also being assessed. Printing of fibroblasts was included for comparison. In previous studies inkjet printing of neurons and their viability was

reported,[102,124] but in previous work, a maximum of 80 V was used. The current study expands the printing parameters to 230 V, and describes a more detailed phenotypic analysis of Schwann cells.

To the best of the author's knowledge, the use of piezoelectric inkjet printing to organize neuronal and Schwann cells on a substrate has not been reported previously, nor have cells been printed with voltages in excess of 80 V. The outcome of this work provides a broad platform for developing inkjet printed nerve constructs e.g. for 3D *in vitro* devices, nerve regeneration approaches or the study of neurodegenerative diseases. Cells were analysed with trypan blue, light microscopy, and for neuronal cells (NG108-15); qualitative measurements of their dendritic outgrowths were measured. Previous research groups had reported cell printing was only possible for 40-20 minutes before printing failure,[124,140] and this time limit was investigated to understand this reported behaviour.

In summary, several investigations were undertaken to understand cell printing when the voltage was varied;

1. Viability of inkjet printed cells immediately after printing
2. Cell proliferation after inkjet printing (during day 1, 3 and 7)
3. Quality of neuronal cells (NG108s) after inkjet printing
4. Purity of supporting cells (glial cells; Schwann cells) after inkjet printing
5. Limitations of cell printing

6.2 Viability of inkjet printed cells immediately after printing

6.2.1 Introduction

The procedure of inkjet printing cells can be considered a hazardous experience for cells as a method of controlled cell delivery onto a substrate. Compared to the environment cells experience during standard cell seeding, inkjet printing has the potential to be more damaging to the cells, as they undergo acceleration and potential shear stresses from being jetted out through the printhead. It should be noted that piezoelectric printing should be seen as less harmful than thermal inkjet printing, since thermal inkjet printing requires a local area within the ink to be heated up to cause an expansion of pressure, and this temperature change should be more damaging to cells. Saunders had reported that cell survival rates decreased due to piezo inkjet printing; controls had a viability of >98%, cells printed at 40 V had cell survival rates of 98% whereas those printed at 80 V had a survival rate of 94%.[140] Xu had reported 97% survival rates when investigating Chinese Hamster Ovary cells with a voltage of 40 V.[259] The decrease was not significant in Xu's work; however the average viability was less compared to controls. It was previously thought that neuronal cells were more sensitive to stresses, and their viability would decrease more through the inkjet printing process. Keith Martin's group (Lorber et al) had shown that glial and retinal cells had an average viability of 69$\pm$12.2% and 74.3$\pm$2.6%, compared to a control of 78.4$\pm$8.2% and 69$\pm$5.3% respectively.[124] There is a large difference in experimental results from different research groups caused by the use of different cell types, of which each can be more sensitive to certain stresses induced by the printing system. Several causes had been postulated for a decrease in viability due to the inkjet printing procedure; high shear stress during the jetting process through the glass capillary of the printhead, steep acceleration rate being jetting out of the nozzle and onto the substrate. It is to be noted that the research groups mentioned within this section all used Microfab piezoelectric inkjet devices; such as the same that was used within this thesis (Jetlab printing platform).

To understand the viability of cells that underwent inkjet printing, the trypan blue staining protocol was used to determine cell viability immediately after inkjet printing. The voltage of jetting was examined to determine their effects to cell viability on fibroblasts, NG108-15s and Schwann cells.

6.2.2 Results

Figure 6.2.1 shows the effect of inkjet printing voltage on the viability of human dermal fibroblasts, NG108-15 neuronal cells and primary porcine Schwann cells assessed by Trypan blue staining. The addition of the blue bars are from results extrapolated from Saunder's work with HT1080 cells, at 40 V and 80 V to give a comparison. Fibroblast cells were printed as another form of control, and as a reference to previously published work (Saunders et al. 2008).

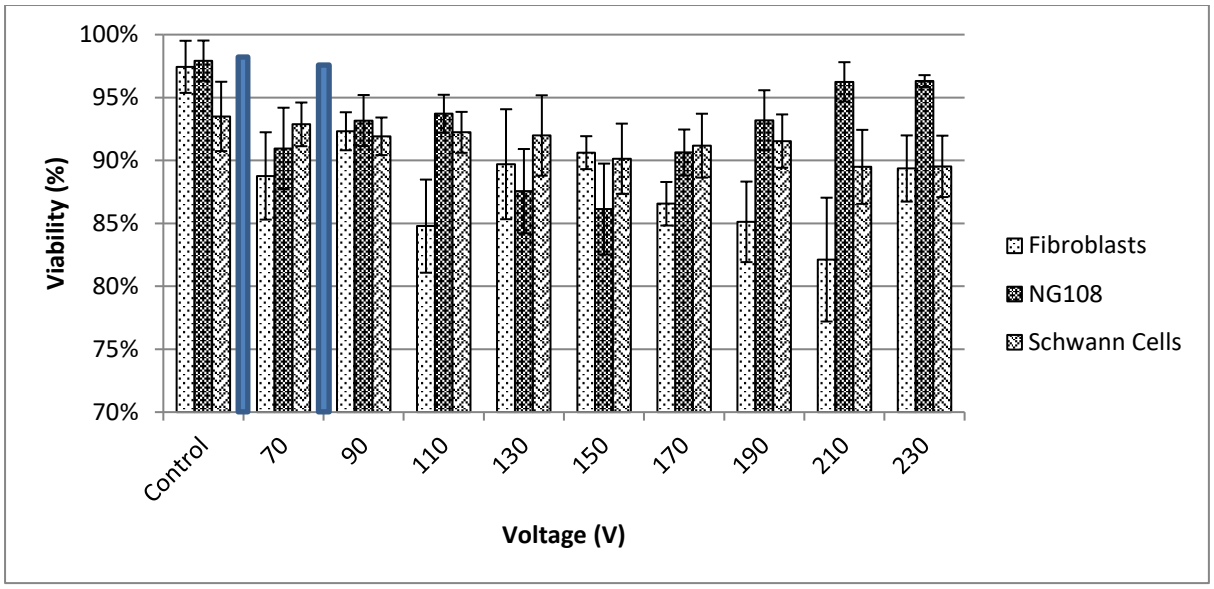

Figure 6.2.1 Analysis of mean viability of cells assessed using trypan blue staining immediately after inkjet printing, with standard deviation error bars at different voltages with each cell type. The blue bars represent 40 V and 80 V respectively, derived from Saunder's work with printing HT1080 cells. N=30.

Non-printed control samples showed cell viability of >90%. Inkjet printing resulted in a cell viability of 82-92% for fibroblasts, 86-96% for neuronal cells and 89-92% for Schwann cells. There was no correlation between the range of voltages used (between 70-230 V) and cell viability. It was hypothesised that an increase in voltage would increase the shear stress to the cells passing through the glass nozzle of the printhead, given that the accelerated velocity would cause greater stress around the periphery when travelling through an orifice, and had been previously studied,[260] whereby cell death was characterised within the cell media through an increase in DNA fragmentation. Figure 6.2.2 shows the calculated droplet velocity of each voltage used. The velocity was calculated through measuring the distance a jetted droplet travelled within a given amount of time travelling to the substrate. However, the use of this range of forces did not show a proportionate amount of damage to the cells.

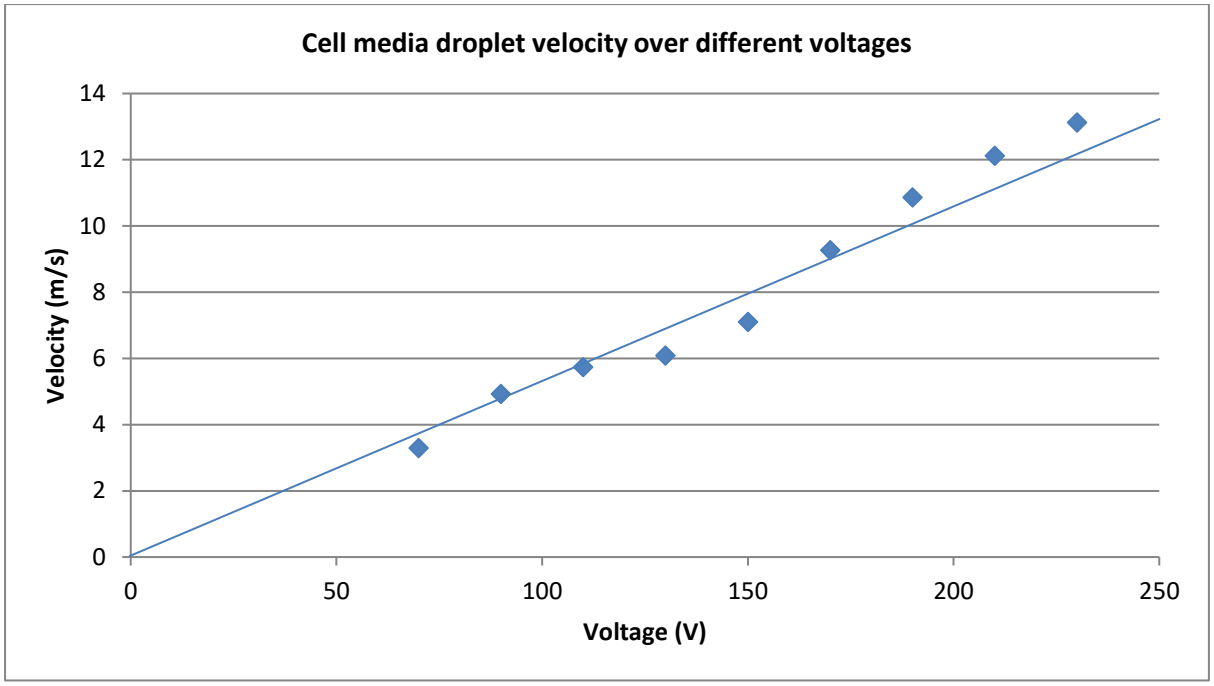

Figure 6.2.2 Velocity of inkjet printed droplets landed on the substrate. An increase in voltage equated to an increase in velocity, and therefore energy. This factor was not considered significant to the viability of the printed cells, as they were jetted into wells containing cell media, dampening the impact of the cells into the well plate.

Cell viability was not proportional to the velocity at which the cells were jetted at and it was speculated that this was due to the cell culture medium (which contains 10% foetal calf serum) behaving to buffer the physical shock between the cell and the interior of the printhead, thus decreasing the shear experienced by cells. The viability determined was comparable with that reported previously for fibroblasts (Saunders et al. 2008), where an HT1080 fibroblast cell line had 94% viability when printed at 80 V. However, fibroblasts used in the present study were human primary cells, in contrast to that of Saunders (*et al* 2008), who used HT1080 fibroblasts, which are a human cell line derived from a fibrosarcoma

The viability of neuronal cells, glial cells and fibroblasts were similar with no significant differences in metabolic activity identified between the cell types at any of the voltages studied compared with non-printed control cells. It is important to note that the applied voltage caused the actuation of the piezoelectric crystal and hence, under the optimum parameters, will eject a droplet out of the nozzle. The voltage applied to the printhead does not come into direct contact with the cell culture medium and is therefore not subject to direct conductive electron transfer. An increase in voltage causes a stronger

piezoelectric response and cells in the culture medium are ejected with more force through a narrow orifice. The velocity that droplets travelled was calculated between 3.2 – 13.1 ms^{-1} at 70 – 230 V, and corresponded to a shear rate of 5 x 10^4 – 2 x 10^5 s^{-1} respectively.

6.3 Schwann and NG108 neuronal cell proliferation 1, 3 and 7 days after inkjet printing

6.3.1 Introduction

The immediate effects to cell viability was determined in the previous section. Although cell viability was high, the inkjet printing process could have caused cell damage that may reveal itself at a later stage. It was previously studied that thermal inkjet printed cells (porcine aortic endothelial cell line) caused temporary microdisruption of their cell membranes, that allowed the researchers to transfect such cells with plasmids (with 90% viability).[261] The cells were studied *in vivo* and *in vitro*, however there was no categorical study of cell viability over a period of 7 days as their study focused on the biocompatibility with implantation with mice, and their transfection rate of cells with plasmids.

Cell metabolic activity was measured after inkjet printing, at day 1, 3 and 7 to determine if there were long-term damaging effects. The normal voltage of 80 V was used for these experiments. The MTT assay was used, as a cell culture's metabolic activity was proportional to the population of cells present within a sample. If inkjet printing caused damage to the cells, not shown immediately after inkjet printing, then a metabolic assay over a period of 7 days would reveal any long term damage to cells. When compared to a control sample, inkjet printed cell metabolic activity would decrease or be significantly lower compared to controls, if there was any permanent long-term damage to the cells.

There has been debate about the ideal surface coatings to culture Schwann cells. Poly-L-Lysine was the standard coating used in research,[262,263] but there is suggestion that Schwann cells proliferate slightly better on fibronectin-coated tissue culture plastic (TCP).[169] Fibronectin is an extracellular glycoprotein involved in wound healing and remylination for functional nerve regeneration.[264,265] Therefore TCP,

poly-L-lysine and fibronectin were tested to determine the ideal surface coating, along with investigating the metabolic activity of inkjet printed cells.

6.3.2 Results

Schwann cell concentration on different surface coatings was assessed after printing. As shown in Figure 6.3.1 all Schwann cells experiments showed an increase in metabolic activity through MTT analysis, with the largest differences arising between days 3 and 7. The studies confirmed fibronectin as the best culture surface compared to TCP or poly-L-lysine for Schwann cells. The largest difference observed was at day 7, which showed that inkjet printed cells, and cells cultured on fibronectin, had a higher viability versus control, and consequently had a higher cell number at this time after printing. This research supports previous findings that fibronectin is a better culturing environment than TCP and Poly-L-Lysine.[169]

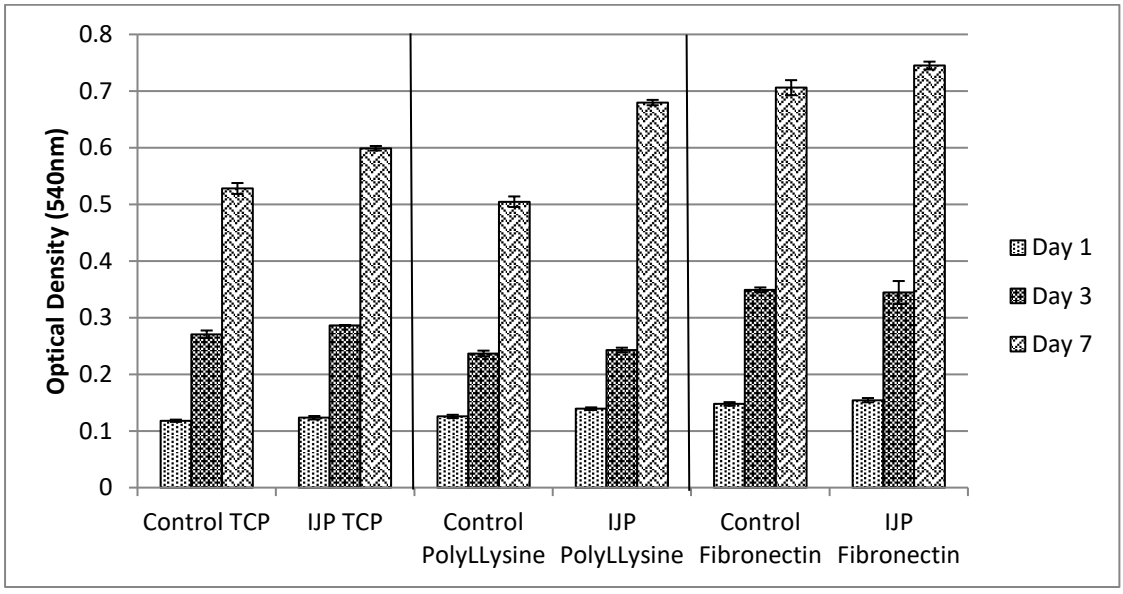

Figure 6.3.1 MTT assay results of printed and non-printed Schwann cells after 1, 3 and 7 days on different substrate surfaces, printed at 80 V, with standard deviation. N=3

Light microscopy images were taken and compared to MTT results to confirm validity of optical density values (Figure 6.3.2, Figure 6.3.3 and Figure 6.3.4).

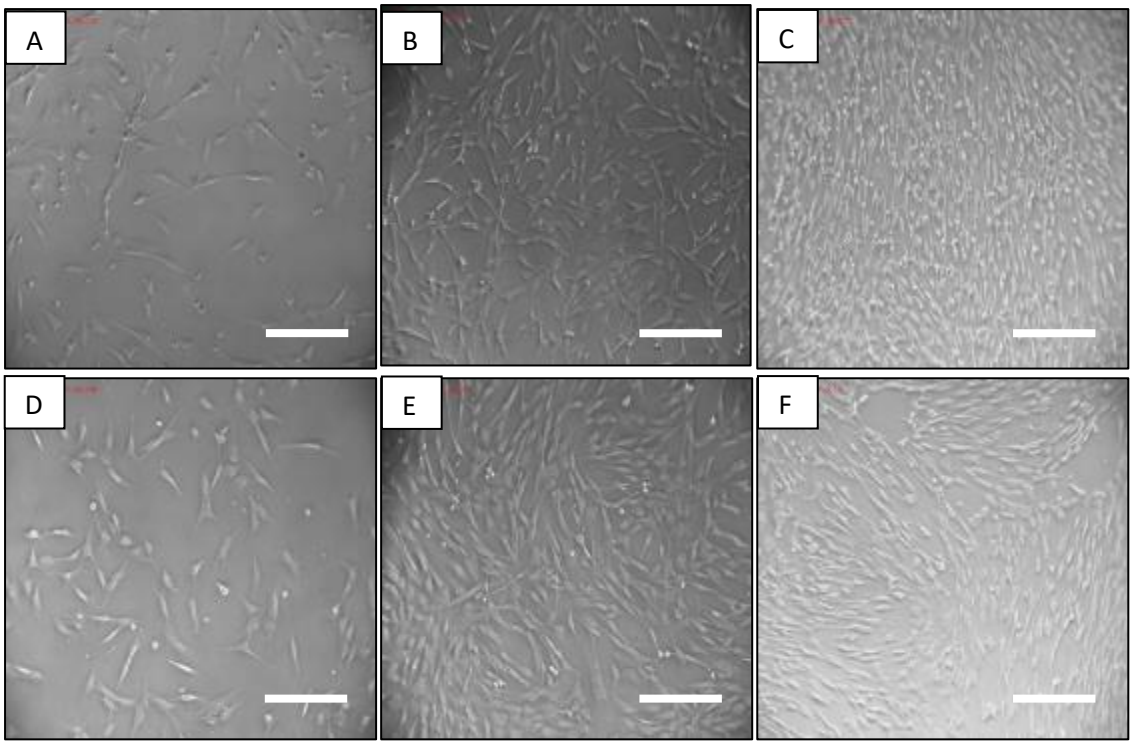

Figure 6.3.2 Light microscopy images of Schwann cells grown on fibronectin surface coatings (A-C) Inkjet printed at 80 V, Schwann cells on day 1 (A), day 3 (B), day 7 (C). (D-F) Control Schwann cells seeded with a pipette onto fibronectin coatings on day 1 (D), day 3 (E), day 7 (F). Scale bar = 200 µm

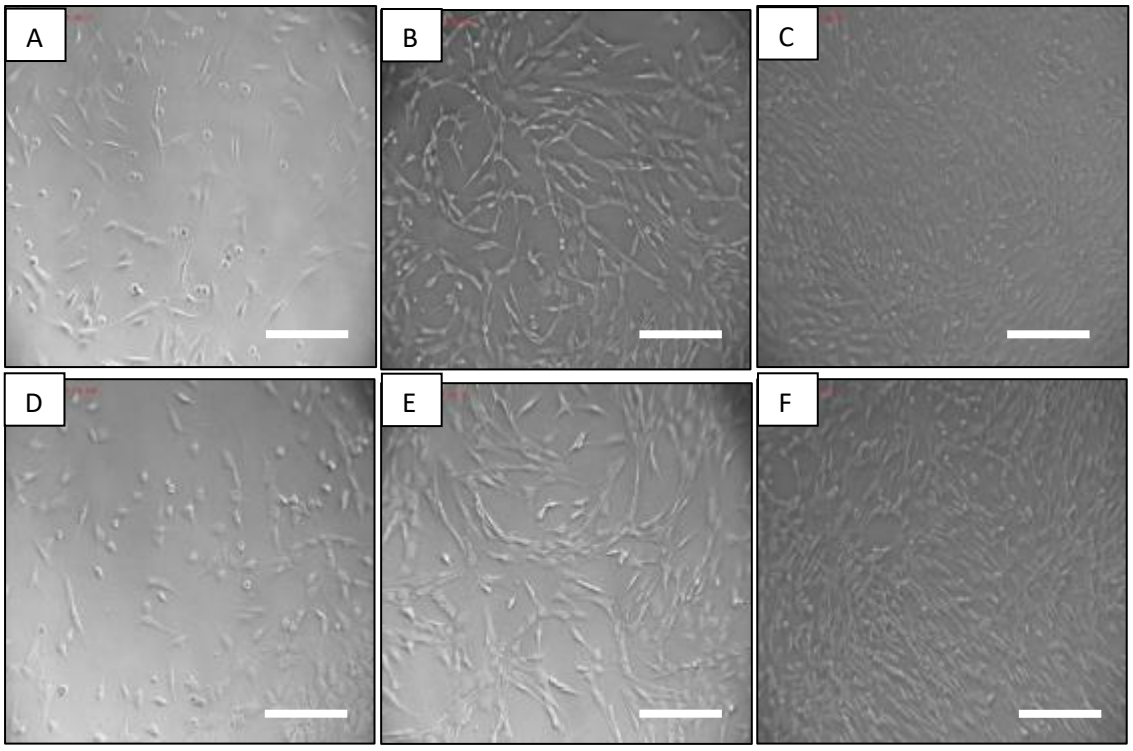

Figure 6.3.3 Light microscopy images of Schwann cells grown on poly-L-lysine surface coatings (A-C) Inkjet printed at 80 V, Schwann cells on day 1 (A), day 3 (B), day 7 (C). (D-F) Control Schwann cells seeded with a pipette onto poly-L-lysine coatings on day 1 (D), day 3 (E), day 7 (F). Scale bar = 200 µm

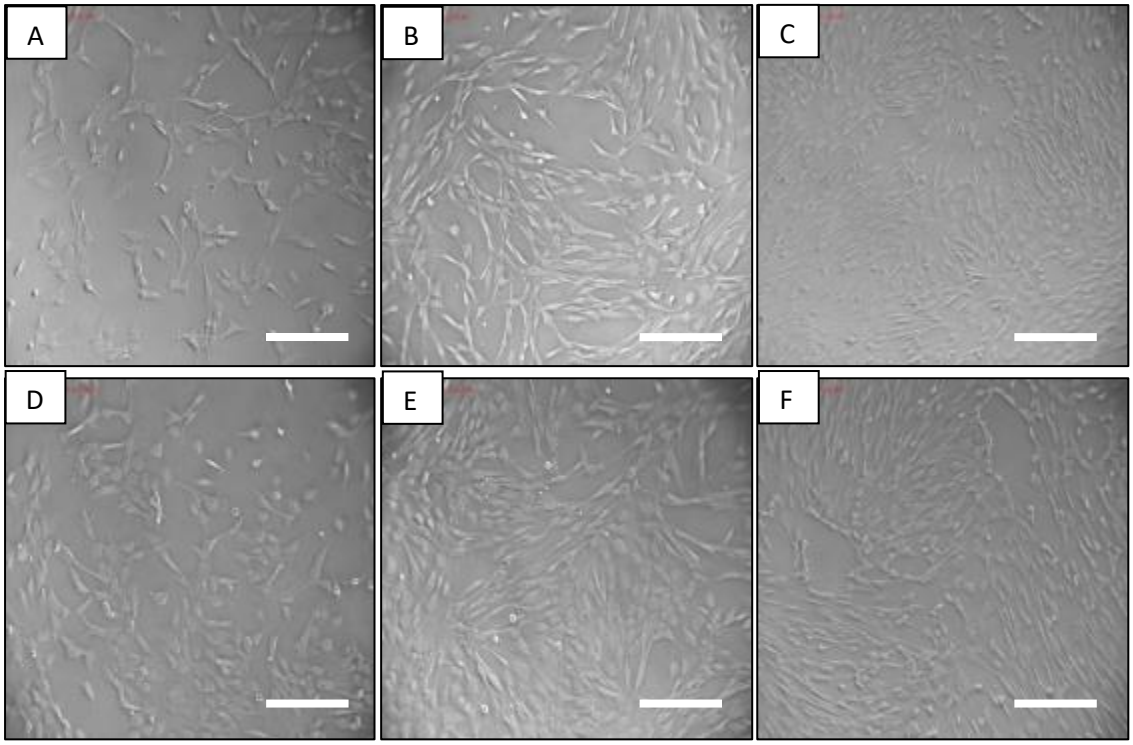

Figure 6.3.4 Light microscopy images of Schwann cells grown on TCP surface coatings (A-C) Inkjet printed Schwann cells on day 1 (A), day 3 (B), day 7 (C). (D-F) Control Schwann cells seeded with a pipette onto TCP coatings on day 1 (D), day 3 (E), day 7 (F). Scale bar = 200 µm

NG108-15 neuronal cells were inkjet printed at 80 V and had very similar viabilities to control samples, increasing exponentially over time (Figure 6.3.5).

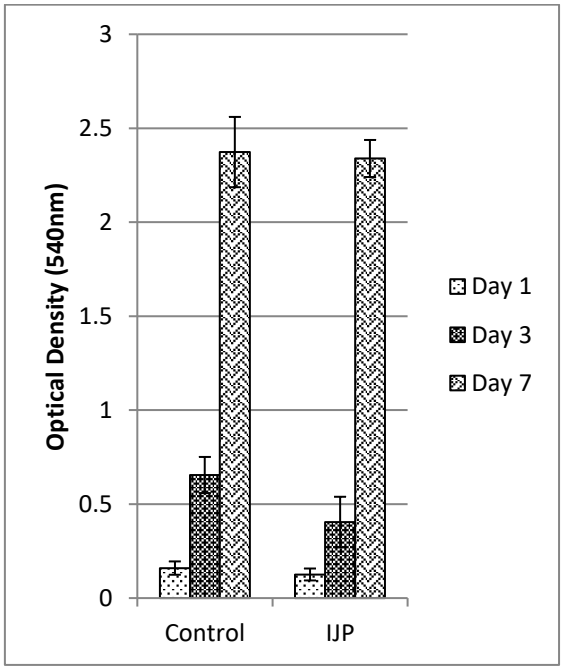

Figure 6.3.5 MTT assay results of NG108-15 neuronal cells when grown with serum in media after inkjet printing (80 V), with standard deviation. N=3

By day 7, using light microscopy and viability measurements, cells were shown to be confluent and growing at an exponential rate, compared to day 1 and day 3 results, and were not significantly different to control samples. This increase in proliferation rate indicates that cells were healthy and were proliferating at the same rate as control samples.

If inkjet printing had a significant detrimental effect on cells, a decrease in cell number would be seen compared to controls over time from which the cells might not recover. This would have been clear through a decrease in MTT values, and would be seen as a decrease in cell number through light microscopy. However this was not seen and the cells were comparable to control samples. This finding is of interest as it confirms that inkjet printing does not affect cell viability or growth over 7 days post printing. This is encouraging as it supports the development of this technique for applications such as tissue engineered constructs and 3D models. It was previously assumed neuronally relevant cells (NG108-15 and Schwann cells) would have a decreased viability compared to fibroblasts undergoing inkjet printing, however with the results seen with experiments documented in this chapter, neuronally relevant cells are not negatively affected by inkjet printing.

When comparing the optical density readings of Schwann cells (Figure 6.3.1) with NG108 neuronal cells (Figure 6.3.5), it is clear that neuronal cells have a higher metabolic activity than Schwann cells. This is due to the nature of cell lines having a higher metabolic activity than primary cells, which both have very different growth rates due to their differences in function and origin.

6.4 Schwann cell purity after inkjet printing

6.4.1 Introduction

Schwann cells can be cultured for several passages and maintain their function. Through excessive damage and change, Schwann cells can differentiate and lose their function. S100β immunolabelling was assessed to determine Schwann cell purity after inkjet printing at 80 V on different substrates (Figure 6.4.1). Schwann cells positively immunolabelled with S100β and DAPI, whilst fibroblasts

(arising from differentiated Schwann cells and which can potentially contaminate cultures from the isolation procedure) stain only with DAPI.

6.4.2 Results

All cells were identified as Schwann cells irrespective of being inkjet printed at 80 V or not on the different substrates and this therefore confirm that Schwann cells maintain their purity, and grow at the same rate as control samples after inkjet printing.

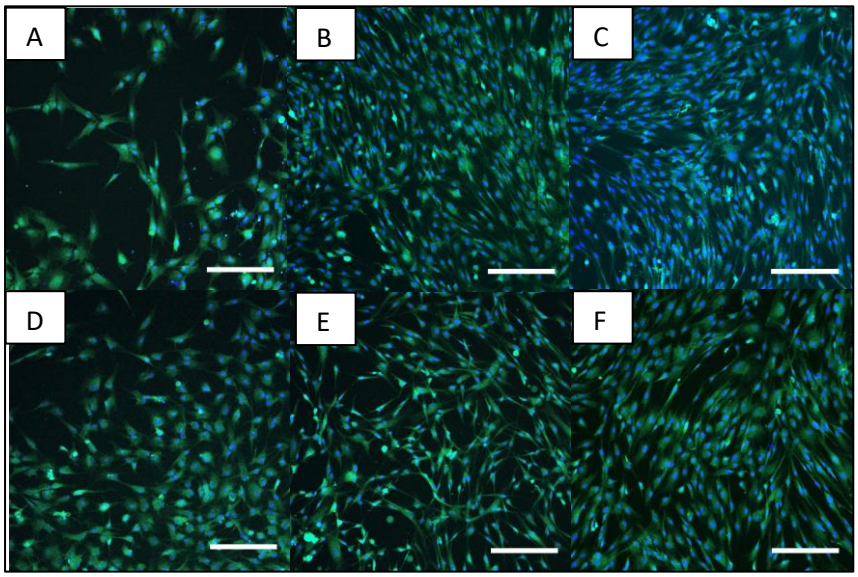

Figure 6.4.1 Confocal micrograph images showing Schwann cells stained for actin (green; S100β) and nuclei (blue; DAPI). Top micrographs show inkjet printed Schwann cells at 80 V after 1, 3 and 7 days respectively. Bottom micrographs show control samples without inkjet printing after 1, 3 and 7 days respectively. Bar = 200 µm

The results confirm that the inkjet printing procedure does not significantly damage Schwann cells enough to cause the loss of their function. The cells that survive inkjet printing and are able to proliferate up to 7 days can be confirmed to be Schwann cells.

6.5 NG108-15 neuronal cell phenotype after inkjet printing on days 1, 3 and 7

6.5.1 Introduction

NG108-15 neuronal cells were inkjet printed into well plates at 80 V, and grown without serum to trigger neurite extensions from the cells. A control was used side-by-side with the inkjet printed samples

to determine if the inkjet printing process would affect the quality of neurites produced by NG108-15 cells.

6.5.2 Results

Figure 6.5.1 shows an example of a set of images that were analysed in accordance to the factors that follow the qualitative protocols used in Daud's paper;[169] average neurite length, average number of neurites per cell body, average percentage of NG108s bearing neurites. A total of 50 separate images were analysed for each day of inspection, for both control and inkjet printed samples.

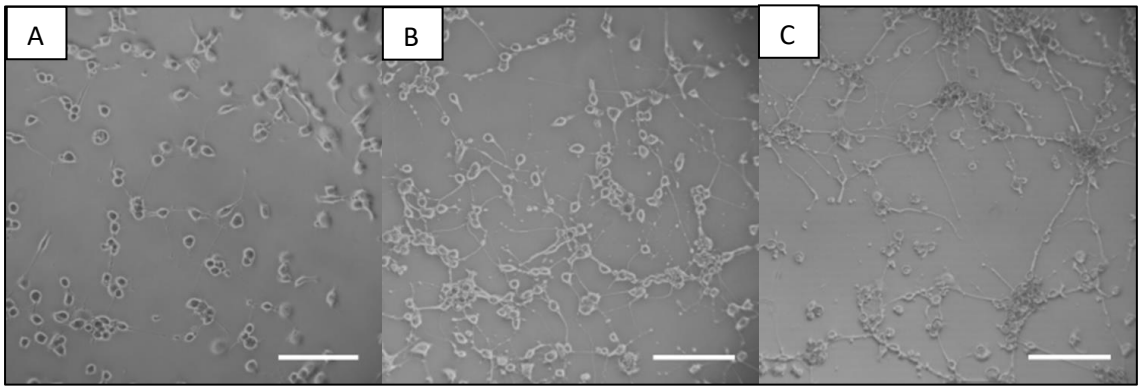

Figure 6.5.1 Example of greyscale micrographs of NG108-15 cells after inkjet printing at 80 V and cultured without serum, after 1, 3 and 7 days respectively. Bar = 100 µm

Inkjet printed neuronal cells were found to have slightly longer neurites on average compared to control non-printed cells, and this difference was observed to increase over time until it became significant by day 7 (Figure 6.5.2A). By day 3 neurites were becoming visibly longer compared to control, with an average of 65 µm versus 55 µm. By day 7, on average, inkjet printed cells had 0.25 more neurites, 12% more cells displayed neurites compared to controls and the longest neurites of inkjet printed cells were 20 µm longer.

It was clear that not all neuronal cells produced neurites after serum starvation, even after 7 days. Over 85% of control cells expressed neurites versus 95% for ink-jet printed cells by day 7. While this difference was not significant, it was established that ink-jet printing, far from damaging neuronal cells, actually increased experimental differentiation. Figure 6.5.2B shows that neuronal cells more readily expressed neurites within the first day post printing compared to control. It is postulated that this is due either to a piezo electric effect, or results from a transient high shear stress during ejection through the

small preface, or a combination of both. Figure 6.5.2C shows the average number of neurites was 1.7 and 1.1 per cell on day 1, to a maximum of 2.5 and 2.2 by day 7, for inkjet printed and control cells respectively (Figure 6.5.2C).

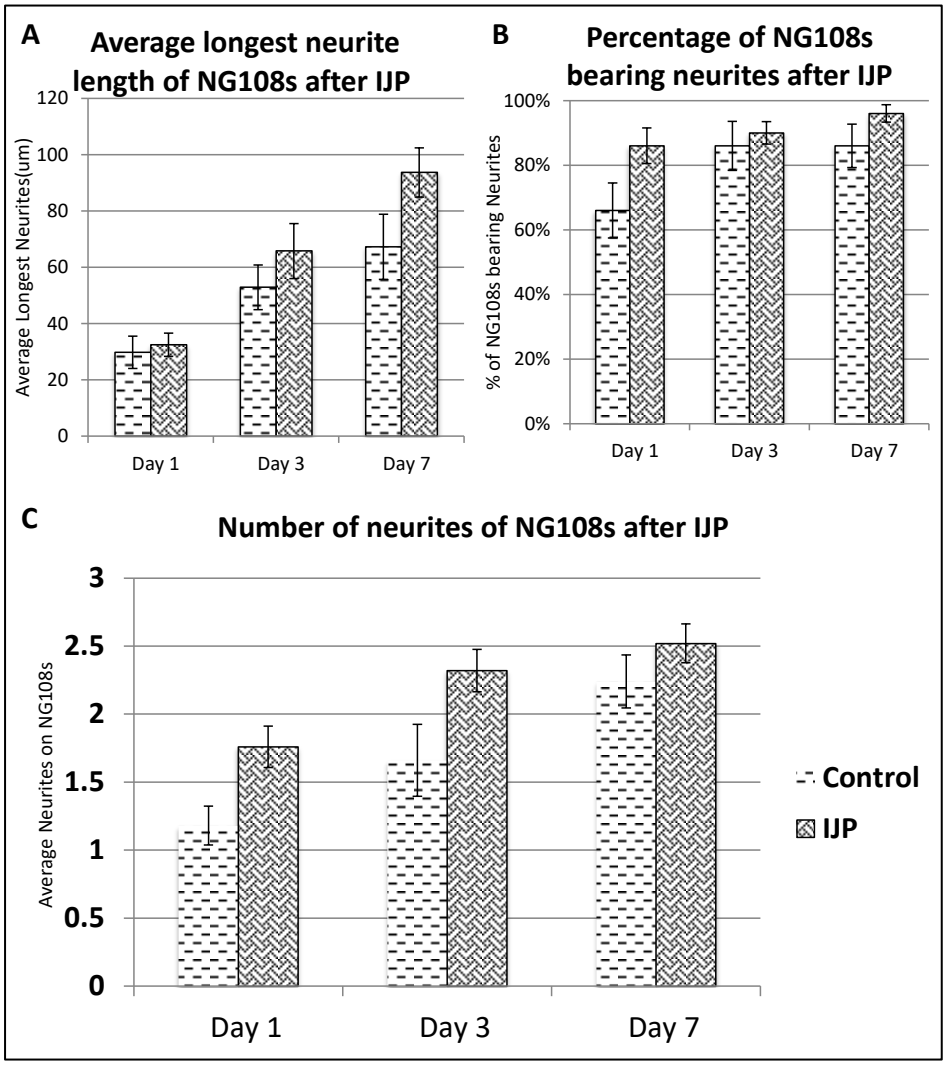

Figure 6.5.2 Quantitative measurements of NG108-15 cells that include standard deviation of average longest neurite length (A), percentage of cells bearing neurites (B) and number of neurites (C). Cells were cultured in serum-free cell medium to induce differentiation and the generation of neurites. (n = 50).

Thus, piezoelectric printing caused neuronal cells to develop more neurites during the first 3 days after printing. By day 7, no other trends were observed that reached statistical significance except for neurite length, and the number of neurites were similar to controls.

It is observed that the inkjet printing process caused nerve cells to generate neurites earlier than normal and had longer neurites. This can be explained if it was assumed that the rate of growth of neurites is constant, and because more neurites were established by day 1 through the printing process, by day 7, the neurites from printed cells would be longer as they had longer to form. The implications of this

study, showing inkjet printed cells generating more neurites initially post printing, could be of benefit to future research in cell-cell interactions, as inkjet printed nerves form more neurites initially (up to 3 days post printing, and then no statistical difference in number can be seen by day 7) and they have more time to extend and elongate compared to controls.

This research shows for the first time that NG108-15 neuronal cells and primary Schwann cells can be piezoelectrically printed with no adverse effects over a range of experimental voltages that have not been used previously. The process of piezoelectrically printing cells was not detrimental, as assessed immediately after printing at 80 V and when assessed throughout 7 days following printing. The viability data for fibroblasts was comparable to that reported by Saunders (et al. 2008), who found a range of 94%-98% for piezoelectric voltages of 40 V to 80 V. In the present work this was extended to 230 V - at this voltage fibroblasts had a viability of 89%, neuronal cells 96% and Schwann cells 90%, respectively. The higher voltages studied indicate better freedom of use of inkjet printing parameters can be used to create successful droplet formation for cell printing than previously investigated. Schwann cells maintained their phenotype through the process of inkjet printing as shown by the presence of S100β, with data showing a slight increase in viability 7 days after printing compared to controls. Initial analysis showed more neurites were formed with inkjet printed cells, however by day 7, no statistical significance was seen. The initial increase in the number of neurites per cell with printed samples had an influence on neurite lengths, as they had more time to grow compared to controls. Printed neuronal NG108 cells displayed longer neurites than controls. Future work could focus on printing co-cultures that will interact to form biologically relevant *in vitro* tissue engineered constructs. Using inkjet printing to position neuronal cells could produce finer neuronal networks than previously produced, as printed cells produced longer neurites, with the implication that fewer cells may be required for a continuous neuronal system. The next stages could include the ability of printed networks to propagate action potentials. Action potentials are a change in the electoral membrane potential of a cell, and travels through to adjacent neuronal cells through synapses to allow communication of distant neuronal cells. Such systems will be of benefit for advancing 3D *in vitro* lab chip devices and studies on neurodegenerative disorders.

6.6 Cell printing behaviour

6.6.1 Introduction

Bioinks containing biological cells have different viscosity and surface tension compared to standard inks, and little is done to optimise the rheological behaviour of such inks, since additions (e.g. ethylene glycol) can be potentially hazardous to cells. Over time, cells begin to aggregate within the printing system and eventually clog the printhead, stopping further inkjet printing. The clogging of the printhead did not affect the printing experiments reported so far contained within this chapter, as no cell printing was required to be carried out for extended periods of time. In commercial applications and more complicated sets of experiments, it is possible that long periods of printing would be required, such as organ printing and lining tissue engineered scaffolds with cell printed designs.

Thomas Boland and his group used 3x phosphate-buffered saline (PBS) for cell printing solutions, which shrank the cells (caused by osmosis) to reduce printhead clogging, but lead to an increase in cell death [259]. Parsa (et al. 2010) and Chahal (et al. 2012) used biocompatible surfactants such as Pluronic in combination with physical agitation (stirring) and Ficoll PM400 respectively to alleviate restrictions in printing time and maintain cell printing consistency, delaying cell sedimentation and overall increasing the reliability in the cell printing process. The use of stirring within the reservoir has also been considered for bioprinting applications, however for the Microfab system used in this thesis, this methodology would be ineffective as the reservoirs and capacity within the printing system has insufficient space for such apparatus.[243]

This section discusses the printing behaviour of NG108s over time at 80 V. The printing quality was assessed through printing NG108-15s at 40,000/mL at 100Hz into 96 well plates for 1 minute per well. The cells deposited in each well w counted with a light microscope and tallied, up to 96 minutes to determine the cell count per minute.

6.6.2 Results

Figure 6.6.1 shows the results of cell number at each time interval, from 1 minute to 96 minutes. Cell numbers were initially high; with 150-50 cells being jetted per minute. However the cell numbers

decreased steadily over time. By 40 minutes, the cell number through inkjet printing becomes significantly low; after an hour, only one or two cells would be seen to be jetted from the system.

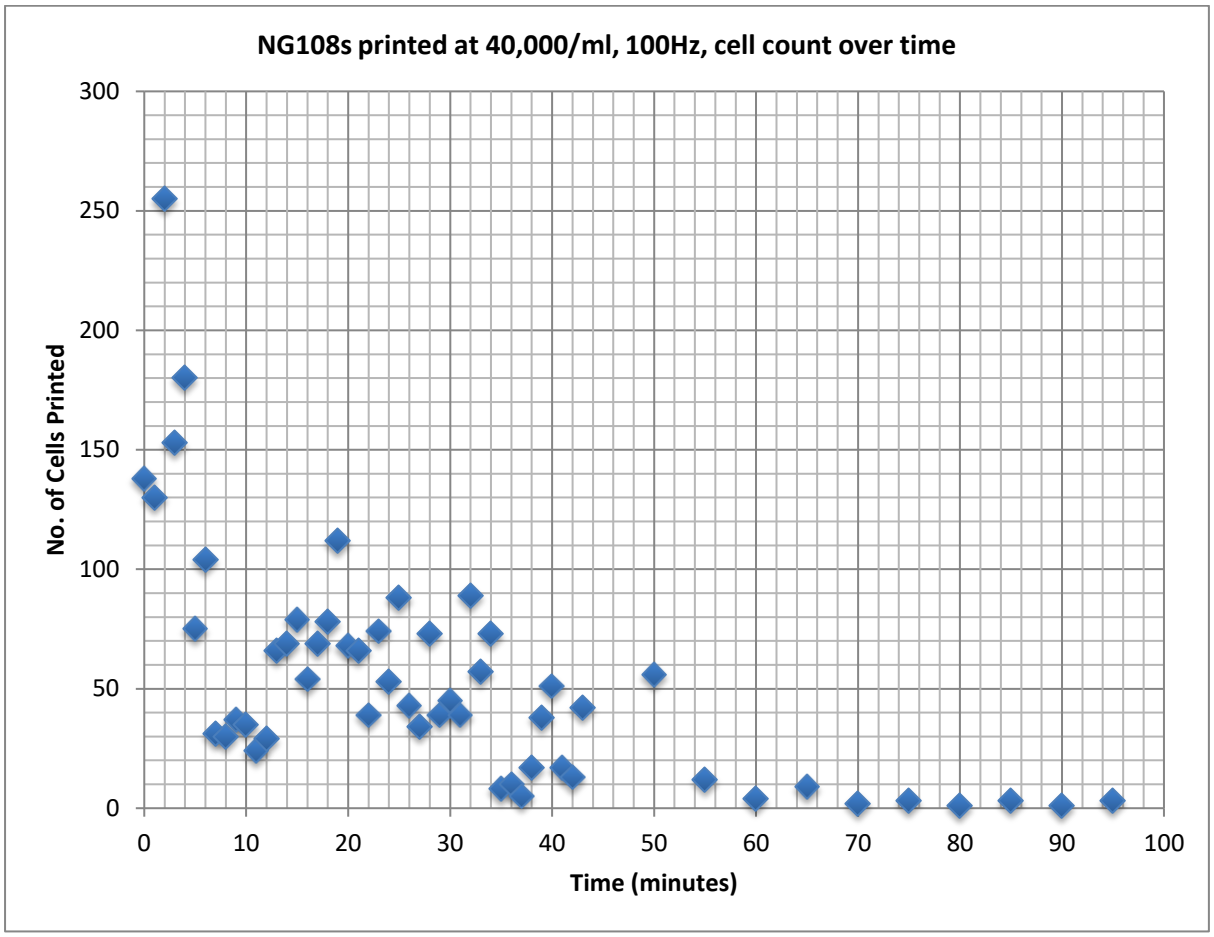

Figure 6.6.1 Number of cells deposited through inkjet printing over time 40,000 cells/mL.

This experiment showed cell printing produced viable cells up to a maximum of 40 minutes after loading into the inkjet printer without the need for surfactants or stirring. This finding is in line with previous studies that report a 20 to 40 minute cell deposition time is possible before cell aggregation (Lorber et al. 2013; Pepper et al. 2011; Saunders et al. 2008). Such studies showed a decrease in cell number after 40 minutes and it was speculated that this was caused by sedimentation of cells to the bottom of the print reservoir and also through adherence to the tubing and glass capillary of the printhead.[267]

The cause of the decrease in cell numbers was concluded to be caused by cell aggregation at the bottom of the reservoir containing the bioink. Immediately after installing the bioink-filled reservoir into the printing system, gravitational and inertial forces cause a change in uniformity within the reservoir and aggregation slowly accumulates (Figure 6.6.2).

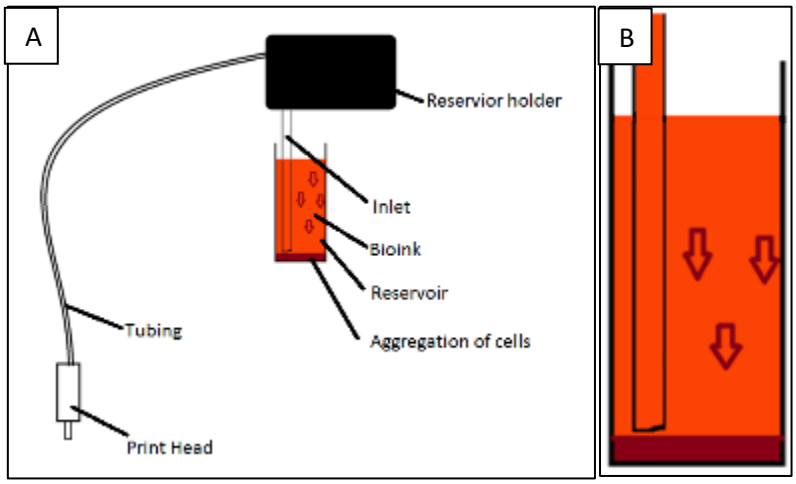

Figure 6.6.2 A) Schematic of printer design. Over time, cells within the bioink aggregate to the bottom of the reservoir and are unable to travel through the inlet and reach the printhead. B) Close-up of reservoir to highlight the occurrence of cell aggregation at the bottom of the reservoir over time

The assumption of cells aggregating at the bottom of the reservoir was confirmed visually by seeing a denser material forming at the bottom of the reservoir over time (Figure 6.6.3). In Figure 6.6.3, cells can be seen highlights with white, and shows the difference in the amount of cells present in each compartment of the printing system, the most seen in the PTFE tubing and the reservoir. This was caused by the cells within the bioink sedimenting to the bottom of the reservoir. Clogging did occur occasionally and can be explained because aggregation increases the particle size travelling through the system, and therefore blockages can occur.

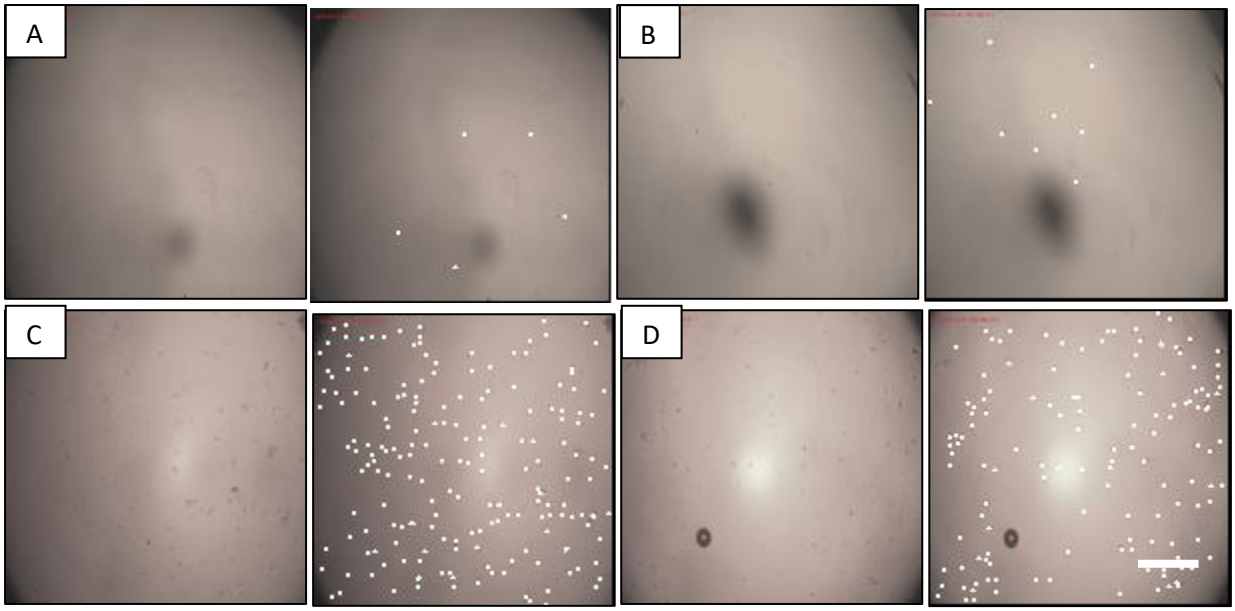

Figure 6.6.3 Microscopy images in sets of two of cell solution contained in; (A) holder, (B) printhead, (C) reservoir, (D) PTFE tubing. Adjacent images of each labelled image highlights cells using white. Cell solutions were extracted through using flushing with trypsin to detach cells. Cell can be seen in the reservoir and PTFE tubing. Scale bar = 200 µm

Trypsin was used to flush each section of the system to identify if cells had adhered to any other part of the system, and it was found that the PTFE tubings connecting the reservoir to the printhead had cells present after experimentation.

This experiment showed cells adhered and aggregated within the reservoir and PTFE tubings of the printing system (Jetlab 4, Microfab).

6.7 Aspirating the printer to reset bioprinting printing behaviour

6.7.1 Introduction

The number of cells that were printed decreased over time, and on average, up to 40 minutes of printing could be done before cell printing became ineffective due to cell aggregation within the printing system. Surfactants could be added to the ink to increase the longevity of the cell-laden inks, but what was tested with this section was the use of pressure to increase the maximum time of printing.

Using the pressure generator that is part of the printing system, the pressure was manipulated to "flush" and "mix" the bioink. It was hypothesised that this manipulation could alleviate the problems of cell clogging and aggregation. This process has been termed aspirating in this section (and the term aspirating will be seen several times).

Outlined in Figure 6.7.1 is how cells in the ink behave. Initially, cells are homogenously dispersed when the ink is first deposited in the reservoir in the printing system (Figure 6.7.1A), and over time, gravitational forces causes cells to fall. Over time, a thin layer of cells are deposited at the bottom of the reservoir whilst the ink is being sucked up into the PTFE tubing to the printer for jetting (Figure 6.7.1B). After around 40 minutes, the cell concentration in the ink suspension decreases significantly as the majority of cells line the bottom of the reservoir, and there is minimal amount of cells being jetted from the printing system (Figure 6.7.1C). It was postulated that using the air pressure generator of the printing system, cycling between maximum negative and positive pressure ($\pm$300 psi) within the system would dislodge the cells at the bottom of the reservoir (Figure 6.7.1D), taking 10-20 seconds, until the cell population goes back to its original concentration (Figure 6.7.1E). The cycling between positive and negative pressure would cause the ink to travel back to the reservoir and bubble through with air, along with any blockages and would disrupt the aggregation occurring at the bottom of the reservoir. The intake of air causes dispersion within the cell media, and dissociates aggregated cells. After aspirating the vial, positive pressure is applied to reintroduce the cell media back into the printhead, and the pressure re-calibrated to create an optimal jetting setup.

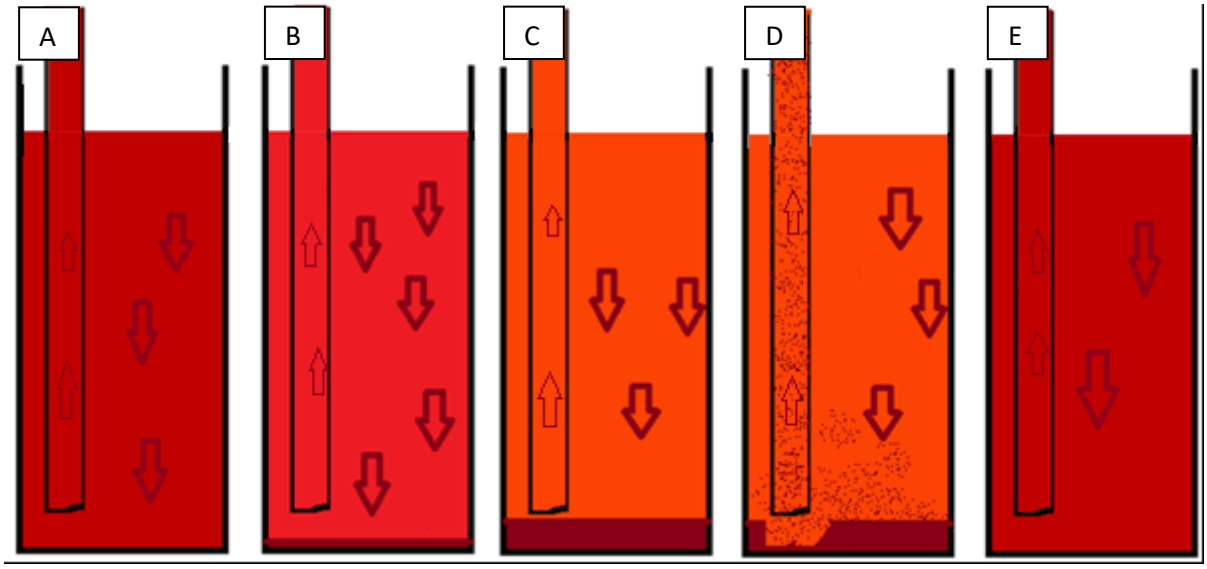

Figure 6.7.1 Cell printing over time. A) Initial condition for the cell suspension in the printer. The suspension has a uniform cell concentration. B) Over a few minutes, gravitational and inertial forces pull cells downwards, causing a slight build-up of cells at the bottom of the vial. C) At longer periods of time, cells aggregate more, decreasing the total cells being jetted out of the printer, until a clump of cells form and is sucked into the printer tubing, which will eventually cause a clog at the printhead. D) To remove this problem, the cell media can be aspirated with a negative purge, causing a disruption in the vial containing the cells. If this is done at too short of a duration, the concentration of cells in the cell media would not be uniform, and when the setup is re-optimised, a higher concentration of cells may be deposited due to taking up a pool of higher concentration cell solution that hasn't been mixed uniformly. E) If the cell solution is mixed thoroughly, the cell solution would have a uniform cell concentration again, and this can be re-introduced to the printing setup.

It was speculated that aspirating the system at regular intervals would be able to prolong the printing time of the bioink with cells. NG108s were printed at 80 V, 40,000 cells/mL at 100Hz into 96 well plates for 1 minute per well. The printer was aspirated at different time intervals and the cells deposited in each well were counted with a light microscope and tallied, up to 96 minutes to determine the cell count per minute.

6.7.2 Results

Figure 6.7.2 shows the results of aspirating the printing system when printing cells. Aspirating does not produce an effective means to restore the cell deposition rate. With this set of experiments, cell deposition started very high (just below 900 cells in the first minute), and decreased steadily, and by 20 minutes, the cell count reached just under 100 cells per minute. When the system was aspirated, there was an increase in cells deposited to around 250 cells (x2.5 more than without aspirating), however the cell count quickly returned to very low values after a few minutes. The second time the system was aspirated showed similar results; an increase in cell number immediately after aspirating, but then the cell count returned to control values.

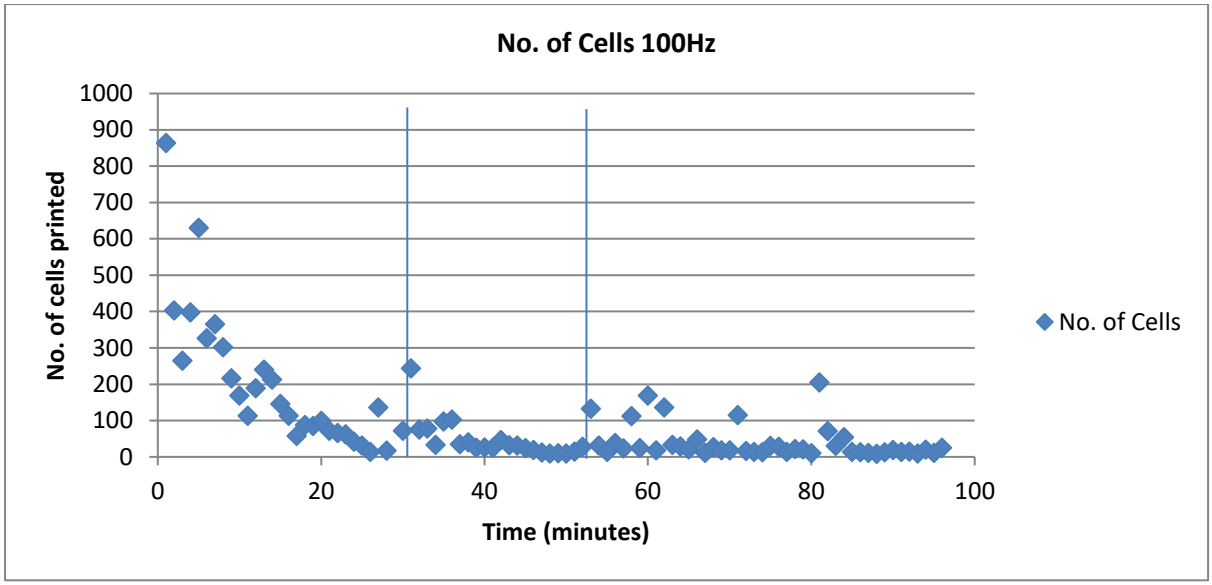

Figure 6.7.2 Cell count over time. The system was aspirated at 30 minutes and 55 minutes (vertical lines)

The number of cells that were printed out after aspirating did not return to initial numbers and it was speculated that cells within the reservoir was able to aggregate together and form clumps within the reservoir, as opposed to making a homogenous solution. The average cell count fluctuates too irregularly, which limits the use of this method of increasing the printing duration of cell-laden inks, as cell distribution within a sample would not be regular, which can affect the viability of samples if there are too little cells within a given population. If there are too little cells within a population, there is a possibility that cells would not grow very well due to the lack of cell-to-cell interactions to encourage proliferation.[228]

There are several moments during the experiment where the cell number spiked after aspiration. As seen in Figure 6.7.2, after the second aspiration at 55 minutes, spikes in cell number can be seen around 60 minutes, 73 minutes and 80 minutes. These values could be explained as being caused by the jetting of aggregated collective of cells being jetted through the printer, that have been separated from the main aggregate of cells at the bottom of the reservoir by the aspiration processes. These smaller aggregates are jetted out at random times from the printer and there are no hypothesised methods to control the deposition of such aggregates within the system, since factors such as aspiration duration and force

become significant factors that cannot be calculated in relation to the dissociation of the layer of cells at the bottom of the reservoir.

Aspirating the system could be done at shorter intervals, but this should be kept at a minimum, as aspirating the system involved stopping the printing procedure and is labour intensive to reset and optimise the jetted droplet.

In summary, the use of pressure through aspirating the system doesn't seem to be a sufficient method to mix and re-suspend the cells within the bioink. The aggregates that are successfully dissociated from the reservoir have non-consistent particle diameters, which can be the cause of further blockages within the printing system later in time when such aggregated are able to travel through the PTFE tubing and into the printhead. If the printing duration needs to exceed 40 minutes, the use of surfactants that have been reported in research papers would be more ideal than rely on the use of aspiration to homogenise the cell-laden ink within the printing system.[143,266]

6.8 Conclusions

This chapter showed that eukaryotic cells, ranging from fibroblasts to neuronal cells such as Schwann cells and NG108-15s could be printed within a range of voltages from 50-230 V without significant damage. It had been reported that cells could be inkjet printed with minimal damage by research groups around the world [81,99,102,140]. What has been shown in this set of work is that neuronal cells such as NG108-15s and supporting Schwann cells (porcine) can also be printed with a high level of viability. At up to 230 V, fibroblasts had a viability of 89%, neuronal cells 96% and Schwann cells 90%, respectively, and proliferated in a similar manner as controls after inkjet printing. NG108-15s grew slightly longer dendritic processes when inkjet-printed. This was speculated to be caused by the cells experiencing stress whilst being jetted through the printer, which caused the cells to differentiate quicker than normal, and therefore over a given time, their dendritic processes would be longer because they had longer to grow.

No group had previously inkjet printed Schwann cells, and now there is now a strong basis for the combination of inkjet printing of cells, growth factors and extracellular matrix components to create neural tissue for research. Inkjet printing shows no significant damage to be done to cells

It was confirmed that cell-printing could only be done within 40 minutes of installing the cell-laden ink into the printer, as previously shown by other groups.[124,140,251] The use of aspirating the cell-laden solution to homogenise the ink over time was tested and concluded that this was not a viable method to re-suspend the cells, as cells aggregated together still remain clumped together, which can be jetted through the system at random time points after aspirating, or be the cause of clogging later during the printing process.

7 Future directions

Inkjet printing more variety of cell types

There is more scope in printing different cell types to understand how this technique influences cell behaviour, proliferation and differentiation. Neuronal cells were inkjet printed within the thesis and showed that they can endure the printing environment with minimal loss and detriment.

An area of interest to pursue would be the inkjet printing of stem cells. There has been more research undertaken with laser printing of stem cells,[268] and inkjet printing of polymers to direct stem cell patterning,[43] however the direct use of inkjet printing of stem cells has yet to be investigated.

Fabricating crosslinked gelatin scaffolds for neuronal applications

The main advantage of using inkjet printing techniques to create crosslinked gelatin scaffolds is because this allows the creation of ordered scaffolds within a micron scale, and due to the nature of hydrogels (consisting of >80% water), cell infiltration into the scaffold is possible. Other techniques such as electrospinning are more rapid and would be more suitable should the user need a bulk material for space filling i.e. for wound repair, or the creation of mats with nano scale fibres and very high porosity.

Being able to make long continuous fibres on the micron scale (100-200 µm), it would be interesting to investigate the potential of seeding neuronal cells with/without their supporting cells for neuronal tissue engineering. Neuronal cells proliferate much more slowly compared to fibroblasts, and it would be possible to create a continuous neuronal circuit with seeded neuronal cells, and the researcher can design a suitable neuronally relevant shaped scaffold; suitable for biomedical and lab-on-a-chip applications. Previously, Li et al[269] created electrospun gelatin fibres containing a conductive polymer called polyaniline that showed to create a conductive scaffold. A similar approach could be applied with the use of inkjet printing, by the addition of polyaniline into the gelatin to create biologically compatible and conductive scaffolds of complex design for cardiac and neuronal tissue engineering. For electrospun scaffolds, an additional technique such as laser sintering to selectively cut the mat of electrospun fibres would be required to create the desired complex shapes.

Creating patterned co-culture environments

The technique to deposit cells into predefined patterns using inkjet printed wax could have great potential when used in the co-culture of cells; after wax removal, the deposited cells are positioned at predetermined locations, and another cell seeding can take place to organise cells easily. Currently, such a process takes time and requires more experimental equipment if done with standard practices (single-cell automated deposition, printing cell-adhering proteins, laser directed deposition).

Native tissue anatomy can be very complicated, and to study more than single cell populations, more innovative methods are required to mimic such tissues. Through altering the printing parameters, the volume of wax ejected can be changed, and the printed line behaviour can be manipulated to create isolated wells that are ideal for single cell studies (Figure 6.8.1).

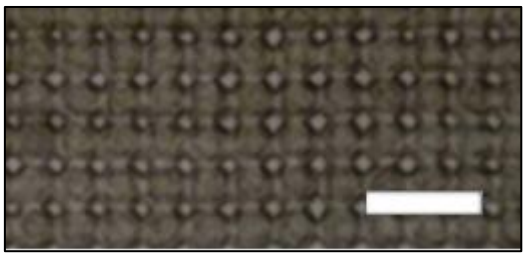

Figure 6.8.1 Through the manipulation of droplet spacing, non-interconnected spaces suitable for deposition of individual cells can be created, whereby the spaces are suitable for single cells to occupy. The grid structure was created through using the same droplet spacing of 40 µm, but the inkjet printing parameters were altered to create smaller droplets. Scale bar = 100 µm.

Naturally most eukaryotic cells favour to be grown in clusters with neighbouring cells together, as neighbouring cells encourage one another to proliferate and survive through the deposition of extracellular matrix and release of mitogens (chemicals that encourage proliferation).[228] This gives a positive feedback that promotes the cells to differentiate as more cells in the surrounding area is a sign of favourable conditions for cell growth. The example of single cell deposition mentioned above would compliment more complicated experimental designs, including spatially controlled co-culture of cells. Having the ability to remove the wax scaffold can benefit the control of the deposition of cells within wax printed devices. An example of an application is for neuronal research. Within the endoneurial space, Schwann cells comprise 90% of the space, and the rest being composed of axons and nucleated cells.[37] By printing a volume/space ratio comparable to the endoneurial space, in vitro models can better

imitate native nerve tissue. Figure 6.8.2 shows how this could be implemented with inkjet printing; whereby the first set of cells which are seeded can be nerve cells, and which, once the wax has been removed, the substrate can be covered with supporting Schwann cells to better study the interaction between glia and nerve cells.

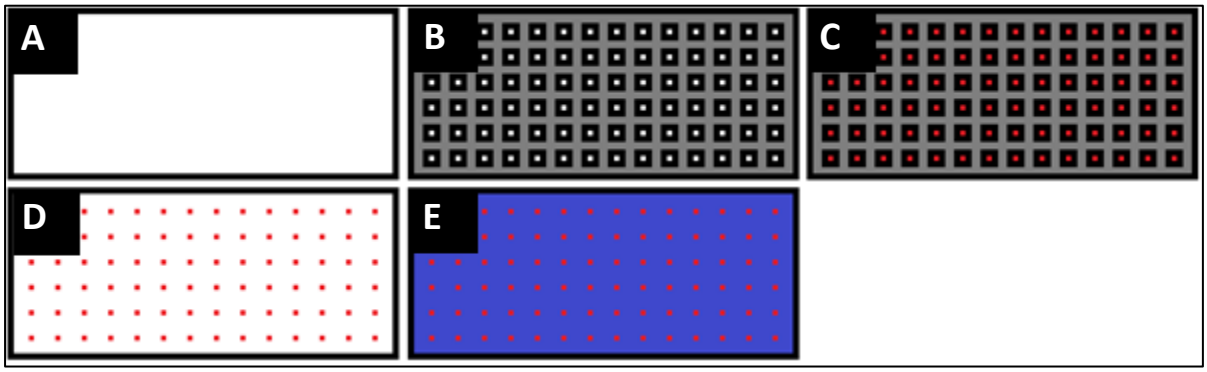

Figure 6.8.2 Step-by-step depiction of creating spatially patterned co-culture. (A) Plain substrate, (B) inkjet print a relevant wax mold, (C) seed cell type A onto the substrate, whereby the cells will adhere to the substrate where there is no wax present, (D) physically remove wax to only leave the adhered cells on the substrate, (E) Seed cell type B onto the substrate to create a bespoke co-culture with selectively arranged cells.

Analysis of phantoms

A better non-invasive method of analysing 3D space within the phantoms is required to better understand the rheological characteristics of the fabricated phantoms. The problems found with using a confocal microscope with fluorescent microbeads was that only a 2D plane could be analysed, which limited the ability to identify rheological behaviour within the phantoms in a non-invasive way. In the future, the use of ultrasonic equipment would alleviate such limitations, as it would allow the analysis of the 3D space within the model.

8 Appendix ONE

Inkjet printing gelatin

Initial experiments were created to inkjet print gelatin scaffolds that could be patterned to desired biologically relevant patterns. It was shown (Figure 6.81) that gelatin concentration of 2% and lower could be printed, as their viscosity lies within printable values (1-10 mPa.s). For gelatin concentrations that were above 2%, the printing temperature needed to be increased (through the use of the heated polymer jet) to create conditions ideal for printing.

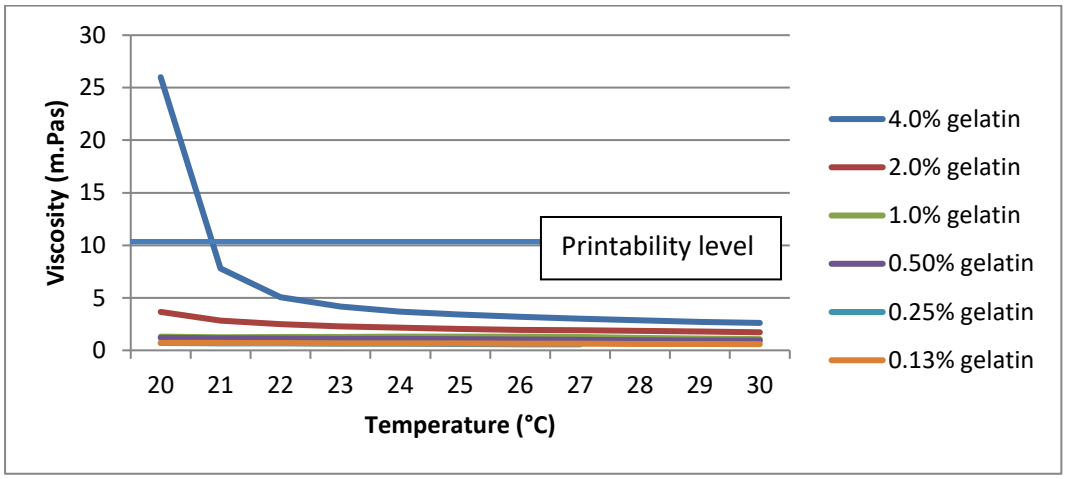

Figure 6.81 graph showing viscosity values of varying gelatin concentrations at different temperatures through the use of a rheometer. Line drawn at 10 m.Pas to indicate maximum printability level of inkjet printing.

Figure 6.8.2 (Above) and (Bottom) show inkjet printed gelatin on a glass cover slip. 4% gelatin was put inside the inkjet printing system, and the temperature increased to 30°C. Each time a successful droplet formation could be produced, printing became clogged and failed within 5 minutes of cleaning the apparatus. This made optimising the droplet spacing and printing parameters difficult. Therefore printing gelatin was not considered in future experiments, but instead, glutaraldehyde was printed onto a bed of gelatin.

Table 5 showing data gathered through adding different concentrations of glutaraldehyde onto different concentrations of gelatin, at 5 µL and left overnight. The samples were then washed in warm water to remove uncrosslinked gelatin, and the diameter of crosslinked gelatin was measured. Using this value, and knowing the height of the gelatin, the amount of crosslinking could be calculated, with a dimensionless number can be created to give a value to the amount of gelatin was crosslinked with glutaraldehyde (n=3). No data shown for 0.50% glutaraldehyde with 2% gelatin as the construct was too fragile and washed off during the removal of uncrosslinked gelatin.

Average diameter (mm)	Gelatin	Conc.			
Glutaraldehyde Concentration	20%	10%	8%	4%	2%
25%	12	13.5	14.5	15	14.5
10%	9.5	10.5	11	13	11
5%	8	9	8.66	9.5	9.5
2%	6	6.2	6.7	7.2	7.8
1%	5.3	5.3	5.3	5.3	5.3
0.50%	5	4.2	4.2	4.2	n/a
Total Volume crosslinked (µL)	Gelatin Conc.				
Glutaraldehyde Concentration	20%	10%	8%	4%	2%
25%	177.79	225.01	259.58	277.8	259.58
10%	111.43	136.12	149.39	208.66	149.39
5%	79.02	100.01	92.59	111.43	111.43
2%	44.45	47.46	55.42	64	75.12
1%	34.68	34.68	34.68	34.68	34.68
0.50%	30.87	21.78	21.78	21.78	n/a
crosslinked gelatin (µL)	Gelatin Conc.				
Glutaraldehyde Concentration	20%	10%	8%	4%	2%
25%	35.558	22.501	20.7664	11.112	5.1916
10%	22.286	13.612	11.9512	8.3464	2.9878
5%	15.804	10.001	7.4072	4.4572	2.2286
2%	8.89	4.746	4.4336	2.56	1.5024
1%	6.936	3.468	2.7744	1.3872	0.6936
0.50%	6.174	2.178	1.7424	0.8712	n/a
Efficacy of glutaraldehyde	Gelatin Conc.				
Glutaraldehyde Concentration	20%	10%	8%	4%	2%
25%	28.4464	18.0008	16.61312	8.8896	4.15328
10%	44.572	27.224	23.9024	16.6928	5.9756
5%	63.216	40.004	29.6288	17.8288	8.9144

2%	88.9	47.46	44.336	25.6	15.024
1%	138.72	69.36	55.488	27.744	13.872
0.50%	246.96	87.12	69.696	34.848	n/a

Total glutaraldehyde volume = Volume of glutaraldehyde solution (5 µL) * Glutaraldehyde concentration

Total crosslinked gelatin volume = $\pi \times r^2 \times h$

Total crosslinked gelatin = total volume crosslinked x gelatin concentration

Efficacy of glutaraldehyde = total crosslinked gelatin / total glutaraldehyde volume

Day1

			Healthy	80%	50%	20%	Dead
1hr	0.50%	0.25				x	
1hr	0.50%	0.5				x	
1hr	0.50%	0.125			x		
1hr	0.50%	1				x	
1hr	0.50%	Control	x				
1hr	1.00%	0.25			x		
1hr	1.00%	0.5					x
1hr	1.00%	0.125		x			
1hr	1.00%	1					x
1hr	1.00%	2					x
1hr	1.00%	Control	x				
1hr	2.00%	0.25		x			
1hr	2.00%	0.5			x		
1hr	2.00%	0.125		x			
1hr	2.00%	1					x
1hr	2.00%	2					x
1hr	2.00%	Control	x				
1hr	4%	0.25		x			
1hr	4%	0.5			x		
1hr	4%	0.125	x				
1hr	4%	1					x
1hr	4%	2					x
1hr	4%	Control	x				
2hrs	0.50%	0.25		x			
2hrs	0.50%	0.5				x	
2hrs	0.50%	0.125			x		
2hrs	0.50%	1					x
2hrs	0.50%	2					x
2hrs	0.50%	Control	x				

2hrs	1.00%	0.25					x
2hrs	1.00%	0.5					x
2hrs	1.00%	0.125		x			
2hrs	1.00%	1					x
2hrs	1.00%	2					x
2hrs	1.00%	Control	x				
2hrs	2.00%	0.25			x		
2hrs	2.00%	0.5					x
2hrs	2.00%	0.125		x			
2hrs	2.00%	1					x
2hrs	2.00%	2					x
2hrs	2.00%	Control	x				
2hrs	4%	0.25		x			
2hrs	4%	0.5				x	
2hrs	4%	0.125	x				
Day1							
			Healthy	80%	50%	20%	Dead
2hrs	4%	2					x
2hrs	4%	Control		x			
5 minutes	0.50%	0.25		x			
5 minutes	0.50%	0.5			x		
5 minutes	0.50%	0.125	x				
5 minutes	0.50%	1				x	
5 minutes	0.50%	2					x
5 minutes	0.50%	Control		x			
5 minutes	1.00%	0.25					
5 minutes	1.00%	0.5		x			
5 minutes	1.00%	0.125		x			
5 minutes	1.00%	1				x	
5 minutes	1.00%	2					x
5 minutes	1.00%	Control	x				
5 minutes	2.00%	0.25	x				
5 minutes	2.00%	0.5		x			
5 minutes	2.00%	0.125	x				
5 minutes	2.00%	1			x		
5 minutes	2.00%	2					x
5 minutes	2.00%	Control	x				
5 minutes	4%	0.25	x				
5 minutes	4%	0.5	x				
5 minutes	4%	0.125	x				
5 minutes	4%	1			x		
5 minutes	4%	2				x	
5 minutes	4%	Control	x				
5 hrs	0.50%	0.25	x				
5 hrs	0.50%	0.5				x	
5 hrs	0.50%	0.125	x				

5 hrs	0.50%	1					x
5 hrs	0.50%	2					x
5 hrs	0.50%	Control	x				
5 hrs	1.00%	0.25					x
5 hrs	1.00%	0.5					x
5 hrs	1.00%	0.125				x	
5 hrs	1.00%	1					x
5 hrs	1.00%	2					x
5 hrs	1.00%	Control	x				
5 hrs	2.00%	0.25					x
5 hrs	2.00%	0.5					x
5 hrs	2.00%	0.125			x		
5 hrs	2.00%	1					
5 hrs	2.00%	2					
5 hrs	2.00%	Control					
Day1							
			Healthy	80%	50%	20%	Dead
5 hrs	4%	0.5					x
5 hrs	4%	0.125		x			
5 hrs	4%	1					
5 hrs	4%	2					
5 hrs	4%	Control					
24hrs	0.50%	0.25					
24hrs	0.50%	0.5					
24hrs	0.50%	0.125					
24hrs	0.50%	1					
24hrs	0.50%	2					
24hrs	0.50%	Control					
24hrs	1.00%	0.25					
24hrs	1.00%	0.5					
24hrs	1.00%	0.125					
24hrs	1.00%	1					
24hrs	1.00%	2					
24hrs	1.00%	Control					
24hrs	2.00%	0.25					
24hrs	2.00%	0.5					
24hrs	2.00%	0.125					
24hrs	2.00%	1					
24hrs	2.00%	2					
24hrs	2.00%	Control					
24hrs	4%	0.25				x	
24hrs	4%	0.5					x
24hrs	4%	0.125			x		
24hrs	4%	1					x
24hrs	4%	2					x
24hrs	4%	Control	x				

30 minutes	0.50%	0.25	x				
30 minutes	0.50%	0.5				x	
30 minutes	0.50%	0.125		x			
30 minutes	0.50%	1					x
30 minutes	0.50%	2					x
30 minutes	0.50%	Control	x				
30 minutes	1.00%	0.25		x			
30 minutes	1.00%	0.5				x	
30 minutes	1.00%	0.125		x			
30 minutes	1.00%	1					x
30 minutes	1.00%	2					x
30 minutes	1.00%	Control	x				
30 minutes	2.00%	0.25		x			
30 minutes	2.00%	0.5				x	
30 minutes	2.00%	0.125		x			

Day1

			Healthy	80%	50%	20%	Dead
30 minutes	2.00%	2					x
30 minutes	2.00%	Control	x				
30 minutes	4%	0.25			x		
30 minutes	4%	0.5				x	
30 minutes	4%	0.125		x			
30 minutes	4%	1					x
30 minutes	4%	2					x
30 minutes	4%	Control	x				

Day 3

			Healthy	80%	50%	20%	Dead
1hr	0.50%	0.25					
1hr	0.50%	0.5					
1hr	0.50%	0.125					
1hr	0.50%	1					
1hr	0.50%	Control					
1hr	1.00%	0.25				x	
1hr	1.00%	0.5					x
1hr	1.00%	0.125			x		
1hr	1.00%	1					x
1hr	1.00%	2					
1hr	1.00%	Control	x				
1hr	2.00%	0.25			x		
1hr	2.00%	0.5				x	
1hr	2.00%	0.125		x			
1hr	2.00%	1					
1hr	2.00%	2					

1hr	2.00%	Control	x				
1hr	4%	0.25			x		
1hr	4%	0.5					x
1hr	4%	0.125		x			
1hr	4%	1					x
1hr	4%	2					
1hr	4%	Control	x				
2hrs	0.50%	0.25					
2hrs	0.50%	0.5					
2hrs	0.50%	0.125					
2hrs	0.50%	1					
2hrs	0.50%	2					
2hrs	0.50%	Control					
2hrs	1.00%	0.25					x
2hrs	1.00%	0.5					x
Day 3							
			Healthy	80%	50%	20%	Dead
2hrs	1.00%	1					x
2hrs	1.00%	2					
2hrs	1.00%	Control	x				
2hrs	2.00%	0.25					x
2hrs	2.00%	0.5					x
2hrs	2.00%	0.125			x		
2hrs	2.00%	1					x
2hrs	2.00%	2					
2hrs	2.00%	Control	x				
2hrs	4%	0.25				x	
2hrs	4%	0.5					x
2hrs	4%	0.125			x		
2hrs	4%	1					
2hrs	4%	2					
2hrs	4%	Control	x				
5 minutes	0.50%	0.25		x			
5 minutes	0.50%	0.5				x	
5 minutes	0.50%	0.125	x				
5 minutes	0.50%	1					x
5 minutes	0.50%	2					x
5 minutes	0.50%	Control					
5 minutes	1.00%	0.25		x			
5 minutes	1.00%	0.5			x		
5 minutes	1.00%	0.125	x				x
5 minutes	1.00%	1					x
5 minutes	1.00%	2					
5 minutes	1.00%	Control	x				
5 minutes	2.00%	0.25		x			
5 minutes	2.00%	0.5			x		

5 minutes	2.00%	0.125	x				
5 minutes	2.00%	1				x	
5 minutes	2.00%	2					x
5 minutes	2.00%	Control	x				
5 minutes	4%	0.25	x				
5 minutes	4%	0.5		x			
5 minutes	4%	0.125		x			
5 minutes	4%	1					x
5 minutes	4%	2					x
5 minutes	4%	Control	x				
5 hrs	0.50%	0.25					x
5 hrs	0.50%	0.5					x
5 hrs	0.50%	0.125				x	
5 hrs	0.50%	1					x
5 hrs	0.50%	2					x
Day 3							
			Healthy	80%	50%	20%	Dead
5 hrs	1.00%	0.25					
5 hrs	1.00%	0.5					
5 hrs	1.00%	0.125					
5 hrs	1.00%	1					
5 hrs	1.00%	2					
5 hrs	1.00%	Control					
5 hrs	2.00%	0.25					
5 hrs	2.00%	0.5					
5 hrs	2.00%	0.125					
5 hrs	2.00%	1					
5 hrs	2.00%	2					
5 hrs	2.00%	Control					
5 hrs	4%	0.25					x
5 hrs	4%	0.5					x
5 hrs	4%	0.125					x
5 hrs	4%	1					
5 hrs	4%	2					
5 hrs	4%	Control	x				
24hrs	0.50%	0.25					
24hrs	0.50%	0.5					
24hrs	0.50%	0.125					
24hrs	0.50%	1					
24hrs	0.50%	2					
24hrs	0.50%	Control					
24hrs	1.00%	0.25					
24hrs	1.00%	0.5					
24hrs	1.00%	0.125					
24hrs	1.00%	1					
24hrs	1.00%	2					

24hrs	1.00%	Control					
24hrs	2.00%	0.25					
24hrs	2.00%	0.5					
24hrs	2.00%	0.125					
24hrs	2.00%	1					
24hrs	2.00%	2					
24hrs	2.00%	Control					
24hrs	4%	0.25					x
24hrs	4%	0.5					x
24hrs	4%	0.125					x
24hrs	4%	1					
24hrs	4%	2					
24hrs	4%	Control	x				
30 minutes	0.50%	0.25	x				
30 minutes	0.50%	0.5					x
Day 3							
			Healthy	80%	50%	20%	Dead
30 minutes	0.50%	1					
30 minutes	0.50%	2					
30 minutes	0.50%	Control	x				
30 minutes	1.00%	0.25					x
30 minutes	1.00%	0.5					x
30 minutes	1.00%	0.125				x	
30 minutes	1.00%	1					
30 minutes	1.00%	2					
30 minutes	1.00%	Control	x				
30 minutes	2.00%	0.25				x	
30 minutes	2.00%	0.5					x
30 minutes	2.00%	0.125		x			
30 minutes	2.00%	1					
30 minutes	2.00%	2					
30 minutes	2.00%	Control	x				
30 minutes	4%	0.25					x
30 minutes	4%	0.5					x
30 minutes	4%	0.125			x		
30 minutes	4%	1					
30 minutes	4%	2					
30 minutes	4%	Control	x				

Figure 9.3 showing the raw data of phenotypic analysis of each sample studied under the microscope and categorising each condition in accordance to cell viability. Health = >80% viability, Dead = <20% viability.

9 APPENDIX TWO

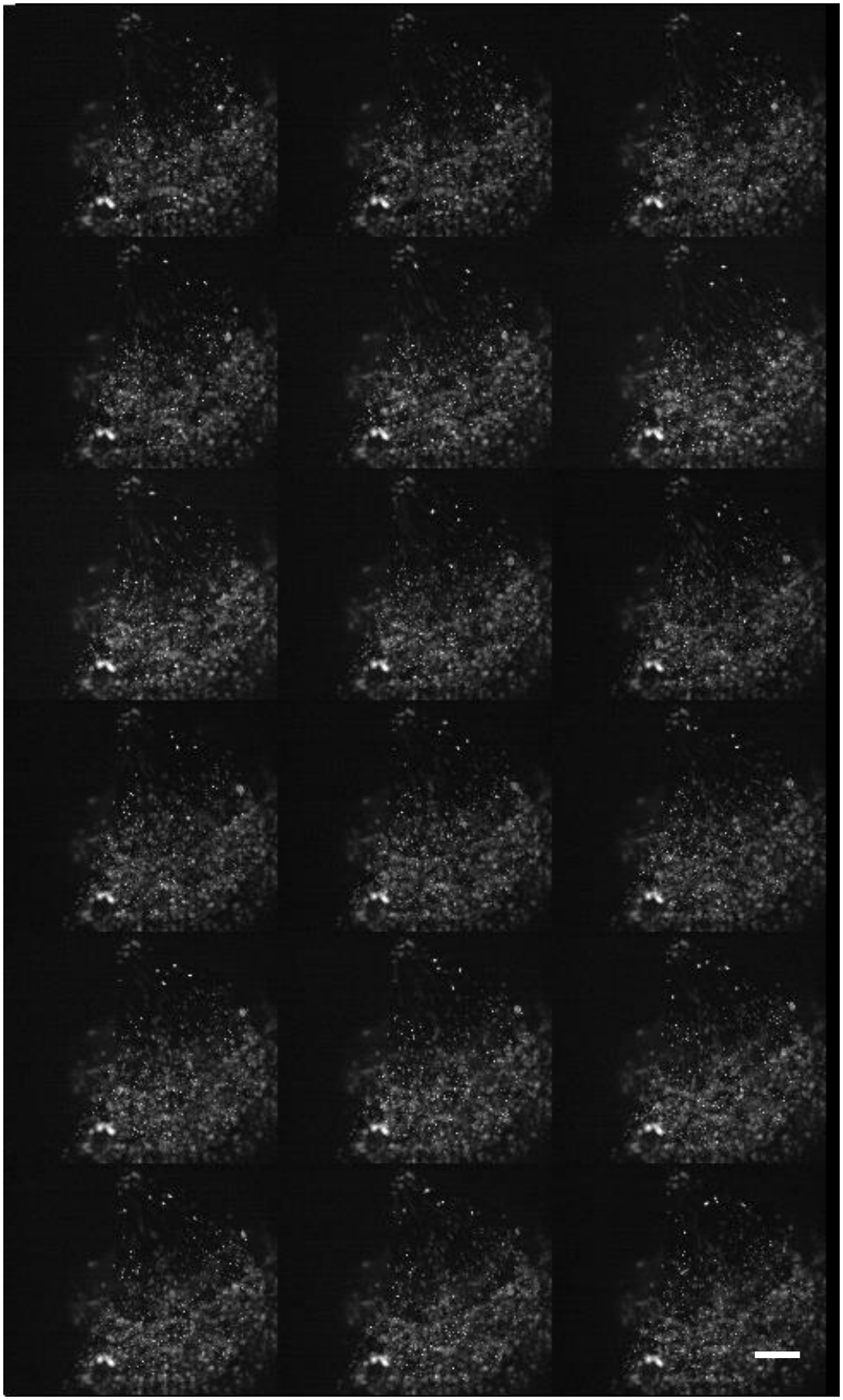

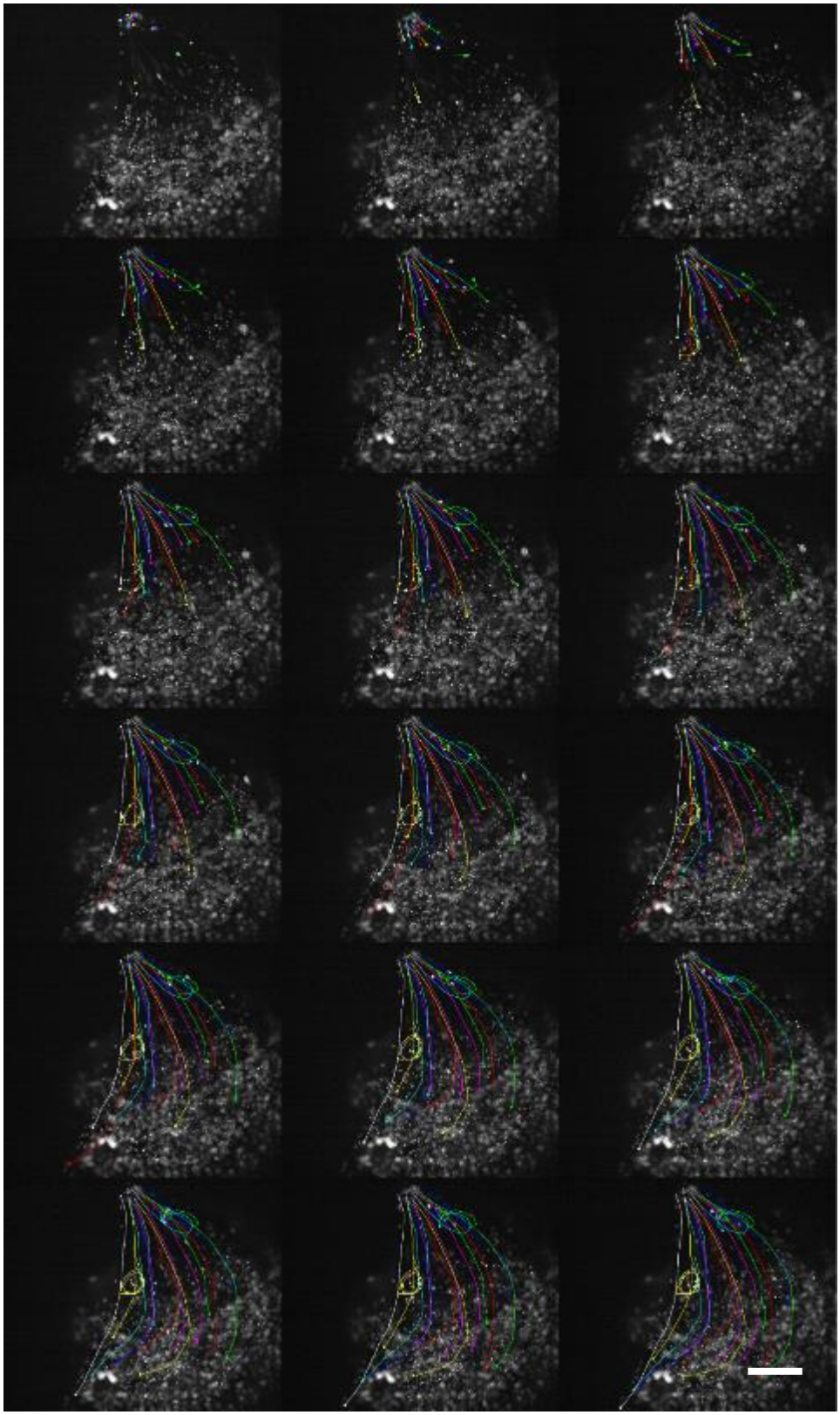

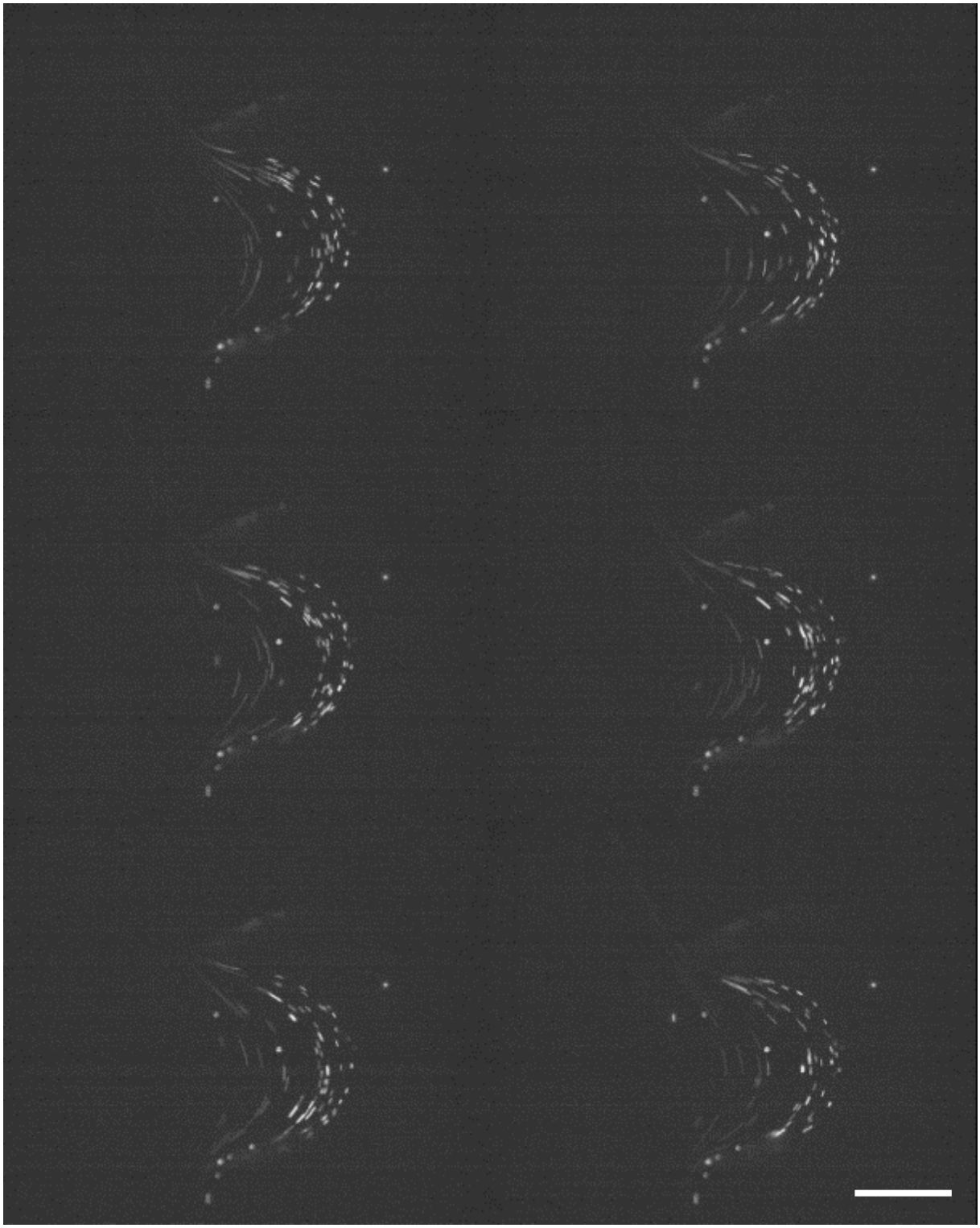

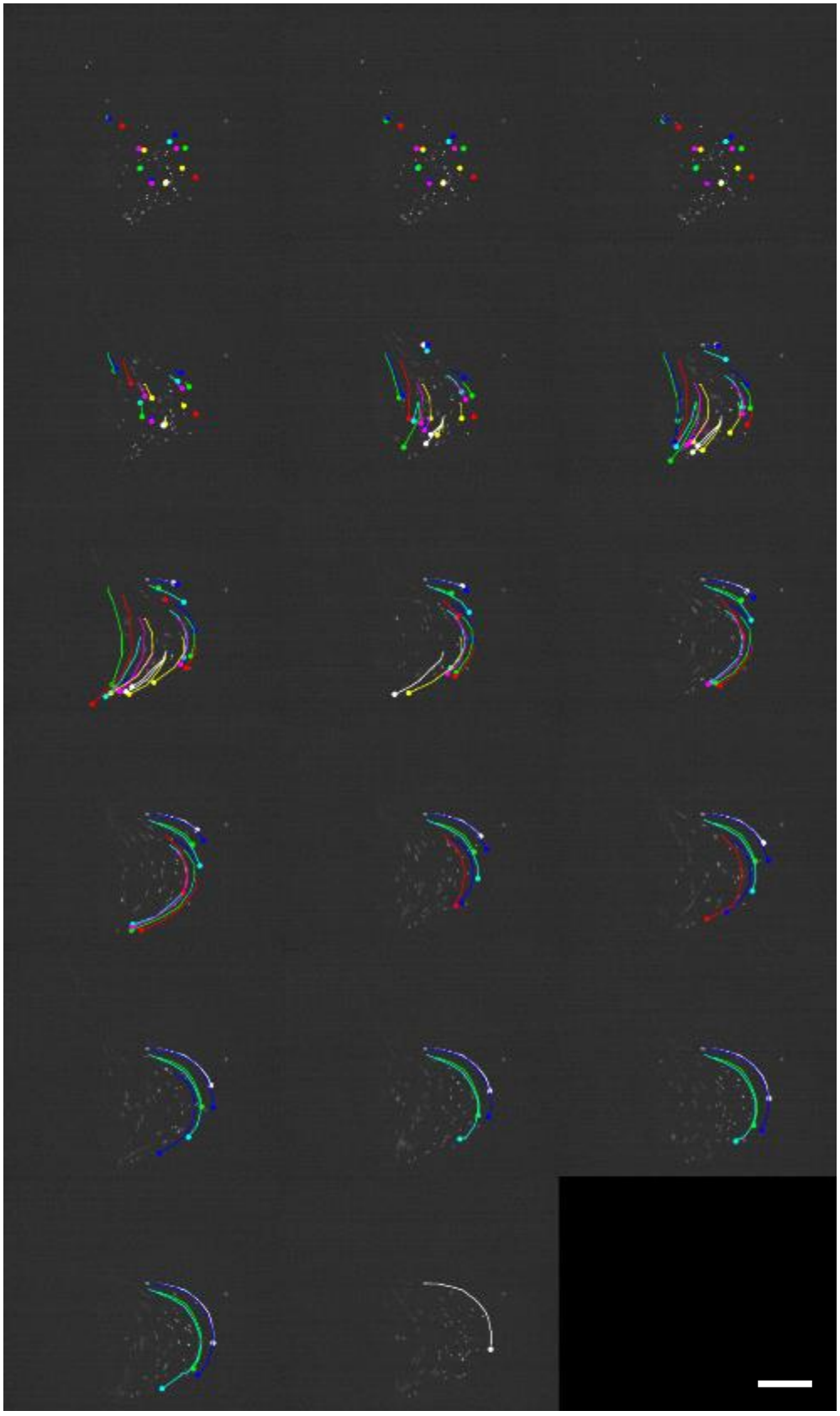

Figure 16.8.1 Images taken at 50 µs apart, showing the movement of fluorescent micro beads traveling through the phantom. Using Manual Tracker (a plugin in ImageJ), individual beads could be tracked through each consecutive image. This allowed the tracking of beads travelling through the phantom. Scale bar = 1000 µm

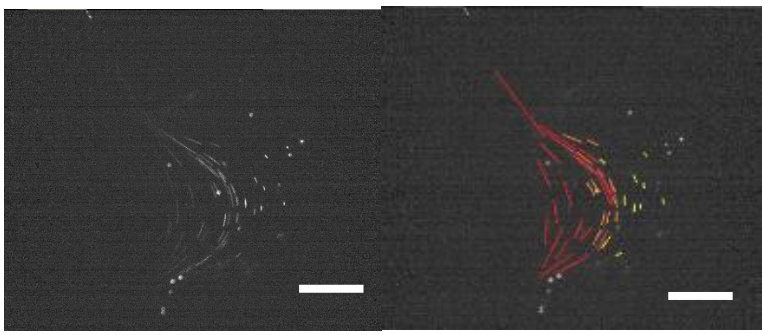

Figure 16.8.2 another method of analysing the data set captured with epifluorescent microscopy with the phantoms created; knowing the exposure time and the size of the micro beads, the motion blur can be used to extrapolate the speed of the beads in the phantom.

10 APPENDIX THREE

10.1 Oral Presentations

Materials KTN Annual Event, “Anti-theft cable technology”, May 2012, London, UK

An Afternoon with ADAM, “Overview of Inkjet Printing”, December 2012, Sheffield, UK

BiTEG 14th Annual White Rose Meeting, “Utilising Inkjet Printing Technology for the Generation of Biological Scaffolds”, December 2012, York, UK,

Careers in Academia, “Life of a PhD Student”, February 2012, Sheffield, UK

Discovery Night, “3D printing in bioengineering”, March 2012, Sheffield, UK

Discovery Night, “3D printing in bioengineering”, March 2015, Sheffield, UK

10.2 Poster Presentations

BiTEG 13th Annual White Rose Meeting, “Fabricating 3D structures for soft tissue engineering applications with inkjet printing”, December 2011, Sheffield, UK

Materials KTN Annual Event, “Anti-theft cable technology”, May 2012, London, UK

10.3 Awards

Sheffield Startup weekend, awarded best presenter during three-day event, November 2011, Sheffield, UK

Enterprise Celebration Dinner, finalist during Awards Ceremony, December 2012, Sheffield, UK

10.4 Publications

Review Paper: Y. Zhang, C. Tse, D. Rouholamin and P. J. Smith, Scaffolds for tissue engineering produced by inkjet printing, Cent. Eur. J. Eng., 2012, 2, 325–335.

Research paper: Tse Christopher, Ng Shea Shin, Stringer Jonathan, MacNeil Sheila, Haycock W. John and Smith Patrick, Utilising Inkjet Printed Paraffin Wax for Cell Patterning Applications, Internation Journal of Bioprinting (Submitted August 18th 2015, minor corrections 7th October 2015, accepted 14th October 2015)

Research paper: Solis-Gonzalez Obed A; Tse Christopher; Fairclough Patrick; Smith Patrick, A new methodology for preparation of giant vesicles using an inkjet printing and confined geometry technique. Soft Matter (Submitted August 5th 2015)

Research paper: Tse Christopher; Whiteley Robert; Yu Tracy; Stringer Jonathan; MacNeil Sheila; Haycock John; Smith Patrick, Inkjet printing Schwann cells and neuronal analogue NG108-15 cells, Biofabrication (Submitted July 8th 2015)

Communication Paper: Rider Patrick, Zhang Yu, Tse Christopher, Zhang Yi, Jayawardane Dharana, Stringer Jonathan, Callaghan Jill, Brook I. M, Miller Cheryl A., Zhao Xiubo, Smith Patrick, Biocompatible Silk Fibroin Scaffold Prepared by Reactive Inkjet Printing, Soft Matter (Submitted October 6th 2015)

Research paper: Tse Christopher; Stringer Jonathan; MacNeil Sheila; Haycock John; Smith Patrick, Crosslinking gelatin scaffolds with inkjet printed glutaraldehyde for cell seeding applications (to be submitted)

11 REFERENCES

1. Langer, R. & Vacanti, J. P. Tissue engineering. *Science (80-.).* **260,** 920–926 (1993).
2. Naderi, H., Matin, M. M. & Bahrami, A. R. Review paper: Critical Issues in Tissue Engineering: Biomaterials, Cell Sources, Angiogenesis, and Drug Delivery Systems. *Journal of Biomaterials Applications* **26,** 383–417 (2011).
3. Flecknell, P. Replacement, reduction and refinement. *ALTEX Altern. zu Tierexperimenten* **19,** 73–78 (2002).
4. Dvir, T., Timko, B. P., Kohane, D. S. & Langer, R. Nanotechnological strategies for engineering complex tissues. *Nat. Nanotechnol.* **6,** 13–22 (2011).
5. Subbiah, T., Bhat, G. S., Tock, R. W., Parameswaran, S. & Ramkumar, S. S. Electrospinning of nanofibers. *J. Appl. Polym. Sci.* **96,** 557–569 (2005).
6. MacDiarmid, A. G. *et al.* Electrostatically-generated nanofibers of electronic polymers. *Synth. Met.* **119,** 27–30 (2001).
7. Bognitzki, M. *et al.* Nanostructured fibers via electrospinning. *Adv. Mater.* **13,** 70–72 (2001).
8. Reneker, D. ., Kataphinan, W., Theron, A., Zussman, E. & Yarin, A. . Nanofiber garlands of polycaprolactone by electrospinning. *Polymer (Guildf).* **43,** 6785–6794 (2002).
9. Demir, M. ., Yilgor, I., Yilgor, E. & Erman, B. Electrospinning of polyurethane fibers. *Polymer (Guildf).* **43,** 3303–3309 (2002).
10. Yoshimoto, H., Shin, Y. M., Terai, H. & Vacanti, J. P. A biodegradable nanofiber scaffold by electrospinning and its potential for bone tissue engineering. *Biomaterials* **24,** 2077–2082 (2003).
11. Townsend-Nicholson, A. & Jayasinghe, S. N. Cell electrospinning: A unique biotechnique for encapsulating living organisms for generating active biological microthreads/scaffolds. *Biomacromolecules* **7,** 3364–3369 (2006).
12. Bhatia, S. K., Hickman, J. J. & Ligler, F. S. New approach to producing patterned biomolecular assemblies. *J. Am. Chem. Soc.* **114,** 4432–4433 (1992).
13. Hsieh, T. M., Benjamin Ng, C. W., Narayanan, K., Wan, A. C. A. & Ying, J. Y. Three-dimensional microstructured tissue scaffolds fabricated by two-photon laser scanning photolithography. *Biomaterials* **31,** 7648–7652 (2010).
14. Kane, R. S., Takayama, S., Ostuni, E., Ingber, D. E. & Whitesides, G. M. Patterning proteins and cells using soft lithography. *Biomaterials* **20,** 2363–2376 (1999).
15. Xia, Y. & Whitesides, G. M. SOFT LITHOGRAPHY. *Annu. Rev. Mater. Sci.* **28,** 153–184 (1998).
16. Singh, M., Haverinen, H. M., Dhagat, P. & Jabbour, G. E. Inkjet printing-process and its applications. *Adv. Mater. Deerf. Beach Fla* **22,** 673–685 (2010).
17. Liu, C., Xia, Z. & Czernuszka, J. T. Design and Development of Three-Dimensional Scaffolds for Tissue Engineering. *Chem. Eng. Res. Des.* **85,** 1051–1064 (2007).
18. Karageorgiou, V. & Kaplan, D. Porosity of 3D biomaterial scaffolds and osteogenesis. *Biomaterials* **26,** 5474–5491 (2005).
19. Harley, B. A., Hastings, A. Z., Yannas, I. V. & Sannino, A. Fabricating tubular scaffolds with a radial pore size gradient by a spinning technique. *Biomaterials* **27,** 866–874 (2006).
20. Roy, T. D. *et al.* Performance of degradable composite bone repair products made via three-dimensional fabrication techniques. *J. Biomed. Mater. Res. A* **66,** 283–291 (2003).
21. Lin, H.-R. & Yeh, Y.-J. Porous alginate/hydroxyapatite composite scaffolds for bone tissue engineering: preparation, characterization, and in vitro studies. *J. Biomed. Mater. Res. B. Appl.*

Biomater. **71,** 52–65 (2004).

22. Hutmacher, D. W. Scaffolds in tissue engineering bone and cartilage. *Biomaterials* **21,** 2529–2543 (2000).
23. Rouholamin, D., Smith, P. J. & Ghassemieh, E. Control of morphological properties of porous biodegradable scaffolds processed by supercritical CO2 foaming. *J. Mater. Sci.* **48,** 3254–3263 (2013).
24. Yeung, T. *et al.* Effects of substrate stiffness on cell morphology, cytoskeletal structure, and adhesion. *Cell Motil. Cytoskeleton* **60,** 24–34 (2005).
25. Guo, W., Frey, M. T., Burnham, N. A. & Wang, Y. Substrate rigidity regulates the formation and maintenance of tissues. *Biophys. J.* **90,** 2213–2220 (2006).
26. Bettinger, C. J., Langer, R. & Borenstein, J. T. Engineering substrate topography at the Micro- and nanoscale to control cell function. *Angewandte Chemie - International Edition* **48,** 5406–5415 (2009).
27. Genzer, J. & Bhat, R. R. Surface-bound soft matter gradients. *Langmuir* **24,** 2294–2317 (2008).
28. Smyth, S. S., Joneckis, C. C. & Parise, L. V. Regulation of vascular integrins. *Blood* **81,** 2827–43 (1993).
29. Halfter, W. The behavior of optic axons on substrate gradients of retinal basal lamina proteins and merosin. *J. Neurosci.* **16,** 4389–4401 (1996).
30. Cao, X. & Shoichet, M. S. Defining the concentration gradient of nerve growth factor for guided neurite outgrowth. *Neuroscience* **103,** 831–840 (2001).
31. Dertinger, S. K. W., Jiang, X., Li, Z., Murthy, V. N. & Whitesides, G. M. Gradients of substrate-bound laminin orient axonal specification of neurons. *Proc. Natl. Acad. Sci. U. S. A.* **99,** 12542–12547 (2002).
32. Wood, M. D. *et al.* Affinity-based release of glial-derived neurotrophic factor from fibrin matrices enhances sciatic nerve regeneration. *Acta Biomater.* **5,** 959–968 (2009).
33. Villalona, G. A. *et al.* Cell-seeding techniques in vascular tissue engineering. *Tissue Eng. Part B. Rev.* **16,** 341–350 (2010).
34. Griffith, L. G. & Naughton, G. Tissue engineering--current challenges and expanding opportunities. *Science* **295,** 1009–1014 (2002).
35. Sachlos, E. & Czernuszka, J. T. Making tissue engineering scaffolds work. Review: the application of solid freeform fabrication technology to the production of tissue engineering scaffolds. *Eur. Cell. Mater.* **5,** 29–39; discussion 39–40 (2003).
36. van Susante, J. L. *et al.* Culture of chondrocytes in alginate and collagen carrier gels. *Acta Orthop. Scand.* **66,** 549–556 (1995).
37. Jessen, K. R. & Mirsky, R. The origin and development of glial cells in peripheral nerves. *Nat. Rev. Neurosci.* **6,** 671–682 (2005).
38. Miki, Y. *et al.* The advantages of co-culture over mono cell culture in simulating in vivo environment. *The Journal of Steroid Biochemistry and Molecular Biology* **131,** 68–75 (2012).
39. Bhatia, S. N., Yarmush, M. L. & Toner, M. Controlling cell interactions by micropatterning in co-cultures: Hepatocytes and 3T3 fibroblasts. *J. Biomed. Mater. Res.* **34,** 189–199 (1997).
40. Fukuda, J. *et al.* Micropatterned cell co-cultures using layer-by-layer deposition of extracellular matrix components. *Biomaterials* **27,** 1479–1486 (2006).
41. Zhanga, S. *et al.* Biological surface engineering: A simple system for cell pattern formation. *Biomaterials* **20,** 1213–1220 (1999).
42. Albrecht, D. R., Tsang, V. L., Sah, R. L. & Bhatia, S. N. Photo- and electropatterning of

hydrogel-encapsulated living cell arrays. *Lab Chip* **5,** 111–118 (2005).

43. Kim, J. D., Choi, J. S., Kim, B. S., Chan Choi, Y. & Cho, Y. W. Piezoelectric inkjet printing of polymers: Stem cell patterning on polymer substrates. *Polymer (Guildf).* **51,** 2147–2154 (2010).

44. Lin, R. Z., Ho, C. T., Liu, C. H. & Chang, H. Y. Dielectrophoresis based-cell patterning for tissue engineering. *Biotechnology Journal* **1,** 949–957 (2006).

45. Nilsson, J., Evander, M., Hammarström, B. & Laurell, T. Review of cell and particle trapping in microfluidic systems. *Analytica Chimica Acta* **649,** 141–157 (2009).

46. Odde, D. J. & Renn, M. J. Laser-guided direct writing of living cells. *Biotechnol. Bioeng.* **67,** 312–318 (2000).

47. Pelham, R. J. & Wang, Y. L. Cell locomotion and focal adhesions are regulated by the mechanical properties of the substrate. in *Biological Bulletin* **194,** 348–350 (1998).

48. Cukierman, E., Pankov, R., Stevens, D. R. & Yamada, K. M. Taking cell-matrix adhesions to the third dimension. *Science* **294,** 1708–1712 (2001).

49. Stevens, M. M. & George, J. H. Exploring and engineering the cell surface interface. *Science* **310,** 1135–1138 (2005).

50. Badylak, S. F. The extracellular matrix as a biologic scaffold material. *Biomaterials* **28,** 3587–3593 (2007).

51. Badylak, S. F., Freytes, D. O. & Gilbert, T. W. Extracellular matrix as a biological scaffold material: Structure and function. *Acta Biomaterialia* **5,** 1–13 (2009).

52. Shapiro, S. D. Matrix metalloproteinase degradation of extracellular matrix: Biological consequences. *Current Opinion in Cell Biology* **10,** 602–608 (1998).

53. Juliano, R. L. & Haskill, S. Signal transduction from the extracellular matrix. *J. Cell Biol.* **120,** 577–85 (1993).

54. Hay, E. D. *Cell Biology of Extracellular Matrix*. (Springer Science & Business Media, 1991). at <https://books.google.com/books?hl=en&lr=&id=ctSMNCf_U2AC&pgis=1>

55. Bu-Lin, Z. *et al.* A polyacrylamide gel phantom for radiofrequency ablation. *Int. J. Hyperthermia* **24,** 568–576 (2008).

56. Zheng, H. *et al.* Ultrasound-Driven Microbubble Oscillation and Translation Within Small Phantom Vessels. *Ultrasound Med. Biol.* **33,** 1978–1987 (2007).

57. Lu, T. & Zang, H. Photoacoustic tomography of micro-blood vessels in tissue mimicking phantom. in *Proceedings - 2010 3rd International Conference on Biomedical Engineering and Informatics, BMEI 2010* **2,** 456–458 (2010).

58. Jiang, C.-P. Vessel phantom fabrication using rapid prototyping technique for investigating thermal dosage profile in HIFU surgery. *Rapid Prototyping Journal* **16,** 417–423 (2010).

59. Paraskevas, K. I., Mikhailidis, D. P. & Perrea, D. Experimental models of abdominal aortic aneurysms: an overview. *Curr. Pharm. Des.* **14,** 325–337 (2008).

60. Hieu, L. C. *et al.* Medical rapid prototyping applications and methods. *Assembly Automation* **25,** 284–292 (2005).

61. Gabbrielli, R., Turner, I. G. & Bowen, C. R. Development of modelling methods for materials to be used as bone substitutes. *Key Eng. Mater.* **361-363 II,** 901–906 (2008).

62. Almeida, H. de A. & da Silva Bártolo, P. J. Virtual topological optimisation of scaffolds for rapid prototyping. *Med. Eng. Phys.* **32,** 775–782 (2010).

63. Woodfield, T. B. F. *et al.* Design of porous scaffolds for cartilage tissue engineering using a three-dimensional fiber-deposition technique. *Biomaterials* **25,** 4149–4161 (2004).

64. Gratson, G. M., Xu, M. & Lewis, J. A. Microperiodic structures: direct writing of three-

dimensional webs. *Nature* **428,** 386 (2004).

65. Woodfield, T. B. F. *et al.* Design of porous scaffolds for cartilage tissue engineering using a three-dimensional fiber-deposition technique. *Biomaterials* **25,** 4149–61 (2004).

66. Malda, J. *et al.* 25th anniversary article: Engineering hydrogels for biofabrication. *Advanced Materials* **25,** 5011–5028 (2013).

67. Place, E. S., George, J. H., Williams, C. K. & Stevens, M. M. Synthetic polymer scaffolds for tissue engineering. *Chem. Soc. Rev.* **38,** 1139–1151 (2009).

68. Boland, T., Mironov, V., Gutowska, A., Roth, E. A. & Markwald, R. R. Cell and organ printing 2: fusion of cell aggregates in three-dimensional gels. *Anat. Rec. A. Discov. Mol. Cell. Evol. Biol.* **272,** 497–502 (2003).

69. Mironov, V. *et al.* Organ printing: Tissue spheroids as building blocks. *Biomaterials* **30,** 2164–2174 (2009).

70. Mironov, V., Kasyanov, V. & Markwald, R. R. Organ printing: from bioprinter to organ biofabrication line. *Current Opinion in Biotechnology* **22,** 667–673 (2011).

71. Liu Tsang, V. & Bhatia, S. N. Three-dimensional tissue fabrication. *Advanced Drug Delivery Reviews* **56,** 1635–1647 (2004).

72. Liu, C., Xia, Z. & Czernuszka, J. T. Design and Development of Three-Dimensional Scaffolds for Tissue Engineering. *Chem. Eng. Res. Des.* **85,** 1051–1064 (2007).

73. Hutmacher, D. W. Biomaterials offer cancer research the third dimension. *Nat. Mater.* **9,** 90–93 (2010).

74. Benya, P. D. & Shaffer, J. D. Dedifferentiated chondrocytes reexpress the differentiated collagen phenotype when cultured in agarose gels. *Cell* **30,** 215–224 (1982).

75. Baker, B. M. & Chen, C. S. Deconstructing the third dimension - how 3D culture microenvironments alter cellular cues. *Journal of Cell Science* **125,** 3015–3024 (2012).

76. Pati, F. *et al.* Printing three-dimensional tissue analogues with decellularized extracellular matrix bioink. *Nat. Commun.* **5,** 3935 (2014).

77. Melchels, F. P. W. *et al.* Additive manufacturing of tissues and organs. *Prog. Polym. Sci.* **37,** 1079–1104 (2012).

78. Murphy, S. V., Skardal, A. & Atala, A. Evaluation of hydrogels for bio-printing applications. *J. Biomed. Mater. Res. - Part A* **101 A,** 272–284 (2013).

79. Cohen, D. L. *et al.* Increased mixing improves hydrogel homogeneity and quality of three-dimensional printed constructs. *Tissue Eng. Part C. Methods* **17,** 239–248 (2011).

80. Duan, B., Hockaday, L. A., Kang, K. H. & Butcher, J. T. 3D Bioprinting of heterogeneous aortic valve conduits with alginate/gelatin hydrogels. *J. Biomed. Mater. Res. - Part A* **101 A,** 1255–1264 (2013).

81. Cui, X., Breitenkamp, K., Finn, M. G., Lotz, M. & D'Lima, D. D. Direct human cartilage repair using three-dimensional bioprinting technology. *Tissue Eng. A* **18,** 1304–1312 (2012).

82. Fedorovich, N. E. *et al.* Hydrogels as extracellular matrices for skeletal tissue engineering: state-of-the-art and novel application in organ printing. *Tissue Eng.* **13,** 1905–1925 (2007).

83. Visconti, R. P. *et al.* Towards organ printing: engineering an intra-organ branched vascular tree. *Expert Opin. Biol. Ther.* **10,** 409–420 (2010).

84. Klebe, R. J. Cytoscribing: a method for micropositioning cells and the construction of two- and three-dimensional synthetic tissues. *Exp. Cell Res.* **179,** 362–373 (1988).

85. Wilson, W. C. & Boland, T. Cell and organ printing 1: protein and cell printers. *Anat. Rec. A. Discov. Mol. Cell. Evol. Biol.* **272,** 491–496 (2003).

86. Sirringhaus, H. *et al.* High-resolution inkjet printing of all-polymer transistor circuits. *Science*

290, 2123–2126 (2000).

87. Bharathan, J. & Yang, Y. Polymer electroluminescent devices processed by inkjet printing: I. Polymer light-emitting logo. *Appl. Phys. Lett.* **72,** 2660 (1998).

88. Hayes, D. J., Grove, M. E. & Cox, W. R. Development and application by ink-jet printing of advancedpackaging materials. *Proc. Int. Symp. Adv. Packag. Mater. Process. Prop. Interfaces (IEEE Cat. No.99TH8405)* (1999). doi:10.1109/ISAPM.1999.757293

89. Sachs, E., Cima, M. & Cornie, J. Three-Dimensional Printing: Rapid Tooling and Prototypes Directly from a CAD Model. *CIRP Ann. - Manuf. Technol.* **39,** 201–204 (1990).

90. Setti, L. *et al.* An amperometric glucose biosensor prototype fabricated by thermal inkjet printing. *Biosens. Bioelectron.* **20,** 2019–2026 (2005).

91. Boland, T., Xu, T., Damon, B. & Cui, X. Application of inkjet printing to tissue engineering. *Biotechnol. J.* **1,** 910–917 (2006).

92. Derby, B. Inkjet Printing of Functional and Structural Materials: Fluid Property Requirements, Feature Stability, and Resolution. *Annual Review of Materials Research* **40,** 395–414 (2010).

93. Derby, B. Inkjet Printing of Functional and Structural Materials: Fluid Property Requirements, Feature Stability, and Resolution. *Annual Review of Materials Research* **40,** 395–414 (2010).

94. Wang, Y. Maskless lithography using drop-on-demand inkjet printing method. *Emerg. Lithogr. Technol. VIII* **5374,** 628–636 (2004).

95. Sankhe, A. Y., Booth, B. D., Wiker, N. J. & Kilbey, S. M. Inkjet-printed monolayers as platforms for tethered polymers. *Langmuir* **21,** 5332–5336 (2005).

96. Pardo, L., Cris Wilson, W. & Boland, T. Characterization of patterned self-assembled monolayers and protein arrays generated by the ink-jet method. *Langmuir* **19,** 1462–1466 (2003).

97. Xu, T. *et al.* Construction of High-Density Bacterial Colony Arrays and Patterns by the Ink-Jet Method. *Biotechnol. Bioeng.* **85,** 29–33 (2004).

98. Di Biase, M., Saunders, R. E., Tirelli, N. & Derby, B. Inkjet printing and cell seeding thermoreversible photocurable gel structures. *Soft Matter* **7,** 2639 (2011).

99. Xu, T. *et al.* Viability and electrophysiology of neural cell structures generated by the inkjet printing method. *Biomaterials* **27,** 3580–3588 (2006).

100. Roth, E. a *et al.* Inkjet printing for high-throughput cell patterning. *Biomaterials* **25,** 3707–3715 (2004).

101. Cui, X., Dean, D., Ruggeri, Z. M. & Boland, T. Cell damage evaluation of thermal inkjet printed Chinese hamster ovary cells. *Biotechnol. Bioeng.* **106,** 963–969 (2010).

102. Xu, T., Jin, J., Gregory, C., Hickman, J. J. J. J. & Boland, T. Inkjet printing of viable mammalian cells. *Biomaterials* **26,** 93–99 (2005).

103. Gan, H. Y., Shan, X., Eriksson, T., Lok, B. K. & Lam, Y. C. Reduction of droplet volume by controlling actuating waveforms in inkjet printing for micro-pattern formation. *Journal of Micromechanics and Microengineering* **19,** 055010 (2009).

104. Bogy, D. B. & Talke, F. E. Experimental and Theoretical Study of Wave Propagation Phenomena in Drop-on-Demand Ink Jet Devices. *IBM Journal of Research and Development* **28,** 314–321 (1984).

105. Dijksman, J. F. Hydrodynamics of small tubular pumps. *Journal of Fluid Mechanics* **139,** 173 (1984).

106. Tekin, E., Smith, P. J. & Schubert, U. S. Inkjet printing as a deposition and patterning tool for polymers and inorganic particles. *Soft Matter* **4,** 703 (2008).

107. Gans, B.-J. De, Schubert, U. S. & de Gans, B.-J. Inkjet Printing of Well-Defined Polymer Dots

and Arrays. *Langmuir* **20,** 7789–7793 (2004).

108. Soltman, D. B. Understanding Inkjet Printed Pattern Generation. *Program* (2011).

109. Soltman, D. & Subramanian, V. Inkjet-printed line morphologies and temperature control of the coffee ring effect. *Langmuir* **24,** 2224–2231 (2008).

110. Deegan, R. D. *et al.* Capillary flow as the cause of ring stains from dried liquid drops. *Nature* **389,** 827–829 (1997).

111. Yong, Z., Lifeng, C., Shoufeng, Y. & Evans, J. R. G. Preparation of ceramic well plates for combinatorial methods using the morphogenic effects of droplet drying. *J. Am. Ceram. Soc.* **89,** 3858–3860 (2006).

112. Lim, J. A. *et al.* Self-organization of ink-jet-printed triisopropylsilylethynyl pentacene via evaporation-induced flows in a drying droplet. *Adv. Funct. Mater.* **18,** 229–234 (2008).

113. Saunders, R. E., Gough, J. E. & Derby, B. Delivery of human fibroblast cells by piezoelectric drop-on-demand inkjet printing. *Biomaterials* **29,** 193–203 (2008).

114. Chen, G., Ushida, T. & Tateishi, T. Scaffold design for tissue engineering. *Macromolecular Bioscience* **2,** 67–77 (2002).

115. Derby, B. Bioprinting: inkjet printing proteins and hybrid cell-containing materials and structures. *J. Mater. Chem.* **18,** 5717 (2008).

116. Delaney, J. T., Smith, P. J. & Schubert, U. S. Inkjet printing of proteins. *Soft Matter* **5,** 4866 (2009).

117. Zhang, Y., Tse, C., Rouholamin, D. & Smith, P. J. Scaffolds for tissue engineering produced by inkjet printing. *Cent. Eur. J. Eng.* **2,** 325–335 (2012).

118. Xu, T. *et al.* Hybrid printing of mechanically and biologically improved constructs for cartilage tissue engineering applications. *Biofabrication* **5,** 015001 (2013).

119. Xu, T. *et al.* Complex heterogeneous tissue constructs containing multiple cell types prepared by inkjet printing technology. *Biomaterials* **34,** 130–9 (2013).

120. Thibaudeau, L. *et al.* A tissue-engineered humanized xenograft model of human breast cancer metastasis to bone. *Dis. Model. Mech.* **7,** 299–309 (2014).

121. Phillippi, J. A. *et al.* Microenvironments engineered by inkjet bioprinting spatially direct adult stem cells toward muscle- and bone-like subpopulations. *Stem Cells* **26,** 127–134 (2008).

122. Suntivich, R., Drachuk, I., Calabrese, R., Kaplan, D. L. & Tsukruk, V. V. Inkjet printing of silk nest arrays for cell hosting. *Biomacromolecules* **15,** 1428–1435 (2014).

123. Haufová, P., Dohnal, J., HanuŠ, J. & Štěpánek, F. Towards the inkjet fabrication of artificial cells. *Colloids Surfaces A Physicochem. Eng. Asp.* **410,** 52–58 (2012).

124. Lorber, B., Hsiao, W.-K., Hutchings, I. M. & Martin, K. R. Adult rat retinal ganglion cells and glia can be printed by piezoelectric inkjet printing. *Biofabrication* **6,** 015001 (2013).

125. Cooper, G. M. *et al.* Inkjet-based biopatterning of bone morphogenetic protein-2 to spatially control calvarial bone formation. *Tissue Eng. Part A* **16,** 1749–1759 (2010).

126. Xu, C., Chai, W., Huang, Y. & Markwald, R. R. Scaffold-free inkjet printing of three-dimensional zigzag cellular tubes. *Biotechnol. Bioeng.* **109,** 3152–60 (2012).

127. Khalil, S. & Sun, W. Bioprinting endothelial cells with alginate for 3D tissue constructs. *J. Biomech. Eng.* **131,** 111002 (2009).

128. Nishiyama, Y. *et al.* Development of a three-dimensional bioprinter: construction of cell supporting structures using hydrogel and state-of-the-art inkjet technology. *J. Biomech. Eng.* **131,** 035001 (2009).

129. Ilkhanizadeh, S., Teixeira, A. I. & Hermanson, O. Inkjet printing of macromolecules on hydrogels to steer neural stem cell differentiation. *Biomaterials* **28,** 3936–3943 (2007).

130. Nishioka, G. M., Markey, A. a & Holloway, C. K. Protein damage in drop-on-demand printers. *J. Am. Chem. Soc.* **126,** 16320–16321 (2004).

131. Wang, J. Z., Zheng, Z. H., Li, H. W., Huck, W. T. S. & Sirringhaus, H. Dewetting of conducting polymer inkjet droplets on patterned surfaces. *Nat. Mater.* **3,** 171–176 (2004).

132. Campbell, P. G., Miller, E. D., Fisher, G. W., Walker, L. M. & Weiss, L. E. Engineered spatial patterns of FGF-2 immobilized on fibrin direct cell organization. *Biomaterials* **26,** 6762–6770 (2005).

133. Miller, E. D. *et al.* Inkjet printing of growth factor concentration gradients and combinatorial arrays immobilized on biologically-relevant substrates. *Comb. Chem. High Throughput Screen.* **12,** 604–618 (2009).

134. Zheng, Q. *et al.* Application of inkjet printing technique for biological material delivery and antimicrobial assays. *Anal. Biochem.* **410,** 171–176 (2011).

135. Cai, K. *et al.* Inkjet printing of laminin gradient to investigate endothelial cellular alignment. *Colloids Surf. B. Biointerfaces* **72,** 230–235 (2009).

136. Hansen, A., Zhang, R. & Bradley, M. Fabrication of arrays of polymer gradients using inkjet printing. *Macromol. Rapid Commun.* **33,** 1114–8 (2012).

137. Roth, E. A. *et al.* Inkjet printing for high-throughput cell patterning. *Biomaterials* **25,** 3707–3715 (2004).

138. Watanabe, M. Microfluidic devices easily created using an office inkjet printer. *Microfluidics and Nanofluidics* **8,** 403–408 (2010).

139. Cui, S., Breitenkamp, K., Finn, M. ., Lotz, M. & Lima, D. D. D. Direct Human Cartilage Repair Using Three-Dimensional Bioprinting Technology 1,2. *Tissue Eng. Part A* **18,** 1304–1313 (2012).

140. Saunders, R. E., Gough, J. E. & Derby, B. Delivery of human fibroblast cells by piezoelectric drop-on-demand inkjet printing. *Biomaterials* **29,** 193–203 (2008).

141. Xu, T. *et al.* Inkjet-mediated gene transfection into living cells combined with targeted delivery. *Tissue Eng. Part A* **15,** 95–101 (2009).

142. Seetharam, R. & Sharma, S. K. *Purification and Analysis of Recombinant Proteins*. (CRC Press, 1991). at <https://books.google.com/books?hl=en&lr=&id=CN53kDLCOjAC&pgis=1>

143. Parsa, S., Gupta, M., Loizeau, F. & Cheung, K. C. Effects of surfactant and gentle agitation on inkjet dispensing of living cells. *Biofabrication* **2,** 025003 (2010).

144. Wagoner Johnson, A. J. & Herschler, B. A. A review of the mechanical behavior of CaP and CaP/polymer composites for applications in bone replacement and repair. *Acta Biomater.* **7,** 16–30 (2011).

145. Cui, X. & Boland, T. Human microvasculature fabrication using thermal inkjet printing technology. *Biomaterials* **30,** 6221–6227 (2009).

146. Smith, P. J. & Morrin, A. Reactive inkjet printing. *Journal of Materials Chemistry* **22,** 10965 (2012).

147. Hollister, S. J. Porous scaffold design for tissue engineering. *Nat. Mater.* **4,** 518–524 (2005).

148. Lendlein, A. & Langer, R. Biodegradable, elastic shape-memory polymers for potential biomedical applications. *Science* **296,** 1673–1676 (2002).

149. Baroli, B. Hydrogels for tissue engineering and delivery of tissue-inducing substances. *Journal of Pharmaceutical Sciences* **96,** 2197–2223 (2007).

150. Nguyen, K. T. & West, J. L. Photopolymerizable hydrogels for tissue engineering applications. *Biomaterials* **23,** 4307–4314 (2002).

151. Drury, J. L. & Mooney, D. J. Hydrogels for tissue engineering: Scaffold design variables and

applications. *Biomaterials* **24,** 4337–4351 (2003).

152. Kuijpers, A. J. *et al.* Cross-linking and characterisation of gelatin matrices for biomedical applications. *J. Biomater. Sci. Polym. Ed.* **11,** 225–243 (2000).

153. Esposito, E., Cortesi, R. & Nastruzzi, C. Gelatin microspheres: influence of preparation parameters and thermal treatment on chemico-physical and biopharmaceutical properties. *Biomaterials* **17,** 2009–20 (1996).

154. Wissemann, K. W. & Jacobson, B. S. Pure gelatin microcarriers: synthesis and use in cell attachment and growth of fibroblast and endothelial cells. *In Vitro Cell. Dev. Biol.* **21,** 391–401 (1985).

155. Elisseeff, J. *et al.* Transdermal photopolymerization for minimally invasive implantation. *Proc. Natl. Acad. Sci. U. S. A.* **96,** 3104–3107 (1999).

156. Yung, C. W. *et al.* Transglutaminase crosslinked gelatin as a tissue engineering scaffold. *J. Biomed. Mater. Res. - Part A* **83,** 1039–1046 (2007).

157. Bigi, A., Cojazzi, G., Panzavolta, S., Roveri, N. & Rubini, K. Stabilization of gelatin films by crosslinking with genipin. *Biomaterials* **23,** 4827–4832 (2002).

158. Otani, Y., Tabata, Y. & Ikada, Y. Hemostatic capability of rapidly curable glues from gelatin, poly(L-glutamic acid), and carbodiimide. *Biomaterials* **19,** 2091–2098 (1998).

159. Olde Damink, L. H. H. *et al.* Glutaraldehyde as a crosslinking agent for collagen-based biomaterials. *Journal of Materials Science: Materials in Medicine* **6,** 460–472 (1995).

160. Bigi, A., Cojazzi, G., Panzavolta, S., Rubini, K. & Roveri, N. Mechanical and thermal properties of gelatin films at different degrees of glutaraldehyde crosslinking. *Biomaterials* **22,** 763–8 (2001).

161. Tabata, Y. & Ikada, Y. Protein release from gelatin matrices. *Adv. Drug Deliv. Rev.* **31,** 287–301 (1998).

162. Holland, T. A., Tabata, Y. & Mikos, A. G. Dual growth factor delivery from degradable oligo(poly(ethylene glycol) fumarate) hydrogel scaffolds for cartilage tissue engineering. in *Journal of Controlled Release* **101,** 111–125 (2005).

163. Ito, A., Honda, H. & Ueda, M. Transglutaminase-Mediated Gelatin Matrices Incorporating Cell Adhesion Factors as a Biomaterial for Tissue Engineering. **95,** 196–199 (2003).

164. Masuda, T., Furue, M. & Matsuda, T. Photocured, styrenated gelatin-based microspheres for de novo adipogenesis through corelease of basic fibroblast growth factor, insulin, and insulin-like growth factor I. *Tissue Eng.* **10,** 523–35

165. Wei, C., Cai, L., Sonawane, B., Wang, S. & Dong, J. High-precision flexible fabrication of tissue engineering scaffolds using distinct polymers. *Biofabrication* **4,** 025009 (2012).

166. Gong, X. *et al.* Wax-bonding 3D microfluidic chips. *Lab Chip* **10,** 2622–2627 (2010).

167. Lu, Y., Shi, W., Jiang, L., Qin, J. & Lin, B. Rapid prototyping of paper-based microfluidics with wax for low-cost, portable bioassay. *Electrophoresis* **30,** 1497–500 (2009).

168. Carrilho, E., Martinez, A. W. & Whitesides, G. M. Understanding wax printing: A simple micropatterning process for paper-based microfluidics. *Anal. Chem.* **81,** 7091–7095 (2009).

169. Daud, M. F. B., Pawar, K. C., Claeyssens, F., Ryan, A. J. & Haycock, J. W. An aligned 3D neuronal-glial co-culture model for peripheral nerve studies. *Biomaterials* **33,** 5901–5913 (2012).

170. Baron-Van Evercooren, A., Kleinman, H. K., Seppa, H. E. J., Rentier, B. & Dubois-Dalcq, M. Fibronectin promotes rat Schwann cell growth and motility. *J. Cell Biol.* **93,** 211–216 (1982).

171. Seidman, K. J., Barsuk, J. H., Johnson, R. F. & Weyhenmeyer, J. A. Differentiation of NG108-15 neuroblastoma cells by serum starvation or dimethyl sulfoxide results in marked differences in angiotensin II receptor subtype expression. *J. Neurochem.* **66,** 1011–1018 (1996).

172. Kowtha, V. C., Quong, J. N., Bryant, H. J. & Stenger, D. A. Comparative electrophysiological properties of NG108-15 cells in serum-containing and serum-free media. *Neurosci. Lett.* **164,** 129–133 (1993).

173. Ito, A. *et al.* Transglutaminase-mediated gelatin matrices incorporating cell adhesion factors as a biomaterial for tissue engineering. *J. Biosci. Bioeng.* **95,** 196–199 (2003).

174. Paguirigan, a & Beebe, D. J. Gelatin based microfluidic devices for cell culture. *Lab Chip* **6,** 407–13 (2006).

175. Yao, C. H., Liu, B. S., Chang, C. J., Hsu, S. H. & Chen, Y. S. Preparation of networks of gelatin and genipin as degradable biomaterials. *Mater. Chem. Phys.* **83,** 204–208 (2004).

176. Lin, F. H., Yao, C. H., Sun, J. S., Liu, H. C. & Huang, C. W. Biological effects and cytotoxicity of the composite composed by tricalcium phosphate and glutaraldehyde cross-linked gelatin. *Biomaterials* **19,** 905–17 (1998).

177. Sung, H. W., Huang, D. M., Chang, W. H., Huang, R. N. & Hsu, J. C. Evaluation of gelatin hydrogel crosslinked with various crosslinking agents as bioadhesives: in vitro study. *J. Biomed. Mater. Res.* **46,** 520–30 (1999).

178. Ou, Y.-C. *et al.* Attachment of Tumor Cells to the Micropatterns of Glutaraldehyde (GA)-Crosslinked Gelatin. **20,** 435–446 (2008).

179. McGuigan, A. P. & Sefton, M. V. Modular tissue engineering: Fabrication of a gelatin-based construct. *J. Tissue Eng. Regen. Med.* **1,** 136–145 (2007).

180. Wollensak, G., Aurich, H., Wirbelauer, C. & Sel, S. Significance of the riboflavin film in corneal collagen crosslinking. *J. Cataract Refract. Surg.* **36,** 114–120 (2010).

181. Bigi, A., Cojazzi, G., Panzavolta, S., Rubini, K. & Roveri, N. Mechanical and thermal properties of gelatin films at different degrees of glutaraldehyde crosslinking. *Biomaterials* **22,** 763–768 (2001).

182. Damink, L. H. H. O. *et al.* Glutaraldehyde as a crosslinking agent for collagen-based biomaterials. *J. Mater. Sci. Mater. Med.* **6,** 460–472 (1995).

183. Nichol, J. W. *et al.* Cell-laden microengineered gelatin methacrylate hydrogels. *Biomaterials* **31,** 5536–5544 (2010).

184. Yang, L.-J. & Ou, Y.-C. The micro patterning of glutaraldehyde (GA)-crosslinked gelatin and its application to cell-culture. *Lab Chip* **5,** 979–984 (2005).

185. Zhang, Y. Z., Venugopal, J., Huang, Z. M., Lim, C. T. & Ramakrishna, S. Crosslinking of the electrospun gelatin nanofibers. *Polymer (Guildf).* **47,** 2911–2917 (2006).

186. Ai, H., Mills, D. K., Jonathan, A. S. & Jones, S. A. Gelatin-glutaraldehyde cross-linking on silicone rubber to increase endothelial cell adhesion and growth. *In Vitro Cell. Dev. Biol. Anim.* **38,** 487–492 (2002).

187. Matsuda, S., Iwata, H., Se, N. & Ikada, Y. Bioadhesion of gelatin films crosslinked with glutaraldehyde. *J. Biomed. Mater. Res.* **45,** 20–27 (1999).

188. Nesic, D. *et al.* Cartilage tissue engineering for degenerative joint disease. *Advanced Drug Delivery Reviews* **58,** 300–322 (2006).

189. Bannasch, H. *et al.* [Skin tissue engineering]. *Chirurg.* **74,** 802–7 (2003).

190. Théry, M. Micropatterning as a tool to decipher cell morphogenesis and functions. *J. Cell Sci.* **123,** 4201–4213 (2010).

191. Kumar, S. & LeDuc, P. R. Dissecting the molecular basis of the mechanics of living cells. *Exp. Mech.* **49,** 11–23 (2009).

192. Chen, C. S., Mrksich, M., Huang, S., Whitesides, G. M. & Ingber, D. E. Geometric control of cell life and death. *Science* **276,** 1425–1428 (1997).

193. Dike, L. E. *et al.* Geometric control of switching between growth, apoptosis, and differentiation during angiogenesis using micropatterned substrates. *In Vitro Cell. Dev. Biol. Anim.* **35,** 441–448 (1999).

194. McBeath, R., Pirone, D. M., Nelson, C. M., Bhadriraju, K. & Chen, C. S. Cell shape, cytoskeletal tension, and RhoA regulate stem cell lineage commitment. *Dev. Cell* **6,** 483–495 (2004).

195. Banerjee, S., Sknepnek, R. & Marchetti, M. C. Optimal shapes and stresses of adherent cells on patterned substrates. *Soft Matter* **10,** 2424–30 (2014).

196. Geiger, B., Spatz, J. P. & Bershadsky, A. D. Environmental sensing through focal adhesions. *Nat. Rev. Mol. Cell Biol.* **10,** 21–33 (2009).

197. Duclos, G., Garcia, S., Yevick, H. G. & Silberzan, P. Perfect nematic order in confined monolayers of spindle-shaped cells. *Soft Matter* **10,** 2346–53 (2014).

198. Alvarado, J., Mulder, B. M. & Koenderink, G. H. Alignment of nematic and bundled semiflexible polymers in cell-sized confinement. *Soft Matter* **10,** 2354–64 (2014).

199. Tomba, C., Braïni, C., Wu, B., Gov, N. S. & Villard, C. Tuning the adhesive geometry of neurons: length and polarity control. *Soft Matter* **10,** 2381–7 (2014).

200. Röttgermann, P. J. F., Alberola, A. P. & Rädler, J. O. Cellular self-organization on micro-structured surfaces. *Soft Matter* **10,** 2397–404 (2014).

201. Hampe, N. *et al.* Defined 2-D microtissues on soft elastomeric silicone rubber using lift-off epoxy-membranes for biomechanical analyses. *Soft Matter* **10,** 2431–2443 (2014).

202. Schwarz, U. S., Nelson, C. M. & Silberzan, P. Proteins, cells, and tissues in patterned environments. *Soft Matter* **10,** 2337–40 (2014).

203. Fujii, T. PDMS-based microfluidic devices for biomedical applications. in *Microelectronic Engineering* **61-62,** 907–914 (2002).

204. Duffy, D. C., McDonald, J. C., Schueller, O. J. A. & Whitesides, G. M. Rapid prototyping of microfluidic systems in poly(dimethylsiloxane). *Anal. Chem.* **70,** 4974–4984 (1998).

205. Liu, J., Enzelberger, M. & Quake, S. A nanoliter rotary device for polymerase chain reaction. *Electrophoresis* **23,** 1531–1536 (2002).

206. Linder, V., Wu, H., Jiang, X. & Whitesides, G. M. Rapid prototyping of 2D structures with feature sizes larger than 8 μm. *Anal. Chem.* **75,** 2522–2527 (2003).

207. McDonald, J. C. *et al.* Prototyping of microfluidic devices in poly(dimethylsiloxane) using solid-object printing. *Anal. Chem.* **74,** 1537–1545 (2002).

208. Sanjana, N. E. & Fuller, S. B. A fast flexible ink-jet printing method for patterning dissociated neurons in culture. *J. Neurosci. Methods* **136,** 151–163 (2004).

209. Müller, A., Meyer, J., Paumer, T. & Pompe, T. Cytoskeletal transition in patterned cells correlates with interfacial energy model. *Soft Matter* **10,** 2444–52 (2014).

210. Love, J. C., Wolfe, D. B., Jacobs, H. O. & Whitesides, G. M. Microscope projection photolithography for rapid prototyping of masters with micron-scale features for use in soft lithography. *Langmuir* **17,** 6005–6012 (2001).

211. Kwon, K. W., Choi, J. C., Suh, K. Y. & Doh, J. Multiscale fabrication of multiple proteins and topographical structures by combining capillary force lithography and microscope projection photolithography. *Langmuir* **27,** 3238–3243 (2011).

212. Renault, C., Koehne, J., Ricco, A. J. & Crooks, R. M. Three-dimensional wax patterning of paper fluidic devices. *Langmuir* **30,** 7030–7036 (2014).

213. Yun, Y. H. *et al.* A glucose sensor fabricated by piezoelectric inkjet printing of conducting polymers and bienzymes. *Anal. Sci.* **27,** 375 (2011).

214. Setti, L. *et al.* An amperometric glucose biosensor prototype fabricated by thermal inkjet printing. *Biosens. Bioelectron.* **20,** 2019–2026 (2005).

215. Wang, T. W. T., Cook, C. & Derby, B. Fabrication of a Glucose Biosensor by Piezoelectric Inkjet Printing. *2009 Third Int. Conf. Sens. Technol. Appl.* (2009). doi:10.1109/SENSORCOMM.2009.20

216. Bietsch, A., Zhang, J., Hegner, M., Lang, H. P. & Gerber, C. Rapid functionalization of cantilever array sensors by inkjet printing. *Nanotechnology* **15,** 873–880 (2004).

217. Li, Z., Hou, L., Zhang, W. & Zhu, L. Preparation of PDMS microfluidic devices based on drop-on-demand generation of wax molds. *Anal. Methods* **6,** 4716 (2014).

218. Wang, W., Zhao, S. & Pan, T. Lab-on-a-print: from a single polymer film to three-dimensional integrated microfluidics. *Lab Chip* **9,** 1133–1137 (2009).

219. Liao, Y. *et al.* Direct laser writing of sub-50 nm nanofluidic channels buried in glass for three-dimensional micro-nanofluidic integration. *Lab Chip* **13,** 1626–31 (2013).

220. Koroleva, A. *et al.* Two-photon polymerization-generated and micromolding-replicated 3D scaffolds for peripheral neural tissue engineering applications. *Biofabrication* **4,** 025005 (2012).

221. Schiaffino, S. & Sonin, A. Molten droplet deposition and solidification at low Weber numbers. *Phys. Fluids* **9,** 3172–3187 (1997).

222. Gans, B.-J. De, Schubert, U. S. & de Gans, B.-J. Inkjet Printing of Well-Defined Polymer Dots and Arrays. *Langmuir* **20,** 7789–7793 (2004).

223. Li, R., Ashgriz, N., Chandra, S. & Andrews, J. R. Shape and surface texture of molten droplets deposited on cold surfaces. *Surf. Coatings Technol.* **202,** 3960–3966 (2008).

224. Stringer, J. & Derby, B. Formation and stability of lines produced by inkjet printing. *Langmuir* **26,** 10365–10372 (2010).

225. Discher, D. E., Janmey, P. & Wang, Y.-L. Tissue cells feel and respond to the stiffness of their substrate. *Science* **310,** 1139–1143 (2005).

226. Schwarz, U. S. & Gardel, M. L. United we stand - integrating the actin cytoskeleton and cell-matrix adhesions in cellular mechanotransduction. *Journal of Cell Science* **125,** 3051–3060 (2012).

227. Evans, E. A. & Calderwood, D. A. Forces and bond dynamics in cell adhesion. *Science* **316,** 1148–1153 (2007).

228. Théry, M. & Bornens, M. Cell shape and cell division. *Current Opinion in Cell Biology* **18,** 648–657 (2006).

229. Li, J., Chen, J. & Kirsner, R. Pathophysiology of acute wound healing. *Clin. Dermatol.* **25,** 9–18 (2007).

230. Sirringhaus, H. *et al.* High-resolution inkjet printing of all-polymer transistor circuits. *Science* **290,** 2123–2126 (2000).

231. Russ, C., Gessagt, M., Falk, V. & Székely, G. Rapid Prototyping of Silicone-based Phantom Models for Stent Simulation Validation. *MICCAI Stent* 1–8 (2012).

232. Ramnarine, K. V., Anderson, T. & Hoskins, P. R. Construction and geometric stability of physiological flow rate wall-less stenosis phantoms. *Ultrasound Med. Biol.* **27,** 245–250 (2001).

233. Gu, S., Gupta, R. & Kyprianou, I. Computational high-resolution heart phantoms for medical imaging and dosimetry simulations. *Phys. Med. Biol.* **56,** 5845–5864 (2011).

234. Dennison, S. E. & Delaney, F. A. An in-house phantom as an alternative to commercially available doppler flow phantoms. *Vet. Radiol. Ultrasound* **51,** 545–547 (2010).

235. Poepping, T. L., Nikolov, H. N., Thorne, M. L. & Holdsworth, D. W. A thin-walled carotid vessel phantom for Doppler ultrasound flow studies. *Ultrasound Med. Biol.* **30,** 1067–1078 (2004).

236. Geoghegan, P. H., Buchmann, N. A., Spence, C. J. T., Moore, S. & Jermy, M. Fabrication of rigid and flexible refractive-index-matched flow phantoms for flow visualisation and optical flow measurements. *Exp. Fluids* **52,** 1331–1347 (2012).

237. Lai, S. S. M., Yiu, B. Y. S., Poon, A. K. K. & Yu, A. C. H. Design of anthropomorphic flow phantoms based on rapid prototyping of compliant vessel geometries. *Ultrasound Med. Biol.* **39,** 1654–1664 (2013).

238. Taylor, C. A. & Figueroa, C. A. Patient-specific modeling of cardiovascular mechanics. *Annu. Rev. Biomed. Eng.* **11,** 109–134 (2009).

239. Raine-Fenning, N. J. *et al.* Determining the relationship between three-dimensional power Doppler data and true blood flow characteristics: An in-vitro flow phantom experiment. *Ultrasound Obstet. Gynecol.* **32,** 540–550 (2008).

240. Taylor, C. a, Hughes, T. J. & Zarins, C. K. Finite element modeling of three-dimensional pulsatile flow in the abdominal aorta: relevance to atherosclerosis. *Ann. Biomed. Eng.* **26,** 975–87 (1998).

241. Yunker, B. E. *et al.* The design and fabrication of two portal vein flow phantoms by different methods. *Med. Phys.* **41,** 023701 (2014).

242. Park, M. A., Zimmerman, R. E., Vannah, J. T. & Moore, S. C. Design and fabrication of small phantoms using stereolithography. in *IEEE Nuclear Science Symposium Conference Record* **5,** 3738–3740 (2007).

243. Nguyen, N.-T. & Wu, Z. Micromixers—a review. *Journal of Micromechanics and Microengineering* **15,** R1–R16 (2004).

244. Carrig, C. B. & Pyle, R. L. Anatomic models and phantoms for diagnostic ultrasound instruction. *Vet. Radiol. Ultrasound* **42,** 320–328 (2001).

245. Langer, R. & Vacanti, J. P. Tissue engineering. *Science (80-.).* **260,** 920–926 (1993).

246. Xu, T. *et al.* Complex heterogeneous tissue constructs containing multiple cell types prepared by inkjet printing technology. *Biomaterials* **34,** 130–9 (2013).

247. Ilkhanizadeh, S., Teixeira, A. I. & Hermanson, O. Inkjet printing of macromolecules on hydrogels to steer neural stem cell differentiation. *Biomaterials* **28,** 3936–3943 (2007).

248. Phillippi, J. a *et al.* Microenvironments engineered by inkjet bioprinting spatially direct adult stem cells toward muscle- and bone-like subpopulations. *Stem Cells* **26,** 127–134 (2008).

249. Schmidt, C. E. & Leach, J. B. Neural tissue engineering: strategies for repair and regeneration. *Annu. Rev. Biomed. Eng.* **5,** 293–347 (2003).

250. Ma, W. *et al.* CNS stem and progenitor cell differentiation into functional neuronal circuits in three-dimensional collagen gels. *Exp. Neurol.* **190,** 276–288 (2004).

251. Pepper, M. E. *et al.* Cell settling effects on a thermal inkjet bioprinter. *2011 Annu. Int. Conf. IEEE Eng. Med. Biol. Soc.* 3609–3612 (2011). doi:10.1109/IEMBS.2011.6090605

252. Mironov, V. *et al.* Organ printing: Tissue spheroids as building blocks. *Biomaterials* **30,** 2164–2174 (2009).

253. Elliott, N. T. & Yuan, F. A review of three-dimensional in vitro tissue models for drug discovery and transport studies. *Journal of Pharmaceutical Sciences* **100,** 59–74 (2011).

254. Visconti, R. P. *et al.* Towards organ printing: engineering an intra-organ branched vascular tree. *Expert Opin. Biol. Ther.* **10,** 409–420 (2010).

255. Saunders, R., Gough, J. & Derby, B. Ink jet printing of mammalian primary cells for tissue engineering applications. *Mater. Res. Soc. Symp. Proc.* **845,** 57–62 (2005).

256. Miller, J. S. *et al.* Rapid casting of patterned vascular networks for perfusable engineered three-dimensional tissues. *Nature Materials* **11,** 768–774 (2012).

257. Inamdar, N. K. & Borenstein, J. T. Microfluidic cell culture models for tissue engineering. *Current Opinion in Biotechnology* **22,** 681–689 (2011).

258. Wang, X., Yan, Y. & Zhang, R. Rapid prototyping as a tool for manufacturing bioartificial livers. *Trends Biotechnol.* **25,** 505–13 (2007).

259. Xu, T., Jin, J., Gregory, C., Hickman, J. J. J. J. & Boland, T. Inkjet printing of viable mammalian cells. *Biomaterials* **26,** 93–99 (2005).

260. Triyoso, D. H. & Good, T. A. Pulsatile shear stress leads to DNA fragmentation in human SH-SY5Y neuroblastoma cell line. *J. Physiol.* **515 (Pt 2,** 355–365 (1999).

261. Xu, T. *et al.* Inkjet-mediated gene transfection into living cells combined with targeted delivery. *Tissue Eng. Part A* **15,** 95–101 (2009).

262. Porter, S., Glaser, L. & Bunge, R. P. Release of autocrine growth factor by primary and immortalized Schwann cells. *Proc. Natl. Acad. Sci. U. S. A.* **84,** 7768–7772 (1987).

263. Hu, M., Sabelman, E. E., Tsai, C., Tan, J. & Hentz, V. R. Improvement of Schwann cell attachment and proliferation on modified hyaluronic acid strands by polylysine. *Tissue Eng.* **6,** 585–593 (2000).

264. Ahmed, Z. & Brown, R. A. Adhesion, alignment, and migration of cultured Schwann cells on ultrathin fibronectin fibres. *Cell Motil. Cytoskeleton* **42,** 331–343 (1999).

265. Akassoglou, K., Yu, W. M., Akpinar, P. & Strickland, S. Fibrin inhibits peripheral nerve remyelination by regulating Schwann cell differentiation. *Neuron* **33,** 861–875 (2002).

266. Chahal, D., Ahmadi, A. & Cheung, K. C. Improving piezoelectric cell printing accuracy and reliability through neutral buoyancy of suspensions. *Biotechnol. Bioeng.* **xxx,** 1–9 (2012).

267. Hsieh, H. Ben *et al.* Ultra-high-throughput microarray generation and liquid dispensing using multiple disposable piezoelectric ejectors. *J. Biomol. Screen. Off. J. Soc. Biomol. Screen.* **9,** 85–94 (2004).

268. Koch, L. *et al.* Laser printing of skin cells and human stem cells. *Tissue Eng. Part C. Methods* **16,** 847–854 (2010).

269. Li, M., Guo, Y., Wei, Y., MacDiarmid, A. G. & Lelkes, P. I. Electrospinning polyaniline-contained gelatin nanofibers for tissue engineering applications. *Biomaterials* **27,** 2705–15 (2006).